Development of Photo-CIDNP Methods for NMR Sensitivity Enhancement in Solution & Conformational Changes of the drkN SH3 Protein upon Interaction with the Hsp70 Molecular Chaperone

By

Jung Ho Lee

A dissertation submitted in partial fulfillment of
the requirements for the degree of

Doctor of Philosophy
(Biophysics)

at the
UNIVERSITY OF WISCONSIN-MADISON
2013

Date of final oral examination: 08/19/13

The dissertation is approved by the following members of the Final Oral Committee:

Silvia Cavagnero, Professor, Chemistry
John Wright, Professor, Chemistry
John Markley, Professor, Biochemistry
J. R. Schmidt, Assistant Professor, Chemistry
Sam Butcher, Professor, Biochemistry

어머니, 아버지, 그리고 형에게

To my family

Acknowledgments

I would like to express my deepest gratitude to my advisor Dr. Silvia Cavagnero for the opportunity to participate in the exciting research in her group and for the kind guidance. I owe much of what I am as a scientist to her.

I would like to also thank Dr. Ashok Sekhar for all the teaching and helpful discussions in NMR and for being a good friend. In addition, I was very lucky to be in a department with excellent NMR specialists: Dr. Charlie Fry, Dr. Monika Ivancic and Bob Shanks. Special thanks to Dr. Charlie Fry for sitting restless hours with me to answer my questions on NMR. I also thank Dr. Marco Tonelli and Dr. Milo Westler for their kindness and patience to guide me on NMR experiments in NMRFAM.

I am grateful to my collaborators Yusuke Okuno and Dongyun Zhang. I very much enjoyed talking to Yusuke about science and life. Dongyun (Allison) was probably the most helpful person in the practical aspects of my research. I appreciate her positive spirit and kindness. I am also thankful to Neşe Kurt, Ken Lam, Arelys Rosado, Yufan Wu, Jon Lang and other Cavagnero group members for their continuous support.

Sincere thanks to Dr. John Markley and Dr. John Wright for their support in my postdoctoral application. I also thank Rayna Addabbo and Angela Varela for their helpful advice during this process.

My friends in U.S. and Korea have always been the source of inspiration, peace and energy. I thank them for their company and support.

My family guided me through the brightest and toughest moments of my Ph.D. study. I cannot thank them enough for their endless love and support.

Table of Contents

Abstract viii

Chapter 1 Introduction 1

1.1. NMR Sensitivity 2
  1.1.1. Definition of NMR Sensitivity 2
  1.1.2. Efforts to Improve NMR Sensitivity 5
    1.1.2.1. Fourier Transform NMR 5
    1.1.2.2. Superconducting Magnets and Probe Technology 6
    1.1.2.3. Reduction of Aliased Noise 7
    1.1.2.4. Transfer of Nuclear Polarization from Sensitive to Insensitive Nuclei 8
    1.1.2.5. Sensitivity Enhancement by Attenuation of T_2 Relaxation 8
    1.1.2.6. Other Efforts to Enhance NMR Sensitivity 9
  1.1.3. Hyperpolarization Methods 10
    1.1.3.1. Dynamic Nuclear Polarization 11
    1.1.3.2. Dissolution DNP 14
    1.1.3.3. Para-Hydrogen Induced Polarization 15
    1.1.3.4. Optical Pumping 17
    1.1.3.5. Quantum Rotor Polarization 18
    1.1.3.6. Transfer of Molecular Rotational Polarization to Nuclei 19
1.2. Photochemically Induced Dynamic Nuclear Polarization (Photo-CIDNP) 20
  1.2.1. Instrumental Setup 21
  1.2.2. The Radical Pair Mechanism 23
  1.2.3. Previous Efforts to Enhance NMR Sensitivity by Photo-CIDNP 27
  1.2.4. Major Challenges in Photo-CIDNP 28
  1.2.5. ^{1}H-Detected ^{13}C Photo-CIDNP to Achieve Additional NMR Sensitivity and Heteronuclear Photo-CIDNP Probes 30

1.2.6. A Novel Tri-enzyme System for More Efficient Photo-CIDNP Data Collection 30

1.3. Hsp70 Chaperone – Substrate Interactions 33

1.3.1. Molecular Chaperones 33

1.3.2. Heat Shock Protein 70 (Hsp70) Molecular Chaperone 34

1.3.3. *E. coli* Hsp70: DnaK 35

1.3.4. Molecular Details of the Hsp70 – Substrate Interaction 37

1.3.5. Experimental Conditions 40

1.3.6. Effect of ADP-DnaK on SH3 conformation 41

1.4. References 44

Chapter 2 ^{1}H-detected ^{13}C Photo-CIDNP as a Sensitivity Enhancement Tool in Solution NMR 59

Abstract 60

2.1. Introduction 61

2.2. Experimental Methods 62

2.3. Results and Discussion 64

2.4. Conclusions 81

2.5. References 84

Chapter 3 A Novel Tri-Enzyme System in Combination with Laser-Driven NMR Enables Efficient Nuclear Polarization of Biomolecules in Solution 89

Abstract 90

3.1. Introduction 91

3.2. Experimental Methods 96

3.3. Results and Discussion 100
- 3.3.1. Design of a tri-enzyme system for efficient photo-CIDNP under low-photodegradation conditions 100
- 3.3.2. Efficient photo-CIDNP at low sample concentration (200 μM) in the presence of the tri-enzyme system 102
- 3.3.3. Extending the applicability of the tri-enzyme system to other amino acids and polypeptides at even lower concentration (20 μM) 111
- 3.3.4. Stretching the concentration limits down to 5 μM 118
- 3.3.5. Efficient photo-CIDNP at high sample concentration (5 mM) 121
- 3.3.6. Identity of FMN photodegradation products after prolonged laser irradiation 124
- 3.3.7. Alternative strategies and future perspectives 128

3.4. Conclusions 130

3.5. References 131

Appendix 3A Supplementary Information for Chapter 3 140

Chapter 4 Transient Interactions of a Slow-Folding Protein with the Hsp70 Chaperone Machinery 155

Abstract 156

4.1. Introduction 157

4.2. Experimental Methods 160

4.3. Results 165
- 4.3.1. RNase H^D is a good model substrate to monitor client interaction with the K/J/E chaperone system 165
- 4.3.2. The apparent folding rate of RNase HD decreases in the presence of K/J/E 166
- 4.3.3. Stopped-flow circular dichroism (CD) is consistent with the generation of a partially unfolded K/J-bound substrate, in the absence of GrpE 172

4.3.4. Burst phase CD amplitudes support the existence of transient interactions between RNaseHD and chaperones 174
4.3.5. Analytical size-exclusion, reverse-phase HPLC and SDS-PAGE confirm the existence of a kinetically trapped RNase HD-chaperone complex in the presence of K/J 176
4.3.6. RNase activity assays further support the presence of a substrate complex with K/J, upon refolding RNase HD in the absence of GrpE 182
4.4. Discussion 186
4.5. Conclusions 191
4.6. References 192

Chapter 5 Conformational Changes of the DrkN SH3 Protein upon Interaction with the Hsp70 Molecular Chaperone 200

Abstract 201
5.1. Introduction 202
5.2. Experimental Methods 204
5.3. Results and Discussion 208
5.3.1. Significant Decrease in Native SH3 Population upon Addition of DnaK Chaperone 208
5.3.2. Both Native and Unfolded SH3 States are Associated with DnaK 208
5.3.3. Spectral Analysis of SH3 Resonances in the absence and presence of the DnaK Chaperone 214
5.3.4. Significant Population of SH3 is Bound to DnaK 218
5.3.5. GrpE does not Affect the DnaK-SH3 Interaction 220
5.4. Conclusions 222
5.5. References 225
Appendix 5A Supplementary Information for Chapter 5 229

Chapter 6 Future Directions 232

6.1. Photo-CIDNP 233
6.2. Mechanism of Hsp70 Chaperone – Substrate Interaction 237
6.3. References 240

Abstract

Development of Photo-CIDNP Methods for NMR Sensitivity Enhancement in Solution & Conformational Changes of the drkN SH3 Protein upon Interaction with the Hsp70 Molecular Chaperone

Jung Ho Lee

Under the Supervision of Professor Silvia Cavagnero
in the Biophysics Program and the Department of Chemistry
University of Wisconsin-Madison

Despite the power of many available nuclear hyperpolarization methods, a number of technical challenges often prevent NMR analysis of low-concentration macromolecules in solution. Photochemically induced dynamic nuclear polarization (Photo-CIDNP) provides great opportunities to enhance NMR sensitivity and facilitate the analysis of small and large biomolecules in solution. The first part of my Ph.D. thesis involves the development of a novel photo-CIDNP pulse sequence and the introduction of a tri-enzyme system to improve the performance of photo-CIDNP experiments.

. First, I developed a ^{1}H-detected ^{13}C Photo-CIDNP pulse sequence (Chapter 2), which exploits ^{13}C photo-CIDNP-inducing laser irradiation followed by polarization transfer to ^{1}H for detection. Using this sequence, I was able to achieve large NMR

sensitivity enhancements (up to 16-fold compared to SE-HSQC), for both side chain and backbone resonances of model polypeptides in solution.

Second, I introduced a novel tri-enzyme system to simultaneously recycle the photosensitizer inactive form and prevent sample photodegradation during prolonged high-power laser pulse irradiation (Chapter 3). The addition of catalytic amounts of the try-enzyme system to NMR samples enables long-term sensitivity-enhanced photo-CIDNP data collection, with up to 48-fold greater sensitivity relative to SE-HSQC, at low-micromolar biomolecule concentrations.

The second part of my Ph.D. thesis involves the high-resolution study of protein conformational changes upon interaction with the Hsp70 chaperone. The Hsp70 molecular chaperones are ~70 kDa proteins that play a central role in protein folding, misfolding prevention/correction, and degradation. Kinetic and equilibrium studies were performed to provide insights into how Hsp70 interacts with its substrate.

First, the fact that most proteins have Hsp70 binding sites raises the question of whether Hsp70 interacts with even nonobligatory substrate, i.e., proteins that do not require chaperones to fold. Kinetic studies showed that the interaction of DnaK, the *E. coli* Hsp70, and its co-chaperones with a nonobligatory substrate is short-lived, not interfering with the timely production of substrate and enabling the chaperone to assist other proteins that are prone to aggregation (Chapter 4).

Second, although the conformational changes experienced by chaperone substrates provide key insights into DnaK's function, very few studies were carried out toward this end, especially with full-length protein substrates. By using multidimensional NMR and native gel analysis, we show here that the majority of the marginally stable full-length protein substrate drkN SH3 is associated with DnaK, when the chaperone is added to the medium (Chapter 5). A large shift in population towards the unfolded state, which is believed to be mostly bound, was observed. One or more NMR-invisible “dark states” are proposed to explain the decrease in the overall NMR-detectable populations upon addition of DnaK to the medium.

Future directions are discussed in Chapter 6.

Chapter 1

Introduction

1.1 NMR Sensitivity

Nuclear Magnetic Resonance (NMR) spectroscopy plays a unique role in the determination of molecular structure and dynamics. However, NMR has an intrinsically low sensitivity due to the small energy gap between nuclear spin states, even at high applied magnetic fields. In the past decades, numerous techniques (sections 1.1.2, 1.1.3) have been developed to increase the sensitivity of NMR to extend its applicability. Figure 1.1 illustrates the dramatic increase in the NMR signal-to-noise ratio achieved over the past 40 years. Yet, micromolar and sub-micromolar sample concentrations, which are particularly relevant to the *real* biological world (e.g., proteins in an *in vivo* environment, aggregation-prone biomolecules, and ribosome-bound nascent polypeptides), are still largely inaccessible to NMR investigation.

1.1.1 Definition of NMR Sensitivity

Before discussing NMR sensitivity in further detail, I will first define the term.[1] Sensitivity is defined as the signal-to-noise ratio per unit acquisition time.

$$\text{Sensitivity} = \frac{S}{\sigma_N \sqrt{t}} \tag{1.1}$$

where S is the signal peak amplitude, σ_N is the root mean square (r.m.s.) noise amplitude, and t is the total data acquisition time.

Practically, the r.m.s. noise amplitude can be determined either by r.m.s. time averaging of the noise (by ergodic assumption) or by estimating the expectation value of the peak-to-peak noise amplitude (N_{ptp}) over 100 zero crossings. After calculating N_{ptp},

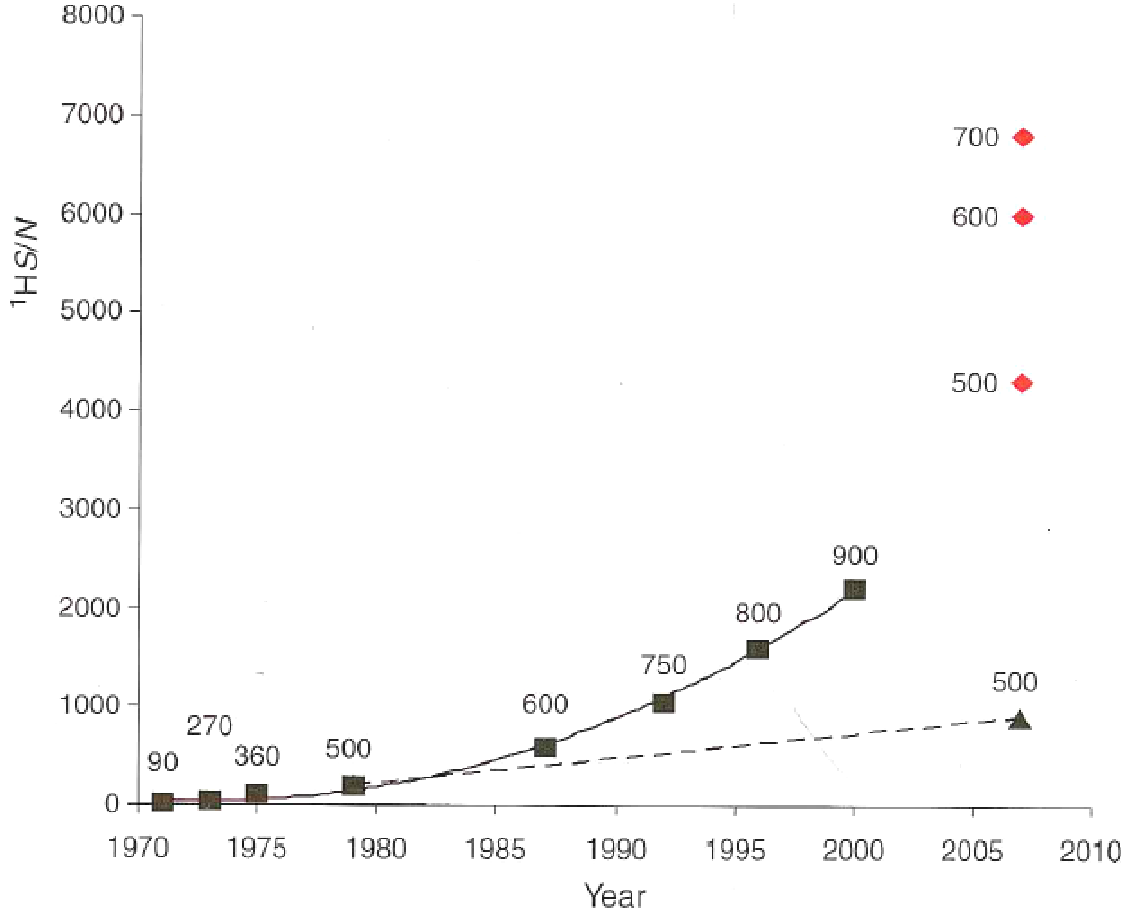

Figure 1.1 Improvements in ^{1}H NMR signal-to-noise ratio (S/N) over the past 40 years. The numbers in the graph indicate the applied magnetic field in MHz. The sensitivity test was performed with the same representative sample, ethyl benzene. Red diamonds denote data collected on cryogenic probes. The dashed line compares the 500MHz S/N at the time of its launch (1979) to the 500MHz S/N in 2007, highlighting the improvement in overall instrument and probe technology. Image adapted from Ref (2); the original source is from Bruker Biospin (2007).

we can used the below equation to estimate σ_N .

$$\langle N_{ptp} \rangle \sim 5.0 \ \sigma_N \tag{1.2}$$

Then the formula for experimentally determining the NMR sensitivity becomes (after introducing a customary factor 2 to account for the ± signs of noise),

$$\text{Sensitivity} = \frac{S}{2\,\sigma_N \sqrt{t}} = \frac{2.5\ S}{\langle N_{ptp} \rangle \sqrt{t}} \tag{1.3}$$

Now one may ask, 'what is the analytical expression for NMR sensitivity?' First, we assume that the Ernst flip angle is employed and matched weighting function is used for processing. Then the sensitivity can be expressed as [1,3,4]

$$\text{Sensitivity} = \frac{S}{\sigma_N \ \sqrt{t}} \propto (\gamma\ B_0) M_0 \left(\frac{T_2}{T_1}\right)^{1/2} \frac{1}{\rho}$$

$$\propto \frac{N\ \gamma^3\ B_0^2\ T_2^{1/2}\ T_1^{-1/2}}{\sqrt{T_c\,R_c + T_a\,(R_c + R_s) + T_s\,R_s}} \tag{1.4}$$

The bulk magnetization M_0 is proportional to $N\gamma^2 B_0$,[5] and (γ B_0) in the upper line denotes the frequency dependence of magnetic induction in the NMR coil. N is the number of NMR-active nuclei in the detection region, γ is the gyromagnetic ratio of the nucleus of interest, B_0 is the applied magnetic field, T_1 and T_2 denote the longitudinal and transverse relaxation time constants, ρ is the square root of the noise power per unit bandwidth, T_c and R_c are the temperature and resistance of the coil, T_s is the sample temperature, R_s is the resistance generated by the sample, and T_a is the noise temperature of the preamplifier. I will refer to equation (1.4) when I explain how different techniques affect NMR sensitivity using different strategies.

Note that the formula corresponding to equation (1.4) differs slightly depending on the literature source. For instance, the dependence of sensitivity on external magnetic field (B_0) is sometimes described as $B_0^{3/2}$ Ref (6,7) or $B_0^{7/4}$ Ref (8). Therefore, I believe that the exact expression for NMR sensitivity is subject to further investigation.

1.1.2 Efforts to Improve NMR Sensitivity

1.1.2.1 Fourier Transform NMR

Before the 1970's, NMR experiments were performed in the continuous wave (CW) mode. In CW NMR, the radiofrequency (RF) wave (or the external magnetic field) is progressively varied to find each resonant RF absorption. On the other hand, Fourier transform (FT) NMR is based on exciting several nuclei at once and recording the free induction decay followed by Fourier transformation. In essence, different frequencies can be probed simultaneously in FT NMR whereas all frequencies have to be scanned individually in CW NMR.

The sensitivity of FT NMR over that of CW NMR is proportional to $\left(\frac{\Omega_{tot}}{\Delta w}\right)^{1/2}$, where Ω_{tot} is the total spectral range and Δw is the FWHH linewidth.[1] This term represents the square root of the number of resonances that can pack into a spectrum. The sensitivity enhancement can reach ~100 fold, highlighting the importance of FT NMR.

1.1.2.2 Superconducting Magnets and Probe Technology

The definition of NMR sensitivity implies that the most straightforward way to enhance sensitivity is to boost the NMR signal or minimize the background noise. The most straightforward way to increase NMR signal is to increase the strength of the applied magnetic field (B_0), as the signal is proportional to B_0^2 according to equation (1.4). The continuous increase in applied magnetic fields (Fig. 1.1) owes much to the development of superconducting magnets. Due to near-zero resistance, superconducting magnets can exceed the magnetic field limit imposed by the iron-based electromagnets (~2.3 T) and also enable cheap operation of the spectrometer since virtually no heat is dissipated during operation. Currently, YBCO and Bi2223 conductors are employed to make 1.3 GHz NMR spectrometers.[9]

Probe design has also greatly improved to match the sensitivity needs.[2] This is illustrated by the dotted line in Figure 1.1, where even at the same magnetic field, the sensitivity has increased by 5-fold at 2007 compared to 1979. First, modern receiver coils are made of composite metals with virtually no magnetic susceptibility causing no distortion to the magnetic field, leading to better lineshape and signal-to-noise. In addition, active sample volume (in which the magnetic field is uniform) has increased due to improvements in shimming systems, leading to a larger number of NMR-active nuclei in the detection region (N in equation 1.4). Additionally, electronics have improved to give rise to smaller system noise, especially at the preamplifier stage. Furthermore, strategies have been developed to minimize aliased noise (next section).

Another important breakthrough to improve NMR sensitivity was the introduction of cryogenic probes.[8,10,11] By cooling the RF coils to ~ 25K and preamplifier to ~70K, the thermal noise can be reduced significantly. This was a remarkable technical challenge since the detection coil has to be cooled to 25K, while the sample has to be maintained at room temperature, while the two are only a few millimeters apart. A more formal description of the contribution of cryogenic probes to NMR sensitivity relies on equation (1.4). When the T_c (temperature of the coil) and T_a (noise temperature of the preamplifier) are lowered, the first two terms of the denominator in equation (1.4) are reduced, contributing to the overall gain in sensitivity.

1.1.2.3 Reduction of Aliased Noise [2,5]

When a resonance falls outside the acquired spectral window, it can be detectable but shows up at an incorrect frequency. This resonance is said to be aliased or folded. This is also the case for noise, and since the noise is expected to be nearly white (i.e. characterized by all frequency components), infinite amount of noise can fold back into the spectral window and wipe out NMR signals.

Thus, analog filters are used to limit the bandwidth of the signal. However, since the analog filters cannot give ideal sharp cutoffs, filter passband should be greater than the spectral range of interest, and some noise unavoidably gets aliased into the spectrum. When sharp cutoffs are used, analog filters introduce a variety of distortions in the spectrum.

Therefore, a commonly used strategy is to first apply an analog filter (with a larger passband than the desired spectral window and with relaxed cutoff criteria to minimize distortion) to the audio-frequency analog signals to remove broadband noise. Then, oversampling is performed (faster sampling than required by the Nyquist condition) to get a much larger spectral window than necessary. The wings of the large spectral window contain the aliased noise. The following digital filtration removes the wings of the large spectral window and acquires the desired spectrum without the aliased noise. Oversampling also has implications for quantization noise, a “rounding error” inherent in the digitization process. When data are digitized at a much faster rate than required by the Nyquist condition and the running average is calculated for the digitized points via the digital filtration, the “rounding error” or “quantization noise” is minimized.

1.1.2.4 Transfer of Nuclear Polarization from Sensitive to Insensitive Nuclei

The INEPT (Insensitive Nuclei Enhanced by Polarization Transfer)[12] NMR experiment can be employed to transfer magnetization in the presence of scalar coupling between sensitive and insensitive nuclei. INEPT is used in numerous pulse sequences in solution NMR. Heteronuclear NOE (Nuclear Overhauser Effect)[13] can also be used when sensitive and insensitive nuclei are in close proximity in space. For instance, ^1H saturation, producing steady-state NOE, leads to higher ^{13}C sensitivity. Lastly, CP (Cross Polarization)[14] is usually used in solid-state NMR to transfer polarization from ^1H to ^{13}C and ^{15}N. The CP polarization transfer occurs in the presence of dipolar coupling between two nuclei of interest.

1.1.2.5 Sensitivity Enhancement by Attenuation of T_2 Relaxation

Improving spectral resolution can also lead to improvements in sensitivity, which is proportional to $\sqrt{T2}$ as illustrated in equation (1.4). In Transverse Relaxation

Optimized SpectroscopY (TROSY) experiments, T_2 relaxation is attenuated by selecting the longest-lived coherences caused by the destructive interference between dipolar and chemical shift anisotropy (CSA) relaxation mechanisms[15] or between ^1H–^1H and ^1H–^{13}C dipolar relaxation mechanisms[16]. Other methods[17,18] lead to the narrowing of the spectral lines broadened by conformational exchange according to the "chemical shift scaling"[19] concept via CPMG (Carr-Purcell-Meiboom-Gill)[20] sequences or WAHUHA[21] based four-pulse sequences applied during the chemical shift evolution time. This strategy leads to slower chemical shift evolution while the physical conformational transitions are not affected, thereby pushing the exchange regime to 'fast' on the NMR chemical shift time scale, and leading to sharper linewidths.

1.1.2.6 Other Efforts to Enhance NMR Sensitivity

Various other methods are employed to achieve additional NMR sensitivity. First of all, sample preparation can be tailored for high sensitivity. For instance, ^{13}C-, ^{15}N-, and ^2H-enriched biomolecules can be prepared so that sensitivity is not limited by the natural abundance of the NMR-active nuclei, and so that dipolar relaxation pathways, spin diffusion and passive scalar couplings are reduced.[22,23] In addition, NMR samples can be prepared in Shigemi tubes to concentrate limited amount of samples in the detection coil region. Second, in ^1H-detected multidimensional NMR experiments, the "preservation of equivalent pathways" method[24] can be used to gain sensitivity improvements by factors up to $\sqrt{2}$ relative to conventional experiments. In addition, optimization of pulse sequences (e.g. utilization of pulse field gradients, minimization of time that the magnetization stays in the transverse plane, or efficient guidance of nuclear polarization to the preferred pathway without loss) can contribute to NMR sensitivity. Furthermore, fast NMR data acquisition (e.g. SOFAST NMR)[25] or nonuniform sampling[122] strategies can be employed to reduce NMR data collection times to achieve the same S/N. After NMR data collection, window functions can be applied to the free induction decay to improve sensitivity (often at the cost of spectral resolution).

The plethora of efforts to enhance NMR sensitivity described in section 1.1.2 testifies the importance of high sensitivity in NMR. Despite the successful efforts, NMR sensitivity is still limited, especially for applications involving biological samples.

One must not forget that the NMR signal originates from the negligible difference in thermal spin populations even in the presence of strong magnetic fields. The goal of the next section 1.1.3 is to describe efforts to perturb this negligible difference to achieve higher NMR sensitivity.

1.1.3 Hyperpolarization Methods

The NMR signal arises from the differences in Zeeman populations of the nuclear spin states in the presence of a magnetic field. Even in the presence of the strongest known magnet, however, the nuclear spin polarization of ^{1}H, defined as the population difference between the alpha and beta spins over the total spin population, is less than 10^{-4} at physiologically relevant temperatures. The NMR sensitivity improvement strategies discussed in section 1.1.2 build upon this marginal nuclear polarization at thermal equilibrium. Hyperpolarization methods, on the other hand, take a different approach to directly perturb the thermal equilibrium upon coupling nuclei to other highly polarized quantum states.

1.1.3.1 Dynamic Nuclear Polarization

Dynamic Nuclear Polarization (DNP)[26,27] is a method based on the saturation of the energy level differences between certain electron-nuclear spin states in the presence of a magnetic field to transfer spin polarization from electrons to nuclei. The large gyromagnetic ratio difference between electron and nucleus (e.g. γ_e / γ_{H1} = 660) reflects the huge spin polarization that can be transferred between the two species. The exact mechanism of DNP (Fig. 1.2) (and the matching microwave saturation frequency) depends on the experimental conditions on whether DNP is performed in solution or solid state, the kind of radical as the source of unpaired electrons, and the concentration of the radical.

Overhauser Effect (OE)[28] is a mechanism by which nuclei can be directly polarized in solution. The applied microwave frequency is exactly centered on the electron Larmor frequency to saturate the levels between $\left|\,\alpha\,\alpha\,\right\rangle$ ($\left|\text{electron, nucleus}\right\rangle$) and $\left|\,\beta\,\alpha\,\right\rangle$, as well as $\left|\,\alpha\,\beta\,\right\rangle$ and $\left|\,\beta\,\beta\,\right\rangle$ states (Fig. 1.2a). This phenomenon leads to time-dependent double-quantum and zero-quantum relaxation, driven by electron-nucleus dipolar interaction and hyperfine scalar coupling, leading to nuclear spin polarization. OE is limited by the microwave power due to heating of solvents and nonlinear decrease of DNP enhancements upon increase of magnetic field.[27] However, recent innovative approaches have been able to tackle these problems.[29,30]

a) Overhauser Effect

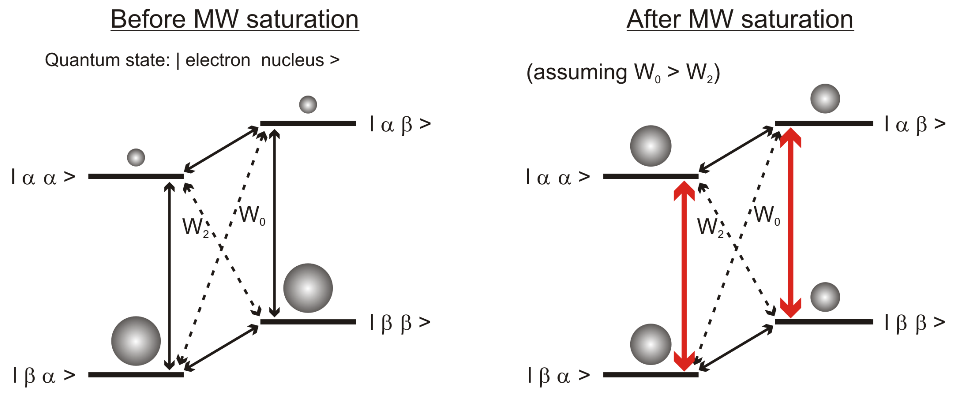

Before MW saturation

After MW saturation

Quantum state: | electron nucleus >

(assuming $W_0 > W_2$)

b) Solid Effect

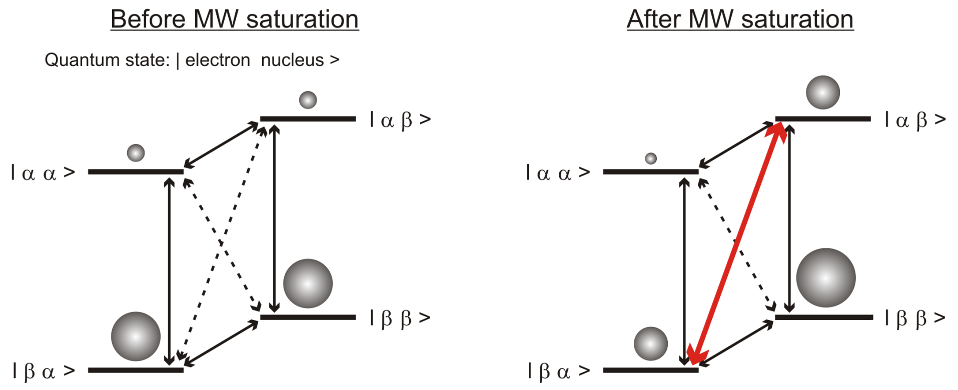

Before MW saturation

After MW saturation

Quantum state: | electron nucleus >

c) Cross Effect & Thermal Mixing

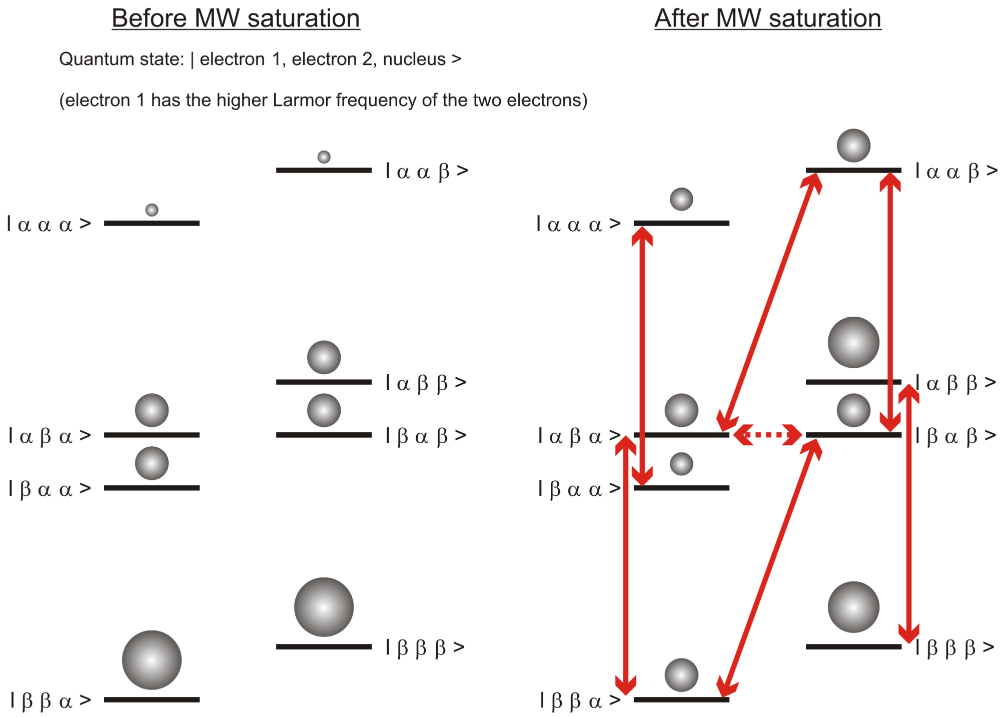

Before MW saturation

After MW saturation

Quantum state: | electron 1, electron 2, nucleus >

(electron 1 has the higher Larmor frequency of the two electrons)

Figure 1.2 Energy level diagrams for different DNP mechanisms. The black lines denote allowed transitions, while the black dotted lines indicate forbidden transitions. The thick red lines denote the transitions that are saturated by the microwave (MW) radiation. Note that the α state indicates a spin magnetic moment aligned with the magnetic field, and the β state is the moment aligned against the field. In addition, the size of the sphere on top of each eigenstate represents its population. a) Overhauser effect. After saturation, the nuclear spin is polarized to the α state. b) Solid effect. After saturation, the nuclear spin is polarized to the β state. The other forbidden transition can be saturated instead, which leads to the polarization of the α nuclear state. c) Cross effect and Solid effect. After saturation, the nuclear spin is polarized to the β state (the right hand side). Similarly, microwave frequency can be chosen as the difference between the Larmor frequencies of electron 2 and the nucleus, which leads to nuclear polarization of the α state. The fact that the two energy levels connected by the red dotted line are the same allows mixing of these two states and produces the saturation pattern shown in the figure.

Solid Effect (SE) is a mechanism responsible for DNP in the solid-state samples at low temperature. Here, microwave frequency is set to electron Larmor frequency ± nuclear Larmor frequency to directly excite the zero and double quantum transitions (Fig. 1.2b). The DNP enhancement scales with B_0^{-2} (in contrast to B_0^{-1} in CE and TM, the mechanisms described below),[27] imposing a limit to SE at high field strengths. At the low temperatures, quantum rotor transitions in methyl groups (section 1.1.3.5) also take place.

In Cross Effect (CE) and Thermal Mixing (TM) mechanisms, biradicals such as TOTAPOL[31] are usually employed, although the effect can be observed with the high concentration monoradicals as well. The difference between the Larmor frequencies of the two unpaired electrons in a biradical matches the nuclear Larmor frequency such that energy diagram looks like Fig. 1.2c (note that the energy levels connected by the red dotted line are the same). In principle, the microwave frequency should be set to the higher-Larmor-frequency unpaired electron, but practically it is set to a value that gives maximum polarization. Although the CE and TM mechanisms are similar, TM requires higher radical concentrations to generate homogeneous ESR line broadening arising from strong electron dipolar interactions.

1.1.3.2 Dissolution DNP

Dissolution DNP gives the highest signal-to-noise ratio enhancement among all DNP methods.[27] The nuclear polarization is prepared by microwave irradiation at ~1.1 K in a low-magnetic-field spectrometer. Then the sample is rapidly melted and dissolved in a hot pressurized solvent and transferred to conventional NMR spectrometer for detection. The above steps can lead to sensitivity enhancements greater than 10,000-fold.[32] this number is derived from the Boltzmann enhancement (nuclear polarization is prepared at 1.1 K and detected at 300K) multiplied by the DNP enhancement. In addition, NMR detection in solution state gives rise to additional sensitivity due to rapid molecular tumbling.

Although the dissolution DNP enhancement mechanism is usually attributed to SE or TM, the exact mechanism at this low temperature is not well understood. Higher polarizations at higher field strengths are often observed in dissolution DNP,[33] which is in clear disagreement with the B_0^{-2} or B_0^{-1} dependence of nuclear polarization observed in SE or TM.

One major drawback of dissolution DNP is that it works through an irreversible single step, only allowing NMR data acquisition within the nuclear T_1 timescale. Furthermore, this single freeze-and-thaw cycle is rather harsh, preventing most biological macromolecules to be studied by this method. However, the huge attainable enhancements enabled many *in vivo* applications in metabolic imaging.[34,35] Furthermore, the fast data acquisition[36,37] and the divided usage of magnetization[38] schemes enable multidimensional NMR using a single hyperpolarized magnetization.

1.1.3.3 Para-Hydrogen Induced Polarization (PHIP)

The hydrogen molecule can exist in two nuclear spin configurations, namely, triplet state (ortho-H_2) and singlet state (para-H_2). Although 75% ortho-H_2 and 25% para-H_2 exist at room temperature, para-H_2 can be polarized to 99.9% at 4K in the presence of a charcoal catalyst. PHIP[39] works by transferring the spin-ordered atoms in the para-H_2 to the substrate of interest, for example by Wilkinson's catalyst. There are two ways in which PHIP can be implemented; PASADENA[40] and ALTADENA[41].

In PASADENA (parahydrogen and synthesis allow dramatically enhanced nuclear alignment), para-H_2 reacts with substrate inside the high-field magnet. Right after the singlet nuclear spin state, $\frac{1}{\sqrt{2}}\left(|\alpha\beta\rangle - |\beta\alpha\rangle\right)$, is transferred from para-H_2 to the substrate, the singlet state is immediately broken by the chemical shift difference between the two transferred protons in the substrate, leading to polarization of the two eigenstates in the high magnetic field, $|\alpha\beta\rangle$ and $|\beta\alpha\rangle$. Thus the NMR spectrum is characterized by two polarized antiphase doublets.

In ALTADENA (adiabatic longitudinal transport after dissociation engenders net alignment), para-H_2 reacts with substrate in low magnetic field, followed by adiabatic transfer of the sample to the NMR spectrometer for detection. In this case, singlet nuclear spin state, $\frac{1}{\sqrt{2}}\left(|\alpha\beta\rangle - |\beta\alpha\rangle\right)$, is not immediately broken but adiabatically changes to only one of the $\alpha\beta$ or $\beta\alpha$ states. Now the NMR spectrum is characterized by two polarized opposite sign peaks. In case there are other magnetically active nuclei in the substrate, NOE, scalar coupling and dipolar coupling can cause spin order to spread throughout the substrate during the low field period.[42]

Although it was traditionally thought that a covalent modification of the substrate is necessary for PHIP, NMR signal amplification by reversible exchange (NMR-SABRE)[43] technique was recently developed to facilitate metal-complex-mediated reversible interaction of para-H_2 with organic substrates for nuclear polarization transfer.

This technique works in ALTADENA mode and can lead to 800-fold signal increase in ^{1}H, ^{13}C, and ^{15}N in a pyridine substrate.

1.1.3.4 Optical Pumping

By using circularly polarized light excite electronic transitions, selection rules can be controlled. Note that in the hyperfine structure of a molecule, the electron's orbital angular momentum, the electron’s spin, and the nuclear spin add up to be the total angular momentum J. In the presence of an applied magnetic field, M = -J, …, J-1, J quantum states become non-degenerate. When right-circularly-polarized light is irradiated in the same direction as the applied magnetic field, only $\Delta M = 1$ is selected during excitation. Likewise, when left-circularly-polarized light is irradiated in the same direction as the applied magnetic field, only $\Delta M = -1$ can occur. Since the relaxation process does not have a preferred ΔM, continuous molecular excitation by circularly-polarized light pushes M to its extreme values (J or –J). The optical pumping method employs this strategy to enhance nuclear polarization.

In alkali-metal spin exchange optical pumping, the unpaired electron in the ground state of rubidium, 5 $^2S_{1/2}$ (m=-1/2), is first excited to 5 $^2P_{1/2}$ (m=1/2) by using right-circularly-polarized light. Upon collisions, 5 $^2P_{1/2}$ (m=1/2) is equilibrated with 5 $^2P_{1/2}$ (m=-1/2) followed by relaxation to 5 $^2S_{1/2}$ (m=1/2) and 5 $^2S_{1/2}$ (m=-1/2) states. Consequently, 5 $^2S_{1/2}$ (m=-1/2) is continuously pumped to 5 $^2S_{1/2}$ (m=1/2) and 5 $^2S_{1/2}$ (m=-1/2) leading to a polarized 5 $^2S_{1/2}$ (m=1/2) state. When ^{129}Xe is introduced into the system, spin exchange between rubidium and ^{129}Xe occurs by Fermi-contact hyperfine interactions leading to hyperpolarization of the ^{129}Xe gas. In the metastability exchange optical pumping, the ground electronic state (1 $^1S_0$) of helium is first excited to the metastable state (2 $^3S_1$) by RF field. Right-circularly-polarized light is irradiated on 2 $^3S_1$ m=-3/2 and -1/2 states to yield 2 $^3P_0$ m= -1/2 and 1/2 states, respectively, followed by relaxation to 2 $^3S_1$ with the average ΔM of zero. Again, collision between polarized 2 $^3S_1$ with 1 $^1S_0$ leads to nuclear polarization of the helium ground states (1 $^1S_0$).[44,45]

Applications of optical pumping are very diverse, range from semiconductor quantum wells[46] to lung imaging[47].

1.1.3.5 Quantum Rotor Polarization (QRP)[48,49]

In QRP, also known as Haupt effect, nuclear polarization stems from the coupling between the nuclear spin states and the rotational quantum states of methyl groups.

Methyl groups exist in three rotational-symmetry-allowed eigenstates, namely, A, E_a, and E_b. They cannot be separated from the nuclear spin degrees of freedom, and thus the exclusion principle confines the A state to the nuclear spin-3/2 quartet, and the E states to the nuclear spin-1/2 doublet.

Torsional energy levels determine the relative energy levels between A, E_a, and E_b. At low temperature, methyl groups are in the ground torsional state, where A state occupies the lowest energy (highest population) and transition between the A, E_a, and E_b states occur by quantum tunneling. The A-E transition rate is very slow, since the process has to couple both the space (A → E) and the spin (3/2 → 1/2) degrees of freedom.

Upon temperature jump to low temperature, A, E_a, and E_b distributions relax to their equilibrium states, where A is the dominant population. The methyl intramolecular dipolar Hamiltonian allows the A-E transition, albeit slow, with a flip of one proton spin simultaneously with the change in the rotational symmetry state. This leads to accumulation of nuclear polarization over a long period of time.

Recently, the solid-state Haupt effect has been coupled to dissolution process for solution NMR detection and tested on many small molecules.[50]

1.1.3.6 Transfer of Molecular Rotational Polarization to Nuclei

In the course of efforts to accurately characterize electronic angular momentums in photodissociated products, atoms with zero nuclear spins were used so that electronic polarization is not depolarized by the nuclear spin (hyperfine depolarization).[51] In order to study molecules that possess nonzero nuclear spins, large nuclear polarization can be created to suppress the hyperfine depolarization.[52]

This experiment was carried out by first preparing a highly polarized rotational molecular state by pulsed laser or microwave excitation. The hyperfine beating that results from this excitation cycles the nuclear polarization between zero and a maximum value, with the rotational polarization showing the opposite behavior. Timely photodissociation of the molecule when nuclear polarization reaches the maximum value “freezes” the high nuclear polarization.

From the NMR standpoint, this technique can be used not to optimize molecular photodissociation, but to maximize nuclear polarization. Although this method can only be used in small molecules where molecular rotational states are well defined, and it involves photodissociation, close to 100% nuclear polarization can be achieved by this approach.[52,53]

1.2 Photochemically Induced Dynamic Nuclear Polarization (Photo-CIDNP)

Hyperpolarization methods provide great opportunity to enhance NMR sensitivity by directly polarizing the nuclear spin states. However, these methods usually involve solid states, small molecules or nonnative conditions and therefore generally unsuitable for the analysis of biological macromolecules. I will describe an alternative approach that I explored in my Ph.D. project.

Chemically Induced Dynamic Nuclear Polarization (CIDNP)[54,55] was first discovered in polymerization reactions using free radical initiators[56] and halogen-metal exchange reactions[57]. Soon after,[58] it was shown that the CIDNP effect can also be generated upon light irradiation. This phenomenon is now known as photochemically induced dynamic nuclear polarization (photo-CIDNP).

Photo-CIDNP has been traditionally used to study free radical chemistry,[59,60] biomolecular interactions,[54, 61,62] and protein folding,[63-65] since the photo-CIDNP mechanism (section 1.2.2) involves the physical interaction between a dye and the substrate of interest, followed by transient radical pair formation.

Given that Photo-CIDNP gives rise to nuclear polarization under mild solution conditions, this technique offers considerable potential and opportunities, mostly unexplored to date (section 1.2.3), as an NMR sensitivity enhancement tool for the study of both small and large biomolecules in solution.

In order for photo-CIDNP to become a general NMR sensitivity enhancement tool, however, challenges remain (section 1.2.4). My Ph.D. thesis focuses on the efforts to render the photo-CIDNP method a more powerful tool to enhance NMR sensitivity in solution. My approach is summarized in sections 1.2.5 and 1.2.6.

1.2.1 Instrumental Setup

Compared to other nuclear polarization methods described in section 1.1.3, the photo-CIDNP hardware setup is quite simple (Fig. 1.3). I will start by introducing how the photo-CIDNP experiments are practically implemented.

An argon ion laser (2017-AR, Spectra-Physics - Newport Corporation, Irvine, CA) in multiline mode (main lines at 488 and 514 nm) is used as a light source. The laser light is focused into an optical fiber using a convex lens (LB4330, Thorlabs, Newton, NJ) and a fiber-coupler (F-91-C1-T, Newport Corporation). The optical fiber is guided into the NMR sample tube via a coaxial insert (WGS-5BL, Wilmad-Labglass, Buena, NJ). The position of the coaxial insert is adjusted such that the tip of the fiber is located 5 mm above the receiver coil region. This setup provides ~50% laser-to-fiber coupling efficiency.

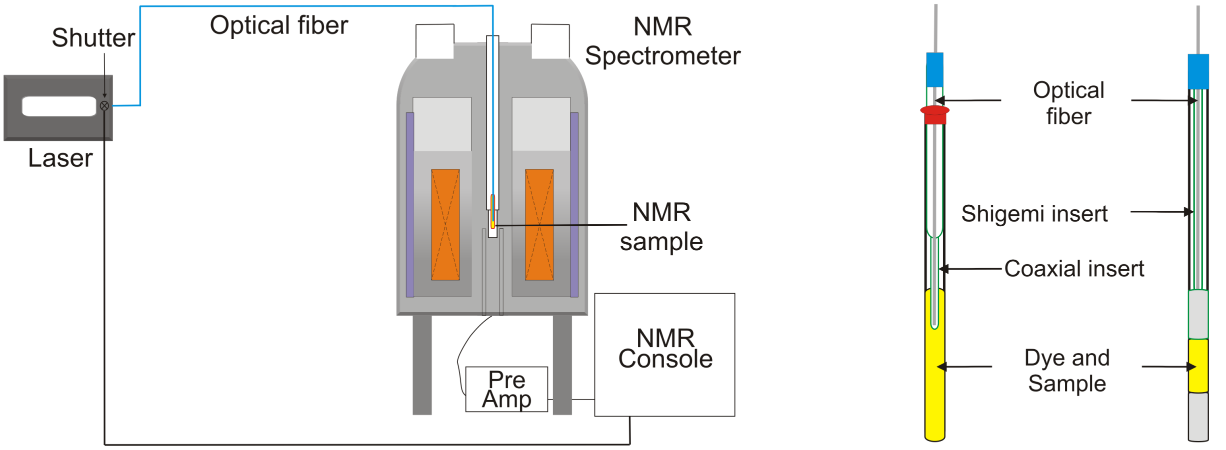

a) Layout of the Photo-CIDNP Experiment

b) Inside the NMR tube

c) Stabilite 2017 Argon-Ion Laser (6W, multiline mode)

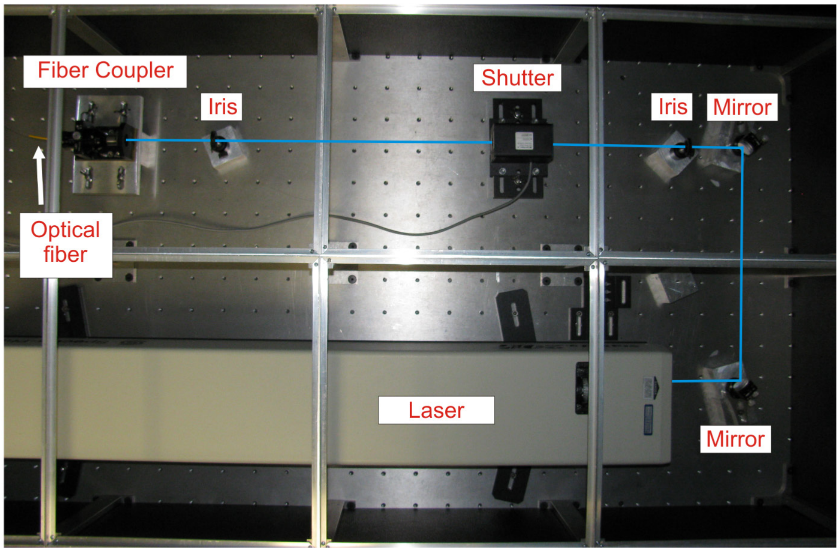

Figure 1.3 Photo-CIDNP instrumentation. a) In addition to the NMR spectrometer, light source (often an argon ion laser) and optical fiber are installed to guide the light into the NMR spectrometer. b) The coaxial insert guides the optical fiber into the sample. Shigemi NMR tubes can also be used. c) The laser light is focused into the optical fiber by using convex lens. The shutter is controlled by the pulse sequence program.

1.2.2 The Radical Pair Mechanism[66-69]

According to the Radical Pair Mechanism, photo-CIDNP proceeds via laser-triggered formation of a transient radical pair between oxidizable amino acids (typically Trp, His and Tyr) and a light-absorbing oxidizing dye (often flavin mononucleotide, FMN). After laser irradiation, the photo-excited dye in its triplet state extracts an electron from a nearby residue, giving rise to a transient radical pair. Recombination takes place next, to generate the original species. Recombination rates depend on the hyperfine coupling between unpaired electron and the surrounding nuclei. (Fig. 1.4)

The effect of hyperfine coupling can be highly nuclear-spin-state-dependent, resulting in the selectively faster recombination of one of the nuclear spin states (α or β, in case of spin-1/2 nuclei). This process leads to enrichment in the fast-recombining nuclear spins, and is the key aspect of photo-CIDNP. The fraction of molecules bearing the nuclear spin state with slower recombination rate does not effectively contribute to the net polarization. In this class of molecules, the radical pairs are often sufficiently long-lived to dissociate and then undergo rapid paramagnetic nuclear relaxation, leading to thermally equilibrated spin populations at the applied field. (Fig. 1.5)

All magnetically active nuclei of the solvent-exposed samples oxidizable by the excited dyes are potential photo-CIDNP candidates. In order for the sample to be oxidizable, the oxidation potential of the sample should be less than the reduction potential of the excited dye. The fact that only Trp, His and Tyr (Met to a weaker extent) have lower oxidation potentials than the FMN reduction potential,[70] explains why they are the only photo-CIDNP-active amino acids.

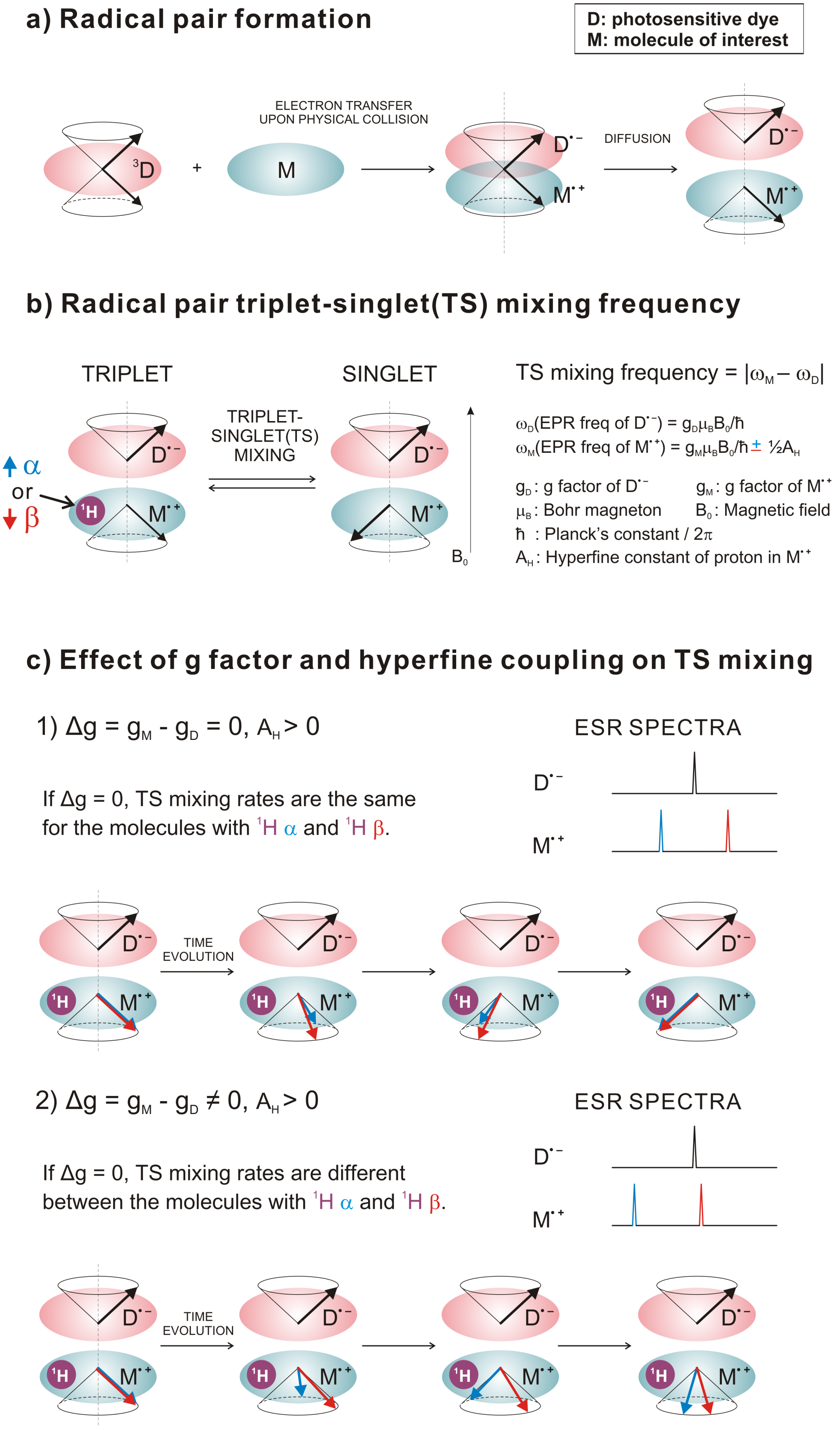

a) Radical pair formation

b) Radical pair triplet-singlet(TS) mixing frequency

c) Effect of g factor and hyperfine coupling on TS mixing

Figure 1.4 Key concepts in photo-CIDNP. a) Radical pair formation by electron transfer from the molecule of interest to the dye is the first step of photo-CIDNP. The two radicals composing the pair diffuse apart, leading to similar energy levels between the triplet $\frac{1}{\sqrt{2}}\left(\left|\alpha\,\beta\right\rangle+\left|\beta\alpha\right\rangle\right)$ and the singlet $\frac{1}{\sqrt{2}}\left(\left|\alpha\,\beta\right\rangle-\left|\beta\alpha\right\rangle\right)$ radical pairs, thus enabling triplet-singlet (TS) mixing. b) Hyperfine coupling between the unpaired electron and the nuclei in the oxidized molecule can affect the TS mixing frequency. c) Difference in nuclear spin states can cause difference in TS mixing rates only when $\Delta g \neq 0$. To illustrate this point, vector diagrams for unpaired electron spin precession (caused by the applied magnetic field) as well as corresponding ESR spectra are shown for both the $\Delta g = 0$ and $\Delta g \neq 0$ cases.

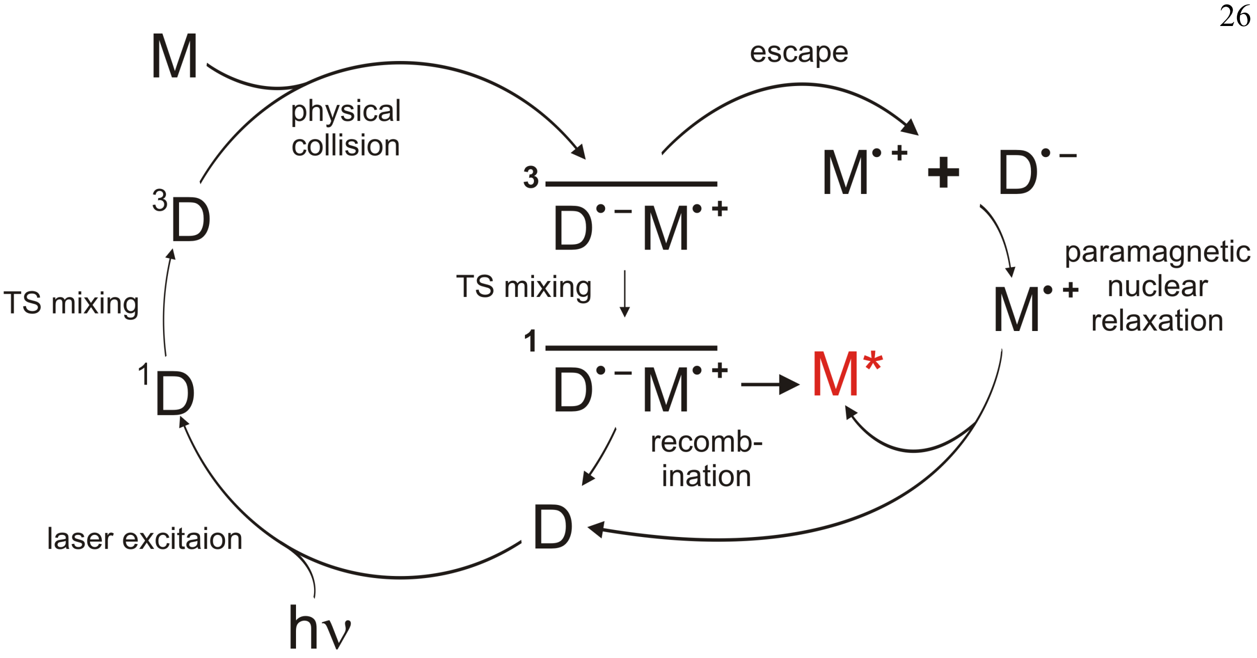

D: photosensitive dye
M: molecule of interest (aromatic amino acid or nucleotide)

Figure 1.5 The radical pair mechanism. The red M* denotes the nuclear-spin-polarized molecule. Assume that a particular ^{1}H in the α spin state enhances the rate of radical pair TS mixing and the β spin state (of the same ^{1}H) slows down the process. Then the α spin is preserved by rapid recombination while the β spin is paramagnetically relaxed to comparable α and β spin populations, leading to an overall α spin polarization. This diagram was modified from Ref (54).

1.2.3 Previous Efforts to Enhance NMR Sensitivity by Photo-CIDNP

The heteronuclear photo-CIDNP sensitivity enhancement efforts carried out so far focused on the Trp indole ^{15}N-^{1}H bond pair, and exploited a) ^{15}N CIDNP followed by $^{15}N \rightarrow ^{1}H$ nuclear polarization transfer,[71] b) ^{1}H CIDNP followed by $^{1}H \rightarrow ^{15}N \rightarrow ^{1}H$ transfer,[71,72] c) $^{1}H \rightarrow ^{15}N$ nuclear polarization transfer followed by ^{15}N CIDNP and $^{15}N \rightarrow ^{1}H$ transfer,[73] or a combination of b) and c).[73] While these early studies led to promising enhancements, their applicability is limited by the fact that the ^{15}N-^{1}H pair in the Trp indole is the only viable probe. Furthermore, the Trp indole ^{15}N-^{1}H resonances tend to be poorly dispersed in nonnative proteins.[74]

In addition, another method was developed to sustain photo-CIDNP-polarized longitudinal magnetization for longer time periods.[75] When the photo-CIDNP experiment is performed at low applied magnetic fields, the singlet states are directly populated (or depleted) in comparison to triplet states. This phenomenon arises from the fact that hyperfine couplings (like J couplings)[76] become the dominant Hamiltonian in low fields. The stored magnetization can be adiabatically transferred to the NMR spectrometer for detection. The long-lived magnetization can be utilized in imaging and quantum computing applications.

It is also worth mentioning that very high nuclear polarizations can be generated by photo-CIDNP in special systems. In solid[77] and solution[78] states, photosynthetic reaction centers are known to provide ~10,000-fold photo-CIDNP sensitivity enhancements. A similar effect is observed for blue-light photoreceptors in the solid state.[79] These observations stem from the large hyperfine couplings in the electron-donor chlorophyll (or flavin in case of the blue-light photoreceptors) as well as the different photo-CIDNP mechanisms that prevail in very slowly tumbling systems.[80]

1.2.4 Major Challenges in Photo-CIDNP

Despite the efforts to improve NMR sensitivity by photo-CIDNP (section 1.2.3), challenges remain to render photo-CIDNP a general NMR sensitivity enhancement tool (Fig. 1.6).

First of all, despite the uniqueness of photo-CIDNP among all nuclear polarization methods to study macro-biomolecules in solution, the sensitivity enhancement achieved so far has not been as huge as the enhancements provided by other hyperpolarization methods.[81] Thus, in order to study very low concentration (μM-nM) samples or combine photo-CIDNP with fast data acquisition schemes,[36] additional methods to further the sensitivity of photo-CIDNP are needed.

One of the major advantages in photo-CIDNP is that no pre-polarization period is necessary unlike most of the hyperpolarization methods. This enables a multi-scan photo-CIDNP experiment to collect multidimensional NMR spectra and achieve additional sensitivity enhancement by signal averaging. However, in reality, dye photoreduction as well as sample photodegradation prevent prolonged photo-CIDNP data collection. Therefore, methods to reverse or prevent these side effects caused by high-power laser pulses are highly desirable.

Finally, photo-CIDNP-active probes are limited. In the case of polypeptides, the probes are confined to solvent-exposed Trp, Tyr, and His amino acids. Even more, heteronuclear photo-CIDNP experiments are restricted to the Trp indole ^{1}N-^{1}H pair. Therefore efforts to extend the photo-CIDNP-active probes are highly needed.

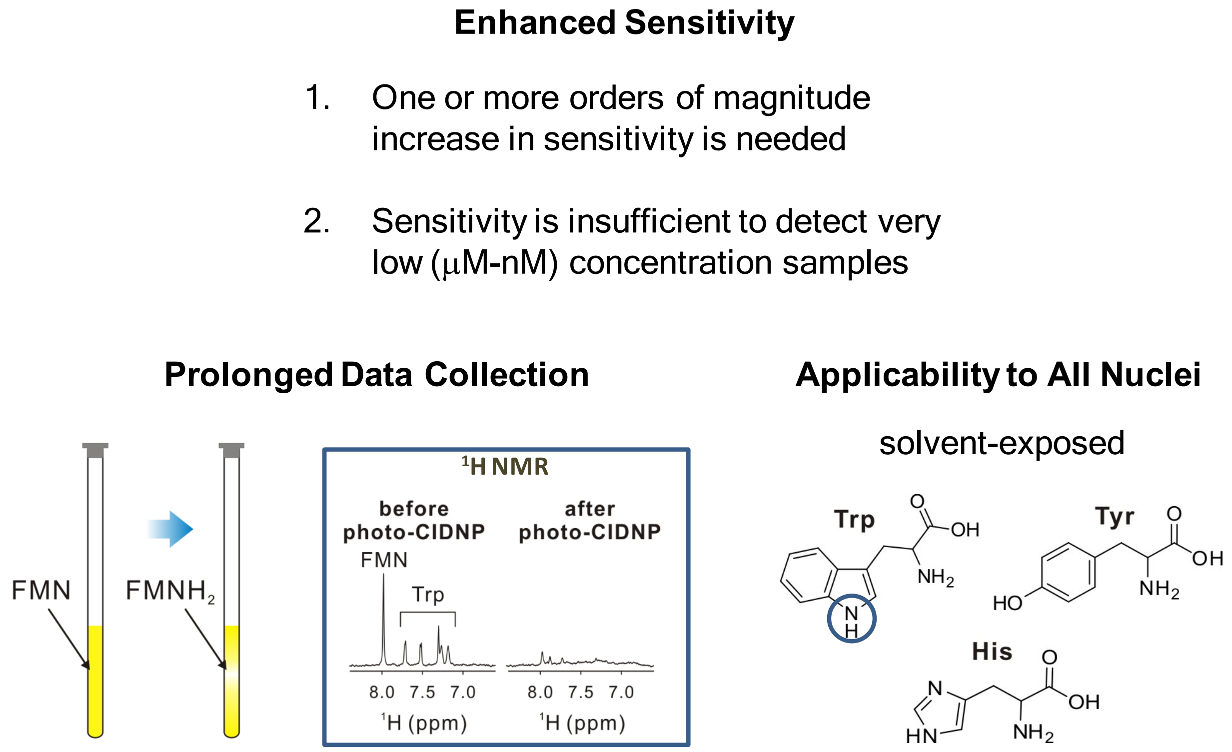

Figure 1.6 Major Challenges in Photo-CIDNP. Increasing sensitivity, enabling long-term data collection by preserving sample and dye integrity, and extending the number of photo-CIDNP-active moieties are the prominent current challenges in photo-CIDNP.

1.2.5 ^{1}H-detected ^{13}C photo-CIDNP to achieve additional NMR sensitivity and heteronuclear photo-CIDNP probes[82] (Chapter 2)

Inspired by the established existence of ^{13}C photo-CIDNP,[79 83] the large enhancements achieved via ^{1}H-detected ^{15}N heteronuclear photo-CIDNP,[71, 73] and considering that there are many ^{13}C-^{1}H bond pairs in aromatic residues, I explored the potential of heteronuclear ^{1}H-detected ^{13}C photo-CIDNP. As shown in Chapter 2, this effect leads to large NMR sensitivity enhancements in several ^{13}C-^{1}H resonances of Trp, His and Tyr, including both side chain and, intriguingly, also backbone ^{13}C$^{\alpha}$-^{1}Hs. Thus, ^{13}C photo-CIDNP followed by polarization transfer to ^{1}H enables the highly sensitive detection of both side chain and backbone resonances in amino acids, polypeptides and proteins.

1.2.6 A Novel Tri-enzyme System for More Efficient Photo-CIDNP Data Collection [84] (Chapter 3)

Two major drawbacks have limited the applicability of photo-CIDNP to experiments involving long-term data acquisition. First, the transiently reduced photosensitizer dye (typically flavin mononucleotide, i.e., FMN) is often not readily re-oxidized in the course of the experiment. Second, repeated laser pulses often cause significant photo-damage of the sample. Thus, 1D experiments involving lengthy signal averaging to detect weak NMR signals from dilute biomolecules or multidimensional NMR experiments are often not practically accessible via photo-CIDNP. Furthermore, despite the fact that higher laser power leads to larger photo-CIDNP enhancements, low

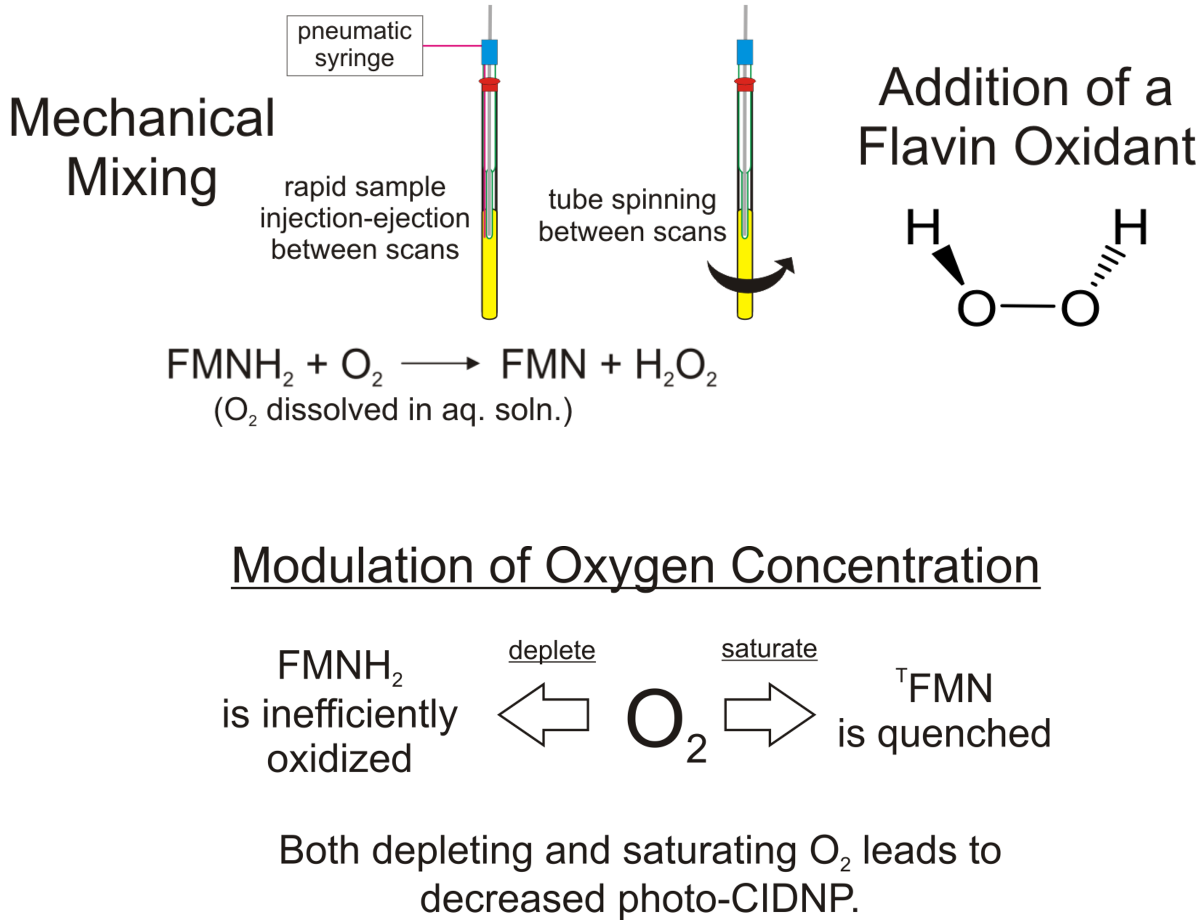

Figure 1.7 Previous efforts to prevent dye (FMN) photoreduction and sample photodegradation during photo-CIDNP experiments. Mechanical mixing and addition of H_2O_2 were performed to facilitate re-oxidation of the dye. In addition, ambient O_2 level was modulated to observe the effect on photo-CIDNP.

laser power is often used for practical applications, to minimize photodegradation.

Previous efforts (Fig. 1.7) to facilitate long-term photo-CIDNP include (a) regenerating the yellow FMN dye from its photo-reduced colorless $FMNH_2$ upon mechanical mixing of the sample during the experiment to facilitate oxidation by oxygen,[85,86] (b) addition of an oxidizing agent (i.e., H_2O_2) before data collection[86] and (c) deliberately modulating the oxygen concentration in the sample.[87] Approaches (a) and (b) are effective but not optimal. Approach (c) leads to decreased photo-CIDNP regardless of whether oxygen is added or depleted. Under oxygen saturation conditions, $FMNH_2$ is efficiently regenerated but the photo-excited triplet-state dye ^{T}FMN, whose interaction with the sample causes photo-CIDNP, is readily quenched by the abundant oxygen. Under oxygen depletion conditions, photodegradation by singlet oxygen is efficiently suppressed but the photoreduced $FMNH_2$ is not efficiently re-oxidized to the original FMN.

In Chapter 3, a new method is introduced to decrease the extent of photodegradation and enhance photo-CIDNP in experiments requiring long-term data collection. This method enables efficient regeneration of FMN while minimizing irreversible photodegradation. Since oxygen is known to be involved in many photodegradation pathways, we first deplete oxygen in the NMR sample by introducing glucose, glucose oxidase and catalase. The consequent decrease in photo-CIDNP (given that FMN cannot be efficiently regenerated from $FMNH_2$) is overcome upon the additional introduction of an $FMNH_2$-oxidizing enzyme. The resulting tri-enzyme system improves photo-CIDNP performance while reducing the extent of irreversible sample photodegradation.

1.3 Hsp70 Chaperone - Substrate Interactions

1.3.1 Molecular Chaperones

Based on a set of brilliant experiments, Christian Anfinsen postulated in 1973 that a protein's native structure in a given environment is determined by its amino acid sequence.[88] Given a sequence, the protein's native structure can be tracked down by searching for the lowest free energy state in the funneled energy landscape.[89] However, this does not mean that sequence alone is all that is necessary for proper protein folding. The "environment", including other proteins present in the system, is an essential set of parameters that cannot be neglected.

After unfolding a protein by denaturing agents or heat, simple reinstatement of the physiologically relevant condition often leads to misfolded or aggregated proteins.[90] Even when proteins are synthesized in vectorial nature under normal conditions *in vivo*, the ribosome and molecular chaperones have to work in concert to ensure the native structure after translation.[91] This is also true under physical and chemical stress conditions, where proteins cannot properly turnover without the help of molecular chaperones.

Molecular chaperones are proteins that interact, stabilize, or help non-native proteins to fold into their native conformation. They help co- and post-translational protein folding and are overexpressed under various stress-related (e.g. high temperature) conditions to maintain protein homeostasis. Even under non-stress conditions, the molecular chaperones interact with approximately 30% of the total protein population, reflecting the importance of chaperones in the overall quality control of proteins.[92]

1.3.2 Heat Shock Protein 70 (Hsp70) Molecular Chaperone

Hsp70 chaperones are ubiquitous among prokaryotes and eukaryotes.[93] They are also highly conserved in sequence.[94] Just like most other molecular chaperones, the Hsp70 is overexpressed upon heat shock and other stress-related conditions. It functions co- and post-translationally and regulates protein folding, disaggregation and degradation.[95]

The Hsp70 chaperone has two domains, an N-terminal ~44 kDa nucleotide binding domain (NBD) with ATPase activity and a C-terminal ~25 kDa substrate binding domain (SBD) that directly interacts with the substrate molecules (Fig. 1.8). The relative orientation of NBD and SBD is thought to be quite flexible and the linker region between the two domains forms a dynamic random coil.[96]

The Hsp70 chaperones from all organisms cooperate with various other chaperones and co-chaperones to maintain the correctly folded pool of proteins in the cell. In addition, Hsp70 plays a versatile role in many cellular processes. For instance, Hsp70 is involved in the transport of proteins and vesicles across membranes,[97] activation and regulation of immune cells,[98,99] and regulated assembly and disassembly of protein complexes[100] through interactions with a wide variety of co-chaperone proteins.

Consistent with its diverse function, Hsp70 is involved in the pathology of several diseases.[101] First, overexpression of Hsp70 proteins is frequently observed in multiple type of cancers.[102] Hsp70 is thought to provide a survival advantage because it interacts and inhibits multiple components in apoptotic pathways.[101] Strikingly, transgenic mice overexpressing Hsp70 chaperone spontaneously develop T cell lymphoma.[103] Overexpression of the Hsp70 protein, at the same time, decreases protein aggregation in cultured cell lines and suppresses neurodegenerative phenotypes in animal models.[101] Hsp70 chaperones are implicated in many neurodegenerative diseases[104] and are involved in senescence pathways.[105]

1.3.3 *E. coli* Hsp70: DnaK

DnaK is the *E. coli* Hsp70. In *E. coli* cells, long nascent polypeptide chains interact with DnaK (~30% of total proteins) and fold to their native state after multiple ATP-dependent cycles or get transferred to the chaperonin system.[92] DnaK knocked down *E. coli* cells are not viable under heat shock conditions (42°C)[106] and experience significant protein aggregation even at 37°C.[107]

The recognition motif of DnaK (Fig. 1.9) consists of five hydrophobic residues, especially enriched in leucine, flanked by positively charged residues. This pattern was elucidated by screening cellulose-bound peptide libraries.[108]

The DnaK protein cooperates with other co-chaperones to properly function *in vivo* (Fig. 1.10). Rapid association of DnaK to its substrates occurs in its ATP-bound state (ATP-DnaK), where the substrate can bind independently or as a complex with the

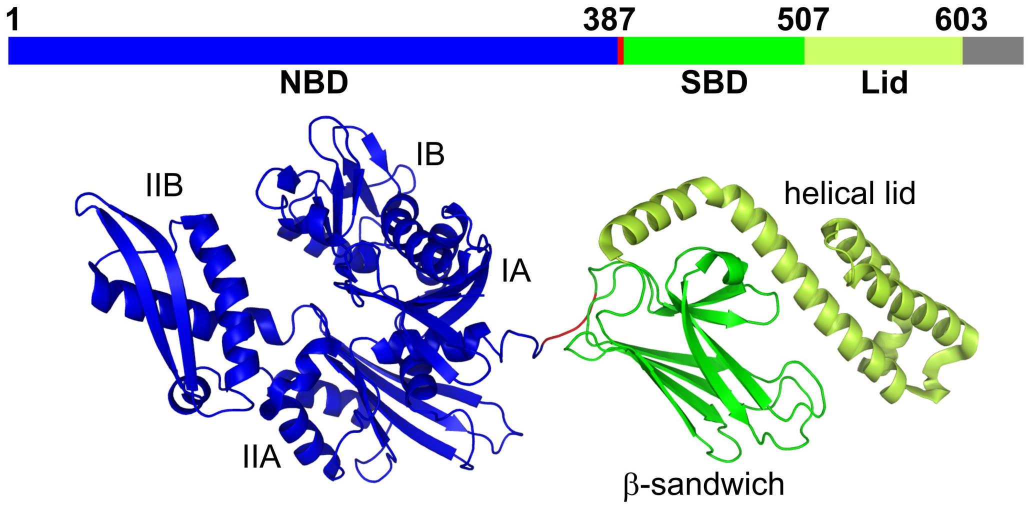

Figure 1.8 Structure of DnaK (*E. coli* Hsp70) in its ADP bound state (PDB ID: 2KHO).[96] DnaK has a 45 kDa N-terminal nucleotide binding domain (NBD) and a 25 kDa C-terminal substrate binding domain (SBD). The SBD is further subdivided into a 15 kDa β-sandwich domain that interacts with client substrates and a 10 kDa helical lid domain. The last 30 C-terminal residues in DnaK are unstructured and of unknown function.

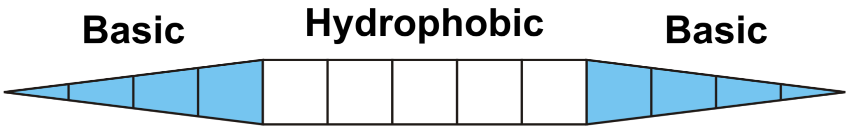

Hydrophobic : Leu, Ile, Val, Phe, Tyr

Basic: Arg, Lys

Figure 1.9 The substrate recognition motif of DnaK.[108]

DnaJ (Hsp40) co-chaperone. The ATP is readily hydrolyzed upon DnaK's interaction with DnaJ and the substrate. Upon ATP hydrolysis to form ADP-DnaK, DnaJ dissociates and the substrate binds tightly to DnaK. Another co-chaperone GrpE (a nucleotide exchange factor) catalyzes ADP release from the DnaK, where DnaK rapidly binds to another ATP, lowering the affinity of DnaK for the substrate followed by its release. This forms the DnaK-DnaJ-GrpE cycle to refold the unfolded or misfolded proteins (Fig. 1.10).[109] The DnaK-DnaJ-GrpE also works together with ClpB (Hsp100) chaperone to render aggregated proteins into their functional forms.[110]

DnaK will be used as our model chaperone in the experiments described in Chapter 4 and 5.

1.3.4 Molecular Details of the Hsp70-Substrate Interaction

The function of Hsp70 is manifested by its action on substrates. Thus, in order to understand how Hsp70 chaperone helps protein folding, it is important to observe how the substrate is affected upon interaction with the chaperone.

Although much has been studied about the function of Hsp70, only few examples tell us about the molecular details of how substrates respond to Hsp70. For instance, X-ray[111] and NMR[112,113] studies showed that short peptides adopt an extended conformation upon binding the substrate-binding-domain (SBD) of Hsp70. (Fig. 1.11) In addition, when apomyoglobin N-terminal fragments bind to the SBD of Hsp70, native and nonnative residual helical structure that resembles the acid-unfolded full-length

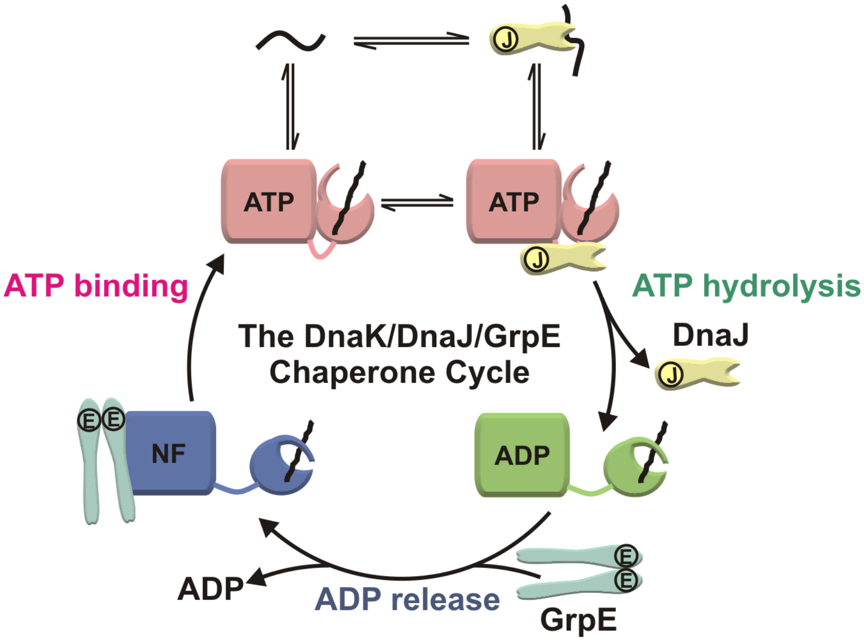

Figure 1.10 The ATP-regulated DnaK/DnaJ/GrpE chaperone cycle.

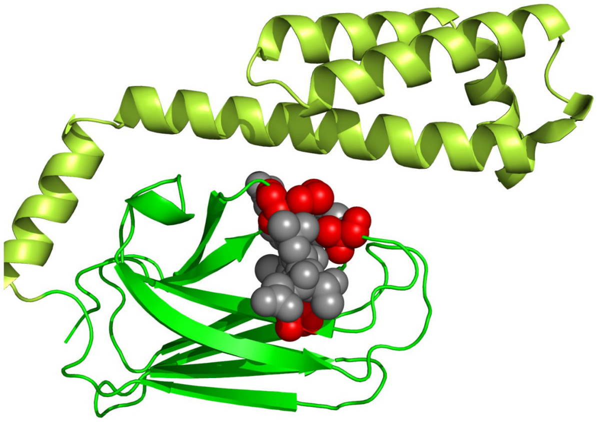

Figure 1.11 X-ray structure of the DnaK SBD (green) bound to NRLLLTG peptide (grey spheres). Hydrophobic arch and central binding cavity residues are shown as red spheres. (PDB ID: 1DKX) [111]

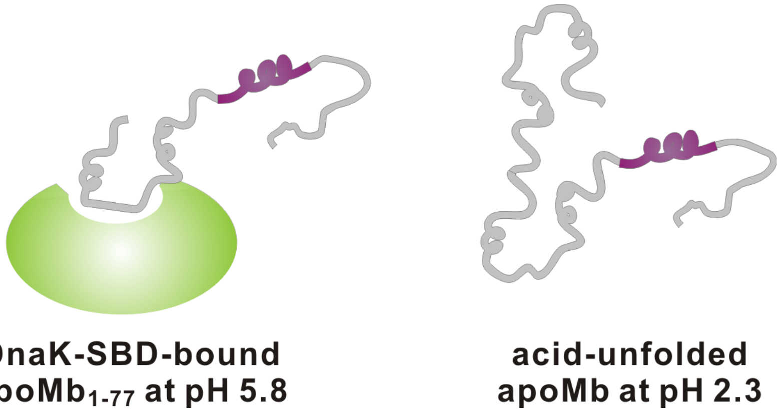

Figure 1.12 Schematic diagrams illustrating the conformational similarity between the N-terminal apomyoglobin bound to DnaK SBD and acid-unfolded full-length apomyoglobin. The purple stretches highlight the similarities in helical propensities.[114]

apomyoglobin is generated. (Fig. 1.12)[114] However, these studies focus on protein fragments and peptides binding to the truncated form of Hsp70. Yet, studies on the interaction between full-length native proteins and full-length Hsp70 are crucial. It is worth mentioning that it has been recently reported that the full-length *E. coli* Hsp70-like protein HscA binds to and stabilizes the disordered form of the iron-sulfur cluster scaffold protein IscU.[115]

In addition, given that the Hsp70 molecular chaperone is known to interact with unfolded and newly synthesized polypeptides as well as with fully and partially folded proteins,[100,101] it is important to investigate how the full-length Hsp70 interacts with both the folded and unfolded states of the protein substrate, to gain more insights into the mechanism of Hsp70-substrate interactions.

1.3.5 Experimental Conditions

To study the molecular mechanism underlying Hsp70-substrate interaction, I observed the interaction between the full-length ADP-bound DnaK (ADP-DnaK) and the drkN SH3 domain by multidimensional NMR spectroscopy.

ATP-DnaK has a low affinity and exchanges fast with bound substrates, while ADP-DnaK has high affinity and slow exchange rates.[109] Thus, ADP-DnaK is a more favorable species to study DnaK-substrate interaction by NMR. In addition, fast ATP hydrolysis by DnaK in the presence of substrates makes it difficult to examine the ATP-DnaK state over the long time span required for NMR experiments.[116] In principle, mutants such as DnaK T199A can greatly reduce ATPase activity, but only at the cost of a concomitant loss of protein folding activity.[117] Various functions of DnaK are implicated with ATP hydrolysis,[118] so I expected that ADP-DnaK-substrate interaction studies would provide valuable insights into DnaK function. Later, I simulated nucleotide-free DnaK states by adding a large amount of GrpE nucleotide exchange factor into my samples.[119]

The N-terminal SH3 domain of the *Drosophila melanogaster* adaptor protein drk (drkN SH3 domain) was used as the substrate. The SH3 domain is marginally stable and slowly exchanges ($k_{ex} \sim 2.2\ s^{-1}$) between folded and unfolded states at the chemical shift NMR timescale, enabling observation of NMR resonances from both states (Fig. 1.13).[120] This will give us the opportunity to observe the interplay between Hsp70 and the folded and unfolded drkN SH3 substrate. In addition, the drkN SH3 domain has a strong DnaK-binding site (Figs. 1.9 and 1.14). Note that only the SH3 domain is ^{13}C, ^{15}N-enriched, since we are mainly interested in the effect of Hsp70 chaperone on the substrate. All experiments were performed at pH 7.2 and 25 °C.

1.3.6 Effect of ADP-DnaK on SH3 conformation

Multidimensional NMR and native gel analysis were performed to monitor the effect of ADP-bound DnaK (the *E. coli* Hsp70) on the drkN SH3 protein substrate, which slowly exchanges between the folded and unfolded states on the NMR chemical shift timescale. When drkN SH3 and DnaK are present in the sample, the translational diffusion of both the folded and unfolded states of SH3 is decelerated, suggesting an interaction of both states with the chaperone. No major changes in substrate conform-

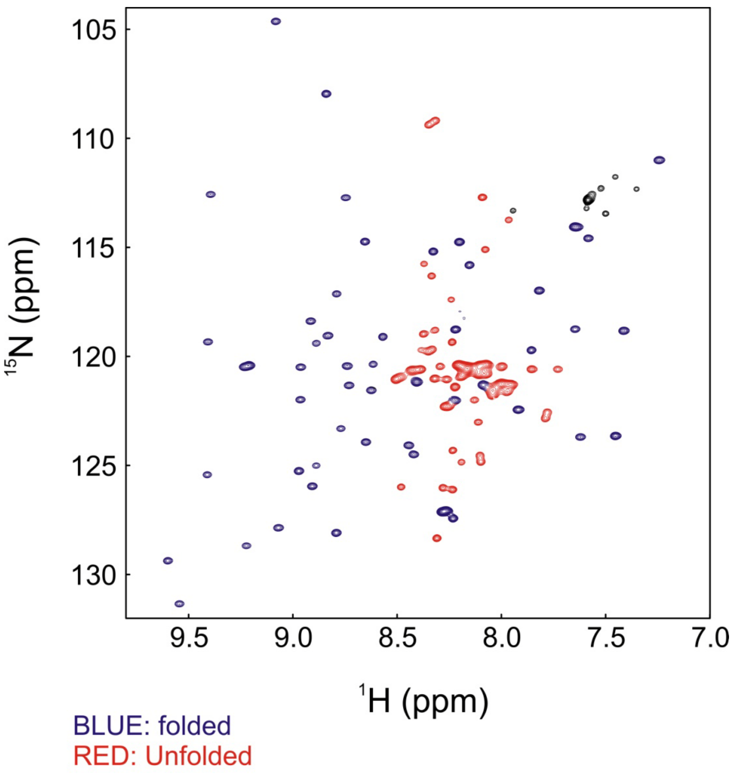

Figure 1.13 ^{1}H-^{15}N HSQC NMR spectrum of drkN SH3. Both folded and unfolded resonances can be clearly observed. The NMR data was collected with 100 μM ^{13}C,^{15}N-enriched SH3 protein at pH 6.0 and 25°C.

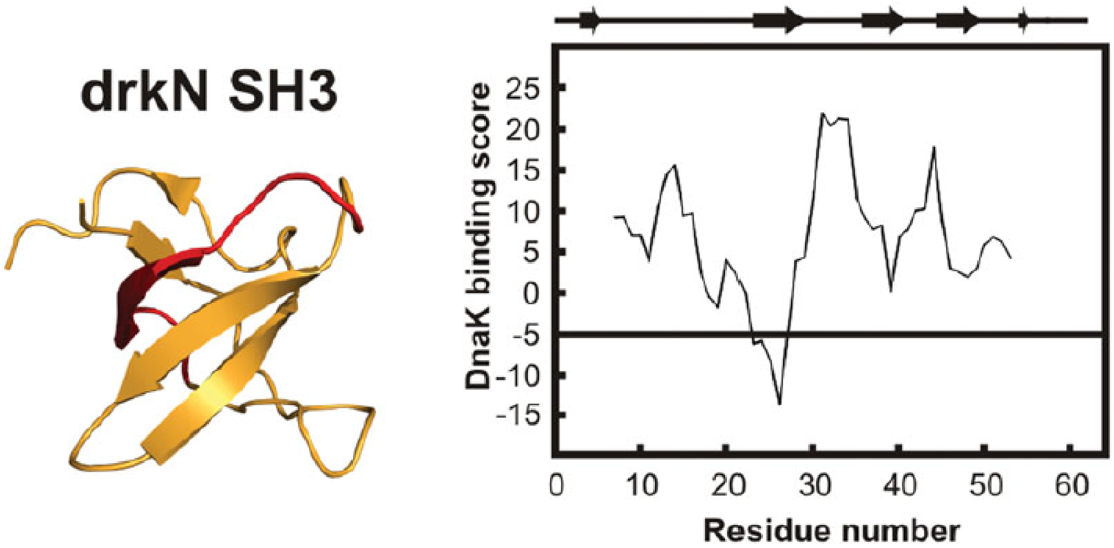

Figure 1.14 Structure (PDB ID: 2A36) and DnaK-binding scores[108] of the SH3 domain.[116] A binding score less than -5 indicates a strong local DnaK binding site. The potential binding site with the lowest score is shown in red in the structure on the left.

ation were detected in the presence of the chaperone. Finally, to account for the overall undetectability of folded SH3 population in the presence of chaperone, we propose that some NMR-invisible, possibly Hsp70-bound “dark” states are populated.[121]

1.4 References

(1) Ernst, R. R.; Bodenhausen, G.; Wokaun, A. *Principles of Nuclear Magnetic Resonance in One and Two Dimensions*; Oxford University Press: Upper Saddle River, 1989.

(2) Claridge, T. D. W. *High-Resolution NMR Techniques in Organic Chemistry*; 2 ed.; Elsevier: Amsterdam, 2009.

(3) Harris, R. K. *Nuclear Magnetic Resonance Spectroscopy: A Physicochemical View*; Longman Scientific and Technical: U.K., 1986.

(4) Kelly, A. E.; Ou, H. D.; Withers, R.; Dötsch, V. Low-Conductivity Buffers for High-Sensitivity NMR Measurements. *J. Am. Chem. Soc.* **2002**, *124*, 12013-12019.

(5) Cavanagh, J.; Fairbrother, W. J.; Palmer, A. G.; Rance, M.; Skelton, N. J. *Protein NMR Spectroscopy: Principles and Practice*; 2 ed.; Elsevier Academic Press: San Diego, 2007.

(6) Abragam, A. *The Principle of Nuclear Magnetism*; Clarendon Press: Oxford, 1961.

(7) van de Ven, F. J. M. *Multidimensional NMR in Liquids: Basic Principles and Experimental Methods*; Wiley-VCH: New York, 1995.

(8) Hoult, D. I.; Richards, R. The Signal-to-Noise Ratio of the Nuclear Magnetic Resonance Experiment. *J. Magn. Reson.* **1976**, *24*, 71-85.

(9) Kim, Y.; Bascunan, J.; Lecrevisse, T.; Hahn, S.; Voccio, J.; Park, D. K.; Iwasa, Y. YBCO and Bi2223 Coils for High Field LTS/HTS NMR Magnets: HTS-HTS Joint Resistivity. *IEEE Trans. Appl. Supercond.* **2013**, *23*, 6800704.

(10) Kovacs, H.; Moskau, D.; Spraul, M. Cryogenically Cooled Probes-a Leap in NMR Technology. *Prog. Nucl. Magn. Reson. Spectrosc.* **2005**, *46*, 131-155.

(11) Styles, P.; Soffe, N. F.; Scott, C. A.; Crag, D. A.; Row, F.; White, D. J.; White, P. C. J. A High-Resolution NMR Probe in Which the Coil and Preamplifier are Cooled with Liquid Helium. *J. Magn. Reson.* **1984**, *60*, 397-404.

(12) Morris, G. A.; Freeman, R. Enhancement of Nuclear Magnetic Resonance Signals by Polarization Transfer. *J. Am. Chem. Soc.* **1979**, *101*, 760-762.

(13) Solomon, I. Relaxation Processes in a System of Two Spins. *Phys. Rev.* **1955**, *99*, 559.

(14) Hartmann, S. R.; Hahn, E. L. Nuclear Double Resonance in the Rotating Frame. *Phys. Rev.* **1962**, *128*, 2042–2053.

(15) Pervushin, K.; Riek, R.; Wider, G.; Wüthrich, K. Attenuated T2 Relaxation by Mutual Cancellation of Dipole–Dipole Coupling and Chemical Shift Anisotropy Indicates an Avenue to NMR Structures of Very Large Biological Macromolecules in Solution. *Proc. Natl. Acad. Sci. U.S.A.* **1997**, *94*, 12366-12371.

(16) Tugarinov, V.; Hwang, P. M.; Ollerenshaw, J. E.; Kay, L. E. Cross-Correlated Relaxation Enhanced 1H-13C NMR Spectroscopy of Methyl Groups in Very High Molecular Weight Proteins and Protein Complexes. *J. Am. Chem. Soc.* **2003**, *125*, 10420-10428.

(17) Zhuravleva, A.; Orekhov, V. Y. Divided Evolution: A Scheme for Suppression of Line Broadening Induced by Conformational Exchange. *J. Am. Chem. Soc.* **2008**, *130*, 3260-3261.

(18) Li, Y.; Palmer, A. G. Narrowing of Protein NMR Spectral Lines Broadened by Chemical Exchange. *J. Am. Chem. Soc.* **2010**, *132*, 8856-8857.

(19) Ellett, J. D.; Waugh, J. S. Chemical-Shift Concertina. *J. Chem. Phys.* **1969**, *51*, 2851.

(20) Meiboom, S.; Gill, D. Modified Spin-Echo Method for Measuring Nuclear Relaxation Times. *Rev. Sci. Instrum.* **1958**, *29*, 688-691.

(21) Waugh, J. S.; Huber, L. M.; Haeberlen, U. Approach to High-Resolution NMR in Solids. *Phys. Rev. Lett.* **1968**, *20*, 180-182.

(22) Grzesiek, S.; Anglister, J.; Ren, H.; Bax, A. 13C Line Narrowing by 2H Decoupling in 2H/13C/15N-Enriched Proteins. Application to Ttriple Resonance 4D J Connectivity of Sequential Amides. *J. Am. Chem. Soc.* **1993**, *115*, 4369-4370.

(23) Gardner, K. H.; Kay, L. E. The Use of 2h, 13C, 15N Multidimensional NMR Gto Study the Structure and Dynamics of Proteins. *Annu. Rev. Biophys. Biomol. Struct.* **1998**, *27*, 357-406.

(24) Palmer, A. G.; Cavanagh, J.; Wright, P. E.; Rance, M. Sensitivity Improvement in Proton-Detected Two-Dimensional Heteronuclear Correlation NMR Spectroscopy. *J. Magn. Reson.* **1991**, *93*, 151-170.

(25) Schanda, P.; Brutscher, B. Very Fast Two-Dimensional NMR Spectroscopy for Real-Time Investigation of Dynamic Events in Proteins on the Time Scale of Seconds. *J. Am. Chem. Soc.* **2005**, *127*, 8014-8015.

(26) Maly, T.; et al. Dynamic Nuclear Polarization at High Magnetic Fields. *J. Chem. Phys.* **2008**, *128*, 052211.

(27) Gunther, U. L. Dynamic Nuclear Hyperpolarization in Liquids. *Top. Curr. Chem.* **2013**, *335*, 23-69.

(28) Overhauser, A. W. Polarization of Nuclei in Metals. *Phys. Rev.* **1953**, *92*, 411.

(29) Dorn, H.; Wang, J.; Allen, L.; Sweeney, D.; Glass, T. Flow Dynamic Nuclear Polarization, a Novel Method for Enhancing NMR Signals in Flowing Fluids. *J. Magn. Reson.* **1988**, *79*, 404-412.

(30) Denysenkov, V.; Prandolini, M. J.; Gafurov, M.; Sezer, D.; Endeward, B.; Prisner, T. F. Liquid State DNP Using a 260 GHz High Power Gyrotron. *Phys. Chem. Chem. Phys.* **2010**, *12*, 5786-5790.

(31) Song, C.; Hu, K.-N.; Joo, C.-G.; Swager, T. M.; Griffin, R. G. Totapol: A Biradical Polarizing Agent for Dynamic Nuclear Polarization Experiments in Aqueous Media. *J. Am. Chem. Soc.* **2006**, *128*, 11385-11390.

(32) Ardenkjær-Larsen, J. H.; Fridlund, B.; Gram, A.; Hansson, G.; Hansson, L.; Lerche, M. H.; Servin, R.; Thaning, M.; Golman, K. Increase in Signal-to-Noise Ratio of > 10,000 Times in Liquid-State NMR. *Proc. Natl. Acad. Sci. U.S.A.* **2003**, *100*, 10158-10163.

(33) Jóhannesson, H.; Macholl, S.; Ardenkjaer-Larsen, J. H. Dynamic Nuclear Polarization of [1-13C] Pyruvic Acid at 4.6 Tesla. *J. Magn. Reson.* **2009**, *197*, 167-175.

(34) Gallagher, F. A.; Kettunen, M. I.; Day, S. E.; Hu, D.-E.; Ardenkjaer-Larsen, J. H. Magnetic Resonance Imaging of pH in vivo Using Hyperpolarized 13C-Labelled Bicarbonate. *Nature* **2008**, *453*, 940-943.

(35) Day, S. E.; Kettunen, M. I.; Gallagher, F. A.; Hu, D.-E.; Lerche, M.; Wolber, J.; Golman, K.; Ardenkjaer-Larsen, J. H.; Brindle, K. M. Detecting Tumor Response to Treatment Using Hyperpolarized 13C Magnetic Resonance Imaging and Spectroscopy. *Nat. Med.* **2007**, *13*, 1382-1387.

(36) Mishkovsky, M.; Frydman, L. Progress in Hyperpolarized Ultrafast 2D NMR Spectroscopy. *ChemPhysChem* **2008**, *9*, 2340-2348.

(37) Panek, R.; Granwehr, J.; Leggett, J.; Köckenberger, W. Slice-Selective Single Scan Proton COSY with Dynamic Nuclear Polarisation. *Phys. Chem. Chem. Phys.* **2010**, *12*, 5771-5778.

(38) Zeng, H.; Bowen, S.; Hilty, C. Sequentially Acquired Two-Dimensional NMR Spectra from Hyperpolarized Sample. *J. Magn. Reson.* **2009**, *199*, 159-165.

(39) Bowers, C. R.; Weitekamp, D. P. Transformation of Symmetrization Order to Nuclear-Spin Magnetization by Chemical Reaction and Nuclear Magnetic Resonance. *Phys. Rev. Lett.* **1986**, *57*, 2645.

(40) Bowers, C. R.; Weitekamp, D. Parahydrogen and Synthesis Allow Dramatically Enhanced Nuclear Alignment. *J. Am. Chem. Soc.* **1987**, *109*, 5541-5542.

(41) Pravica, M. G.; Weitekamp, D. P. Net NMR Alignment by Adiabatic Transport of Parahydrogen Addition Products to High Magnetic Field. *Chem. Phys. Lett.* **1988**, *145*, 255-258.

(42) Natterer, J.; Bargon, J. Parahydrogen Induced Polarization. *Prog. Nucl. Magn. Reson. Spectrosc.* **1997**, *31*, 293-315.

(43) Adams, R. W.; Aguilar, J. A.; Atkinson, K. D.; Cowley, M. J.; Elliott, P. I.; Duckett, S. B.; Green, G. G.; Khazal, I. G.; López-Serrano, J.; Williamson, D. C. Reversible

Interactions with Para-Hydrogen Enhance NMR Sensitivity by Polarization Transfer. *Science* **2009**, *323*, 1708-1711.

(44) Goodson, B. M. Nuclear Magnetic Resonance of Laser-Polarized Noble Gases in Molecules, Materials, and Organisms. *J. Magn. Reson.* **2002**, *155*, 157-216.

(45) Happer, W. Optical Pumping. *Rev. Mod. Phys.* **1972**, *44*, 169-249.

(46) Barrett, S.; Dabbagh, G.; Pfeiffer, L.; West, K.; Tycko, R. Optically Pumped NMR Evidence for Finite-Size Skyrmions in GaAs Quantum Wells near Landau Level Filling N=1. *Phys. Rev. Lett.* **1995**, *74*, 5112.

(47) Albert, M. S.; Cates, G. D.; Driehuys, B.; Happer, W.; Saam, B.; Springer, C. S.; Wishnia, A. Biological Magnetic-Resonance-Imaging Using Laser Polarized Xe-129. *Nature* **1994**, *370*, 199-201.

(48) Haupt, J. A New Effect of Dynamic Polarization in a Solid Obtained by Rapid Change of Temperature. *Phys. Lett. A* **1972**, *38*, 389-390.

(49) Horsewill, A. Quantum Tunnelling Aspects of Methyl Group Rotation Studied by NMR. *Prog. Nucl. Magn. Reson. Spectrosc.* **1999**, *35*, 359-389.

(50) Ludwig, C.; Saunders, M.; Marin-Montesinos, I.; Gunther, U. L. Quantum Rotor Induced Hyperpolarization. *Proc. Natl. Acad. Sci. U.S.A.* **2010**, *107*, 10799-10803.

(51) Suits, A. G.; Vasyutinskii, O. S. Imaging Atomic Orbital Polarization in Photodissociation. *Chem. Rev.* **2008**, *108*, 3706-3746.

(52) Sofikitis, D.; Rubio-Lago, L.; Martin, M. R.; Brown, D. J. A.; Bartlett, N. C.-M.; Alexander, A. J.; Zare, R. N.; Rakitzis, T. P. Optical Control of Ground-State Atomic Orbital Alignment: Cl (P) Atoms from HCl (V= 2, J= 1) Photodissociation. *J. Chem. Phys.* **2007**, *127*, 144307.

(53) Rakitzis, T. P. Highly Spin-Polarized Atoms and Molecules from Rotationally State-Selected Molecules. *Phys. Rev. Lett.* **2005**, *94*, 083005.

(54) Hore, P. J.; Broadhurst, R. W. Photo-CIDNP of Biopolymers. *Prog. Nucl. Magn. Reson. Spectrosc.* **1993**, *25*, 345-402.

(55) Bargon, J. The Discovery of Chemically Induced Dynamic Polarization (CIDNP). *Helv. Chim. Acta* **2006**, *89*, 2082-2102.

(56) Bargon, J.; Fischer, H.; Johnson, U. Nuclear Magnetic Resonance Emission Lines During Fast Radical Reactions. I. Recording Methods and Examples. *Z. Naturforsch. A* **1967**, *22*, 1551-1555.

(57) Ward, H. R.; Lawler, R. G. Nuclear Magnetic Resonance Emission and Enhanced Absorption in Rapid Organometallic Reactions. *J. Am. Chem. Soc.* **1967**, *89*, 5518-5519.

(58) Cocivera, M. Optically Induced Overhauser Effect in Solution. Nuclear Magnetic Resonance Emission. *J. Am. Chem. Soc.* **1968**, *90*, 3261-3263.

(59) Goez, M.; Frisch, I. Activation Energy of a Biradical Rearrangement Measured by Photo-CIDNP. *J. Chem. Phys. A* **2002**, *106*, 8079-8084.

(60) Gould, I. R.; Baretz, B. H.; Turro, N. J. Primary Processes in the Type I Photocleavage of Dibenzyl Ketones. A Pulsed Laser and Photochemically Induced Dynamic Nuclear Polarization Study. *J. Phys. Chem.* **1987**, *91*, 925-929.

(61) Kaptein, R.; Dijkstra, K.; Nicolay, K. Laser Photo-CIDNP as a Surface Probe for Proteins in Solution. *Nature* **1978**, *274*, 293-294.

(62) Weiss, M. A.; Frank, B. H.; Khait, I.; Pekar, A.; Heiney, R.; Shoelson, S. E.; Neuringer, L. J. NMR and Photo-CIDNP Studies of Human Proinsulin and Prohormone

Processing Intermediates with Application to Endopeptidase Recognition. *Biochemistry* **1990**, *29*, 8389-8401.

(63) Mok, K. H.; Nagashima, T.; Day, I. J.; Jones, J. A.; Jones, C. J.; Dobson, C. M.; Hore, P. Rapid Sample-Mixing Technique for Transient NMR and Photo-CIDNP Spectroscopy: Applications to Real-Time Protein Folding. *J. Am. Chem. Soc.* **2003**, *125*, 12484-12492.

(64) Mok, K. H.; Nagashima, T.; Day, I. J.; Hore, P.; Dobson, C. M. Multiple Subsets of Side-Chain Packing in Partially Folded States of a-Lactalbumins. *Proc. Natl. Acad. Sci. U.S.A.* **2005**, *102*, 8899-8904.

(65) Mok, K. H.; Kuhn, L. T.; Goez, M.; Day, I. J.; Lin, J. C.; Andersen, N. H.; Hore, P. J. A Pre-Existing Hydrophobic Collapse in the Unfolded State of an Ultrafast Folding Protein. *Nature* **2007**, *447*, 106-109.

(66) Kaptein, R.; Oosterhoff, J. L. Chemically Induced Dynamic Nuclear Polarization Ii - (Relation with Anomalous ESR Spectra). *Chem. Phys. Lett.* **1969**, *4*, 195-197.

(67) Closs, G. L.; Closs, L. E. Induced Dynamic Nuclear Spin Polarization in Photoreductions of Benzophenone by Toluene and Ethylbenzene. *J. Am. Chem. Soc.* **1969**, *91*, 4549-4550.

(68) Eds. Muus, L. T.; Atkins, P. W.; McLauchlan, K. A.; Pedersen, J. B. *Chemically Induced Magnetic Polarization*; Reidel, Dordrecht: 1977.

(69) Eds. Williams, G. H. *Advances in Free-Radical Chemistry*; Elek Science, London: 1975; Vol. 5.

(70) Seki, H.; Takematsu, A.; Arai, S. Photoinduced Electron Transfer from Amino Acids and Proteins to 4-Nitroquinoline 1-Oxide in Aqueous Solutions. *J. Phys. Chem.* **1987**, *91*, 176-179.

(71) Lyon, C. E.; Jones, J. A.; Redfield, C.; Dobson, C. M.; Hore, P. J. Two-Dimensional 15N-1H Photo-CIDNP as a Surface Probe of Native and Partially Structured Proteins. *J. Am. Chem. Soc.* **1999**, *121*, 6505-6506.

(72) Sekhar, A.; Cavagnero, S. 1H Photo-CIDNP Enhancements in Heteronuclear Correlation NMR Spectroscopy. *J. Phys. Chem. B* **2009**, *113*, 8310-8318.

(73) Sekhar, A.; Cavagnero, S. Epic- and Chance-Hsqc: Two 15N Photo-CIDNP-Enhanced Pulse Sequences for the Sensitive Detection of Solvent-Exposed Tryptophan. *J. Magn. Reson.* **2009**, *200*, 207-213.

(74) Schlorb, C.; Mensch, S.; Richter, C.; Schwalbe, H. Photo-CIDNP Reveals Differences in Compaction of Non-Native States of Lysozyme. *J. Am. Chem. Soc.* **2006**, *128*, 1802-1803.

(75) Kiryutin, A. S.; Korchak, S. E.; Ivanov, K. L.; Yurkovskaya, A. V.; Vieth, H. M. Creating Long-Lived Spin States at Variable Magnetic Field by Means of Photochemically Induced Dynamic Nuclear Polarization. *J. Phys. Chem. Lett.* **2012**, *3*, 1814-1819.

(76) Carravetta, M.; Johannessen, O. G.; Levitt, M. H. Beyond the T1 Limit: Singlet Nuclear Spin States in Low Magnetic Fields. *Phys. Rev. Lett.* **2004**, *92*, 153003.

(77) Zysmilich, M. G.; McDermott, A. Photochemically Induced Dynamic Nuclear Polarization in the Solid-State 15N Spectra of Reaction Centers from Photosynthetic Bacteria Rhodobacter Sphaeroides R-26. *J. Am. Chem. Soc.* **1994**, *116*, 8362-8363.

(78) Daviso, E.; Janssen, G. J.; Alia, A.; Jeschke, G.; Matysik, J.; Tessari, M. A 10,000-Fold Nuclear Hyperpolarization of a Membrane Protein in the Liquid Phase via Solid-State Mechanism. *J. Am. Chem. Soc.* **2011**, *133*, 16754-16757.

(79) Thamarath, S. S.; Heberle, J.; Hore, P. J.; Kottke, T.; Matysik, J. Solid-State Photo-CIDNP Effect Observed in Phototropin LOV1-C57S by C-13 Magic-Angle Spinning NMR Spectroscopy. *J. Am. Chem. Soc.* **2010**, *132*, 15542-15543.

(80) Jeschke, G.; Matysik, J. A Reassessment of the Origin of Photochemically Induced Dynamic Nuclear Polarization Effects in Solids. *Chem. Phys.* **2003**, *294*, 239-255.

(81) Ardenkjaer-Larsen, J. H.; Fridlund, B.; Gram, A.; Hansson, G.; Hansson, L.; Lerche, M. H.; Servin, R.; Thaning, M.; Golman, K. Increase in Signal-to-Noise Ratio of > 10,000 Times in Liquid-State NMR. *Proc. Natl. Acad. Sci. U.S.A.* **2003**, *100*, 10158-10163.

(82) Lee, J. H.; Sekhar, A.; Cavagnero, S. 1H-Detected 13C Photo-CIDNP as a Sensitivity Enhancement Tool in Solution NMR. *J. Am. Chem. Soc.* **2011**, *133*, 8062-8065.

(83) Kiryutin, A. S.; Morozova, O. B.; Kuhn, L. T.; Yurkovskaya, A. V.; Hore, P. J. H-1 and C-13 Hyperfine Coupling Constants of the Tryptophanyl Cation Radical in Aqueous Solution from Microsecond Time-Resolved CIDNP. *J. Phys. Chem. B* **2007**, *111*, 11221-11227.

(84) Lee, J. H.; Cavagnero, S. A Novel Tri-Enzyme System in Combination with Laser-Driven NMR Enables Efficient Nuclear Polarization of Biomolecules in Solution. *J. Phys. Chem. B* **2013**, *117*, 6069-6081.

(85) Scheek, R. M.; Stob, S.; Boelens, R.; Dijkstra, K.; Kaptein, R. Applications of Two-Dimensional 1H Nuclear Magnetic Resonance Methods in Photochemically Induced

Dynamic Nuclear Polarisation Spectroscopy. *Faraday Discuss. Chem. Soc.* **1984**, *78*, 245-256.

(86) Maeda, K.; Lyon, C. E.; Lopez, J. J.; Cemazar, M.; Dobson, C. M.; Hore, P. Improved Photo-CIDNP Methods for Studying Protein Structure and Folding. *J. Biomol. NMR* **2000**, *16*, 235-244.

(87) Connolly, P. J.; Hoch, J. C. Photochemical Degradation of Tryptophan Residues During CIDNP Experiments. *J. Magn. Reson.* **1991**, *95*, 165-173.

(88) Anfinsen, C. B. Principles That Govern the Folding of Protein Chains. *Science* **1973**, *181*, 223-230.

(89) Dill, K. A.; Chan, H. S. From Levinthal to Pathways to Funnels. *Nat. Struct. Biol.* **1997**, *4*, 10-19.

(90) Lang, J.; Wu, Y.; Cavagnero, S. *submitted.*

(91) Fedyukina, D. V.; Cavagnero, S. Protein Folding at the Exit Tunnel. *Annu. Rev. Biophys.* **2011**, *40*, 337-359.

(92) Hartl, F. U.; Hayer-Hartl, M. Converging Concepts of Protein Folding in vitro and in vivo. *Nat. Struct. Mol. Biol.* **2009**, *16*, 574-581.

(93) Macario, A. J.; de Macario, E. C. The Archaeal Molecular Chaperone Machine: Peculiarities and Paradoxes. *Genetics* **1999**, *152*, 1277-1283.

(94) Daugaard, M.; Rohde, M.; Jäättelä, M. The Heat Shock Protein 70 Family: Highly Homologous Proteins with Overlapping and Distinct Functions. *FEBS Lett.* **2007**, *581*, 3702-3710.

(95) Mayer, M. P.; Brehmer, D.; Gässler, C. S.; Bukau, B. Hsp70 Chaperone Machines. *Adv. Protein Chem.* **2001**, *59*, 1-44.

(96) Bertelsen, E. B.; Chang, L.; Gestwicki, J. E.; Zuiderweg, E. R. Solution Conformation of Wild-Type E. Coli Hsp70 (DnaK) Chaperone Complexed with ADP and Substrate. *Proc. Natl. Acad. Sci. U.S.A.* **2009**, *106*, 8471-8476.

(97) Pratt, W. B.; Toft, D. O. Regulation of Signaling Protein Function and Trafficking by the Hsp90/Hsp70-Based Chaperone Machinery. *Exp. Biol. Med.* **2003**, *228*, 111-133.

(98) Li, Z.; Menoret, A.; Srivastava, P. Roles of Heat-Shock Proteins in Antigen Presentation and Cross-Presentation. *Curr. Opin. Immunol.* **2002**, *14*, 45-51.

(99) Salminen, A.; Paimela, T.; Suuronen, T.; Kaarniranta, K. Innate Immunity Meets with Cellular Stress at the IKK Complex: Regulation of the IKK Complex by Hsp70 and Hsp90. *Immunol. Lett.* **2008**, *117*, 9-15.

(100) Young, J. C.; Barral, J. M.; Ulrich Hartl, F. More Than Folding: Localized Functions of Cytosolic Chaperones. *Trends Biochem. Sci* **2003**, *28*, 541-547.

(101) Evans, C. G.; Chang, L.; Gestwicki, J. E. Heat Shock Protein 70 (Hsp70) as an Emerging Drug Target. *J. Med. Chem.* **2010**, *53*, 4585-4602.

(102) Mosser, D. D.; Morimoto, R. I. Molecular Chaperones and the Stress of Oncogenesis. *Oncogene* **2004**, *23*, 2907-2918.

(103) Seo, J.-S.; Park, Y.-M.; Kim, J.-I.; Shim, E.-H.; Kim, C.-W.; Jang, J.-J.; Kim, S.-H.; Lee, W.-H. T Cell Lymphoma in Transgenic Mice Expressing the Human Hsp70 Gene. *Biochem. Biophys. Res. Commun.* **1996**, *218*, 582-587.

(104) Muchowski, P. J.; Wacker, J. L. Modulation of Neurodegeneration by Molecular Chaperones. *Nat. Rev. Neurosci.* **2005**, *6*, 11-22.

(105) Yaglom, J. A.; Gabai, V. L.; Sherman, M. Y. High Levels of Heat Shock Protein Hsp72 in Cancer Cells Suppress Default Senescence Pathways. *Cancer Res.* **2007**, *67*, 2373-2381.

(106) Deuerling, E.; Schulze-Specking, A.; Tomoyasu, T.; Mogk, A.; Bukau, B. Trigger Factor and DnaK Cooperate in Folding of Newly Synthesized Proteins. *Nature* **1999**, *400*, 693-696.

(107) Deuerling, E.; Patzelt, H.; Vorderwülbecke, S.; Rauch, T.; Kramer, G.; Schaffitzel, E.; Mogk, A.; Schulze-Specking, A.; Langen, H.; Bukau, B. Trigger Factor and DnaK Possess Overlapping Substrate Pools and Binding Specificities. *Mol. Microbiol.* **2003**, *47*, 1317-1328.

(108) Rüdiger, S.; Germeroth, L.; Schneider-Mergener, J.; Bukau, B. Substrate Specificity of the DnaK Chaperone Determined by Screening Cellulose-Bound Peptide Libraries. *EMBO J.* **1997**, *16*, 1501-1507.

(109) Bukau, B.; Horwich, A. L. The Hsp70 and Hsp60 Chaperone Machines. *Cell* **1998**, *92*, 351-366.

(110) Mogk, A.; Tomoyasu, T.; Goloubinoff, P.; Rüdiger, S.; Röder, D.; Langen, H.; Bukau, B. Identification of Thermolabile Escherichia Coli Proteins: Prevention and Reversion of Aggregation by DnaK and ClpB. *EMBO J.* **1999**, *18*, 6934-6949.

(111) Zhu, X.; Zhao, X.; Burkholder, W. F.; Gragerov, A.; Ogata, C. M.; Gottesman, M. E.; Hendrickson, W. A. Structural Analysis of Substrate Binding by the Molecular Chaperone DnaK. *Science* **1996**, *272*, 1606-1614.

(112) Pellecchia, M.; Montgomery, D. L.; Stevens, S. Y.; Vander Kooi, C. W.; Feng, H.-p.; Gierasch, L. M.; Zuiderweg, E. R. Structural Insights into Substrate Binding by the Molecular Chaperone DnaK. *Nat. Struct. Mol. Biol.* **2000**, *7*, 298-303.

(113) Chen, Z.; Kurt, N.; Rajagopalan, S.; Cavagnero, S. Secondary Structure Mapping of DnaK-Bound Protein Fragments: Chain Helicity and Local Helix Unwinding at the Binding Site. *Biochemistry* **2006**, *45*, 12325-12333.

(114) Kurt, N.; Cavagnero, S. Nonnative Helical Motif in a Chaperone-Bound Protein Fragment. *Biophys. J.* **2008**, *94*, L48-L50.

(115) Kim, J. H.; Tonelli, M.; Frederick, R. O.; Chow, D. C.-F.; Markley, J. L. Specialized Hsp70 Chaperone (HscA) Binds Preferentially to the Disordered Form, Whereas J-Protein (HscB) Binds Preferentially to the Structured Form of the Iron-Sulfur Cluster Scaffold Protein (IscU). *J. Biol. Chem.* **2012**, *287*, 31406-31413.

(116) Sekhar, A.; Lam, H. N.; Cavagnero, S. Protein Folding Rates and Thermodynamic Stability are Key Determinants for Interaction with the Hsp70 Chaperone System. *Protein Sci.* **2012**, *21*, 1489-1502.

(117) Chang, L.; Thompson, A. D.; Ung, P.; Carlson, H. A.; Gestwicki, J. E. Mutagenesis Reveals the Complex Relationships between ATPase Rate and the Chaperone Activities of Escherichia Coli Heat Shock Protein 70 (Hsp70/DnaK). *J. Biol. Chem.* **2010**, *285*, 21282-21291.

(118) Ravagnan, L.; Gurbuxani, S.; Susin, S. A.; Maisse, C.; Daugas, E.; Zamzami, N.; Mak, T.; Jäättelä, M.; Penninger, J. M.; Garrido, C. Heat-Shock Protein 70 Antagonizes Apoptosis-Inducing Factor. *Nat. Cell. Biol.* **2001**, *3*, 839-843.

(119) Packschies, L.; Theyssen, H.; Buchberger, A.; Bukau, B.; Goody, R. S.; Reinstein, J. GrpE Accelerates Nucleotide Exchange of the Molecular Chaperone DnaK with an Associative Displacement Mechanism. *Biochemistry* **1997**, *36*, 3417-3422.

(120) Zhang, O.; Kay, L. E.; Olivier, J. P.; Forman-Kay, J. D. Backbone 1H and 15N Resonance Assignments of the N-Terminal SH3 Domain of drk in Folded and Unfolded States Using Enhanced-Sensitivity Pulsed Field Gradient NMR Techniques. *J. Biomol. NMR* **1994**, *4*, 845-858.

(121) Bodner, C. R.; Dobson, C. M.; Bax, A. Multiple Tight Phospholipid-Binding Modes of A-Synuclein Revealed by Solution NMR Spectroscopy. *J. Mol. Biol.* **2009**, *390*, 775-790.

(122) Eghbalnia, H. R.; Bahrami, A.; Tonelli, M.; Hallenga, K.; Markley, J. L. High-Resolution Iterative Frequency Identification for NMR as a General Strategy for Multidimensional Data Collection. *J. Am. Chem. Soc.* **2005**, *127*, 12528-12536.

Chapter 2

^{1}H-detected ^{13}C Photo-CIDNP as a Sensitivity Enhancement Tool in Solution NMR

This chapter reproduces an article published by

Jung Ho Lee, Ashok Sekhar, and Silvia Cavagnero

in

Journal of the American Chemical Society (2011) 133, 8062-8065.

J.H.L. designed the project with other co-authors, carried out all experiments, and processed and analyzed the data with other co-authors. J.H.L and S.C. wrote the manuscript with assistance from A.S.

Abstract

NMR is a powerful yet intrinsically insensitive technique. The applicability of NMR to chemical and biological systems would be substantially extended by new approaches going beyond current signal-to-noise capabilities. Here, we exploit the large enhancements arising from ^{13}C photo-chemically induced dynamic nuclear polarization (^{13}C photo-CIDNP) in solution to improve biomolecular NMR sensitivity in the context of heteronuclear correlation spectroscopy. The ^{13}C-PRINT pulse sequence presented here involves an initial ^{13}C nuclear spin polarization via photo-CIDNP followed by conversion to antiphase coherence and transfer to ^{1}H for detection. We observe substantial enhancements, up to >>200-fold, relative to the dark (laser off) experiment. Resonances of both side-chain and backbone CH pairs are enhanced for the three aromatic residues Trp, His and Tyr and the Trp-containing σ^{32} peptide. The sensitivity of this experiment, defined as signal-to-noise per unit time $(S/N)_t$, is unprecedented in the NMR polarization enhancement literature dealing with polypeptides in solution. Up to a 16-fold larger $(S/N)_t$ than the ^{1}H-^{13}C SE-HSQC reference sequence is achieved, for the σ^{32} peptide. This gain leads to a reduction in data collection time up to 256-fold, highlighting the advantages of ^{1}H-detected ^{13}C photo-CIDNP in solution NMR.

2.1 Introduction

NMR is an invaluable spectroscopic tool to probe residue-specific molecular properties such as dynamics, folding and noncovalent interactions. To date, this technique has been largely exploited to study native and nonnative states of biomolecules in solution, including peptides, proteins and nucleic acids.[1-5]

Due to either scarce sample solubility,[6,7] the need to maintain low concentrations to overcome competing processes (e.g., aggregation), or the intrinsically low abundance of the target species in the relevant physiological environment,[8,9] liquid-state biomolecular NMR samples are often rather dilute, requiring highly sensitive data collection. In addition, real-time kinetic studies of fast events by NMR impose a need for rapid and efficient data collection even in concentrated samples.[10-13]

NMR's low sensitivity stems from marginal nuclear polarization at thermal equilibrium. Enhanced polarization methods tackle this problem by perturbing the thermal equilibrium upon coupling nuclei to other highly polarized quantum states.[14] For instance, molecules leads to NMR signal enhancements by the Haupt effect[15] and hyperfine depolarization,[16,17] respectively. In addition, electron polarization of alkali-metals leads to hyperpolarization of noble gases via optical pumping.[18,19] Despite the large signal enhancements attainable by the above methods, substrates amenable to these approaches are confined to the solid-state or to small molecules in liquid solution. Promising DNP methods that polarize samples directly in the liquid state[20-22] or rely on the rapid thawing of prepolarized frozen solutions have proven effective for small molecules (e.g. urea, glucose)[23,24] and dipeptides.[25] On the other hand, the harsh rapid-dissolution procedures necessary for some of these applications are generally not desirable for large biomolecules.

A different method, photo-chemically induced dynamic nuclear polarization (photo-CIDNP) offers considerable potential and opportunities.

2.2 Experimental Methods

Instrument Setup and Sample Preparation

The photo-CIDNP-inducing light beam (generated via a Spectra Physics 2017-AR in multiline mode with main lines at 488 and 514 nm, operating at 5.0 and 0.5 W for 1D and 2D experiments, respectively) was guided into the NMR sample tube inside the magnet via an optical fiber.[26,27] Uniformly ^{13}C, ^{15}N-enriched Trp, His, Tyr, a 13-residue σ^{32} peptide (1.0 mM each) and the N-terminal SH3 domain of the drk adaptor protein from *Drosophila* (drkN SH3, 0.3 mM) were used as model substrates. All data were collected in the presence of 0.2 mM of FMN in 95%H_2O/5%D_2O adjusted to pH 7.0, at 24°C. The chemically synthesized σ^{32} peptide (see primary structure in Fig. 2.4) comprises the 132-144 residues of the *E. coli* σ^{32} transcriptional regulator, with Leu_{135} replaced by ^{13}C,^{15}N-Trp.[28]

drkN SH3 Protein Expression and Purification

The drkN SH3 protein was overexpressed in *E. coli* and purified as described[29] except for the following modifications. A Q HP anion exchange column (GE Healthcare; Piscataway, NJ) was used instead of DE 52. The final ion exchange chromatography step (Mono Q column, GE Healthcare; Piscataway, NJ) was omitted after verifying protein purity by SDS PAGE.

2D NMR Data Collection

All the 2D NMR data were collected according to States-TPPI[30] with 32 increments and 1 scan per increment. For ^{13}C,^{15}N-Trp and the ^{13}C,^{15}N-Trp-labeled σ^{32} peptide, sweep widths of 6,000 Hz and 4,000 Hz were employed for the direct and indirect dimensions, respectively, with 1,000 complex points in the direct dimension. In the case of the drkN SH3 protein, sweep widths of 6,000 Hz and 3,000 Hz were employed for the direct and indirect dimensions, respectively, with 600 complex points in the direct dimension. A relaxation delay of 60 s was employed to ensure uniform photosensitizer dye (FMN) mixing between transients.

Additional Details on 2D ^{13}C-PRINT Data Collection

For ^{13}C, ^{15}N-Trp and the ^{13}C,^{15}N-Trp-labeled σ^{32} peptide, a laser power of 0.5 W and irradiation time (t_L) of 0.1 sec were used for the 2D ^{13}C-PRINT experiments shown in Figures 2.5 and 2.6. For the drkN SH3 protein (which has comparable populations of native and unfolded conformations exchanging slowly on the NMR chemical shift timescale), a short laser irradiation time (20 ms) at high laser power (2W) was used, to minimize photo-CIDNP polarization transfer between the folded and unfolded states during laser irradiation.

2D ^{13}C-PRINT and ^{1}H,^{13}C-SE-HSQC Data Processing

The time-domain data were zero-filled 4 times in both the direct and indirect dimensions. Exponential multiplication and an unshifted Gaussian were then applied to the 2D time-domain data collected on free Trp and the σ^{32} peptide. Exponential multiplication and a 20%-shifted Gaussian were applied in the case of experiments on the drkN SH3 protein, to optimize the resolution of the unfolded state resonances.

NMR Resonance Assignments of drkN SH3

H^N, N and H^α assignments and chemical shift information for the drkN SH3 protein were obtained from published data.[31] C^α assignments and chemical shifts were deduced from the known H^N and N assignments and new 3D HNCA experiment. The 3D data were collected on 0.3 mM DrkN SH3 in the presence of 50mM sodium phosphate in 95%H_2O/5%D_2O, at pH 6.0 and 30°C. HNCA data collection parameters were: 64 (^{13}C) and 32(^{15}N) increments (in States-TPPI mode) and 16 scans per increment. Sweep widths of 9,000 Hz, 4,000 Hz and 2200 Hz were employed for the ^{1}H, ^{13}C and ^{15}N dimensions, respectively, with 900 complex points in the direct dimension.

2.3 Results and Discussion

As shown in Figure 2.1, the ^{13}C photo-CIDNP-enhanced constant time reverse INEPT (^{13}C-PRINT) pulse sequence is designed to enhance ^{13}C polarization followed by transfer to ^{1}H for detection. In the case of emissive photo-CIDNP, the initial ^{13}C π pulse constructively adds ^{13}C longitudinal magnetization to ^{13}C-photo-CIDNP-induced polarization.

Figure 2.2 shows that ^{13}C-^{1}H photo-CIDNP leads to significant increases in signal-to-noise per unit time $(S/N)_t$ for free Trp under laser-on (*light*) conditions, relative to both laser-off (*dark*) conditions and to a reference sensitivity-enhanced pulse-field-gradient ^{1}H-^{13}C HSQC sequence[32] in constant-time mode[33] (denoted as ^{1}H-^{13}C SE-HSQC). The observed enhancements, relative to ^{1}H-^{13}C SE-HSQC, are 12 and 4-fold for $^{13}C^{\eta2}$-^{1}H and $^{13}C^{\alpha}$-^{1}H, respectively (Table 2.1). This result is particularly significant if one considers that ^{1}H-^{13}C SE-HSQC involves a full $^{1}H\rightarrow^{13}C\rightarrow^{1}H$ transfer while ^{13}C-PRINT only entails a $^{13}C\rightarrow^{1}H$ transfer. Even larger enhancements (41- and 22-fold) are detected, relative to dark conditions. A second type of dark experiment, denoted as dark', was also performed, with laser irradiation time (t_L) set to 0 to minimize unnecessary signal losses due to ^{13}C T_1 relaxation in the reference experiment. The observed Trp enhancements for $^{13}C^{\eta2}$-^{1}H and $^{13}C^{\alpha}$-^{1}H relative to the dark' experiments are 27 and 14-fold, respectively (Table 2.1). Figure 2.2b shows how $(S/N)_t$ varies upon increasing t_L. After the maximum enhancement is reached, a decrease in $(S/N)_t$ at long t_L is observed under light conditions, due to reduced sample photostability and ^{13}C T_1 relaxation, both of which counteract ^{13}C photo-CIDNP buildup. This profile shows the main drawback of photo-CIDNP, i.e., the need to properly modulate laser power and irradiation time to minimize photodegradation. Comparable photo-CIDNP enhancements are also found for His and Tyr (Fig. 2.3, Table 2.1). ^{13}C,^{15}N-labeled Leu and Ser, on the other hand, experience no photo-CIDNP enhancement. Note that Tyr displays a significant C^{α} enhancement while this effect is negligible for His. Small C^{β} ^{13}C-PRINT enhancements are also observed for Trp (data not shown). These effects

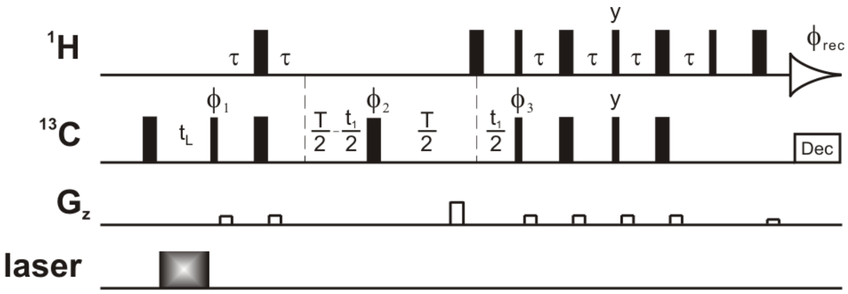

Figure 2.1 ^{13}C-PRINT NMR pulse sequence for ^{1}H-detected ^{13}C Photo-CIDNP-enhanced data collection. T is the total evolution time in the indirect dimension (13 and 27 ms for side chain and C^{α} carbons, respectively), for this constant-time sequence. τ is $1/4J_{CH}$ (1.6 ms) and t_L is the laser irradiation time. All pulses have x phase unless otherwise noted. ^{13}C decoupling during acquisition was performed by WURST140.[34] The phase cycling is ϕ_1 = y, -y; ϕ_2 = y, y, -x, -x, -y, -y, x, x; ϕ_{rec} = x, -x, -x, x. 2D experiments were run in States-TPPI mode (i.e., phase shifting of ϕ_1, ϕ_3, ϕ_{rec} concurrent with sign inversion of the last z-gradient). The initial ^{13}C π pulse is used to constructively add emissive ^{13}C photo-CIDNP polarization to the pre-existing ^{13}C magnetization. In the case of absorptive ^{13}C photo-CIDNP polarization, the π pulse is omitted.

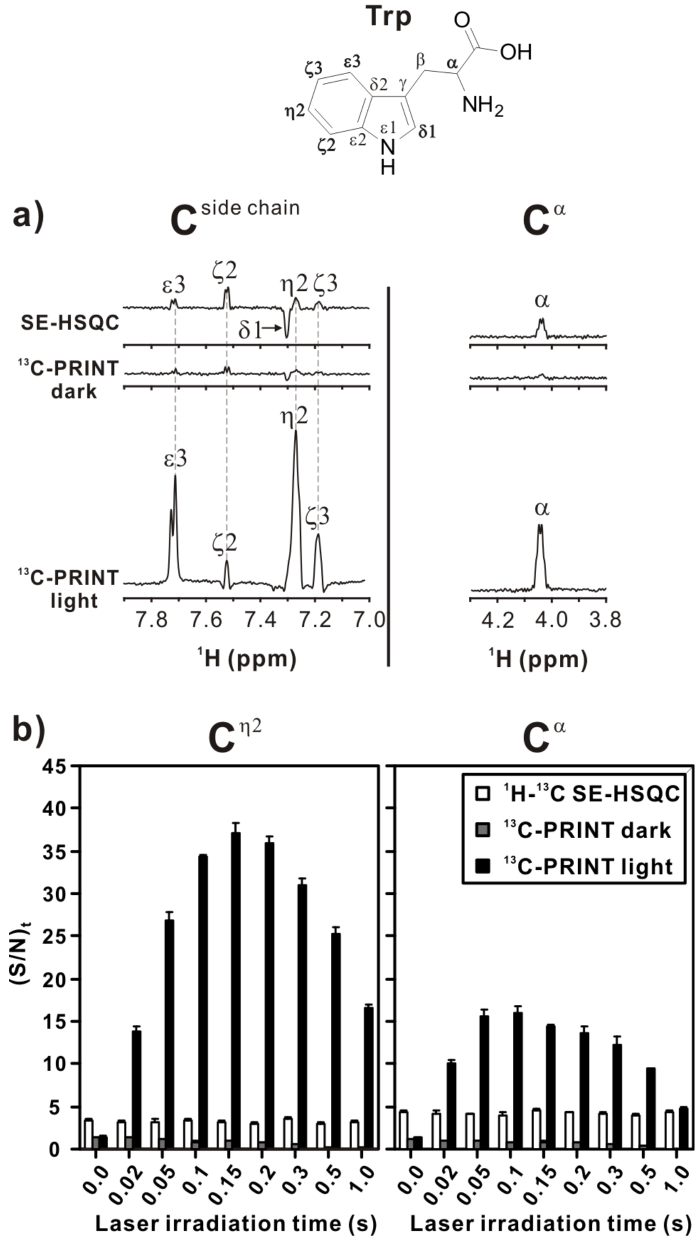

Figure 2.2 a) 1D ^{13}C-PRINT NMR spectra illustrating the ^{1}H-detected ^{13}C photo-CIDNP enhancements of 1.0 mM Trp in aqueous solution. A spectral window of 6,000 Hz with 2,000 complex points was used. The t_1 carbon chemical shift evolution was set to 0. The relaxation delay was set to 1.5 s in all experiments. Four transients and two steady-state scans were collected. The data shown in this panel were acquired with a

laser irradiation time t_L corresponding to the maximum $(S/N)_t$ (see t_L dependence profiles in panel b) Spectra were phased so that resonances resulting from emissive enhancements are positive. All the NMR data shown in this work were collected on Varian INOVA 600 MHz spectrometer equipped with a triple resonance $^1H\{^{13}C,^{15}N\}$ triple axis gradient probe. b) Dependence of ^{13}C photo-CIDNP enhancements on the laser irradiation time t_L. Experimental conditions and acquisition parameters other than t_L are as in a). $(S/N)_t$, defined as $(S/N)/t^{1/2}$, was determined as described.[35] All measurements were carried out on 3 independent samples. Uncertainties are expressed as ±1 standard error of the mean. Note that an increase in t_L leads to a decrease in *dark* $(S/N)_t$ due to ^{13}C T_1 relaxation during laser irradiation.

.

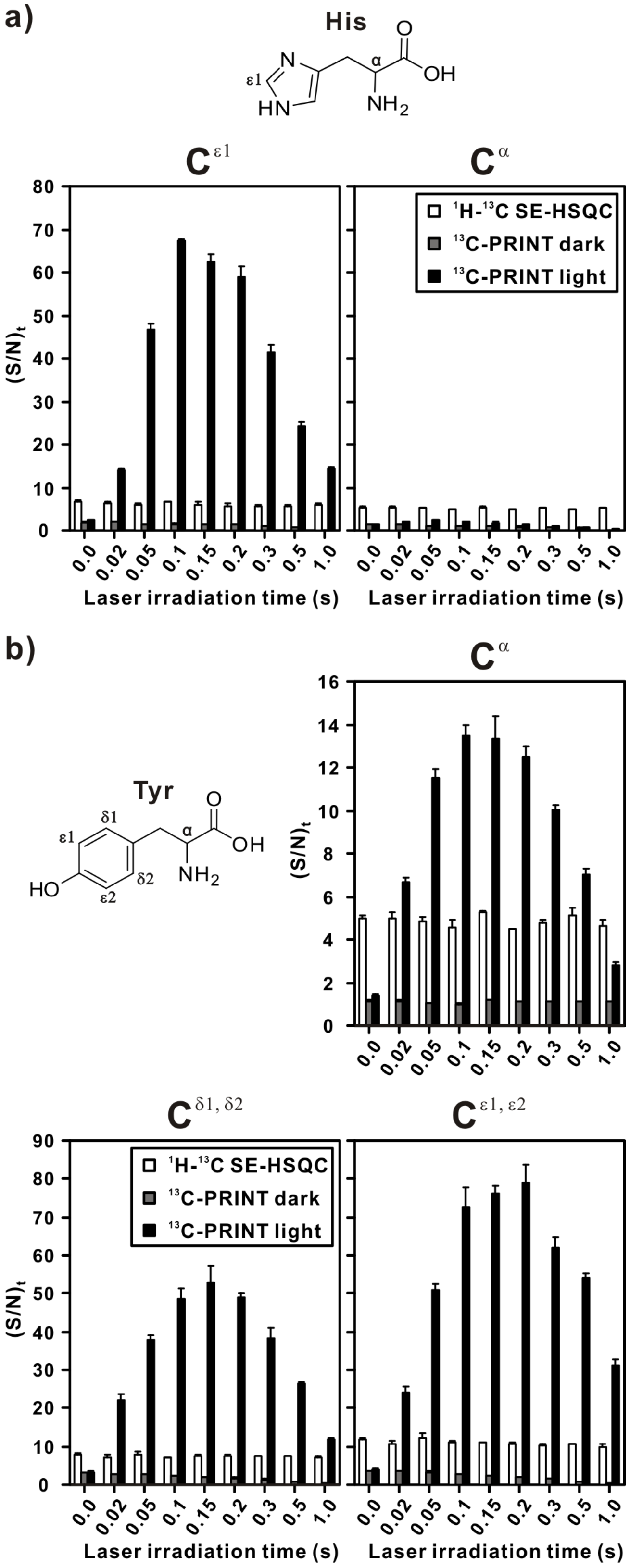
a)
His
ε1
N
HN
α
O
OH
NH2
Cε1
Cα
(S/N)t
0
10
20
30
40
50
60
70
80
□ 1H-13C SE-HSQC
■ 13C-PRINT dark
■ 13C-PRINT light
0.0
0.02
0.05
0.1
0.15
0.2
0.3
0.5
1.0
Laser irradiation time (s)
Laser irradiation time (s)
b)
Tyr
δ1
ε1
HO
ε2
δ2
α
O
OH
NH2
Cα
(S/N)t
0
2
4
6
8
10
12
14
16
Cδ1, δ2
Cε1, ε2
(S/N)t
0
10
20
30
40
50
60
70
80
90
□ 1H-13C SE-HSQC
■ 13C-PRINT dark
■ 13C-PRINT light
Laser irradiation time (s)
Laser irradiation time (s)

Figure 2.3 Laser irradiation time dependence of photo-CIDNP enhancements of a) His and b) Tyr via ^{13}C-PRINT. Experimental parameters and error analysis are as in Figure 2. The initial ^{13}C π pulse was omitted for the data collection on Tyr C^{α} because the photo-CIDNP enhancement is absorptive, in this case.

Table 2.1 $(S/N)_t$ enhancements obtained via 1D ^{13}C-PRINT on Trp, His, Tyr and the σ^{32} peptide in solution.[a,b]

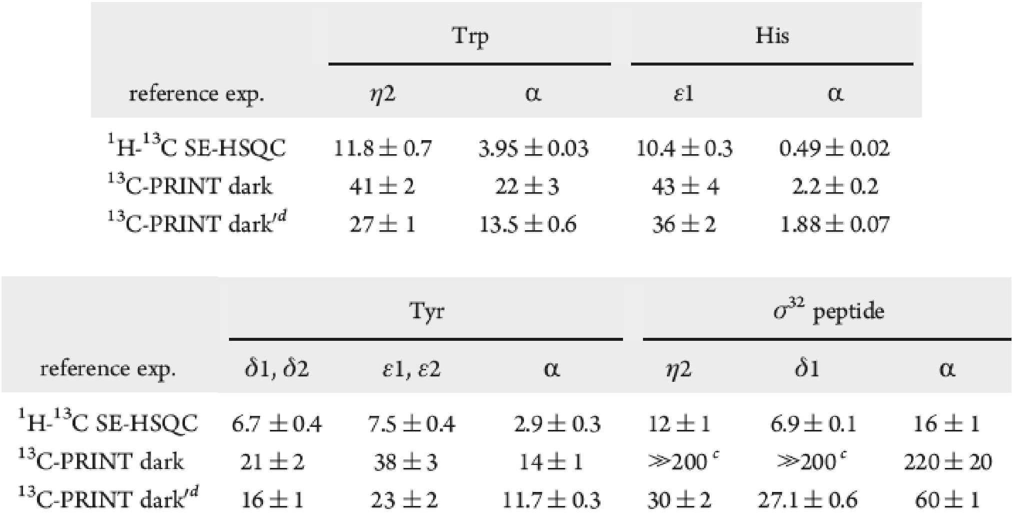

	Trp		His	
reference exp.	$\eta 2$	α	$\varepsilon 1$	α
^{1}H-^{13}C SE-HSQC	11.8 ± 0.7	3.95 ± 0.03	10.4 ± 0.3	0.49 ± 0.02
^{13}C-PRINT dark	41 ± 2	22 ± 3	43 ± 4	2.2 ± 0.2
^{13}C-PRINT dark′[d]	27 ± 1	13.5 ± 0.6	36 ± 2	1.88 ± 0.07

	Tyr			σ^{32} peptide		
reference exp.	$\delta 1, \delta 2$	$\varepsilon 1, \varepsilon 2$	α	$\eta 2$	$\delta 1$	α
^{1}H-^{13}C SE-HSQC	6.7 ± 0.4	7.5 ± 0.4	2.9 ± 0.3	12 ± 1	6.9 ± 0.1	16 ± 1
^{13}C-PRINT dark	21 ± 2	38 ± 3	14 ± 1	$\gg$200[c]	$\gg$200[c]	220 ± 20
^{13}C-PRINT dark′[d]	16 ± 1	23 ± 2	11.7 ± 0.3	30 ± 2	27.1 ± 0.6	60 ± 1

[a] The t_L value giving rise to maximums signal under light conditions (see Figure 2, 3) were used, for calculating the enhancements in this table. [b] All uncertainties were propagated considering the ±1 standard error in $(S/N)_t$ resulting from 3 independent measurements. [c] No explicit $(S/N)_t$ could be evaluated for these experiments because the dark spectrum lacked any detectable signal beyond the noise, even for prolonged data collection (64 transients). [d] The notation *dark'* denotes dark reference experiments with t_L set to 0 s.

are smaller in steady-state than in time-resolved CIDNP[36] likely due to differences in the extent of cancellation effects.[37]

To directly address the method's applicability to larger biological systems, we analyzed the σ^{32} model polypeptide, as shown in Figure 2.4. Interestingly, even larger enhancements than in the case of free Trp are observed for the σ^{32} peptide. ^{13}C-PRINT yields 16-fold larger $(S/N)_t$ than ^{1}H-^{13}C SE-HSQC for C^α, which is 4-fold larger than the enhancement observed for free Trp (Table 2.1). Photo-CIDNP enhancement patterns are also different for the side chain ^{13}Cs of free Trp and the σ^{32} peptide's Trp. Specifically, a dramatic enhancement is observed for $^{13}C^{\delta1}$ of the σ^{32} peptide Trp while a negligible effect is detected for the corresponding nucleus of free Trp (Figs 2.4 and 2.5, and Table 2.1). Therefore, ^{13}C photo-CIDNP enhancement patterns can be sensitive to the surrounding chemical environment.

In order to illustrate the power of ^{13}C photo-CIDNP in cases where high resolution is critical, 2D ^{13}C-PRINT data were collected for the σ^{32} peptide (Fig. 2.4b). Mild laser irradiation (power = 0.5W, t_L = 0.1sec) was employed in this case, to optimize sample photostability (<5% degradation) during data collection. Significant enhancements are evident here too (Fig. 2.4b). A comparison between Figures 2.4b, 2.5 and 2.6 illustrates how $(S/N)_t$ is maximized, in the case of emissive photo-CIDNP (e.g. see Trp $^{13}C^{\varepsilon3}$, $^{13}C^{\eta2}$), by retaining the initial ^{13}C π pulse.

Finally, we collected 2D ^{13}C-PRINT data on drkN SH3, a protein that populates both native and unfolded states in slow exchange on the NMR chemical shift timescale (Fig. 2.7). The greatest $(S/N)_t$ enhancements, up to 2.4-fold relative to ^{1}H-^{13}C SE-

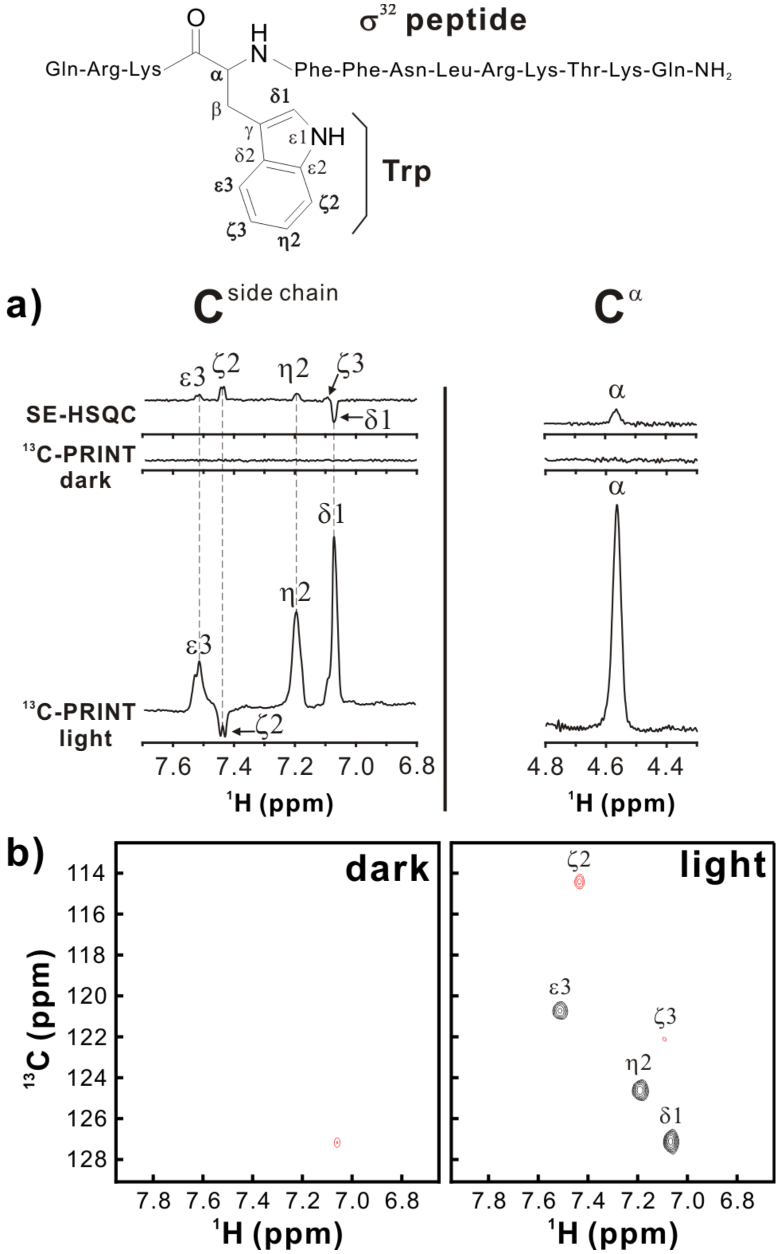

Figure 2.4 a) 1D NMR spectra for the ^{1}H-detected ^{13}C photo-CIDNP enhancement of the σ^{32} peptide. Experimental procedures are as in Figure 2. b) 2D dark and light ^{13}C-PRINT spectra of the σ^{32} peptide. 2D data were collected according to States-TPPI with 32 increments per row and 1 scan per increment. Sweep widths of 6,000 Hz and 4,000

Hz were employed, for the direct and indirect dimensions, respectively. Black and red contours denote positive and negative resonances, respectively. Emissive ^{13}C photo-CIDNP enhancements originate from $C^{\delta1}$, $C^{\varepsilon3}$ and $C^{\eta2}$ while absorptive enhancements are observed for $C^{\zeta2}$ and $C^{\zeta3}$. Note that emissive enhancements are phased to be positive.

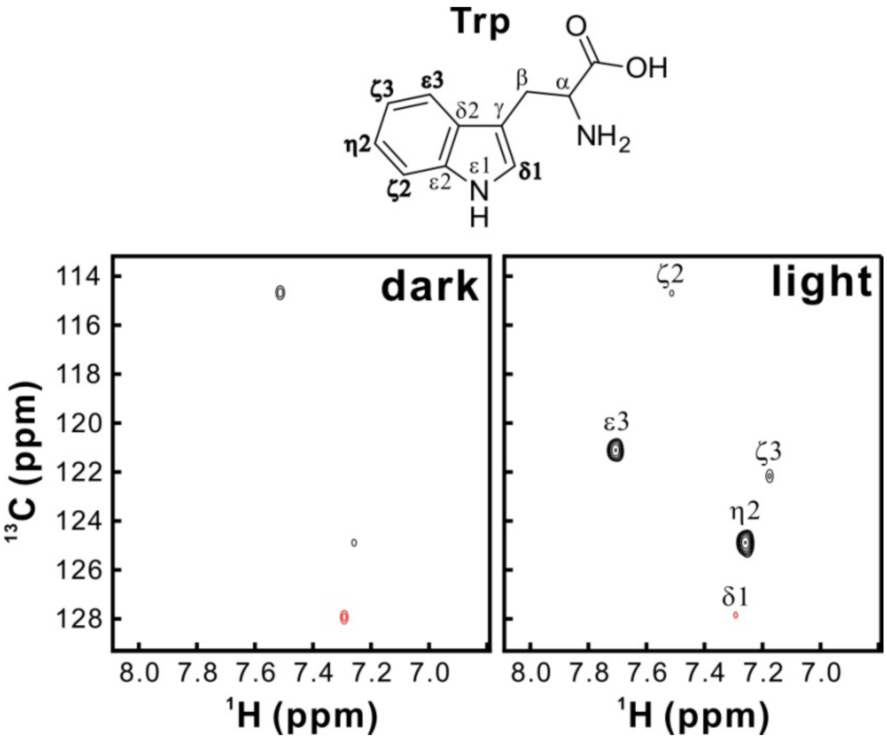

Figure 2.5 Aromatic side-chain region of the 2D ^{13}C-PRINT spectrum of 1.0 mM ^{13}C,^{15}N-Trp and 0.2 mM of FMN in 95%H_2O/5%D_2O adjusted to pH 7.0, at 24°C under dark and light conditions. Black and red contours denote positive and negative resonances, respectively.

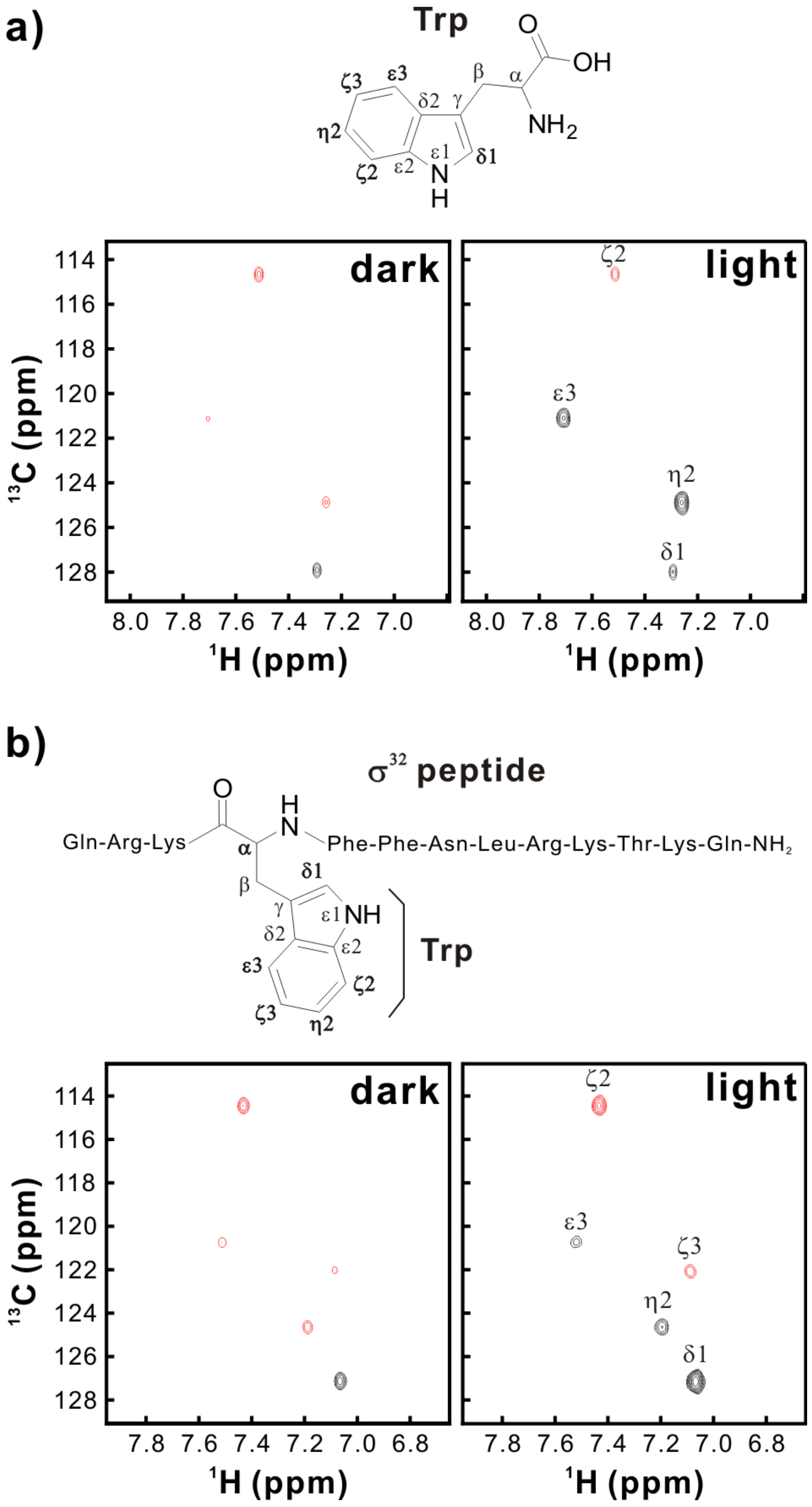
a)
Trp
O
OH
NH2
α
β
γ
δ1
δ2
ε1
ε2
ε3
ζ2
ζ3
η2
N
H
dark
light
ζ2
ε3
η2
δ1
114
116
118
120
122
124
126
128
13C (ppm)
8.0 7.8 7.6 7.4 7.2 7.0
1H (ppm)
b)
σ32 peptide
Gln-Arg-Lys
Phe-Phe-Asn-Leu-Arg-Lys-Thr-Lys-Gln-NH2
O
H
N
α
β
γ
δ1
δ2
ε1
NH
ε2
ε3
ζ2
ζ3
η2
Trp
dark
light
ζ2
ε3
ζ3
η2
δ1
114
116
118
120
122
124
126
128
13C (ppm)
7.8 7.6 7.4 7.2 7.0 6.8
1H (ppm)

Figure 2.6 Aromatic side-chain region of 2D dark and light ^{13}C-PRINT spectra of (a) ^{13}C,^{15}N-Trp and (b) ^{13}C,^{15}N-Trp-labeled σ^{32} peptide. Data were collected with no initial ^{13}C π pulse with 1.0 mM of σ^{32} peptide and 0.2 mM of FMN in 95%H_2O/5%D_2O at pH 7.0 and 24°C. Due to the absence of the initial ^{13}C π pulse, the dark resonances of the σ^{32} peptide have higher intensity and inverted sign, relative to the dark resonances of Figure 2.4b. This phenomenon leads to different-looking light spectra even though the intrinsic nature of the enhancement is the same. Specifically, weaker signals are observed for $C^{\varepsilon 3}$ and $C^{\eta 2}$ while stronger signals are observed for $C^{\delta 1}$, $C^{\zeta 2}$ and $C^{\zeta 3}$, compared to the ^{13}C-PRINT data collected in the presence of the initial ^{13}C π pulse. Similar effects are observed for free Trp (compare the spectrum in panel (a) with the spectrum in Fig. 2.5).

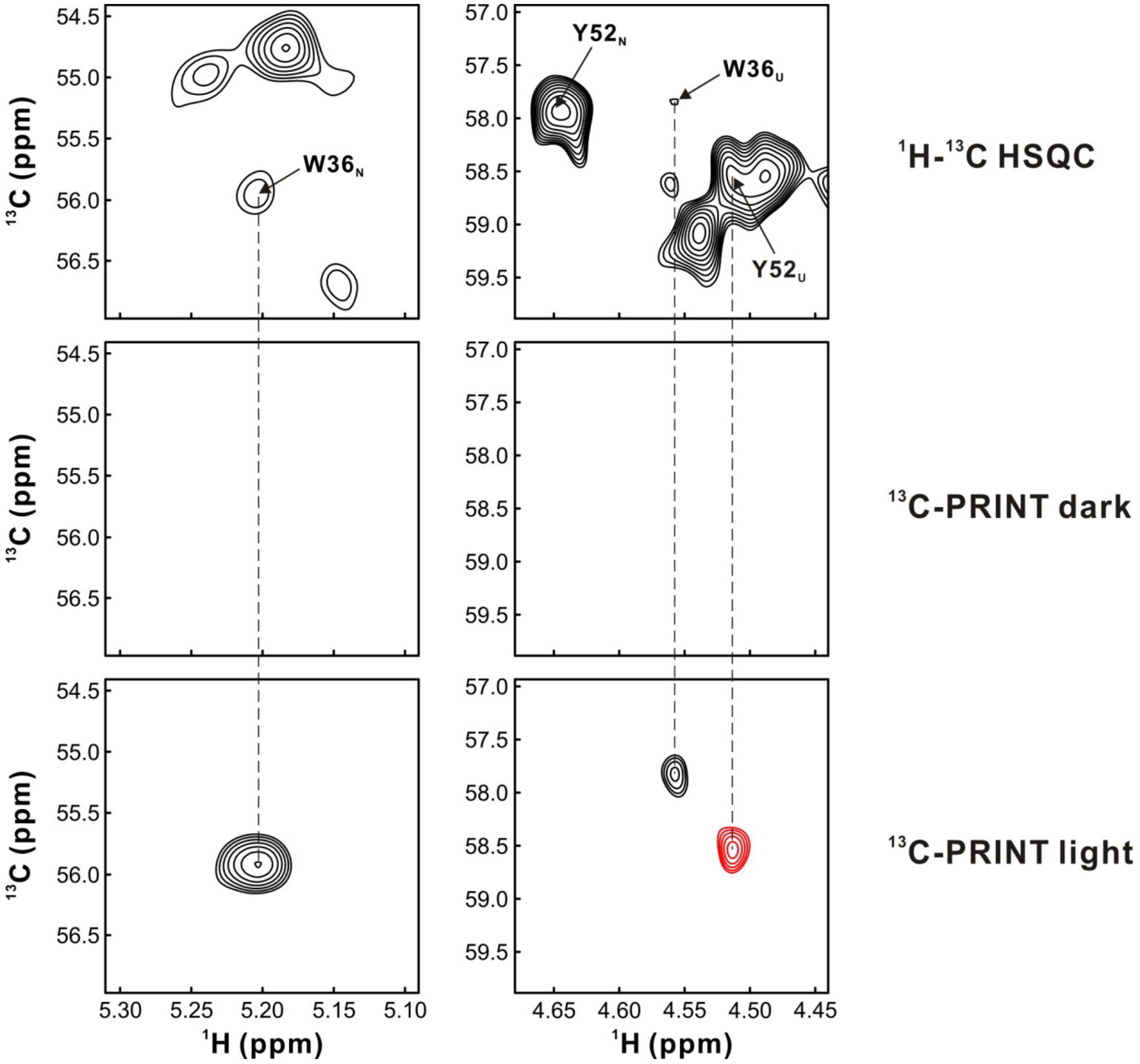

Figure 2.7 2D ^{13}C-PRINT spectra illustrating the most prominent NMR sensitivity enhancements experienced by the solvent-exposed C^{α} backbone resonances of the drkN SH3 protein (0.3 mM). Black and red contours denote positive and negative resonances, respectively. Emissive and absorptive enhancements are phased to be positive and negative, respectively. Note the different signs of the Trp and Tyr H^{α}–C^{α} resonances, which impart additional selectivity to the spectrum. Data were collected in the presence of 0.2mM FMN in 50mM sodium phosphate in D_2O, at pH 6.0 and 30°C.

HSQC, were observed for the Trp_{36} and Tyr_{52} ^{1}H-^{13}C$^{\alpha}$ pairs in the unfolded state, Moderate enhancements (up to 1.7-fold) were also observed for the partially solvent-exposed Trp_{36} in the native state. The above experiments concisely illustrate the fact that ^{13}C-PRINT is an extremely sensitive tool to probe amino acid, peptide and protein backbone conformation.

Comparisons between ^{13}C-PRINT enhancements of amino acids, peptide and protein (Figs. 2.2, 2.4 and 2.7) show different relative intensities and signs. We ascribe these variations to a combination of (a) the greater extent of exchange and recombination cancellation expected for amino acids, relative to proteins, and (b) the different hyperfine constants arising from changes in electronic distribution of the different species, likely due to differences in primary structure, conformation and protonation state of the radical cation within the transient radical ion pair.[37]

Comments on the 2D ^{13}C-PRINT Photo-CIDNP of the drkN SH3 Protein

Figure 2.7 shows the 2D ^{13}C-PRINT dark and light spectra of the *Drosophila* protein drkN SH3, which comprises the 1-59 N-terminal residues of *Drosophila* drk. The figure focuses on the spectral regions corresponding to the resonances undergoing the most prominent NMR sensitivity enhancements in C$^{\alpha}$ region. The native and unfolded states of drkN SH3 are in slow exchange ($k_{ex}=2.2\ s^{-1}$ at 20°C)[38] on the NMR chemical shift timescale, under physiological conditions.[31]

The most significant result is that the intensities of the 2D ^{13}C-PRINT resonances under light conditions are 1.7-, 2.4- and 0.6-fold larger than the corresponding ^{1}H-^{13}C SE-HSQC resonances, for the unique tryptophan in the native state ($\mathrm{W36}_{\mathrm{N}}$), for tryptophan in the unfolded state ($W36_U$), and for tyrosine in the unfolded state ($Y52_U$), respectively. The enhancement factors are likely underestimated due to resonance overlap in the reference ^{1}H-^{13}C SE-HSQC. Therefore, 2D ^{13}C-PRINT is an effective tool for the sensitivity enhancement of Trp and Tyr backbone resonances of drkN SH3, outperforming ^{1}H-^{13}C SE-HSQC. In addition, ^{13}C-PRINT can also be employed to readily estimate the differential degree of solvent-exposure of the target resonances in the native and unfolded states. In the case of drkN SH3, such assessment is particularly convenient as it can be performed in a single NMR experiment, given that the native and unfolded states are comparably populated and in slow exchange at pH 6.0 and 30°C.

In addition, 2D ^{13}C-PRINT intensities under light conditions are 2.3-, 6.0-, 3.0-fold larger than ^{13}C-PRINT intensities under dark conditions, for $W36_N$, $W36_U$, $Y52_U$, respectively. $Y52_N$ and $Y37_{U,N}$ do not show photo-CIDNP enhancements, possibly because they are not solvent-exposed.

Polarization Differences between Time-Resolved and Steady-State Photo-CIDNP

The relative intensities and some of the phases observed for the ^{13}C resonances of our 1D ^{13}C-PRINT experiments on Trp differ from those seen by Kiryutin and coworkers.[36] Specifically, $^{13}C^{\zeta 2}$ and $^{13}C^{\zeta 3}$ resonances in 1D ^{13}C-PRINT light experiments are emissively polarized with smaller relative intensities when compared to Kiryutin *et al.*'s spectra. Other resonances show similar relative intensities and phases.

To address whether continuous rather than time-resolved laser irradiation was responsible for the differences, we performed a control experiment under similar experimental conditions to those of the time-resolved 1D ^{13}C photo-CIDNP study by Kiryutin and coworkers, except for the fact that we employed continuous laser irradiation (3W, 0.1 s per transient; Figure 2.8). We observed the same polarization phases as Kiryutin *et al*., except for $^{13}C^{\zeta 2}$ and $^{13}C^{\zeta 3}$, which show negligible photo-CIDNP enhancement. On the other hand, the relative CIDNP intensities are significantly different for some resonances. The intensity differences are likely due to a combination of a variety of cancellation processes[37] that take place in steady-state photo-CIDNP experiments but not in the time-resolved experiment.

Regarding the observed differences of the $^{13}C^{\zeta 2}$ and $^{13}C^{\zeta 3}$ Trp resonances in 1D ^{13}C photo-CIDNP and 1D ^{13}C-PRINT, we hypothesize that processes operating on multiple timescales (e.g. Photo-CIDNP, NOE etc.) may be responsible for the overall observed polarization.[39] This hypothesis is backed up by the observation that the ^{13}C photo-CIDNP polarization phase for $^{13}C^{\zeta 2}$ resonance changes from emissive to absorptive when laser irradiation conditions vary from 5W, 0.15 s per scan to 5W, 20ms per scan. Indeed, the precise origin of the observed differences cannot be established with certainty at this juncture, and this topic deserves further future investigation.

2.4 Conclusions

This work demonstrates the power of ^{13}C photo-CIDNP in heteronuclear correlation NMR. Indeed, ^{1}H-detected ^{13}C photo-CIDNP leads to sensitivity enhancement for both side-chain and backbone CH pairs in amino acids, peptides and proteins in solution. The σ^{32} peptide sensitivity enhancement, up to 16-fold

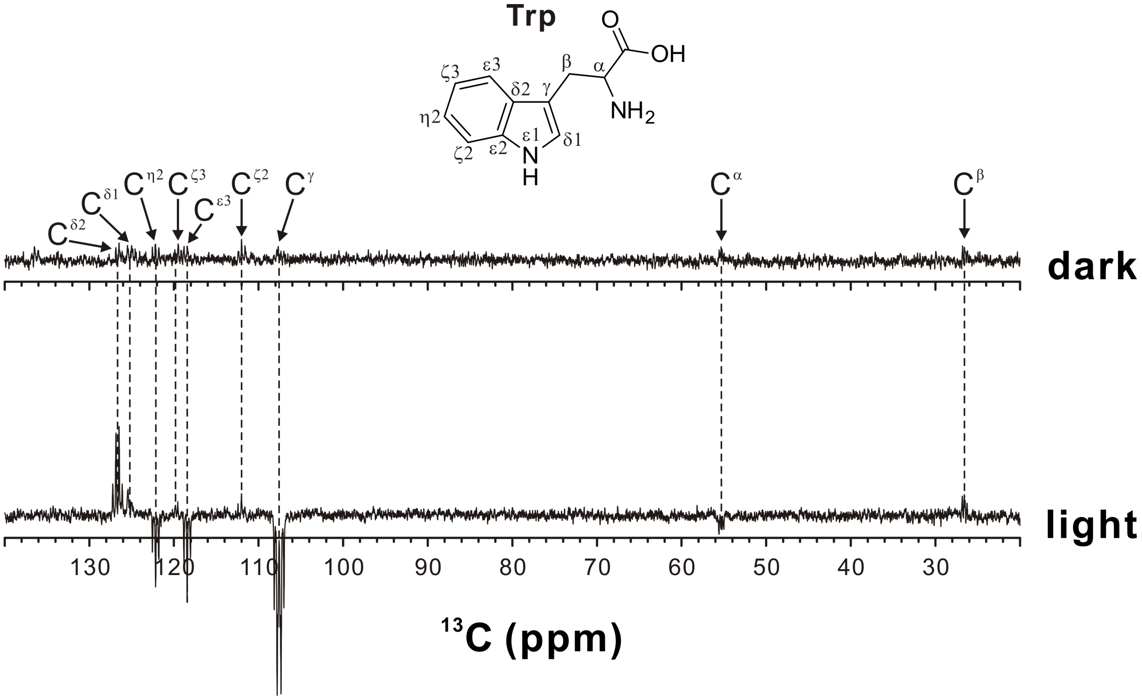

Figure 2.8 1D ^{13}C photo-CIDNP spectrum (pulse sequence: laser irradiation – ^{13}C 90° pulse – detection) of 5.0 mM ^{13}C,^{15}N-Trp and 0.2 mM of FMN in 95%H_2O / 5%D_2O at pH 7.0 and 24°. Sixteen transients and two steady-state scans with 60 s relaxation delay were collected under both dark and light conditions. A laser power of 3 W and a 0.1 s laser irradiation time (t_L) were employed.

over SE-HSQC, yields a reduction in data collection time up to 256-fold and highlights the promise of this approach. $^{13}C^{\alpha}$-^{1}H enhancements are particularly noteworthy, as these nuclei are robust reporters of backbone secondary structure. While ^{13}C-PRINT is tailored to enhance resonances from specific solvent-exposed residues (Tyr, Trp and His), recent advances suggest that in the future it may be possible to transfer photo-CIDNP-enhanced C^{α} and side chain C magnetization to other nearby nuclei via NOE.[40] We anticipate that the ^{1}H-detected ^{13}C photo-CIDNP method highlighted in this work will prove useful to study of both equilibrium biological processes in dilute solutions and kinetic time-courses demanding rapid data collection.

Acknowledgments

We are grateful to Alexandra Yurkovskaya, Lewis Kay, Charles Fry, and Milo Westler for helpful discussions, to Robert Shanks for technical assistance, and to Julie Forman-Kay for donating the drkN SH3 plasmid. This research was funded by the National Institute of Health Grant R21AI088551.

2.5 References

(1) Wright, P. E.; Dyson, H. J. Linking Folding and Binding. *Curr. Opin. Struct. Biol.* **2009**, *19*, 31-38.

(2) Dyson, H. J.; Wright, P. E. Unfolded Proteins and Protein Folding Studied by NMR. *Chem. Rev.* **2004**, *104*, 3607-3622.

(3) Gardner, K. H.; Kay, L. E. The Use of H-2, C-13, N-15 Multidimensional NMR to Study the Structure and Dynamics of Proteins. *Annu. Rev. Biophys. Biomolec. Struct.* **1998**, *27*, 357-406.

(4) Farrow, N. A.; Muhandiram, R.; Singer, A. U.; Pascal, S. M.; Kay, C. M.; Gish, G.; Shoelson, S. E.; Pawson, T.; Formankay, J. D.; Kay, L. E. Backbone Dynamics of a Free and a Phosphopeptide-Complexed Src Homology-2 Domain Studied by N-15 NMR Relaxation. *Biochemistry* **1994**, *33*, 5984-6003.

(5) Zuiderweg, E. R. P. Mapping Protein-Protein Interactions in Solution by NMR Spectroscopy. *Biochemistry* **2002**, *41*, 1-7.

(6) Kurt, N.; Rajagopalan, S.; Cavagnero, S. Effect of Hsp70 Chaperone on the Folding and Misfolding of Polypeptides Modeling an Elongating Protein Chain. *J. Mol. Biol.* **2006**, *355*, 809-820.

(7) Kurt, N.; Cavagnero, S. Nonnative Helical Motif in a Chaperone-Bound Protein Fragment. *Biophys. J.* **2008**, *94*, L48-L50.

(8) Rajagopalan, S.; Chow, C.; Raghunathan, V.; Fry, C. G.; Cavagnero, S. NMR Spectroscopic Filtration of Polypeptides and Proteins in Complex Mixtures. *J. Biomol. NMR* **2004**, *29*, 505-516.

(9) Bakke, C. K.; Jungbauer, L. M.; Cavagnero, S. In Vitro Expression and Characterization of Native Apomyoglobin under Low Molecular Crowding Conditions. *Protein Expr. Purif.* **2006**, *45*, 381-392.

(10) Frydman, L.; Scherf, T.; Lupulescu, A. The Acquisition of Multidimensional NMR Spectra within a Single Scan. *Proc. Natl. Acad. Sci. U.S.A.* **2002**, *99*, 15858-15862.

(11) Shapira, B.; Morris, E.; Muszkat, K. A.; Frydman, L. Sub-Second 2D NMR Spectroscopy at Sub-Millimolar Concentrations. *J. Am. Chem. Soc.* **2004**, *126*, 11756-11757.

(12) Gal, M.; Schanda, P.; Brutscher, B.; Frydman, L. UltraSOFAST HMQC NMR and the Repetitive Acquisition of 2D Protein Spectra at Hz Rates. *J. Am. Chem. Soc.* **2007**, *129*, 1372-1377.

(13) Giraudeau, P.; Shrot, Y.; Frydman, L. Multiple Ultrafast, Broadband 2D NMR Spectra of Hyperpolarized Natural Products. *J. Am. Chem. Soc.* **2009**, *131*, 13902-13903.

(14) Köckenberger, W.; Matysik, J., Hyperpolarization Methods and Applications in NMR. In *Encyclopedia of Spectroscopy and Spectrometry*, John, C. L., Ed. Elsevier: Oxford, 2010; p 963.

(15) Haupt, J. A New Effect of Dynamic Polarization in a Solid Obtained by Rapid Change of Temperature. *Phys. Lett. A* **1972**, *38*, 389-&.

(16) Rakitzis, T. P.; Samartzis, P. C.; Toomes, R. L.; Kitsopoulos, T. N.; Brown, A.; Balint-Kurti, G. G.; Vasyutinskii, O. S.; Beswick, J. A. Spin-Polarized Hydrogen Atoms from Molecular Photodissociation. *Science* **2003**, *300*, 1936-1938.

(17) Van Brunt, R. J.; Zare, R. N. Polarization of Atomic Fluorescence Excited by Molecular Dissociation. *J. Chem. Phys.* **1968**, *48*, 4304.

(18) Navon, G.; Song, Y.; Room, T.; Appelt, S.; Taylor, R. E.; Pines, A. Enhancement of Solution NMR and MRI with Laser-Polarized Xenon. *Science* **1996**, *271*, 1848-1848.

(19) Goodson, B. M. Nuclear Magnetic Resonance of Laser-Polarized Noble Gases in Molecules, Materials, and Organisms. *J. Magn. Reson.* **2002**, *155*, 157-216.

(20) Reese, M.; et al. H-1 and C-13 Dynamic Nuclear Polarization in Aqueous Solution with a Two-Field (0.35 T/14 T) Shuttle DNP Spectrometer. *J. Am. Chem. Soc.* **2009**, *131*, 15086.

(21) Lingwood, M. D.; Han, S. G. Dynamic Nuclear Polarization of C-13 in Aqueous Solutions under Ambient Conditions. *J. Magn. Reson.* **2009**, *201*, 137-145.

(22) Loening, N. M.; Rosay, M.; Weis, V.; Griffin, R. G. Solution-State Dynamic Nuclear Polarization at High Magnetic Field. *J. Am. Chem. Soc.* **2002**, *124*, 8808-8809.

(23) Ardenkjaer-Larsen, J. H.; Fridlund, B.; Gram, A.; Hansson, G.; Hansson, L.; Lerche, M. H.; Servin, R.; Thaning, M.; Golman, K. Increase in Signal-to-Noise Ratio of > 10,000 Times in Liquid-State NMR. *Proc. Natl. Acad. Sci. U.S.A.* **2003**, *100*, 10158-10163.

(24) Joo, C. G.; Casey, A.; Turner, C. J.; Griffin, R. G. In Situ Temperature-Jump Dynamic Nuclear Polarization: Enhanced Sensitivity in Two Dimensional C-13-C-13 Correlation Spectroscopy in Solution. *J. Am. Chem. Soc.* **2009**, *131*, 12-13.

(25) Vasos, P. R.; Comment, A.; Sarkar, R.; Ahuja, P.; Jannin, S.; Ansermet, J. P.; Konter, J. A.; Hautle, P.; van den Brandt, B.; Bodenhausen, G. Long-Lived States to Sustain Hyperpolarized Magnetization. *Proc. Natl. Acad. Sci. U.S.A.* **2009**, *106*, 18469-18473.

(26) Lyon, C. E.; Jones, J. A.; Redfield, C.; Dobson, C. M.; Hore, P. J. Two-Dimensional N-15-H-1 Photo-CIDNP as a Surface Probe of Native and Partially Structured Proteins. *J. Am. Chem. Soc.* **1999**, *121*, 6505-6506.

(27) Sekhar, A.; Cavagnero, S. H-1 Photo-CIDNP Enhancements in Heteronuclear Correlation NMR Spectroscopy. *J. Phys. Chem. B* **2009**, *113*, 8310-8318.

(28) McCarty, J. S.; Rudiger, S.; Schonfeld, H. J.; Schneider-Mergener, J.; Nakahigashi, K.; Yura, T.; Bukau, B. Regulatory Region C of the E. Coli Heat Shock Transcription Factor, Sigma(32), Constitutes a DnaK Binding Site and Is Conserved among Eubacteria. *J. Mol. Biol.* **1996**, *256*, 829-837.

(29) Bezsonova, I.; Singer, A.; Choy, W.-Y.; Tollinger, M.; Forman-Kay, J. D. Structural Comparison of the Unstable drkN SH3 Domain and a Stable Mutant. *Biochemistry* **2005**, *44*, 15550-15560.

(30) Marion, D.; Ikura, M.; Tschudin, R.; Bax, A. Rapid Recording of 2D NMR Spectra without Phase Cycling. Application to the Study of Hydrogen Exchange in Proteins. *J. Magn. Reson.* **1989**, *85*, 393-399.

(31) Zhang, O.; Kay, L. E.; Olivier, J. P.; Forman-Kay, J. D. Backbone 1H and 15N Resonance Assignments of the N-Terminal SH3 Domain of drk in Folded and Unfolded States Using Enhanced-Sensitivity Pulsed Field Gradient NMR Techniques. *J. Biomol. NMR* **1994**, *4*, 845-858.

(32) Kay, L. E.; Keifer, P.; Saarinen, T. Pure Absorption Gradient Enhanced Heteronuclear Single Quantum Correlation Spectroscopy with Improved Sensitivity. *J. Am. Chem. Soc.* **1992**, *114*, 10663-10665.

(33) Cavanagh, J.; Fairbrother, W. J.; Palmer, A. G.; Rance, M.; Skelton, N. J. *Protein NMR Spectroscopy: Principles and Practice*; 2 ed.; Elsevier Academic Press: San Diego, 2007.

(34) Kupce, E.; Freeman, R. Adiabatic Pulses for Wide-Band Inversion and Broad-Band Decoupling. *J. Magn. Reson.* **1995**, *115*, 273-276.

(35) Sekhar, A.; Cavagnero, S. EPIC- and CHANCE-HSQC: Two N-15-Photo-CIDNP-Enhanced Pulse Sequences for the Sensitive Detection of Solvent-Exposed Tryptophan. *J. Magn. Reson.* **2009**, *200*, 207-213.

(36) Kiryutin, A. S.; Morozova, O. B.; Kuhn, L. T.; Yurkovskaya, A. V.; Hore, P. J. H-1 and C-13 Hyperfine Coupling Constants of the Tryptophanyl Cation Radical in Aqueous Solution from Microsecond Time-Resolved CIDNP. *J. Phys. Chem. B* **2007**, *111*, 11221-11227.

(37) Hore, P. J.; Broadhurst, R. W. Photo-CIDNP of Biopolymers. *Prog. Nucl. Magn. Reson. Spectrosc.* **1993**, *25*, 345-402.

(38) Tollinger, M.; Skrynnikov, N. R.; Mulder, F. A.; Forman-Kay, J. D.; Kay, L. E. Slow Dynamics in Folded and Unfolded States of an SH3 Domain. *J. Am. Chem. Soc.* **2001**, *123*, 11341-11352.

(39) Kuprov, I.; Hore, P. Chemically Amplified 19F-1H Nuclear Overhauser Effects. *J. Magn. Reson.* **2004**, *168*, 1-7.

(40) Mok, K. H.; Kuhn, L. T.; Goez, M.; Day, I. J.; Lin, J. C.; Andersen, N. H.; Hore, P. J. A Pre-Existing Hydrophobic Collapse in the Unfolded State of an Ultrafast Folding Protein. *Nature* **2007**, *447*, 106-109.

Chapter 3

A Novel Tri-Enzyme System in Combination with Laser-Driven NMR Enables Efficient Nuclear Polarization of Biomolecules in Solution

This chapter reproduces an article published by

Jung Ho Lee and Silvia Cavagnero

in

The Journal of Physical Chemistry B (2013) 117, 6069–6081.

J.H.L. designed the project with S.C. J.H.L carried out all experiments and simulations. J.H.L and S.C. analyzed the data and wrote the manuscript.

Abstract

NMR is an extremely powerful, yet insensitive technique. Many available nuclear polarization methods that address sensitivity are not directly applicable to low-concentration biomolecules in liquids and are often too invasive. Photochemically induced dynamic nuclear polarization (photo-CIDNP) is no exception. It needs high-power laser irradiation, which often leads to sample degradation, and photosensitizer reduction. Here, we introduce a novel tri-enzyme system that significantly overcomes the above challenges rendering photo-CIDNP a practically applicable technique for NMR sensitivity enhancement in solution. The specificity of the nitrate reductase (NR) enzyme is exploited to selectively *in situ* re-oxidize the reduced photo-CIDNP dye $FMNH_2$. At the same time, the oxygen-scavenging ability of glucose oxidase (GO) and catalase (CAT) is synergistically employed to prevent sample photodegradation. The resulting tri-enzyme system (NR-GO-CAT) enables prolonged sensitivity-enhanced data collection in 1D and 2D heteronuclear NMR, leading to the highest photo-CIDNP sensitivity enhancement (48-fold relative to SE-HSQC) achieved to date for amino acids and polypeptides in solution. NR-GO-CAT extends the concentration limit of photo-CIDNP NMR down to the low micromolar range. In addition, sensitivity (relative to the reference SE-HSQC) is found to be inversely proportional to sample concentration, paving the way to the future analysis of even more diluted samples.

3.1 Introduction

Nuclear magnetic resonance (NMR) is arguably the most powerful technique to determine molecular structure and dynamics in solution at atomic resolution. On the other hand, NMR is intrinsically insensitive due to the similarity in nuclear spin populations of ground and excited states at thermal equilibrium, even in the presence of high applied magnetic fields. Major ongoing efforts in NMR spectroscopy aim at enhancing nuclear spin polarization in solids, liquids and gases by approaches known as dynamic nuclear polarization (DNP),[1-3] dissolution-DNP,[4,5] parahydrogen-induced polarization (PHIP),[6,7] optical pumping,[8,9] Haupt effect[10] and photochemically induced dynamic nuclear polarization (photo-CIDNP).[11-17] The latter technique, photo-CIDNP, is particularly attractive in the case of soluble biomolecules, as it can be used to increase NMR sensitivity under mild solution conditions.

Photo-CIDNP is typically carried out in the presence of a photosensitive dye capable of efficient intersystem crossing (e.g., flavin mononucleotide, also known as FMN) and transient substrate oxidation upon light excitation.[18,19] Sensitivity enhancements up to ca. 200-fold relative to the laser-free *dark* experiment have recently been achieved in solution for a variety of amino acids, peptides and proteins via ^{13}C-PRINT, a ^{1}H-detected ^{13}C photo-CIDNP pulse sequence capable of enhancing the side chain and backbone resonances of Trp, His and Tyr.[20] The photosynthetic reaction center, i.e., a large biomolecular complex susceptible to intra-molecular light-induced electron transfer, can even yield ~ 10,000-fold ^{13}C sensitivity enhancements.[21,22] Photo-CIDNP's primary advantages over other nuclear polarization approaches are the ability to operate under mild solution conditions and the relative simplicity of technical setup. Further, the use of this methodology for sensitivity enhancement purposes is still largely unexplored,[20, 23-27] and holds potential for even larger enhancements upon optimization of dye structure, laser irradiation schemes and other data collection parameters.

The inability to analyze low-concentration samples is one of the major limitations of NMR over other spectroscopies like fluorescence. As a result, typical NMR samples are limited to concentrations spanning from the hundreds-of-micromolar to the millimolar range. This is often a major limitation in biological and biomedical applications, where sample amounts are often scarce and poor solubility may impose additional low-concentration constraints.[28,29] The quest to increase NMR sensitivity is particularly pronounced in physiological environments, where low concentration and solubility are often matched by highly crowded media and inter-molecular interactions, which contribute to further decrease resonance linewidths and intensities. In the case of photo-CIDNP-induced highly polarized magnetization, prolonged signal averaging can potentially enable the analysis of very dilute samples, e.g., in the low-μM concentration range or lower, with significant improvements in signal-to-noise (S/N). In photo-CIDNP, however, three main challenges (Fig. 3.1a) need to be overcome before this goal can be achieved. First, laser irradiation, especially at high power, leads to irreversible photodegradation of the target NMR sample, especially if it bears an aromatic moiety.[30,31] Second, laser irradiation also causes chemical damage of the dye.[32-34] Third, the dye, typically flavin mononucleotide (FMN), experiences reversible reduction (e.g., leading to $FMNH_2$) during photo-CIDNP.[34-36] The reduced dye then needs to be reoxidized so that subsequent rounds of photo-CIDNP can take place.

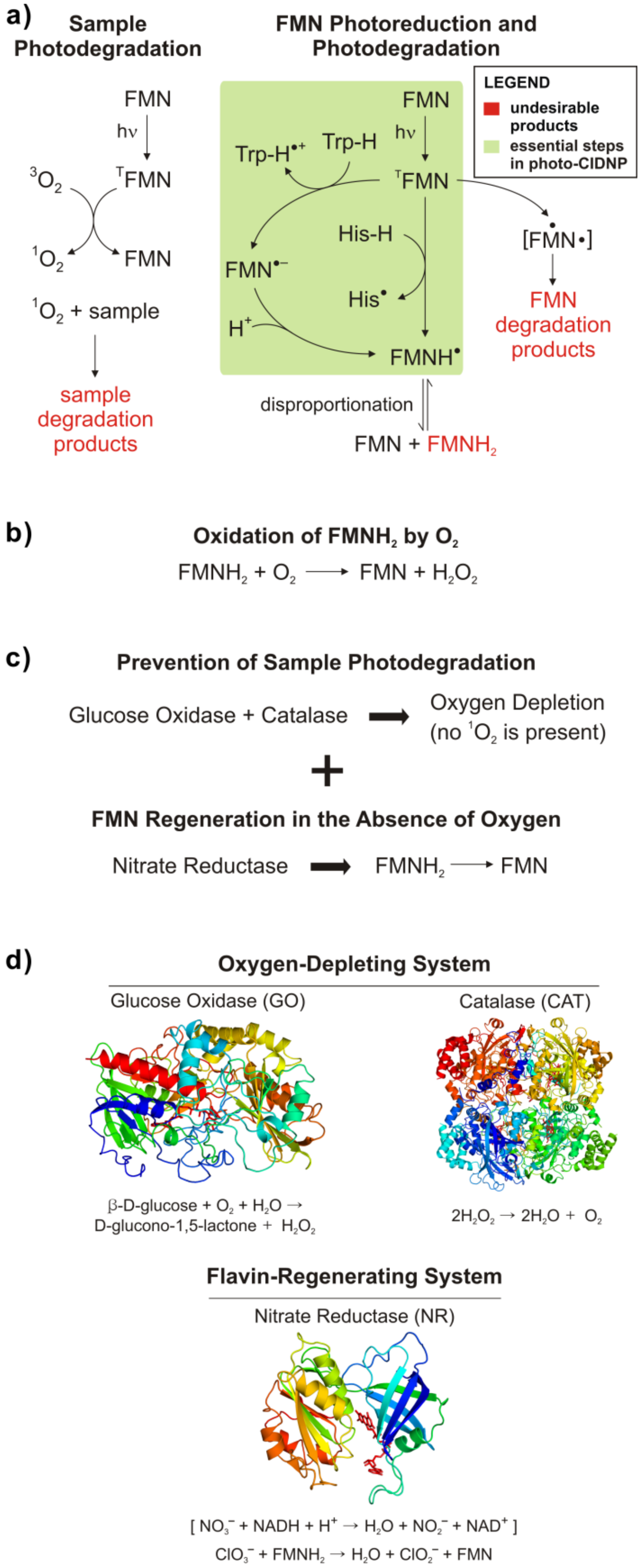
a)
Sample Photodegradation
FMN Photoreduction and Photodegradation
LEGEND
🟥 undesirable products
🟩 essential steps in photo-CIDNP
FMN
hν
^{T}FMN
$^{3}O_2$
$^{1}O_2$
FMN
$^{1}O_2$ + sample
sample degradation products
FMN
hν
Trp-H
$Trp\text{-}H^{\bullet +}$
^{T}FMN
$FMN^{\bullet -}$
His-H
$His^{\bullet}$
H^{+}
$FMNH^{\bullet}$
$[FMN^{\bullet}]$
FMN degradation products
disproportionation
FMN + $FMNH_2$
b)
Oxidation of $FMNH_2$ by O_2
$FMNH_2 + O_2 \longrightarrow FMN + H_2O_2$
c)
Prevention of Sample Photodegradation
Glucose Oxidase + Catalase ➡ Oxygen Depletion (no $^{1}O_2$ is present)
+
FMN Regeneration in the Absence of Oxygen
Nitrate Reductase ➡ $FMNH_2 \longrightarrow FMN$
d)
Oxygen-Depleting System
Glucose Oxidase (GO)
Catalase (CAT)
β-D-glucose + O_2 + H_2O → D-glucono-1,5-lactone + H_2O_2
$2H_2O_2 \rightarrow 2H_2O + O_2$
Flavin-Regenerating System
Nitrate Reductase (NR)
[NO_3^{-} + NADH + H^{+} → H_2O + NO_2^{-} + NAD^{+}]
ClO_3^{-} + $FMNH_2$ → H_2O + ClO_2^{-} + FMN

Figure 3.1 Diagrams illustrating the fundamental challenges underlying the enhancement of NMR signal-to-noise via photo-CIDNP, together with an outline of how the proposed tri-enzyme system meets the challenges. a) Major pathways leading to essential processes (enclosed in the green box) and undesired products (shown in red) in photo-CIDNP NMR. The species shown in square brackets is a putative biradical intermediate in the FMN photodegradation pathway.[33] b) Scheme showing that an advantageous feature of ambient oxygen is its ability to convert $FMNH_2$ back to FMN.[34] c) Proposed strategy for simultaneously overcoming NMR sample photodegradation and regenerating FMN in the presence of the NR-GO-CAT tri-enzyme system. d) Structure of the proposed photo-CIDNP-enhancing enzymes: glucose oxidase (GO, PDB ID: 1GAL),[61] catalase (CAT, PDB ID: 1TGU)[62] and nitrate reductase (NR, PDB ID: 2CND),[63] together with the reactions catalyzed by each enzyme. The FAD-binding domain of *Zea mays* nitrate reductase is displayed here (instead of the *Arabidopsis thaliana* nitrate reductase, NR, used in this work) due to the lack of structural information on NR. The two enzymes have the same biological function and share considerable sequence similarity (71%). The process in square brackets is the physiologically relevant NR reaction. Although both nitrate (NO_3^-) and chlorate (ClO_3^-) ions are viable substrates for NR, only ClO_3^- was used in this work.

Previous efforts to facilitate long-term photo-CIDNP and address the above challenges include *(a)* deliberate modulation of the oxygen concentration in the sample,[30] *(b)* addition of the oxidizing agent H_2O_2 to the NMR sample to regenerate the yellow FMN dye from its photoreduced nearly colorless $FMNH_2$,[35] and *(c)* regeneration of FMN by mechanical mixing during the experiment to facilitate oxidation by ambient oxygen (Fig. 3.1b).[35,37] Approach *a* leads to decreased photo-CIDNP regardless of whether oxygen is added or depleted. Specifically, under oxygen-saturation conditions, ^{T}FMN quenching prevents effective photo-CIDNP (Fig. 3.1a). Under oxygen-depletion conditions, photodegradation is efficiently suppressed (Fig. 3.1a) but the photoreduced $FMNH_2$ is not efficiently reoxidized to the original FMN (Fig. 3.1b). Approaches *b* and *c* are effective. However, long-term photo-CIDNP data collection is not ideal in the presence of oxidizing agents such as H_2O_2 even if they act slowly (approach *b*), and sample disturbance during the experiment is generally undesirable (approach *c*). Moreover, the sample photodegradation problem is not addressed by approaches *b* and *c*.

Here, we introduce a novel tri-enzyme system capable of simultaneously tackling the sample photodegradation and $FMNH_2$ reoxidation challenges (Fig. 3.1c). As shown in Figure 3.1d, the enzyme system comprises glucose oxidase (GO), catalase (CAT) and nitrate reductase (NR). This novel system has two complementary features. The oxygen scavenging component, which includes GO and CAT, prevents the singlet-oxygen-mediated sample degradation caused by the light-induced generation of ^{T}FMN (Fig. 3.1a). In addition, the oxidizing component NR efficiently and specifically oxidizes $FMNH_2$ back to FMN in the absence of oxygen. NR is a molybdenum-containing enzyme known to catalyze the conversion of nitrate to nitrite in plants, algae and fungi.[38] The tri-enzyme system (denoted here as NR-GO-CAT) extends the sample concentration limit of photo-CIDNP NMR down to the low micromolar range and greatly facilitates multidimensional photo-CIDNP applications while largely preserving substrate integrity.

3.2 Experimental Methods

Enzyme stock solutions. Glucose oxidase (GO, from *Aspergillus niger*, catalog number G7141, Enzyme Commission classification code: EC 1.1.3.4) and catalase (CAT, from *bovine* liver, cat. numb. C40, EC 1.11.1.6) were purchased from Sigma-Aldrich (St. Louis, MO), and nitrate reductase (NR, from *Arabidopsis thaliana*, cat. numb. AtNaR, EC 1.7.1.1) was acquired from NECi (Lake Linden, MI). The EC number, established by the Enzyme Commission, provides an unambiguous numerical classification of enzymes based on the source organism and the reactions they catalyze. All enzymes, provided in freeze-dried form, were separately dissolved in 30 mM potassium phosphate (pH 7.0). The GO and CAT stock solution concentrations were 6.3 and 8.0 μM, respectively. The NR stock solution concentration was 10 units/ml, with one unit defined as the amount of enzyme that reduces 1.0 µmole of nitrate to nitrite per min. at pH 7.5 and 30°C, with NADH serving as the substrate. The enzyme solutions were aliquoted and flash-frozen in liquid N_2 and stored at -80°C. Aliquots were thawed in a water bath at 30°C before use.

NMR sample preparation. Trp (574597), Tyr (607991), His (608009) and FMN (F8399) were purchased from Sigma-Aldrich. The σ^{32} peptide and the N-terminal SH3 domain of the drk adaptor protein from *Drosophila melanogaster* (drkN SH3) were prepared as previously described.[20] All NMR samples contained 0.2 mM FMN and 5% D_2O. The aromatic amino acid NMR samples were in 10 mM potassium phosphate (pH 7.0), and had 0.25 μM, 0.16 μM and 2.5 mM GO, CAT and D-glucose (158968, Sigma-Aldrich) concentrations,[39,40] respectively, and 0.54 μM (i.e., 0.3 units per 700 μl) NR concentration.[41] NR was used in combination with 2 mM sodium chlorate (244147, Sigma-Aldrich). The σ^{32} peptide samples were in 50 mM Tris, 5 mM $MgCl_2$ and 100 mM KCl (pH 7.5), and the drkN SH3 protein samples were in 50 mM Tris, 5 mM $MgCl_2$ and 50 mM KCl (pH 7.2). Both samples had a 10-fold smaller concentration of GO and CAT and a 3-fold smaller concentration of NR. Enzyme substrate (i.e. D-glucose, sodium chlorate) concentrations were identical to those of the aromatic amino acid samples. The aromatic amino acid and σ^{32} peptide samples were incubated in the NMR spectrometer for at least 15 min and 1 hr, respectively, to ensure optimal oxygen depletion prior to photo-CIDNP NMR data collection.

Photo-CIDNP setup. An argon ion laser (2017-AR, Spectra-Physics - Newport Corporation, Irvine, CA) in multiline mode (main lines at 488 and 514 nm) was used as a light source for all photo-CIDNP experiments. The laser light was focused into an optical fiber as described,[24] using a convex lens (LB4330, Thorlabs, Newton, NJ) and a fiber-coupler (F-91-C1-T, Newport Corporation). The optical fiber was guided into the NMR sample tube via a coaxial insert (WGS-5BL, Wilmad-Labglass, Buena, NJ). The position of the coaxial insert was adjusted such that the tip of the fiber was located 5 mm above the receiver coil region. Laser powers were measured at the sample-end of the optical fiber. The laser-to-fiber coupling efficiency[42] was ~50%.

Photo-CIDNP NMR experiments. All NMR data were collected at 25°C on a Varian INOVA 600 MHz NMR spectrometer equipped with a triple resonance $^{1}H\{^{13}C,^{15}N\}$ triple-axis gradient probe. The constant evolution time in the indirect dimension was set to 13 ms for both the ^{13}C-PRINT and SE-HSQC experiments. All the 1D data were apodized with a 5 Hz exponential line-broadening function and zero-filled twice. The 2D data were apodized with an unshifted Gaussian function and zero-filled twice in both dimensions. The relaxation delay was 10 s. The laser irradiation time was 0.1 s. The laser irradiation power was 1.5 W and 0.5 W for the 1D and 2D experiments, respectively.

Determination of $(S/N)_t$ and cumulative S/N. The signal-to-noise per unit time $(S/N)_t$ was evaluated as described.[24] Briefly, the NMR signal (S) was determined by measuring the intensity of the NMR resonance of interest relative to the average noise line. Peak-to-peak noise amplitude (N_{PTP}) was evaluated within a 4 ppm spectral width centered around the resonance of interest. The following equations were used

$$\mathrm{S/N} = \frac{2.5 \times \mathrm{S}}{\mathrm{N_{PTP}}} \quad \text{, and} \qquad (1)$$

$$(\mathrm{S/N})_t = \frac{\mathrm{S/N}}{\sqrt{t}} \quad , \qquad (2)$$

where t is the total data collection time.[43] Note that the terms sensitivity and $(S/N)_t$ are intended to have identical meaning and are interchangeably used throughout this work. In the case of low-micromolar control SE-HSQC, the signal was so weak that prolonged data acquisition had to be carried out until a reasonable S/N was attained, to compute $(S/N)_t$. The cumulative S/N in Fig. 3.4 was evaluated from

$$S/N = \frac{2.5 \times \sum_{i=1}^{n} S_i}{\sqrt{\sum_{j=1}^{n} N_{PTP,j}^{2}}} \quad , \qquad (3)$$

where n denotes the experiment number, S_1, S_2 … S_n are the intensities of the signal of interest across different experiments, and $N_{PTP,1}$, $N_{PTP,2}$, $N_{PTP,n}$ are the corresponding peak-to-peak noise amplitudes.

ESI Mass Spectrometry. Electrospray ionization (ESI) mass spectrometry studies were carried out with the 3200 Q TRAP LC/MS/MS System (Applied Biosystems, Foster City, CA) in positive ion mode. The buffer components of all samples were removed by treatment with ZipTip_{C18} devices (standard bed format, EMD Millipore Corporation, Billerica, MA). To remove low-molecular-weight impurities while preserving as much of the weakly-binding Trp on the C18 column as possible, the manufacturer’s recommended procedure was modified as follows. Briefly, the ZipTip_{C18} was subject to a) 3× treatment with 100% acetonitrile, b) 30× treatment with 5% methanol/0.1% TFA in water, c) 10× treatment with 0.1% TFA in water, d) sample binding to the resin by multiple up/down pipetting of 30 μl of the NMR sample solution containing 0.1% TFA, e) resin washing upon 10× treatment with 0.1% TFA in water, and f) sample elution upon multiple up/down pipetting steps with 5 μl of 20% acetonitrile/0.1% TFA in water.

Absorption spectroscopy in the UV-visible region. Absorption spectra of the NMR samples were acquired directly in the NMR tube with an HP 8452A diode array spectrophotometer. In order to properly position the NMR sample for absorption measurements, an NMR-tube cap was glued to the bottom of a disposable absorption cuvette appropriate for data collection at λ > 300 nm (14-955-129, Fisher Scientific, Pittsburgh, PA). The NMR sample was then inserted in the device and the interstitial space between the cuvette and the NMR tube was then filled with water. Complete conversion of FMN to $FMNH_2$, was accomplished in a control experiment upon adding trace amounts of $Na_2S_2O_4$ (157953, Sigma-Aldrich) to a solution containing 0.2 mM FMN, 0.2 mM Trp and 10 mM potassium phosphate at pH 7.0. All data were smoothed via the boxcar averaging procedure with a 4 nm window, using the MATLAB software package (Mathworks, Natick, MA).

3.3 Results and Discussion

Design of a tri-enzyme system for efficient photo-CIDNP under low-photodegradation conditions. Sample photodegradation upon laser irradiation is a major challenge in photo-CIDNP that renders this technique poorly suited to long-term NMR data collection. Oxygen-dependent pathways are a prominent cause of sample photodegradation (Fig. 3.1a).[30,31] Hence, we depleted ambient oxygen via the oxygen scavenging enzymes glucose oxidase and catalase[44] (Fig. 3.1c and 3.1d). The GO and CAT enzymes were previously employed to deplete oxygen in fluorescence microscopy[45] but not in NMR. We favor this method over alternative mechanical procedures (usually based on flushing the system with an inert gas)[46] because it is operationally easier, more efficient, and it enables continuous oxygen depletion. Our earlier efforts based on an alternative oxygen scavenging enzyme system, protocatechuate-3,4-dioxygenase in the presence of protocatechuic acid,[47] were not further pursued because protocatechuic acid significantly quenches photo-CIDNP.

In addition to promoting undesirable sample photodegradation, O_2 is also known to mediate an important, useful purpose in photo-CIDNP, i.e., reoxidation of the dye (Fig. 3.1b). Therefore, in addition to depleting oxygen via GO and CAT, we had to introduce an O_2 substitute capable of efficiently oxidizing the photo-CIDNP byproduct $FMNH_2$ back to FMN, without quenching ^{T}FMN. Our initial efforts focused on strong chemical oxidants. The best performing agents, Co (III) and persulfate, were able to oxidize $FMNH_2$ similarly to ambient oxygen but exhibited undesired solution behavior.

Next, we reasoned that a redox-active enzyme taking up $FMNH_2$ as a specific substrate may more effectively serve our purpose. Towards this goal we initially tested xanthine oxidase and FMN reductase. We found, however, that neither of them is effective at oxidizing $FMNH_2$, as both enzymes thermodynamically favor the conversion of FMN to $FMNH_2$ and not vice versa. In addition, xanthine oxidase was used in the presence of urate as a substrate. However, urate weakly quenches photo-CIDNP. After some initial moderately successful attempts with nitrate reductase from *Pichia pastoris*, we selected nitrate reductase from *Arabidopsis thaliana* (NR, Fig. 3.1c and 3.1d) due to its superior performance. The primary biological function of this enzyme is to reduce nitrate to nitrite while oxidizing NADH to NAD+.[38] Fortunately, $FMNH_2$ is also a viable substrate of the NR enzyme *in vitro*.[38] Similarly, nitrate was replaced by chlorate[48] which turned out to be more efficient at oxidizing $FMNH_2$ than nitrate. The complete reaction scheme adopted here is shown in Figure 3.1d.

In summary, our strategy has been to enzymatically remove molecular oxygen and concurrently reoxidize $FMNH_2$ (Fig. 3.1c). Our tri-enzyme system, denoted here as NR-GO-CAT, consists of glucose oxidase (GO), catalase (CAT) and nitrate reductase (NR) (Fig. 3.1d) and it successfully accomplishes the desired task. The addition of catalytic amounts of NR-GO-CAT enzymes to NMR samples leads to significant reduction in sample photodegradation and preservation of photo-CIDNP efficiency over a much longer time span than enzyme-free solutions.

Efficient photo-CIDNP at low sample concentration (200 μM) in the presence of the tri-enzyme system. The effect of the NR-GO-CAT tri-enzyme system depends critically on the concentration of the target biomolecule. We began by examining 200 μM ^{15}N,^{13}C-Trp, i.e., a model compound at a concentration typically employed in biomolecular NMR. Arrays of twenty ^{13}C-PRINT spectra (^{1}H-detected ^{13}C Photo-CIDNP)[20] were acquired back-to-back employing a high-power Ar ion laser (1.5 W) to examine the variation in photo-CIDNP under light conditions in the absence and presence of different combinations of enzymes (Fig. 3.2b). Photoexcited triplet FMN converts molecular oxygen, $^{3}O_2$, usually present at ca. 0.27 mM in aqueous solution,[49] to singlet oxygen ($^{1}O_2$). The latter, in turn, causes significant sample degradation according to the scheme in Fig. 3.1a. In order to estimate the extent of photodegradation, ^{1}H 1D pulse-acquire data were also collected before and after the

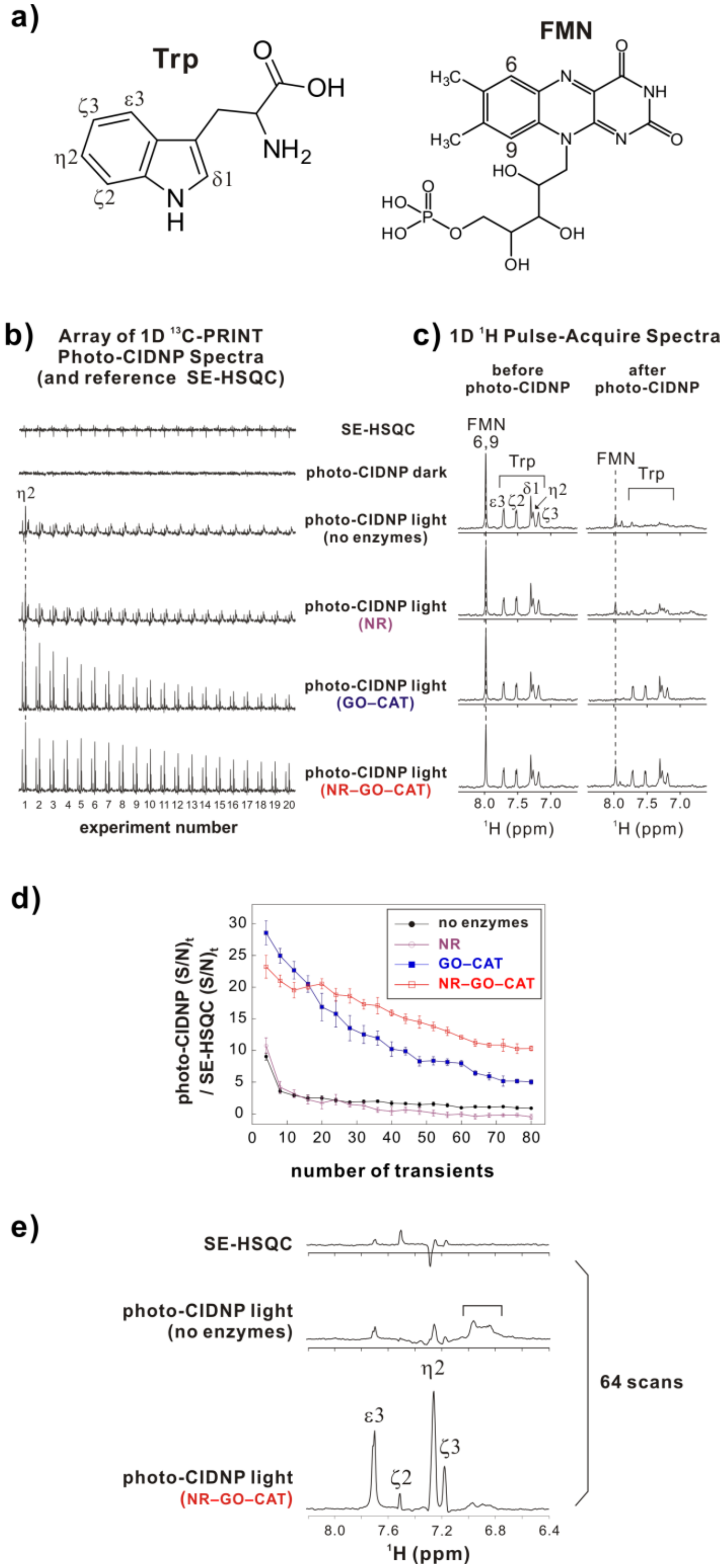
a)
Trp
FMN
b) Array of 1D ¹³C-PRINT Photo-CIDNP Spectra (and reference SE-HSQC)
c) 1D ¹H Pulse-Acquire Spectra
before photo-CIDNP
after photo-CIDNP
SE-HSQC
photo-CIDNP dark
photo-CIDNP light (no enzymes)
photo-CIDNP light (NR)
photo-CIDNP light (GO–CAT)
photo-CIDNP light (NR–GO–CAT)
FMN 6,9
Trp
ε3 ζ2 δ1 η2 ζ3
experiment number
¹H (ppm)
d)
photo-CIDNP (S/N)t / SE-HSQC (S/N)t
number of transients
no enzymes
NR
GO–CAT
NR–GO–CAT
e)
SE-HSQC
photo-CIDNP light (no enzymes)
photo-CIDNP light (NR–GO–CAT)
64 scans
¹H (ppm)

Figure 3.2 Laser-driven photo-CIDNP NMR of 200 μM aqueous Trp in the absence and presence of different enzymes. a) Structure of tryptophan (Trp) and flavin mononucleotide (FMN). b) Array of ^{1}H-detected ^{13}C-PRINT photo-CIDNP spectra in the absence and presence of different enzyme combinations (4 scans per experiment, data collected back-to-back, 80 scans total). This panel also includes ^{1}H-^{13}C SE-HSQC reference spectra (equal number of scans and identical relaxation delay to ^{13}C-PRINT). The resonances detectable under no-enzyme and NR-only conditions are mostly due to photodegradation products. c) ^{1}H spectra before and after the collection of the array of experiments displayed in panel c (1.5W laser power, 0.1s laser pulse duration per scan). d) Graph illustrating the ratio of $(S/N)_t$ for ^{13}C-PRINT (light conditions) and SE-HSQC experiments (η2 Trp resonance) in the absence and presence of different enzyme combinations. Error bars denote standard errors for three independent experiments. e) 1D ^{13}C-PRINT photo-CIDNP spectra (64 scans per spectrum) in the absence and presence of the NR-GO-CAT tri-enzyme system. The bracket in the photo-CIDNP light (no enzymes) condition denotes photodegradation products.

array of photo-CIDNP experiments, as shown in Figure 3.2c.

In the absence of enzymes or in the presence of NR alone, a significant decrease in the Trp ^{13}C-PRINT resonance intensities is observed (Fig. 3.2b). This result is a direct consequence of sample photodegradation, as illustrated in Figure 3.2c, showing the disappearance of most Trp signals after the photo-CIDNP experimental array, under no-enzyme and NR conditions.

In the presence of catalytic amounts of the oxygen-scavenging enzymes GO (0.25 μM) and CAT (0.16 μM), however, much higher photo-CIDNP resonance intensities are observed (Fig. 3.2b). Figure 3.2c provides evidence for the origin of this effect by showing that GO and CAT prevent Trp photodegradation as most of the Trp resonances preserve their original intensity at the end of the experiment. Hence, oxygen depletion prevents sample photodegradation and enables the photo-CIDNP S/N enhancement to persist for many transients.

The prevention of Trp photodegradation is a clear advantage. Yet, it is not sufficient to enable long-term photo-CIDNP data collection because, under GO-CAT conditions, the ^{13}C-PRINT intensity decreases fairly rapidly over time (Fig. 3.2b). This phenomenon limits the ability to exploit the photo-CIDNP sensitivity enhancement in long experiments. Visual analysis of NMR samples after photo-CIDNP reveals that the solution loses a considerable fraction of its yellow color, imparted by FMN. This effect can be ascribed to either the accumulation of the nearly-colorless FMN-reduction product, $FMNH_2$, expected after multiple rounds of photo-CIDNP, or to irreversible FMN photodegradation (Fig. 3.1a). Absorption spectroscopy, performed directly on the NMR samples before and after laser irradiation (Fig. 3.3), helps shedding light on this topic.

The FMN absorption spectral changes observed after photo-CIDNP in the presence of the GO-CAT enzymes suggest that a significant fraction of FMN has been converted into other species (Fig. 3.3b). The 344 nm isosbestic point of the pre- and post-photo-CIDNP spectra of Fig. 3.3b (similar to the isosbestic point of FMN and $FMNH_2$ observed in the literature)^{36} is consistent with the presence of both FMN and $FMNH_2$ in the post-photo-CIDNP sample. The $FMNH_2$ reference spectrum (Fig. 3.3, dotted lines) also naturally (i.e., in agreement with the published spectrum)^{36} extrapolates to this isosbestic point. Note that the $FMNH_2$ reference spectrum is not explicitly shown at wavelengths lower than 400 nm, due to overlap with the absorption band of sodium dithionite, which was introduced in the reference sample to quantitatively convert FMN to $FMNH_2$. Transient exposure of the post-photo-CIDNP sample to molecular oxygen via manual mixing causes regeneration of FMN from $FMNH_2$, as evidenced by the spectral changes in Fig. 3.3c. This regeneration (Fig. 3.3c) is likely slightly overestimated since O_2 exposure upon mixing inevitably involves mixing of the irradiated sample region with the non-irradiated region containing intact FMN. The same argument applies to NR-GO-CAT conditions (Fig. 3.3e).

Incidentally, NMR (Fig. 3.2c) suggests that FMN has been fully depleted, after the photo-CIDNP array in the presence of GO and CAT (Fig. 3.2c, see disappearance of FMN 6 and 9 NMR resonances). However, absorption spectroscopy implies that some FMN is left in solution under the same conditions (Fig. 3.3b). This apparent inconsistency can be explained upon considering that line-broadening beyond detection

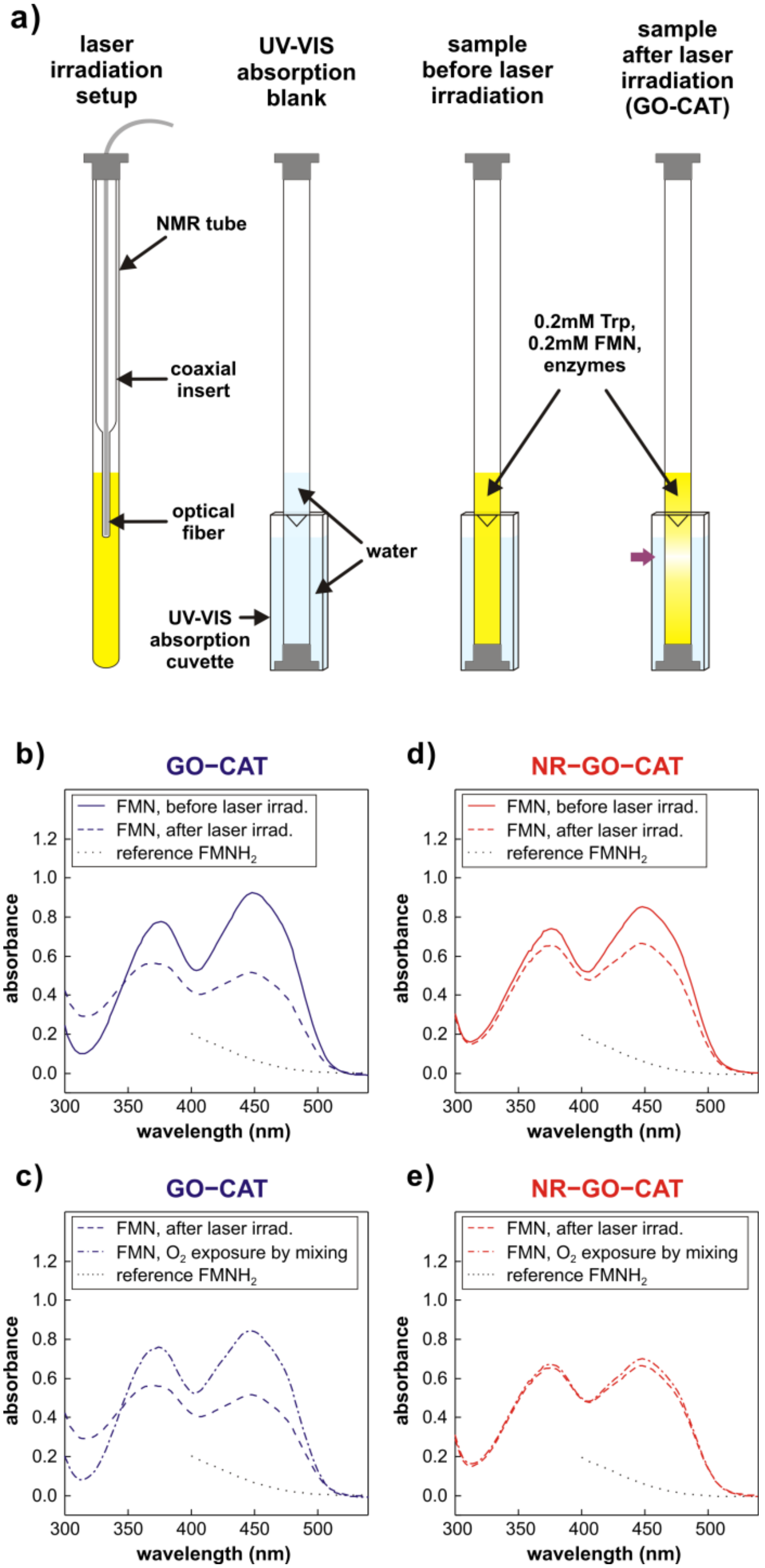
a)
laser irradiation setup
UV-VIS absorption blank
sample before laser irradiation
sample after laser irradiation (GO-CAT)
NMR tube
coaxial insert
optical fiber
UV-VIS absorption cuvette
water
0.2mM Trp, 0.2mM FMN, enzymes
b)
GO−CAT
FMN, before laser irrad.
FMN, after laser irrad.
reference $FMNH_2$
absorbance
wavelength (nm)
0.0
0.2
0.4
0.6
0.8
1.0
1.2
300
350
400
450
500
c)
GO−CAT
FMN, after laser irrad.
FMN, O_2 exposure by mixing
reference $FMNH_2$
absorbance
wavelength (nm)
d)
NR−GO−CAT
FMN, before laser irrad.
FMN, after laser irrad.
reference $FMNH_2$
absorbance
wavelength (nm)
e)
NR−GO−CAT
FMN, after laser irrad.
FMN, O_2 exposure by mixing
reference $FMNH_2$
absorbance
wavelength (nm)

Figure 3.3 Electronic absorption spectroscopy of photo-CIDNP samples. a) Experimental setup to record the absorption spectra of NMR samples directly in the NMR sample tube. FMN spectra before and after laser irradiation are plotted for b) GO-CAT and d) NR-GO-CAT conditions. Note that $FMNH_2$ spectrum is shown only in long wavelength range due to strong absorbance by $Na_2S_2O_4$ (which was used to reduce FMN to $FMNH_2$) at short wavelength range. Absorption spectra of NMR samples after the photo-CIDNP experiments under c) GO-CAT and e) NR-GO-CAT conditions, before and after exposure to O_2 via sample mixing.

of the FMN 6 and 9 overlapping ^1H NMR resonances is likely due to chemical exchange with trace amounts of the FMNH$^\bullet$ radical (Fig. 3.1a),[50] an obligatory species in photo-CIDNP (see further comments below).

The above combined evidence highlights two important facts. First, the nearly quantitative regeneration of FMN in Fig. 3.3c speaks in favor of long-term photo-CIDNP opportunities in the presence of NR-GO-CAT. Second, in order to perform long-term photo-CIDNP, a strategy to oxidize FMNH$_2$ *in situ* and produce FMN in the absence of molecular oxygen is necessary to further improve upon the GO-CAT conditions.

More persistent photo-CIDNP enhancements are observed when catalytic amounts (0.54 μM) of the third enzyme, NR, capable of oxidizing FMNH$_2$ back to FMN, are added to the solution. The latter conditions, including all three enzymes, are denoted here as NR-GO-CAT, and define the tri-enzyme system proposed in this study. NR-GO-CAT enables efficient photo-CIDNP by synergistically (a) minimizing the amount of sample photodegradation via GO and CAT, as shown in Figure 3.2c, and (b) by re-oxidizing the FMNH$_2$ dye due to the specific oxidizing action of NR. The regeneration of FMN under NR-GO-CAT conditions is testified by the post-photo-CIDNP ^1H NMR spectrum of Fig. 3.2c, which shows partially recovered FMN 6 and 9 resonances (with a 43 ± 5 % line-broadening due to chemical exchange with FMNH$^\bullet$ on the fast T_2 timescale) even after many photo-CIDNP cycles. The FMN recycling under NR-GO-CAT conditions is also supported by the absorption data of Figure 3.3d. Here, the post-photo-CIDNP FMN transition centered at ca. 400 nm is closer to the intensity before the laser irradiation, indicating that more FMN is in solution than under GO-CAT conditions (Fig. 3.3b). The incomplete FMN recovery under NR-GO-CAT conditions is likely due to a small extent of irreversible FMN photodegradation (see also mass spectrometry data in Fig. 3A.1). The absence of an isosbestic point in Fig. 3.3d supports the absence of $FMNH_2$ in solution. Interestingly, panel e of Fig. 3.3 shows that upon exposure to molecular oxygen no additional intensity is recovered, indicating that the FMN regeneration ability of the NR enzyme is as good as that of molecular oxygen.

The power of the NR-GO-CAT tri-enzyme system is best recapitulated by the plot of Fig. 3.2d, which shows the sensitivity of ^{13}C-PRINT in the presence of NR-GO-CAT relative to the sensitivity of the reference ^{1}H-^{13}C SE-HSQC. The data show that ^{13}C-PRINT in the presence of the tri-enzyme system is more sensitive than ^{1}H-^{13}C SE-HSQC by up to 25-fold. In addition, the NR-GO-CAT photo-CIDNP experiments are dramatically, i.e., up to 13 ± 2 times, more effective than enzyme-free photo-CIDNP, even after collection of many transients.

The slightly smaller ratio of $(S/N)_t$ observed for NR-GO-CAT (red trace in Fig. 3.2d) relative to GO-CAT (blue trace in Fig. 3.2d) during the initial ~15 scans is likely due to the EDTA in the commercially available NR source.[15] The secondary substrate of NR, sodium chlorate (2 mM), which is also added to the solution, does not have significant effect on photo-CIDNP.

Fig. 3.2e provides a visual illustration of the results achievable in a single relatively long-term experiment (64 scans) in the absence and presence of the NR-GO-CAT enzyme system with minimal (< 10%) photodegradation. The advantages of photo-CIDNP in the presence of the tri-enzyme system over SE-HSQC and regular enzyme-free photo-CIDNP are evident.

The effect of the argon ion laser power on photo-CIDNP experiments carried out in the presence and absence of the tri-enzyme system is shown in Figure 3.4. For all the powers tested (0.2, 0.5 and 1.5W), the NR-GO-CAT-containing samples perform much better than the samples lacking the enzymes. At the highest laser power (1.5 W), the NR-GO-CAT system is particularly effective, highlighting the usefulness of the three enzymes under conditions yielding the largest NMR sensitivity. Panel b of Figure 3.4, which provides cumulative S/N values, is particularly useful at illustrating this point. At 1.5 W and 320 transients, the overall S/N of the sample containing NR-GO-CAT is ca. 8-fold larger than in the no-enzyme and control SE-HSQC cases.

In order to quantitatively characterize the extent of sample photodegradation during photo-CIDNP, ^{1}H pulse-acquire and ^{13}C-PRINT photo-CIDNP data were collected in an interleaved fashion. In the presence of the tri-enzyme system, regardless of laser power, sample integrity is preserved by > 80%, even after 320 laser pulses, as shown in panels c and d of Figure 3.4. Hence it is generally advantageous to use the three-enzyme system for photo-CIDNP experiments at high Ar ion laser power.

Extending the applicability of the tri-enzyme system to other amino acids and polypeptides at even lower concentration (20 μM). To probe the effectiveness of the tri-enzyme system at even lower sample concentration and with more diverse NMR samples, we investigated three aromatic amino acids (Trp, His and Tyr) and the σ^{32} peptide [20] at 20 μM concentration. cases.

For all the aromatic amino acids, we could only observe distinct resonances when the photo-CIDNP experiments were carried out in the presence of the 3 enzymes (Fig. 3.5). The SE-HSQC, photo-CIDNP dark (i.e., laser off) and enzyme-free photo-

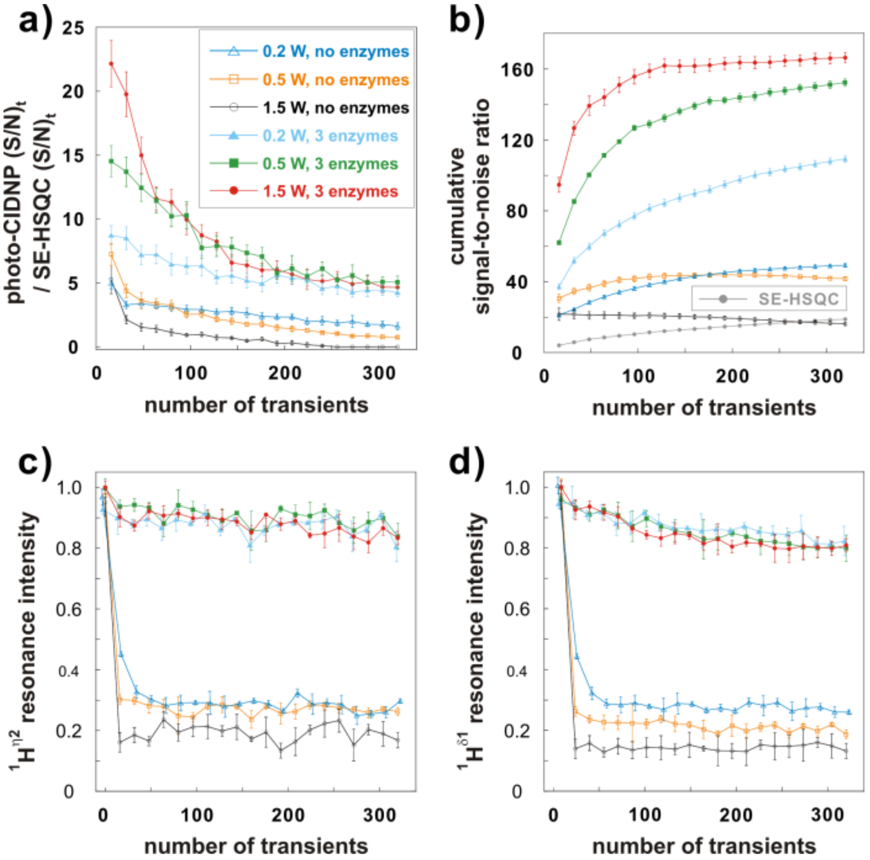

Figure 3.4 Effect of laser power and long-term photo-CIDNP data collection on 200 μM Trp in the absence and presence of the NR-GO-CAT enzymes. a) Ratio of ^{13}C-PRINT (light conditions) and ^{1}H-^{13}C SE-HSQC $(S/N)_t$ values for the η2 Trp resonance, as successive experiments were run on the same sample. Photo-CIDNP experiments were run at variable laser powers. 20 successive data sets, comprising 16 scans each, were collected for each trace shown. b) Cumulative S/N for the η2 Trp resonance under different experimental conditions. This plot was generated from the data in panel a. Variations in c) η2 and d) δ1 ^{1}H Trp resonance intensities during photo-CIDNP experiments in panel a. ^{1}H and photo-CIDNP (panel a) data were collected in an interleaved fashion. Error bars denote standard errors for three independent

experiments. Note that the amount of sample preservation under no-enzyme conditions is overestimated in panel c, given that the $^1H^{\eta2}$, $^1H^{\delta1}$ Trp resonances after the laser irradiations were on top of a blob in the ^1H spectra, which most likely comes from the photodegradation products (Fig. 3.2c).

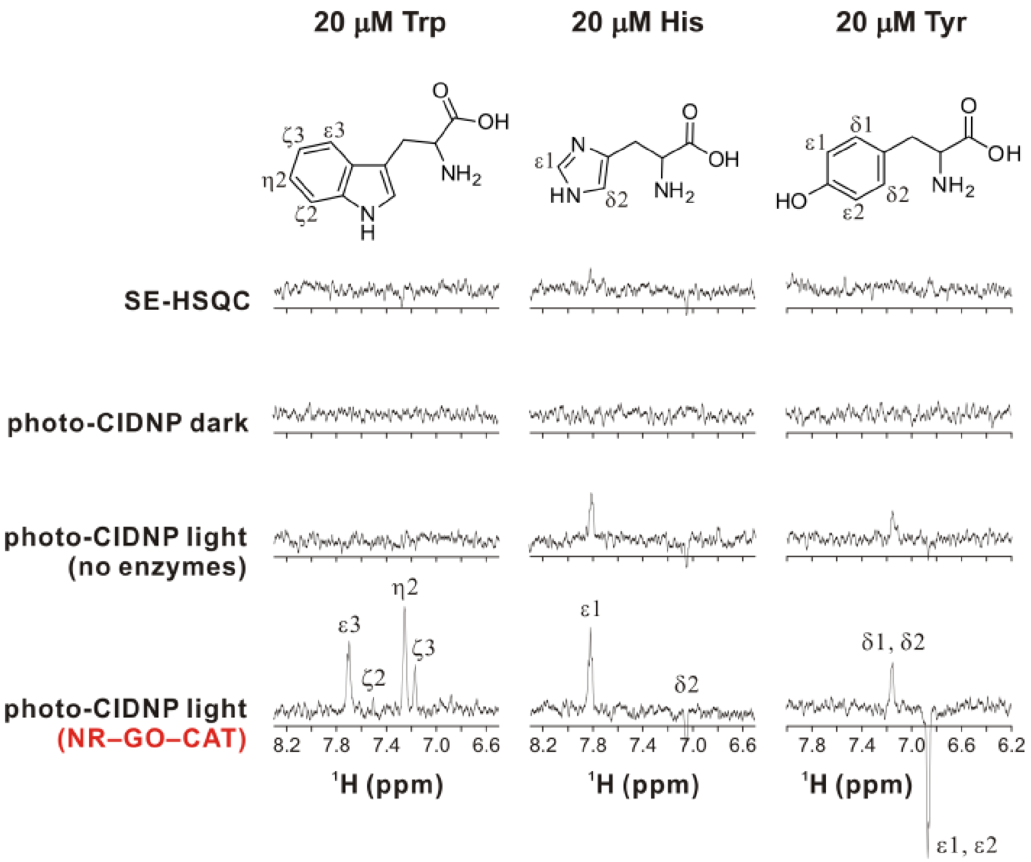

Figure 3.5 ^{13}C-PRINT photo-CIDNP and reference ^{1}H-^{13}C SE-HSQC of Trp, His and Tyr at 20 μM concentration in the absence and presence of the tri-enzyme system (16 scans / experiment). Photo-CIDNP data under light conditions were collected at 1.5W laser power with 0.1s laser pulse/scan.

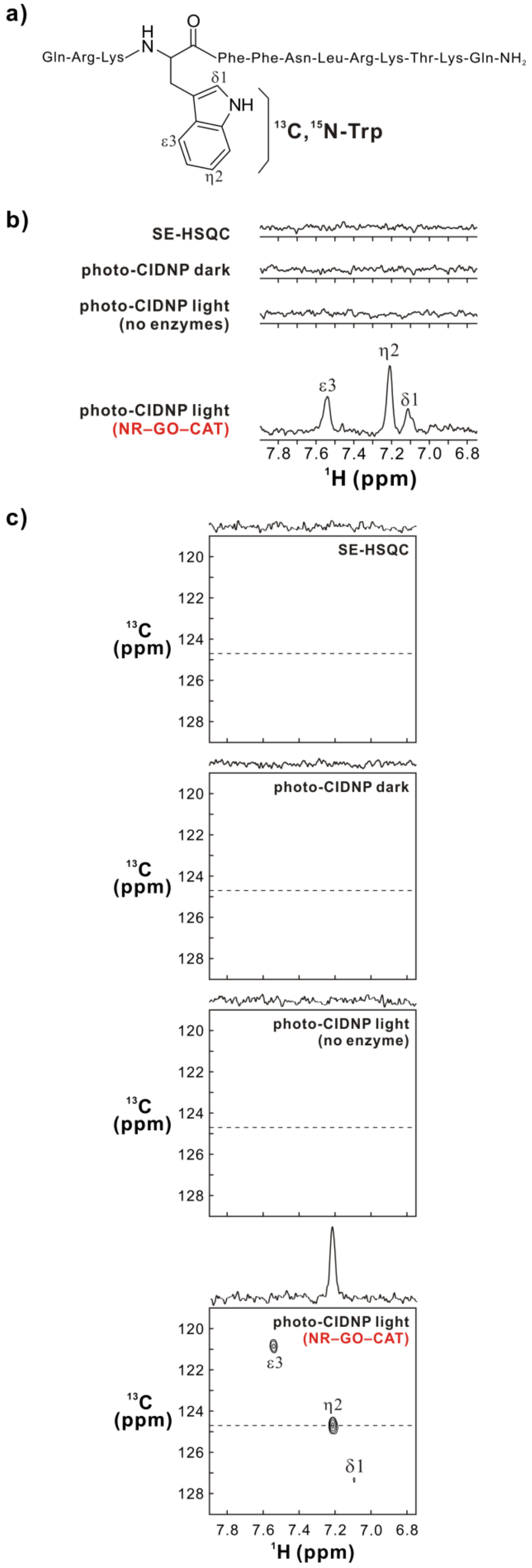
a)
Gln-Arg-Lys
H
N
O
Phe-Phe-Asn-Leu-Arg-Lys-Thr-Lys-Gln-NH2
δ1
NH
ε3
η2
13C, 15N-Trp
b)
SE-HSQC
photo-CIDNP dark
photo-CIDNP light
(no enzymes)
photo-CIDNP light
(NR–GO–CAT)
ε3
η2
δ1
7.8 7.6 7.4 7.2 7.0 6.8
1H (ppm)
c)
SE-HSQC
photo-CIDNP dark
photo-CIDNP light
(no enzyme)
photo-CIDNP light
(NR–GO–CAT)
13C (ppm)
120 122 124 126 128
ε3
η2
δ1
7.8 7.6 7.4 7.2 7.0 6.8
1H (ppm)

Figure 3.6 1D and 2D ^{13}C-PRINT photo-CIDNP spectra of diluted σ^{32} peptide (20 μM) in the absence and presence of the NR-GO-CAT tri-enzyme system. a) Structure of the σ^{32} peptide. b) 1D ^{13}C-PRINT and reference ^{1}H-^{13}C SE-HSQC spectra. Photo-CIDNP under light conditions was carried out at 1.5W laser power with 0.1s laser pulse irradiation time with and without the NR-GO-CAT enzymes. Each experiment consisted of 32 scans. c) 2D ^{13}C-PRINT and reference ^{1}H-^{13}C SE-HSQC spectra. Data were collected according to STATES-TPPI with 32 increments and 1 scan per increment. Spectral widths were 6,000 and 4,000 Hz for the direct and indirect dimensions, respectively. 0.5W laser power and 0.1s laser pulse irradiation time was employed. The dashed lines indicate the position of the 1D ^{1}H spectral slices displayed on top of each 2D spectrum.

CIDNP light spectra yielded very little or no signal. The ratios of the $(S/N)_t$ of the photo-CIDNP resonances in the presence of NR- GO-CAT over the corresponding values for the SE-HSQC control are 24, 5, 14 for Trp, His and Tyr, respectively. The extent of photodamage, defined as the variation in ^{1}H resonance intensity (in ^{1}H 1D pulse-acquire experiments) before and after the photo-CIDNP arrays (Fig. 3.5) is moderate, < 5%, for Trp, His and Tyr in the presence of NR- GO-CAT.

Next, we tested the σ^{32} peptide, which comprises 13 amino acids (i.e., residues 132-144) of the *E. coli* σ^{32} transcription factor. This peptide, which is known to be a high-affinity client of the DnaK *E. coli* chaperone,[51] was modified by replacing Leu_{135} with ^{13}C, ^{15}N-Trp (Fig. 3.6a).[20] 1D ^{13}C PRINT photo-CIDNP experiments in the presence of NR-GO-CAT displayed a 25-fold greater $(S/N)_t$ than the reference ^{1}H-^{13}C-SE-HSQC experiment (Fig. 3.6b). This is a significant increase in sensitivity, which amounts to a 625-fold faster data collection time than in the case of SE-HSQC.

The extent of σ^{32} peptide photodegradation was estimated by acquiring a 1D ^{1}H-^{13}C SE-HSQC spectrum before and after the photo-CIDNP light experiments (in this case 1D ^{1}H pulse-acquire experiments were not appropriate to estimate photodegradation due to excessive resonance overlap). The extent of detected peptide photodegradation was minimal (< 5%, assessed from the variation in Trp resonance intensities).

Finally, to illustrate that the combined use of photo-CIDNP and the tri-enzyme system facilitates multidimensional spectroscopy at high sensitivity, we acquired 2D ^{13}C-PRINT spectra of the 20 μM σ^{32} peptide. As shown in Fig. 3.6c, the spectral quality is excellent, and the data show once again that the only sample yielding any detectable signal, at this very low peptide concentration, is the tri-enzyme-containing σ^{32} solution. The effectiveness of the tri-enzyme system is not limited to amino acids and peptides, and is also evident in larger molecular systems including proteins. The 2D ^{13}C-PRINT photo-CIDNP NMR spectra of the 20 μM drkN SH3 protein (~ 7 kDa) in the absence and presence of the tri-enzyme system, shown in Appendix 3A Figure 3A.2, illustrate this point.

Stretching the concentration limits down to 5 μM. We probed whether photo-CIDNP in combination with the tri-enzyme system may lower typical NMR sample concentrations even further down to the low μM range (we tested 5 μM). This concentration is around two orders of magnitude smaller than concentrations conventionally used in biomolecular NMR.

We tested the tri-enzyme system in the presence of increasingly lower concentrations of the σ^{32} peptide (200 μM, 20 μM and 5 μM). Strikingly, we observed larger relative sensitivity enhancements (with respect to SE-HSQC) at lower sample concentrations (Fig. 3.7). The relative sensitivity enhancement reaches 48.0±5.6-fold in the case of the 5 μM σ^{32} peptide (see Fig. 3.7c for NMR spectra of this sample), corresponding to a 2,304-fold reduction in data collection time, relative to SE-HSQC, as illustrated in Fig. 3.7b.

To explain this interesting phenomenon, we performed kinetic simulations (see details in Appendix 3A Text) and showed that the concentration of the $\text{Trp}^{\bullet +}$ $\text{FMN}^{\bullet -}$ radical ion pair, which is a precursor for photo-CIDNP, is predicted to decrease nonlinearly as the Trp concentration decreases. However, this decrease occurs to a

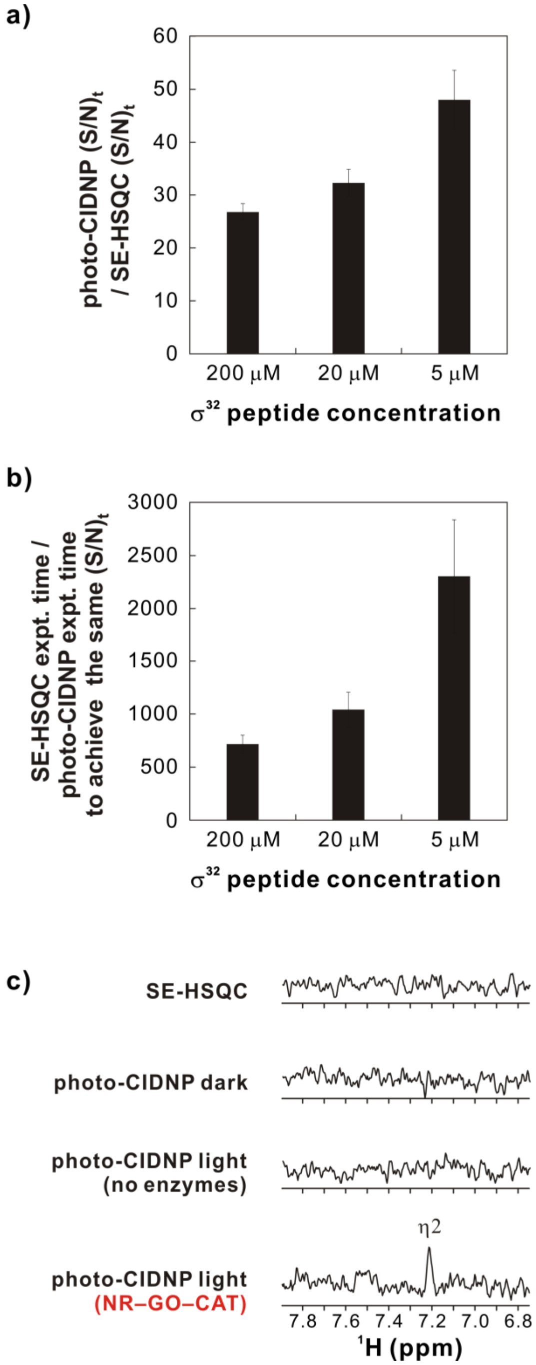

Figure 3.7 Improvement in laser-driven NMR sensitivity at low sample concentrations. a) Block diagram illustrating the ratio of $(S/N)_t$ of 1D ^{13}C-PRINT (light NR-GO-CAT conditions, 16 scans, 1.5 W laser power) and 1D ^{1}H-^{13}C SE-HSQC for the

σ^{32} peptide (Trp η2 resonance) at increasingly low concentration. Photo-CIDNP and control SE-HSQC experiments were performed at the same peptide concentration. In the case of the reference 1D ^{1}H-^{13}C SE-HSQC experiment, data were averaged over 128, 3072 and 14336 scans for 200 μM, 20 μM and 5 μM concentration samples, respectively, in order to achieve measurable S/N. Even after 14336 scans, however, since S/N was poor for the 5 μM sample, 20 μM sample SE-HSQC $(S/N)_t$ was divided by 4 and used as a reference for 5 μM ^{13}C-PRINT experiment. Three independent experiments were performed at each concentration. b) Time required for SE-HSQC to achieve the same sensitivity as photo-CIDNP at different sample concentrations was calculated from panel a. c) ^{13}C-PRINT photo-CIDNP experiments on the σ^{32} peptide in the absence and presence of the tri-enzyme system at extremely low peptide concentration (5 μM). All data were collected with 16 scans and 1.5W, 0.1s laser pulses were employed under light conditions.

much smaller extent than in the case of the reference SE-HSQC, thus explaining the experimentally observed trends of Fig. 3.7a. Similar arguments are likely to apply to other photo-CIDNP substrates than Trp. Note that concentration-dependent phenomena similar to those observed here were previously observed at acidic and basic pH,[52-54] and explained on the basis of degenerate electron exchange. At the neutral pH studied here, degenerate electron exchange is not expected to play a significant role, and the above ^{T}FMN population arguments best explain our results.

Efficient photo-CIDNP at high sample concentration (5 mM). Photo-CIDNP experiments whose goal is either fast data collection of a soluble target (i.e., kinetic studies) or the identification of solvent exposure of selected amino acids[55,56] do not require data collection at very low sample concentration. In this case, photo-CIDNP experiments are often performed at high concentrations, e.g., in the mM range or higher. Even within this concentration regime, the tri-enzyme system provides key advantages. However, the balance between the different chemical paths (Fig. 3.1a) varies dramatically when sample concentration (in this case 5 mM) exceeds both dye (usually 0.2 mM) and ambient oxygen concentration (~ 0.27 mM), as detailed below.

The behavior of the tri-enzyme system at high sample concentration was tested on Trp (5 mM) upon collecting ^{13}C-PRINT spectral arrays in the absence and presence of enzymes, as shown in Fig. 3.8. Once again, we find that enzyme additives are essential to guarantee long-term data collection. Surprisingly, however, the benefits can be ascribed primarily to the NR enzyme. This statement is justified by the fact that the NR and NR-GO-CAT conditions yield substantially identical enhancements (Fig. 3.8). If anything, the presence of GO and CAT has a deleterious effect on the initial spectral

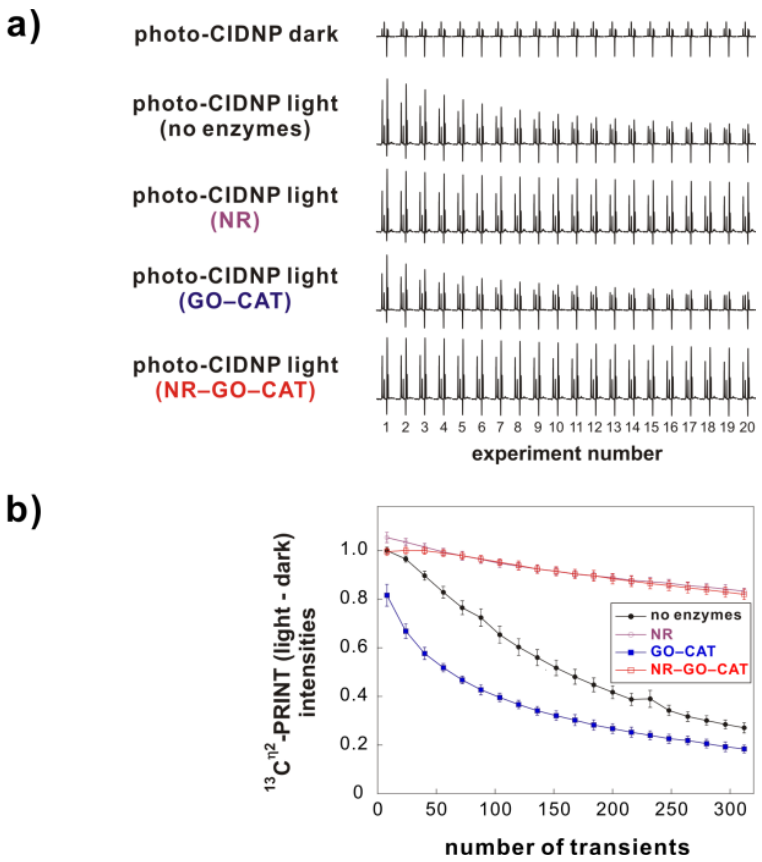

Figure 3.8 Photo-CIDNP NMR of aqueous Trp at high concentration (5 mM) in the absence and presence of different enzymes. a) Spectral arrays illustrating ^{1}H-detected ^{13}C-PRINT photo-CIDNP data (16 scans per spectrum) collected back-to-back in the absence and presence of enzymes. Photo-CIDNP data under light conditions were collected with 1.5W laser power and 0.1 s laser pulse irradiation. b) Plot illustrating the difference between ^{13}C-PRINT photo-CIDNP signal intensities under light (i.e., laser on) and dark (i.e., laser off) conditions for the Trp $\eta 2$ resonance. Three independent data sets were collected.

enhancement, as seen upon comparing the GO-CAT and no-enzyme conditions (Fig. 3.8). This is due to efficient FMN conversion to $FMNH_2$ at high sample concentration (Fig 3.1a). The latter species, in turn, is not reoxidized by oxygen in the presence of GO and CAT. In summary, at high sample concentration the O_2 depletion accomplished by GO and CAT is not necessary for sensitivity enhancement purposes.

Our data show that at 5 mM Trp concentration the fraction of Trp photodegradation in the absence of enzymes is small (Fig. 3A.3), indeed much smaller than at 200 μM sample concentration (e.g., compare Figs. 3.2c and 3A.3). Given that sample photodegradation is mediated primarily by singlet oxygen (Fig. 3.1a), the small extent of photodegradation explains why oxygen depletion via GO and CAT is not necessary. Now, it is important to ask why sample photodegradation is not an issue at high concentrations.

Two arguments help here. First, the equilibrium concentration of dissolved oxygen in aqueous solution, in the absence of oxygen-scavenging agents, is ca. 0.27 mM.[49] Even if all the oxygen molecules were totally committed to photodegradation, the fraction of sample photodegradation would be only 5.4%. Upon considering that oxygen diffuses into the receiver-coil-sensitive region of the NMR-tube solution very slowly in the absence of mixing (see details in Appendix 3A Text), very low oxygen-dependent sample photodegradation is expected for samples whose concentration is much greater than 0.27 mM. Second, Fig. 3.1a shows that both oxygen-dependent sample photodegradation and photo-CIDNP (i.e., the steps in the green box) proceed via the key reaction intermediate ^{T}FMN. According to our simulation (Appendix 3A Text), at higher sample concentration the ^{T}FMN population is significantly lower. Hence it is straightforward to appreciate that high NMR sample concentrations lead to the depletion of most ^{T}FMN in solution, significantly decreasing the rate of oxygen-mediated sample photodegradation.

Mass action arguments related to the high Trp concentration (Fig. 3.1a) explain why most FMN undergoes photoreduction to $FMNH_2$, instead of irreversible decomposition. Hence, the NR enzyme is maximally effective under these conditions, as shown in Fig. 3.8. Indeed, NR is the key enzyme at high sample concentration, and the effect of NR alone is entirely similar to that of the NR-GO-CAT combination (Fig. 3.8). In addition, a comparison between no-enzyme and NR-GO-CAT conditions (Fig. 3.8) illustrates the fact that NR has higher oxidizing power compared to that of oxygen.

Under both NR and NR-GO-CAT conditions a moderate decrease in resonance intensity is observed over long-term data collection (Fig. 3.8b). Fig. 3A.3 shows that this decrease is qualitatively consistent with a small extent of oxygen-dependent sample photodegradation. This undesired effect can be minimized upon collecting data under GO-CAT conditions, though the lack of NR reduces the signal-enhancement benefits of photo-CIDNP (Fig. 3.8b). The moderate extent of sample photodegradation (<10%) observed after extensive data collection under NR or NR-GO-CAT conditions cannot currently be overcome. On the other hand, these conditions are advantageous because they yield remarkable signal enhancements over a prolonged timescale.

Identity of FMN photodegradation products after prolonged laser irradiation. A comparison between Figures 3.4a and 3.8a (at 1.5W laser power) in the absence of enzymes shows that photo-CIDNP is more amenable to the collection of multiple scans when sample concentration is high. To explain the origin of this phenomenon, we performed ESI mass spectrometry before and after the photo-CIDNP experiments of Figures 3.4a and 3.8a (320 scans, 1.5W 0.1s laser pulse/scan, no enzymes, see Fig. 3.9). Although the ESI data are not entirely quantitative due primarily to the different ionization efficiencies of the species involved and to the uneven affinities of the different compounds to the C_{18} reverse-phase desalting pipette tip (used during sample preparation for mass spectrometry), the method provides semi-quantitative information on the species involved, including the identity of any FMN photo-degradation products generated upon extensive high power FMN laser irradiation. Given the mass spectrometry sample preparation conditions, which involve extensive exposure to oxygen, any $FMNH_2$ present in the samples is reversibly oxidized back to FMN. Hence, ESI mass spectrometry is mostly suitable to follow the formation of irreversible photo-degradation products, rather than assessing the FMN / $FMNH_2$ balance.

The results in Fig. 3.9 show that FMN (originally present at 0.2 mM concentration) is no longer present in the low-concentration (0.2 mM) Trp samples while it is distinctly observable at higher Trp concentration (5 mM), after 320 high-power (1.5 W) laser pulses. These data demonstrate that FMN experiences a larger extent of irreversible photo-degradation at low Trp concentrations. The above results can be explained on the basis of the reaction diagram in Fig. 3.1a. At high Trp concentration, the photochemically generated ^{T}FMN follows the green photo-CIDNP pathway due to the mass action of Trp, while at low Trp concentration the FMN irreversible photodegradation pathway dominates.

Finally, ESI mass spectrometry enables assessing the molecular identity of some of the FMN irreversible degradation products, which can be identified from their m/z

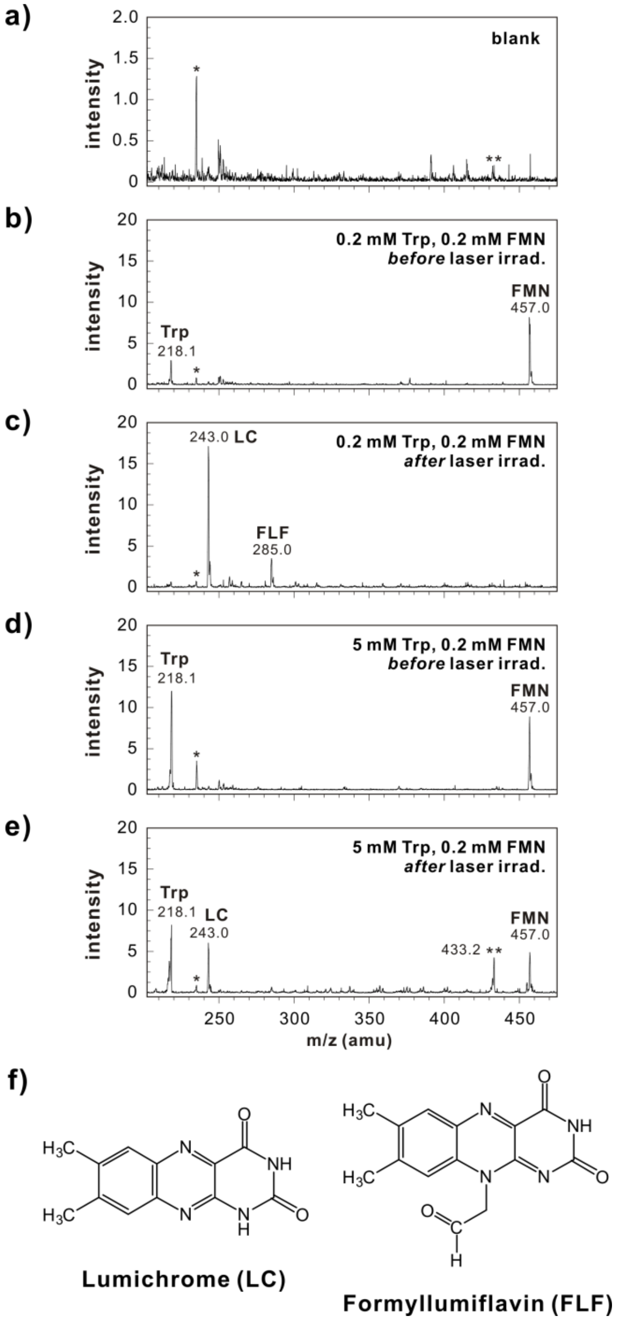

Figure 3.9 Electrospray ionization (ESI) mass spectra of samples containing Trp and FMN before and after 1D ^{1}H-^{13}C SE-HSQC (320 scans, light conditions, 1.5 W laser, 0.1 s laser pulse/scan) experiments. a) Control blank experiment on desalted buffer. Note that the vertical scale of this plot is 10-fold smaller than in all the other plots. b, c) 0.2

mM Trp. d, e) 5 mM Trp. The symbol * denotes peaks that are also observed in the blank. The symbol ** denotes a peak that is unidentified but is also observed in the blank at low intensity. f) Structure of the FMN photodegradation products LC and FLF. Note that FMN peak represents both FMN and $FMNH_2$ species since $FMNH_2$ is oxidized to FMN during the mass spectrometry sample preparation.

values (Fig. 3.9a-e). Consistent with the literature,[32] the low-concentration Trp samples subject to extensive laser irradiation contain both lumichrome (LC, Fig. 3.9f) and formyllumiflavin (FLF, Fig. 3.9f) as the primary FMN degradation products. This result does not exclude that other FMN degradation products undetectable by mass spectrometry (e.g., due to their high molecular weight, poor ionization properties or non-uniform efficiency in desalting process) may also be present.

Alternative strategies and future perspectives. The quest to prevent undesired processes mediated by either singlet oxygen or by the triplet excited state of the dye is shared by techniques other than NMR. For instance, fluorescence microscopy and spectroscopy, which often employ high-power laser sources, have witnessed a variety of advances targeting the suppression of irreversible photodegradation and reversible fluorophore transition to dark states (blinking). To gain a wider perspective, it is useful to compare the features of our tri-enzyme system with those of the popular anti-bleaching/anti-degradation agents used in fluorescence. The oxygen-scavenging system GO-CAT [44] or protocatechuate-3,4-dioxygenase,[47] for instance, are sometimes employed in fluorescence, either alone or in combination with the small molecules TROLOX[57] and ROXS[58]. The latter two agents act by similar principles.[59] ROXS, for instance, contains a mixture of oxidizing and reducing agents that efficiently depopulate triplet excited states of the dye and convert them back to the singlet ground state via redox chemistry. This effect minimizes reversible fluorophore blinking and irreversible photodegradation. TROLOX, ROXS or variations thereof, however, cannot be employed in photo-CIDNP given that they deplete triplet excited states. Photo-CIDNP, on the other hand, exploits the long lifetime of triplet excited states, so that productive collisions between ^{T}FMN and the target photo-CIDNP-active molecule generate triplet radical-pair intermediates. In summary, TROLOX and ROXS overcome photodegradation and blinking in fluorescence but are not appropriate for use in photo-CIDNP.

Oxygen depletion has long been known to prolong the triplet-excited state lifetimes of dyes.[60] This effect is expected to intrinsically benefit photo-CIDNP, and may be partially responsible for the observed sensitivity enhancements in the presence of the GO and CAT enzymes.

Although all photo-CIDNP experiments in this work were performed by ^{1}H-detected ^{13}C photo-CIDNP,[20] the tri-enzyme system is to be considered generally applicable to all other photo-CIDNP experiments.[24,25] In addition to its general applicability, another advantageous feature of NR-GO-CAT is the fact that these enzymes are effective at very low concentrations, in the sub-μM range. Hence, they are minimally perturbative to the system of interest.

In light of the above, what are the future challenges to further photo-CIDNP performance especially at low sample concentrations, where sensitivity improvements are most sorely needed? As much as it is good news that photo-CIDNP sensitivity increases at low sample concentration in the presence of NR-GO-CAT (Fig. 3.7), the extent of FMN photodegradation increases at low sample concentrations. Overcoming the latter effect will be the goal for future developments in this area.

3.4 Conclusions

High sensitivity is crucial in many biomolecular NMR applications. This study introduces a novel tri-enzyme system that dramatically enhances photo-CIDNP performance in the presence of high-power laser irradiation, enhancing the ability to achieve high S/N in NMR. At low-mM concentrations, which have been commonly used in biomolecular photo-CIDNP applications to date, efficient long-term photo-CIDNP data collection is achieved thanks to the extremely efficient FMN-recycling ability of the NR enzyme. Under these conditions, sample photodegradation is minimized in the presence of the GO and CAT enzymes.

Further, at sample concentrations in the low-μM range (where photo-CIDNP experiments could not be performed before), even greater sensitivity enhancements were observed in the presence of the NR-GO-CAT enzymes. For instance, at 5 μM σ^{32} peptide sample concentration, 48-fold larger sensitivity than SE-HSQC was reached with a 2,304-fold saving in data collection time. In summary, our results contribute to render photo-CIDNP a general, desirable methodology to analyze NMR samples containing different types of aromatic amino acids at extremely high sensitivity in solution.

Appendix

Appendix 3A Text and Figures describing *(i)* the computational prediction of radical ion pair and triplet-excited-state FMN (^{T}FMN) populations during continuous-wave laser irradiation, and *(ii)* photodegradation profiles under different conditions are available

Acknowledgments

We thank Charlie Fry, Yusuke Okuno, Steve Burke and John Wright for useful discussions. We are also grateful to Yusuke Okuno for a critical reading of the manuscript. This research was funded by the National Institute of Health Grant R21AI088551.

3.5 References

(1) Overhauser, A. W. Polarization of Nuclei in Metals. *Phys. Rev.* **1953**, *92*, 411-415.

(2) Maly, T.; et al. Dynamic Nuclear Polarization at High Magnetic Fields. *J. Chem. Phys.* **2008**, *128*, 052211.

(3) Griesinger, C.; Bennati, M.; Vieth, H. M.; Luchinat, C.; Parigi, G.; Hofer, P.; Engelke, F.; Glaser, S. J.; Denysenkov, V.; Prisner, T. F. Dynamic Nuclear Polarization at High Magnetic Fields in Liquids. *Prog. Nucl. Magn. Reson. Spectrosc.* **2012**, *64*, 4-28.

(4) Ardenkjaer-Larsen, J. H.; Fridlund, B.; Gram, A.; Hansson, G.; Hansson, L.; Lerche, M. H.; Servin, R.; Thaning, M.; Golman, K. Increase in Signal-to-Noise Ratio of >

10,000 Times in Liquid-State NMR. *Proc. Natl. Acad. Sci. U.S.A.* **2003**, *100*, 10158-10163.

(5) Lee, Y.; Zeng, H.; Mazur, A.; Wegstroth, M.; Carlomagno, T.; Reese, M.; Lee, D.; Becker, S.; Griesinger, C.; Hilty, C. Hyperpolarized Binding Pocket Nuclear Overhauser Effect for Determination of Competitive Ligand Binding. *Angew. Chem., Int. Ed.* **2012**, *51*, 5179-5182.

(6) Natterer, J.; Bargon, J. Parahydrogen Induced Polarization. *Prog. Nucl. Magn. Reson. Spectrosc.* **1997**, *31*, 293-315.

(7) Theis, T.; Ganssle, P.; Kervern, G.; Knappe, S.; Kitching, J.; Ledbetter, M. P.; Budker, D.; Pines, A. Parahydrogen-Enhanced Zero-Field Nuclear Magnetic Resonance. *Nature Phys.* **2011**, *7*, 571-575.

(8) Spence, M. M.; Rubin, S. M.; Dimitrov, I. E.; Ruiz, E. J.; Wemmer, D. E.; Pines, A.; Yao, S. Q.; Tian, F.; Schultz, P. G. Functionalized Xenon as a Biosensor. *Proc. Natl. Acad. Sci. U.S.A.* **2001**, *98*, 10654-10657.

(9) Navon, G.; Song, Y.; Room, T.; Appelt, S.; Taylor, R. E.; Pines, A. Enhancement of Solution NMR and MRI with Laser-Polarized Xenon. *Science* **1996**, *271*, 1848-1848.

(10) Haupt, J. A New Effect of Dynamic Polarization in a Solid Obtained by Rapid Change of Temperature. *Phys. Lett. A* **1972**, *38*, 389-390.

(11) Bargon, J.; Fischer, H.; Johnson, U. Nuclear Magnetic Resonance Emission Lines During Fast Radical Reactions. I. Recording Methods and Examples. *Z. Naturforsch. A* **1967**, *22*, 1551-1555.

(12) Ward, H. R.; Lawler, R. G. Nuclear Magnetic Resonance Emission and Enhanced Absorption in Rapid Organometallic Reactions. *J. Am. Chem. Soc.* **1967**, *89*, 5518-5519.

(13) Cocivera, M. Optically Induced Overhauser Effect in Solution. Nuclear Magnetic Resonance Emission. *J. Am. Chem. Soc.* **1968**, *90*, 3261-3263.

(14) Kaptein, R.; Dijkstra, K.; Nicolay, K. Laser Photo-CIDNP as a Surface Probe for Proteins in Solution. *Nature* **1978**, *274*, 293-294.

(15) Hore, P. J.; Broadhurst, R. W. Photo-CIDNP of Biopolymers. *Prog. Nucl. Magn. Reson. Spectrosc.* **1993**, *25*, 345-402.

(16) Goez, M., Photo-CIDNP Spectroscopy. In *Annual Reports on NMR Spectroscopy*, Webb, G. A., Ed. Academic Press: London, 2009; Vol. 66, pp 77-147.

(17) Morozova, O. B.; Ivanov, K. L.; Kiryutin, A. S.; Sagdeev, R. Z.; Köchling, T.; Vieth, H. M.; Yurkovskaya, A. V. Time-Resolved CIDNP: an NMR Way to Determine the EPR Parameters of Elusive Radicals. *Phys. Chem. Chem. Phys.* **2011**, *13*, 6619-6627.

(18) Kaptein, R.; Oosterhoff, J. L. Chemically Induced Dynamic Nuclear Polarization II - (Relation with Anomalous ESR Spectra). *Chem. Phys. Lett.* **1969**, *4*, 195-197.

(19) Closs, G. L.; Closs, L. E. Induced Dynamic Nuclear Spin Polarization in Photoreductions of Benzophenone by Toluene and Ethylbenzene. *J. Am. Chem. Soc.* **1969**, *91*, 4549-4550.

(20) Lee, J. H.; Sekhar, A.; Cavagnero, S. 1H-detected 13C photo-CIDNP as a sensitivity enhancement tool in solution NMR. *J. Am. Chem. Soc.* **2011**, *133*, 8062-8065.

(21) Daviso, E.; Janssen, G. J.; Alia, A.; Jeschke, G.; Matysik, J.; Tessari, M. A 10,000-fold Nuclear Hyperpolarization of a Membrane Protein in the Liquid Phase via Solid-State Mechanism. *J. Am. Chem. Soc.* **2011**, *133*, 16754-16757.

(22) Zysmilich, M. G.; McDermott, A. Photochemically Induced Dynamic Nuclear Polarization in the Solid-State 15N Spectra of Reaction Centers from Photosynthetic Bacteria Rhodobacter sphaeroides R-26. *J. Am. Chem. Soc.* **1994**, *116*, 8362-8363.

(23) Lyon, C. E.; Jones, J. A.; Redfield, C.; Dobson, C. M.; Hore, P. J. Two-Dimensional 15N-1H Photo-CIDNP as a Surface Probe of Native and Partially Structured Proteins. *J. Am. Chem. Soc.* **1999**, *121*, 6505-6506.

(24) Sekhar, A.; Cavagnero, S. 1H Photo-CIDNP Enhancements in Heteronuclear Correlation NMR Spectroscopy. *J. Phys. Chem. B* **2009**, *113*, 8310-8318.

(25) Sekhar, A.; Cavagnero, S. EPIC- and CHANCE-HSQC: Two 15N Photo-CIDNP-Enhanced Pulse Sequences for the Sensitive Detection of Solvent-Exposed Tryptophan. *J. Magn. Reson.* **2009**, *200*, 207-213.

(26) Kiryutin, A. S.; Korchak, S. E.; Ivanov, K. L.; Yurkovskaya, A. V.; Vieth, H. M. Creating Long-Lived Spin States at Variable Magnetic Field by Means of Photochemically Induced Dynamic Nuclear Polarization. *J. Phys. Chem. Lett.* **2012**, *3*, 1814-1819.

(27) Goez, M.; Kuprov, I.; Hore, P. J. Increasing the Sensitivity of Time-Resolved Photo-CIDNP Experiments by Multiple Laser Flashes and Temporary Storage in the Rotating Frame. *J. Magn. Reson.* **2005**, *177*, 139-145.

(28) Kurt, N.; Rajagopalan, S.; Cavagnero, S. Effect of Hsp70 Chaperone on the Folding and Misfolding of Polypeptides Modeling an Elongating Protein Chain. *J. Mol. Biol.* **2006**, *355*, 809-820.

(29) Rajagopalan, S.; Kurt, N.; Cavagnero, S. High-Resolution Conformation and Backbone Dynamics of a Soluble Aggregate of Apomyoglobin119. *Biophys. J.* **2011**, *100*, 747-755.

(30) Connolly, P. J.; Hoch, J. C. Photochemical Degradation of Tryptophan Residues During CIDNP Experiments. *J. Magn. Reson.* **1991**, *95*, 165-173.

(31) Pattison, D. I.; Davies, M. J. Actions of Ultraviolet Light on Cellular Structures. *EXS* **2006**, *96*, 131-157.

(32) Holzer, W.; Shirdel, J.; Zirak, P.; Penzkofer, A.; Hegemann, P.; Deutzmann, R.; Hochmuth, E. Photo-Induced Degradation of Some Flavins in Aqueous Solution. *Chem. Phys.* **2005**, *308*, 69-78.

(33) Moore, W. M.; Spence, J. T.; Raymond, F. A.; Colson, S. D. Photochemistry of Riboflavin. I. The Hydrogen Transfer Process in the Anaerobic Photobleaching of Flavins. *J. Am. Chem. Soc.* **1963**, *85*, 3367-3372.

(34) Ed. Müller, F. *Chemistry and biochemistry of flavoenzymes*; CRC Press: Boca Raton, 1991.

(35) Maeda, K.; Lyon, C. E.; Lopez, J. J.; Cemazar, M.; Dobson, C. M.; Hore, P. Improved Photo-CIDNP Methods for Studying Protein Structure and Folding. *J. Biomol. NMR* **2000**, *16*, 235-244.

(36) Song, S. H.; Dick, B.; Penzkofer, A. Photo-Induced Reduction of Flavin Mononucleotide in Aqueous Solutions. *Chem. Phys.* **2007**, *332*, 55-65.

(37) Scheek, R. M.; Stob, S.; Boelens, R.; Dijkstra, K.; Kaptein, R. Applications of Two-Dimensional 1H Nuclear Magnetic Resonance Methods in Photochemically Induced Dynamic Nuclear Polarisation Spectroscopy. *Faraday Discuss. Chem. Soc.* **1984**, *78*, 245-256.

(38) Campbell, W. H. Nitrate Reductase Structure, Function and Regulation: Bridging the Gap Between Biochemistry and Physiology. *Annu. Rev. Plant Physiol. Plant Mol. Biol.* **1999**, *50*, 277-303.

(39) Swoboda, B. E. P.; Massey, V. Purification and Properties of the Glucose Oxidase from Aspergillus niger. *J. Biol. Chem.* **1965**, *240*, 2209-2215.

(40) Yousefi, R.; Saboury, A. A.; Ghadermarzi, M.; Moosavi-Movahedi, A. A. Effects of Cysteine on the Inactivation of Bovine Liver Catalase. *Bull. Korean Chem. Soc.* **2000**, *21*, 567-570.

(41) Skipper, L.; Campbell, W. H.; Mertens, J. A.; Lowe, D. J. Pre-Steady-State Kinetic Analysis of Recombinant Arabidopsis NADH:Nitrate Reductase: Rate-Limiting Processes in Catalysis. *J. Biol. Chem.* **2001**, *276*, 26995-27002.

(42) Wirmer, J.; Kuhn, J.; Schwalbe, H. Millisecond Time Resolved Photo-CIDNP NMR Reveals a Non-Native Folding Intermediate on the Ion-Induced Refolding Pathway of Bovine Alpha-Lactalbumin. *Angew. Chem., Int. Ed.* **2001**, *40*, 4248-4251.

(43) Ernst, R. R.; Bodenhausen, G.; Wokaun, A. *Principles of Nuclear Magnetic Resonance in One and Two Dimensions*; Oxford University Press: Upper Saddle River, 1989.

(44) Benesch, R. E.; Benesch, R. Enzymatic Removal of Oxygen for Polarography and Related Methods. *Science* **1953**, *118*, 447-448.

(45) Roy, R.; Hohng, S.; Ha, T. A Practical Guide to Single-Molecule FRET. *Nat. Methods* **2008**, *5*, 507-516.

(46) Englander, S. W.; Calhoun, D. B.; Englander, J. J. Biochemistry Without Oxygen. *Anal. Biochem.* **1987**, *161*, 300-306.

(47) Aitken, C. E.; Marshall, R. A.; Puglisi, J. D. An Oxygen Scavenging System for Improvement of Dye Stability in Single-Molecule Fluorescence Experiments. *Biophys. J.* **2008**, *94*, 1826-1835.

(48) Barber, M. J.; Notton, B. A. Spinach Nitrate Reductase: Effects of Ionic Strength and pH on the Full and Partial Enyzyme Activities. *Plant Physiol.* **1990**, *93*, 537-540.

(49) Murov, S. L.; Carmichael, I.; Hug, G. L. *Handbook of Photochemistry*; Marcel Dekker: New York, 1993.

(50) Ehrenberg, A.; Müller, F.; Hemmerich, P. Basicity, Visible Spectra, and Electron Spin Resonance of Flavosemiquinone Anions. *Eur. J. Biochem.* **1967**, *2*, 286-293.

(51) McCarty, J. S.; Rüdiger, S.; Schönfeld, H. J.; Schneider-Mergener, J.; Nakahigashi, K.; Yura, T.; Bukau, B. Regulatory Region C of the E. coli Heat Shock Transcription Factor, Sigma32, Constitutes a DnaK Binding Site and is Conserved Among Eubacteria. *J. Mol. Biol.* **1996**, *256*, 829-837.

(52) Tsentalovich, Y. P.; Morozova, O. B.; Yurkovskaya, A. V.; Hore, P. J. Kinetics and Mechanism of the Photochemical Reaction of 2,2'-Dipyridyl with Tryptophan in Water: Time-Resolved CIDNP and Laser Flash Photolysis Study. *J. Phys. Chem. A* **1999**, *103*, 5362-5368.

(53) Tsentalovich, Y. P.; Morozova, O. B. Laser Flash Photolysis and Time Resolved CIDNP Study of Photoreaction of 2,2'-Dipyridyl with N-Acetyl Tyrosine in Aqueous Solutions. *J. Photochem. Photobiol., A: Chemistry* **2000**, *131*, 33-40.

(54) Tsentalovich, Y. P.; Morozova, O. B.; Yurkovskaya, A. V.; Hore, P.; Sagdeev, R. Z. Time-Resolved CIDNP and Laser Flash Photolysis Study of the Photoreactions of N-Acetyl Histidine with 2,2'-Dipyridyl in Aqueous Solution. *J. Phys. Chem. A* **2000**, *104*, 6912-6916.

(55) Mok, K. H.; Kuhn, L. T.; Goez, M.; Day, I. J.; Lin, J. C.; Andersen, N. H.; Hore, P. J. A Pre-Existing Hydrophobic Collapse in the Unfolded State of an Ultrafast Folding Protein. *Nature* **2007**, *447*, 106-109.

(56) Buck, F.; Ruterjans, H.; Kaptein, R.; Beyreuther, K. Photochemically Induced Dynamic Nuclear Polarization Investigation of Complex Formation of the NH2-Terminal DNA-Binding Domain of Lac Repressor with Poly[d(AT)]. *Proc. Natl. Acad. Sci. U.S.A.* **1980**, *77*, 5145-5148.

(57) Rasnik, I.; McKinney, S. A.; Ha, T. Nonblinking and Long-Lasting Single-Molecule Fluorescence Imaging. *Nat. Methods* **2006**, *3*, 891-893.

(58) Vogelsang, J.; Kasper, R.; Steinhauer, C.; Person, B.; Heilemann, M.; Sauer, M.; Tinnefeld, P. A Reducing and Oxidizing System Minimizes Photobleaching and Blinking of Fluorescent Dyes. *Angew. Chem., Int. Ed.* **2008**, *47*, 5465-5469.

(59) Cordes, T.; Vogelsang, J.; Tinnefeld, P. On the Mechanism of Trolox as Antiblinking and Antibleaching Reagent. *J. Am. Chem. Soc.* **2009**, *131*, 5018-5019.

(60) Ha, T.; Tinnefeld, P. Photophysics of Fluorescent Probes for Single-Molecule Biophysics and Super-Resolution Imaging. *Annu. Rev. Phys. Chem.* **2012**, *63*,

(61) Hecht, H. J.; Kalisz, H. M.; Hendle, J.; Schmid, R. D.; Schomburg, D. Crystal-Structure of Glucose-Oxidase from Aspergillus-Niger Refined at 2.3 Angstrom Resolution. *J. Mol. Biol.* **1993**, *229*, 153-172.

(62) Sugadev, R.; Ponnuswamy, M.; Sekar, K. Structural Analysis of NADPH Depleted Bovine Liver Catalase and Its Inhibitor Complexes. *Int. J. Biochem. Mol. Biol.* **2011**, *2*, 67.

(63) Lu, G.; Lindqvist, Y.; Schneider, G.; Dwivedi, U.; Campbell, W. Structural Studies on Corn Nitrate Reductase: Refined Structure of the Cytochrome B Reductase Fragment at 2.5 Å, Its ADP Complex and an Active-Site Mutant and Modeling of the Cytochrome B Domain. *J. Mol. Biol.* **1995**, *248*, 931-948.

Appendix 3A

Supporting Information for Chapter 3

A Novel Tri-Enzyme System in Combination with Laser-Driven NMR Enables Efficient Nuclear Polarization of Biomolecules in Solution

This appendix reproduces the supporting information in

The Journal of Physical Chemistry B (2013) 117, 6069–6081.

Appendix 3A Text

Computational prediction of radical ion pair and triplet-excited-state FMN (^{T}FMN) population during continuous-wave (CW) laser irradiation

Introduction

The purpose of this supplementary text is to explain the trends observed in Fig. 3.7a of the manuscript, showing that the ratio of the sensitivity (defined here as $(S/N)_t$) of ^{13}C-PRINT photo-CIDNP under light conditions over the sensitivity of ^{1}H,^{13}C-SE-HSQC (run at the same sample concentration) increases as Trp concentration decreases. Here, we show by kinetic simulations that as the Trp concentration increases, the radical ion pair concentration, which is directly related to the photo-CIDNP sensitivity, does not increase as fast as the HSQC sensitivity. Hence, the simulation results are consistent with the Fig. 3.7 experimental results and enable rationalizing the observed trends.

Experimental Methods

Gepasi simulations.[1,2] Computational modeling was carried out with the Gepasi Simulator software version 3.30, running under Microsoft Windows environment and freely available online. User-generated input files based on Scheme S2 and Table S1 were used. The kinetic simulations were performed with Gepasi's standard routines, based on the Livermore Solver of Ordinary Differential Equations Algorithm (LSODA), which is speed-optimized for solving complex systems of differential equations.

Results and Discussion

Design of the kinetic model. To help us explain the higher sensitivity observed in photo-CIDNP at low Trp concentrations (Fig. 3.7), we propose the energy diagram in Scheme S1, and the matching detailed kinetic model in Scheme S2. We run computer simulations with the kinetic modeling software package Gepasi.[1] In the course of the simulations, we assumed that: *(i)* the only relevant FMN electronic states are the FMN (S_0; ground state), ^{S}FMN (S_1; excited singlet state) and ^{T}FMN (T_1; excited triplet) neglecting the ultrafast vibrational relaxation within the S_1 and T_1 energy manifolds; *(ii)* the Trp NMR samples are virtually oxygen-free due to the presence of the GO-CAT oxygen depleting enzymes and the small diffusion coefficient of oxygen in water (2×10^{-5} cm^2/s),[3] which is predicted to yield a negligible O_2 vertical translational diffusion across the NMR tube, with $\langle z^2 \rangle^{1/2} = (2Dt)^{1/2} = 0.38$ cm over 1 hr (starting from the air-water interface of the NMR sample); and *(iii)* proton transfer following escape (Scheme S2) occurs so rapidly that it can be neglected.[4] In the kinetic simulations, we employed known experimentally determined kinetic rate constants (Table S1) that most closely match our experimental conditions (pH 7, 25 °C). We entered the appropriate input to generate the system of differential equations corresponding to the rate laws of the 1st and 2nd order processes illustrated in the kinetic model of Scheme S2. The time-dependent computationally predicted ^{T}FMN and radical ion pair populations were plotted as a function of time for different initial Trp concentrations.

Scheme S1: Energy diagram illustrating the main features of the FMN fate in photo-CIDNP.

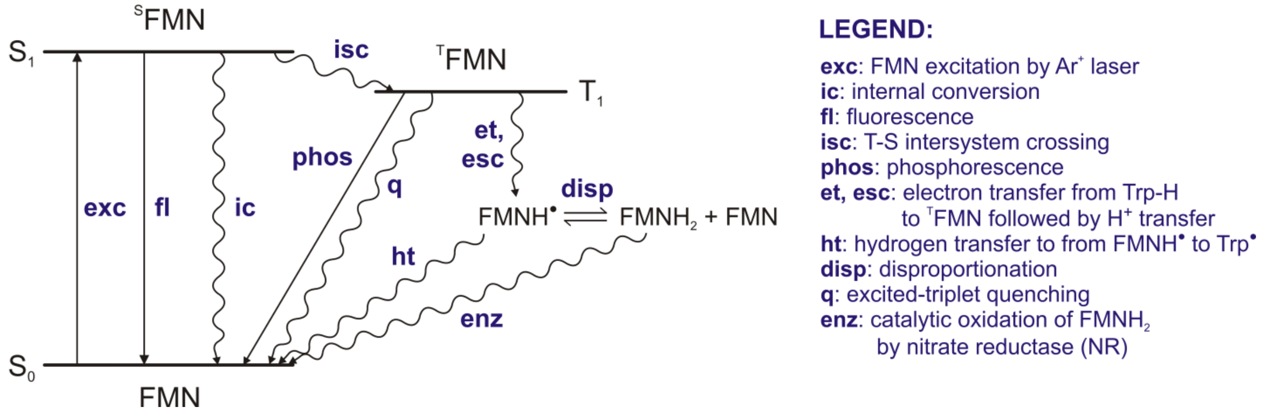

LEGEND:

exc: FMN excitation by Ar$^+$ laser
ic: internal conversion
fl: fluorescence
isc: T-S intersystem crossing
phos: phosphorescence
et, esc: electron transfer from Trp-H to ^{T}FMN followed by H$^+$ transfer
ht: hydrogen transfer to from FMNH$^\bullet$ to Trp$^\bullet$
disp: disproportionation
q: excited-triplet quenching
enz: catalytic oxidation of FMNH$_2$ by nitrate reductase (NR)

Scheme S2: Kinetic model employed in the Gepasi simulations.

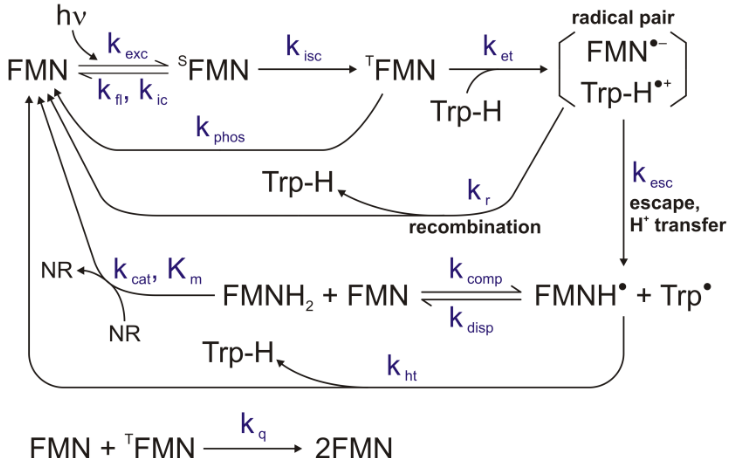

Table S1: Kinetic parameters used in the simulations.

Kinetic parameter	Reference
k_{exc} = 329 s^{-1}	see specific text on k_{exc}
τ [a] = 4.6 ns	Ref 5
Φ_T [b] = 0.6	Ref 6
$k_{fl} + k_{ic}$ [c] = 8.7×10^7 s^{-1}	Ref 7
k_{isc} [d] = 1.3×10^8 s^{-1}	Ref 7
k_{et} = 1.1×10^9 M^{-1} s^{-1}	Ref 8
k_{disp} = 10^9 M^{-1} s^{-1}	Ref 9
k_{comp} [e] = 1.4×10^6 M^{-1} s^{-1}	Ref 10
k_{phos} = 4.9×10^3 s^{-1}	Ref 11
k_q = 1.2×10^8 M^{-1} s^{-1}	Ref 11
k_{cat} [f] = 42 s^{-1}	Ref 12
K_m [f] = 0.7 μM	Ref 12
k_{ht} = 10^9 M^{-1} s^{-1}	Ref 4
k_r [g] = 10^8 M^{-1} s^{-1}	Ref 13
k_{esc} [h] = 3.3×10^{10} M^{-1} s^{-1}	Ref 14

[a] FMN fluorescence lifetime, defines as $\tau = 1 / (k_{isc} + k_{fl} + k_{ic})$ and assessed by time-resolved studies. [b] Triplet excited state quantum yield $\Phi_T = k_{isc} / (k_{isc} + k_{fl} + k_{ic})$ according to Ref 7. [c] $k_{fl} + k_{ic} = 1/\tau \times (1-\Phi_T)$ and [d] $k_{isc} = 1/\tau \times \Phi_T$ according to Ref 7. [e] Comproportionation rate constant. [f] Nitrate reductase (NR) kinetic parameters for NADH were used here, instead of parameters for

$FMNH_2$, which could not be found. [g] Since we could not identify k_r for the FMN-Trp radical pair, we used a representative value for the back electron transfer rates between flavin-substrate pairs according to Ref 13. [h] We neglected the H^+ transfer processes after escape since it is known to occur very rapidly.[4] k_{esc} is known to be ~ 330-fold greater than k_r according to Ref 14. Note that varying k_r across the reported values[13] of 10^6–10^{10} M^{-1} s^{-1}, followed by multiplication by 330 to generate k_{esc}, yields similar trends to those reported in Graphs S1 and S2.

In the simulations, we did not include the actual secondary recombination rate (k_r)[4] for the FMN-Trp radical pair, since it is not available in the literature. Instead, we used the corresponding reported rate for other flavin-substrate pairs, which ranges between 10^6 and 10^{10} $M^{-1}s^{-1}$.[13] Since we observe no substantial change in the trends of Graphs S1 and S2 upon using either extreme of the above range, we estimate that the above approximation has no significant impact on the nature of our results.

Determination of k_{exc} Since k_{exc}, i.e., the rate constant for FMN excitation, depends on the specific laser irradiation conditions, we determined it as follows based on published assessments.[15] First, we assumed that *(i)* the excitation laser light illuminates the NMR sample tube's cross-sectional area uniformly (0.5 cm diameter), *(ii)* the laser light is not attenuated as it travels along the NMR sample solution, *(iii)* there is no FMN and Trp irreversible degradation, and *(iv)* the argon ion laser emits exclusively at 488 nm. Then, we carried out the algebraic steps below.

- Energy of one photon at 488 nm:

$$E = h\frac{c}{\lambda} = 6.626\times10^{-34}\,\mathrm{J\cdot s}\times\frac{3\times10^{8}\,\mathrm{m/s}}{488\times10^{-9}\,\mathrm{m}} = 4.07\times10^{-19}\,\mathrm{J}$$

- $\varepsilon_{\mathrm{FMN,\,488\,nm}}$ was determined from the FMN absorption spectrum and found to be $\varepsilon_{\mathrm{FMN,\,488\,nm}}$ = 4580 $M^{-1}\cdot cm^{-1}$ = 4580 $L\cdot mole^{-1}\cdot cm^{-1}$

  The optical cross section per molecule was determined as follows:

$$\sigma = 4580\,\frac{\mathrm{L}}{\mathrm{mole\cdot cm}}\cdot 1000\,\frac{\mathrm{cm^3}}{\mathrm{L}}\cdot \ln 10\cdot\frac{\mathrm{mole}}{6.022\times10^{23}\ \mathrm{molecule}} = 1.76\times10^{-17}\,\frac{\mathrm{cm^2}}{\mathrm{molecule}}$$

The excitation laser light intensity is

$$I = \frac{1.5\ \text{W}}{\frac{0.5^2 \pi}{4} \text{cm}^2} = 7.64 \frac{\text{J}}{\text{s} \cdot \text{cm}^2} = 7.64 \frac{\text{J}}{\text{s} \cdot \text{cm}^2} \cdot \frac{\text{photon}}{4.07 \times 10^{-19}\ \text{J}} = 1.88 \times 10^{19} \frac{\text{photon}}{\text{s} \cdot \text{cm}^2},$$

where $\frac{0.5^2 \pi}{4} \text{cm}^2$ is the cross-sectional area of the NMR tube.

- Finally, $k_{exc} = \sigma I = 1.75 \times 10^{-17} \frac{\text{cm}^2}{\text{molecule}} \times 1.88 \times 10^{19} \frac{\text{photon}}{\text{s} \cdot \text{cm}^2} = 329\ \text{s}^{-1}$.

Simulation results. The results of the kinetic simulations are shown in Graphs S1 and S2, which illustrate the predicted variation in radical ion pair and ^{T}FMN concentration over time upon continuous laser irradiation, for different Trp concentrations.

Graph S1: Computationally predicted radical ion pair concentration as a function of CW laser irradiation time.

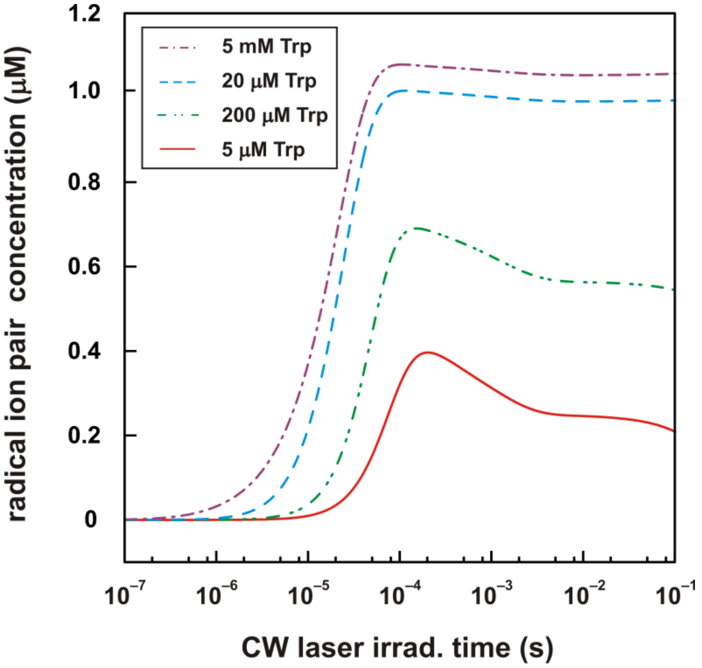

Graph S2: Computationally predicted ^{T}FMN concentration as a function of CW laser irradiation time.

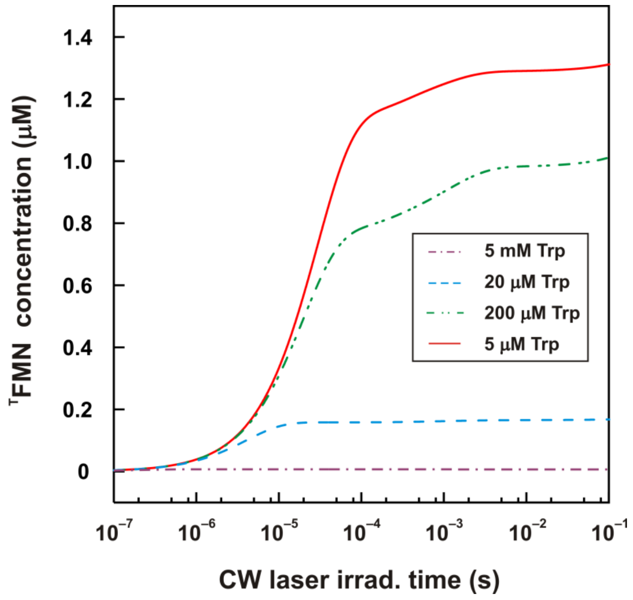

Graph S3: Computationally predicted estimate of ^{13}C PRINT photo-CIDNP (after 0.1 s laser irradiation at 1.5 W) and ^{1}H-^{13}C SE-HSQC sensitivities (in arbitrary units, a.u.) for different total Trp concentrations.

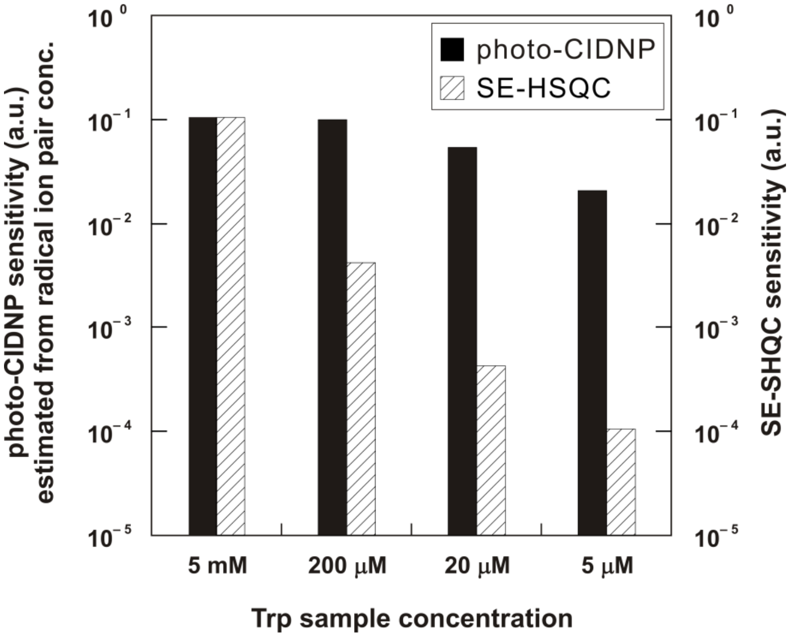

Graph S1 shows that the radical ion pair concentration increases with Trp concentration, at 0.1 s laser irradiation time. Since the radical ion pair concentration is proportional to photo-CIDNP sensitivity, the sensitivity of the photo-CIDNP experiment is bound to increase with Trp concentration. However, a closer inspection of Graph S1 reveals that the estimated radical ion pair concentration does not increase linearly with total Trp concentration. In fact, radical ion pair concentration levels off at high Trp concentrations. Since, the sensitivity of the reference SE-HSQC increases linearly with Trp concentration, the ratio of photo-CIDNP over SE-HSQC sensitivity is expected to decrease at higher Trp concentration (Graph S3). This computational prediction is in qualitative agreement with the experimental results of Fig. 3.7.

The likely scenario leading to Graph S1 follows. As the Trp sample concentration increases, more efficient ^{T}FMN depletion takes place (Graph S2). Thus, since ^{T}FMN and Trp-H are the precursors of the radical ion pair, an increase in Trp-H concentration alone does not guarantee a linear increase in radical ion pair concentration.

Note that the simulations reported here are intended to provide merely rough estimates, appraising only upper limits of the actual radical ion pair and ^{T}FMN concentrations. Indeed, here we are neglecting effects such as light intensity attenuation upon traveling along the NMR tube, and FMN photodegradation pathways. Additionally, the estimated dependence of the photo-CIDNP/SE-HSQC sensitivities upon Trp concentration does not exactly match the experimental Trp concentration dependence of the photo-CIDNP-sensitivity/SE-HSQC-sensitivity ratio (Fig. 3.7). This effect may be ascribed to the fact that the extent of FMN photodegradation increases at low Trp concentrations (Fig. 3.9), and that the kinetic parameters employed in the simulations are only best estimates. In addition, photo-CIDNP sensitivity may not be exactly linearly proportional to radical ion pair concentration.

References

(1) Mendes, P. GEPASI: A Software Package for Modelling the Dynamics, Steady States and Control of Biochemical and Other Systems. *Comput. Appl. Biosci.* **1993**, *9*, 563-571.

(2) Jungbauer, L. M.; Bakke, C. K.; Cavagnero, S. Experimental and Computational Analysis of Translation Products in Apomyoglobin Expression. *J. Mol. Biol.* **2006**, *357*, 1121-1143.

(3) Han, P.; Bartels, D. M. Temperature Dependence of Oxygen Diffusion in H2O and D2O. *J. Phys. Chem.* **1996**, *100*, 5597-5602.

(4) Hore, P. J.; Broadhurst, R. W. Photo-CIDNP of Biopolymers. *Prog. Nucl. Magn. Reson. Spectrosc.* **1993**, *25*, 345-402.

(5) Visser, A. J.; Muller, F. Time-Resolved Fluorescence on Flavins and Flavoproteins. *Methods Enzymol.* **1980**, *66*, 373-385.

(6) Losi, A.; Polverini, E.; Quest, B.; Gartner, W. First Evidence for Phototropin-Related Blue-Light Receptors in Prokaryotes. *Biophys. J.* **2002**, *82*, 2627-2634.

(7) Windsor, M.; Dawson, W.; Systems, T. Quantum Efficiencies of Triplet Formation in Aromatic Molecules. *Mol. Cryst.* **1968**, *4*, 253-258.

(8) Tsentalovich, Y. P.; Lopez, J.; Hore, P.; Sagdeev, R. Mechanisms of Reactions of Flavin Mononucleotide Triplet with Aromatic Amino Acids. *Spectrochim. Acta A* **2002**, *58*, 2043-2050.

(9) Vaish, S. P.; Tollin, G. Flash Photolysis of Flavins. V. Oxidation and Disproportionation of Flavin Radicals. *J. Bioenerg. Biomembr.* **1971**, *2*, 61-72.

(10) Mayhew, S. G. The Effects of pH and Semiquinone Formation on the Oxidation–Reduction Potentials of Flavin Mononucleotide. *Eur. J. Biochem.* **2001**, *265*, 698-702.

(11) Fritz, B. J.; Matsui, K.; Kasai, S.; Yoshimura, A. Triplet Lifetimes of Some Flavins. *Photochem. Photobiol.* **1987**, *45*, 539-541.

(12) Skipper, L.; Campbell, W. H.; Mertens, J. A.; Lowe, D. J. Pre-Steady-State Kinetic Analysis of Recombinant Arabidopsis NADP: Nitrate Reductase - Rate-Limiting Processes in Catalysis. *J. Biol. Chem.* **2001**, *276*, 26995-27002.

(13) Murakami, M.; Ohkubo, K.; Fukuzumi, S. Inter- and Intramolecular Photoinduced Electron Transfer of Flavin Derivatives with Extremely Small Reorganization Energies. *Chem. Eur. J.* **2010**, *16*, 7820-7832.

(14) Eds. Muus, L. T.; Atkins, P. W.; McLauchlan, K. A.; Pedersen, J. B. *Chemically Induced Magnetic Polarization*; Reidel, Dordrecht: 1977.

(15) Tsien, R. Y.; Ernst, L.; Waggoner, A., In *Handbook of Biological Confocal Microscopy*, 3rd ed.; Pawley, J. B., Ed. Springer, New York: 2006; pp 338-352.

Appendix 3A Figures

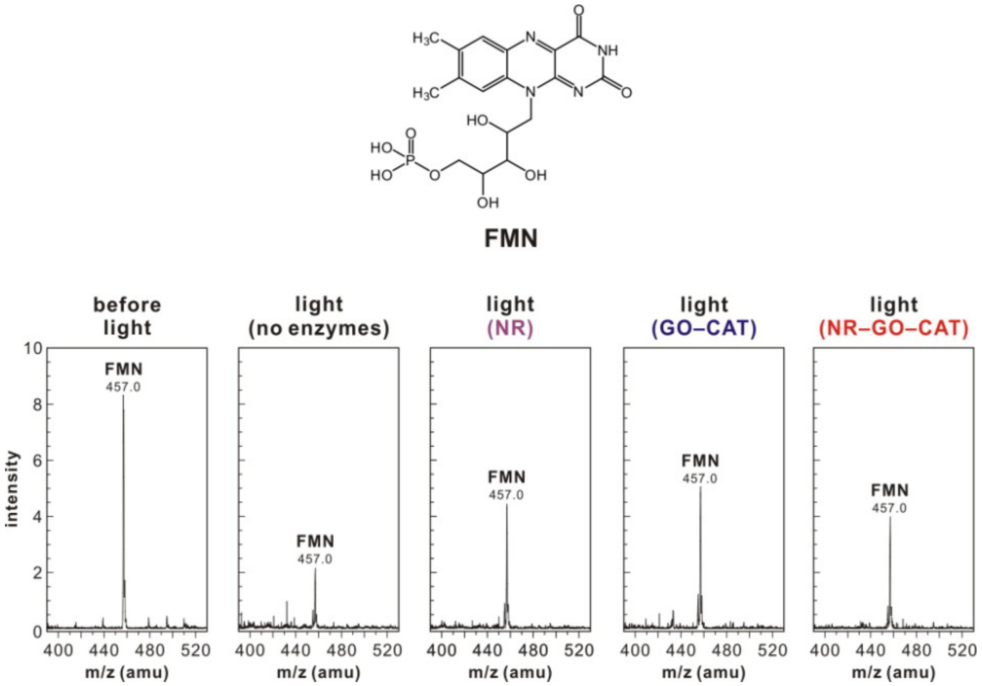

Figure 3A.1 Changes in the electrospray ionization (ESI) mass spectrometry signals of FMN after the photo-CIDNP light experiments of Fig. 3.2b (80 scans total, with 1.5W 0.1s laser pulse/scan) under different conditions. The spectrum on the far left shows FMN before laser irradiation. Note that the FMN peak reports on the presence of both FMN and $FMNH_2$ since $FMNH_2$ is naturally re-oxidized to FMN due to exposure to molecular oxygen during the mass spectrometry sample preparation steps (see Experimental Methods in the main text).

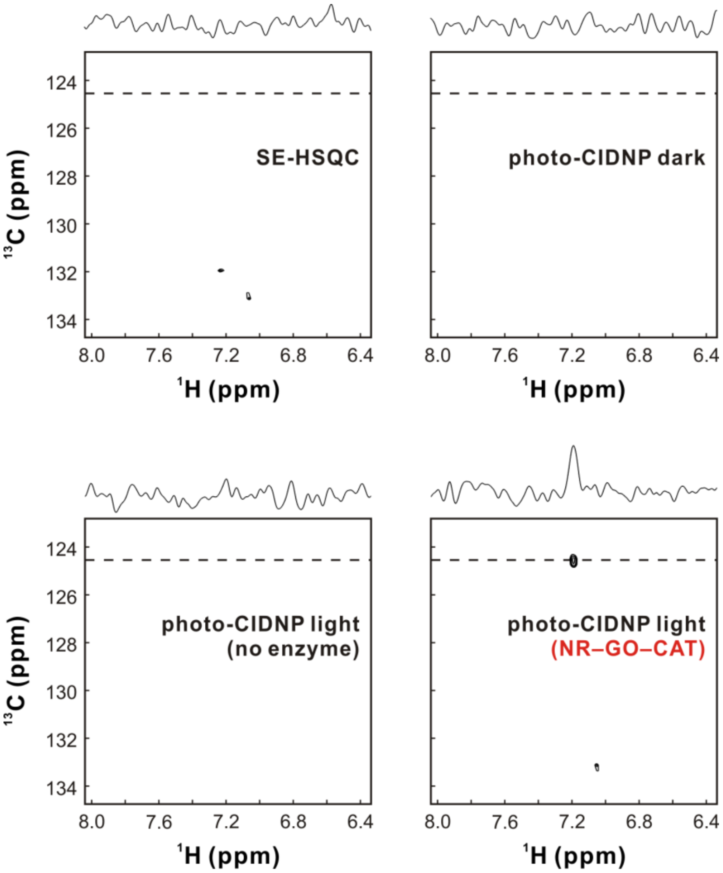

Figure 3A.2 2D ^{13}C-PRINT photo-CIDNP spectra of diluted ^{13}C, ^{15}N-enriched drkN SH3 domain (20 μM) in the absence and presence of the NR-GO-CAT tri-enzyme system. Photo-CIDNP under light conditions was carried out at 0.5W laser power with 0.1s laser pulse irradiation time. 2D ^{13}C-PRINT and reference ^{1}H-^{13}C SE-HSQC spectra were collected according to STATES-TPPI with 32 increments and 1 scan per increment. Spectral widths were 10,000 and 4,500 Hz for the direct and indirect dimensions, respectively. The dashed lines indicate the position of the 1D ^{1}H spectral slices displayed on top of each 2D spectrum.

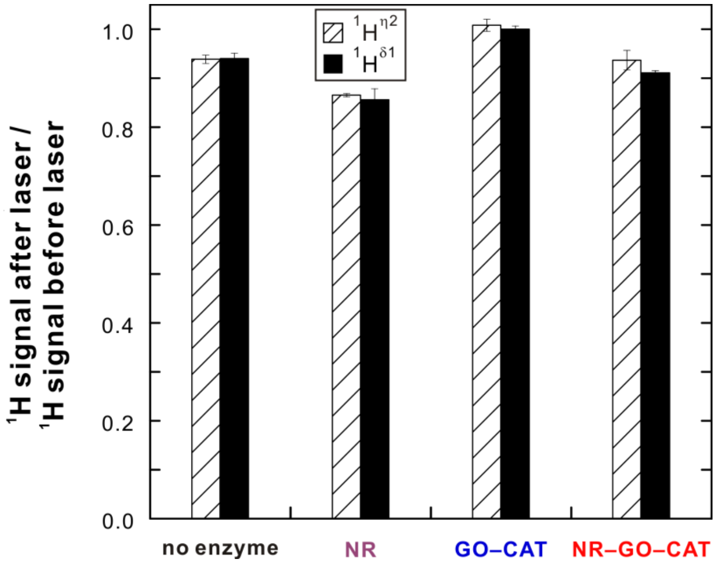

Figure 3A.3 Ratio of ^{1}H 1D pulse-acquire NMR η2 and δ1 resonance intensities before and after the photo-CIDNP experiments of Fig. 3.8 (5mM Trp in the presence of 0.2mM FMN; 320 laser pulses; 1.5W laser power and 0.1 s laser irradiation time per laser pulse).

Chapter 4

Transient Interactions of a Slow-Folding Protein with the Hsp70 Chaperone Machinery

This chapter reproduces an article published by

Ashok Sekhar, Margarita Santiago, Hon Nam Lam, Jung Ho Lee, and Silvia Cavagnero

in

Protein Science (2012) 21, 1042-1055.

J.H.L. performed RNase H^D activity assays and participated in data analysis and interpretation.

Abstract

Most known proteins have at least one local Hsp70 chaperone binding site. Does this mean that all proteins interact with Hsp70 as they fold? This study makes an initial step to address the above question by examining the interaction of the *E.coli* Hsp70 chaperone (known as DnaK) and its co-chaperones DnaJ and GrpE with a slow-folding *E.coli* substrate, RNase H^D. Importantly, this protein is a non-obligatory client, and it is able to fold *in vitro* even in the absence of chaperones. We employ stopped-flow mixing, chromatography and activity assays to analyze the kinetic perturbations induced by DnaK/DnaJ/GrpE (K/J/E) on the folding of RNase H^D. We find that K/J/E slows down RNase H^D's apparent folding, consistent with the presence of transient chaperone-substrate interactions. On the other hand, kinetic retardation is moderate for this slow-folding client and it is expected to be even smaller for faster-folding substrates. Given that the interaction of folding-competent substrates such as RNase H^D with the K/J/E chaperone system is relatively short-lived, it does not significantly interfere with the timely production of folded biologically active substrate. The above mode of action is important because it preserves K/J/E bioavailability, enabling this chaperone system to act primarily on assisting the folding of other misfolded and (or) aggregation-prone cellular proteins that are unable to fold independently. When refolding is carried out in the presence of K/J and absence of the nucleotide exchange factor GrpE, some of the substrate population becomes trapped as a chaperone-bound partially unfolded state.

2.1 Introduction

The ubiquitous Hsp70 chaperone family is involved in preventing protein aggregation and assisting co- and post-translational protein folding[1-3]. The ATP-dependent interaction of Hsp70 with its client proteins is critical for the function of the Hsp70 machinery. DnaK, the cytosolic *E.coli* Hsp70, is the best-studied member of the Hsp70 family[4]. DnaK interacts with its client substrates via the sequence-specific recognition of the DnaK-binding motif, which consists of a core of approximately five nonpolar amino acids flanked by basic residues[5]. This motif is very common in proteins and is predicted to occur with a frequency of about 1 in 40 residues[5], implying that most proteins have at least one local DnaK binding site.

DnaK is an ATP-dependent chaperone and functions in concert with the two co-chaperones DnaJ and GrpE.[6] The kinetics and thermodynamics of the interaction of DnaK with its co-chaperones and with peptide substrates has been extensively characterized[4, 7-11]. Substrates enter the Hsp70 chaperone cycle by binding either DnaJ [12] or to the ATP-bound state of DnaK[13]. ATP hydrolysis, stimulated by binding of both DnaJ and the substrate[14], locks the substrate into a high-affinity ADP-DnaK-bound state. GrpE, the nucleotide exchange factor, then releases the bound ADP[15]. The latter process facilitates the binding of ATP, resulting in substrate release. The chaperone cycle is thus reset, and ready for additional rounds of substrate binding and release.

Fewer investigations have been carried out with larger protein substrates[10,16], which are believed to bind the chaperone in a globally unfolded conformation[17-19]. The DnaK/DnaJ/GrpE (K/J/E) chaperone system is known to significantly accelerate the *in vitro* refolding of large proteins incapable of independent folding, e.g., firefly luciferase[12,

[20], by actively unfolding the misfolded substrate[16, 20]. Luciferase requires chaperones for efficient *in vitro* refolding and tends to aggregate, except at extremely low concentrations[21,22]. However, the generality of the active refolding assistance by K/J/E has not been addressed in the literature. In particular, it is not understood whether K/J/E catalyzes the refolding of all slow-folding proteins, including those that are able to fold even in the absence of chaperones. In summary, the extent of interaction between folding-competent substrates and the K/J/E chaperone network remains poorly characterized.

In this work, we employ a two-state slow-folding variant of *E.coli* RNase H (RNase H^D)[23] as a model client protein for the K/J/E chaperone system. We investigate RNase H^D folding kinetics in the presence of various combinations of DnaK, DnaJ and GrpE. Given that RNase H^D has a strong local binding site for DnaK (Fig. 4.1) and is known to fold slowly on the typical timescale of chaperone binding, one would expect that RNase H^D may significantly interact with K/J/E during folding. Such interaction could lead to either acceleration or retardation of the client protein folding. We find a small but significant decrease in RNase H^D refolding rate, in the presence of K/J/E. This result shows that catalytic acceleration of protein folding by K/J/E, observed for some large multi-domain proteins, is not a universal feature of this chaperone system. Our data also support the presence of transient interactions of K/J/E with the folding-competent substrate RNase H^D. We propose that the physiological role of such contacts may be to decrease any likelihood of misfolding/aggregation while, at the same time, avoiding significant delays in the production of bioactive substrate.

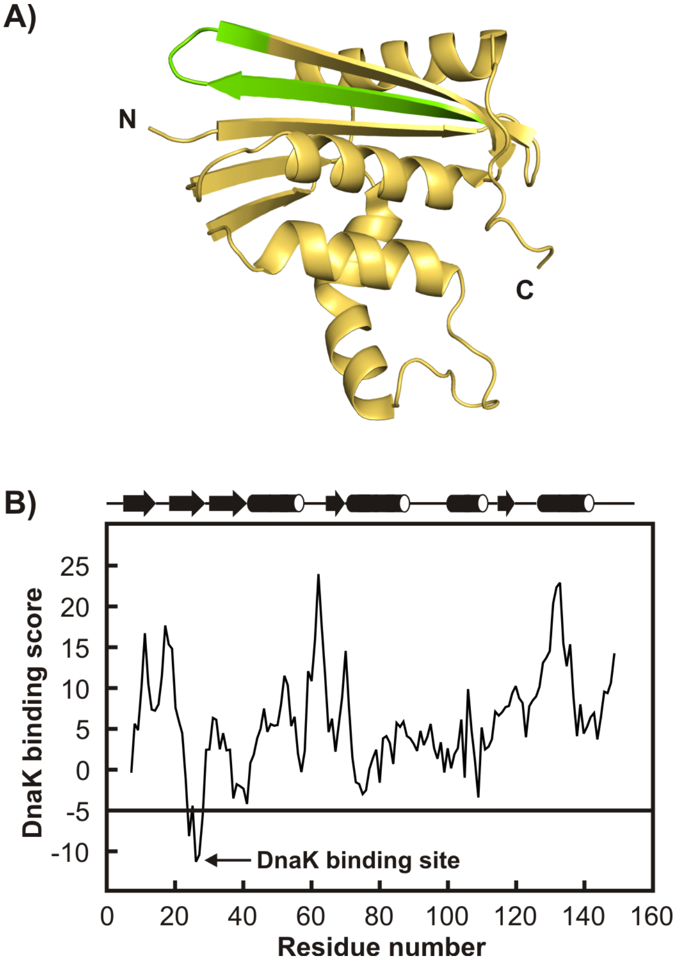

Figure 4.1 A) Three-dimensional structure of *E.coli* RNase H (PDB code: 1F21).[59] The N and C termini are labeled. The unique DnaK binding site is shown in green. B) Predicted local DnaK binding scores [5] of RNase H^D [23]. Regions with a score lower than -5 are potential strong DnaK binding sites. The secondary structure of wild type *E.coli* RNase H derived from the protein crystal structure is mapped above the graph.

4.2 Experimental Methods

Protein Expression and Purification. *RNase H^D.* RNase H^D is a mutant of *E.coli* RNase H with all three native Cys replaced by Ala, in addition to the I53D mutation [23]. The pSM101 plasmid encoding RNase H^D was transformed into *E. coli* cells, and the protein was overexpressed as described[24]. Cell pellets were thawed and resuspended in ice-cold lysis buffer (50mM Tris, pH 8.0, 1mM EDTA, 10mM β-mercaptoethanol), and lysed with lysozyme followed by mild sonication. RNase H^D present in the inclusion bodies was extracted from the pellet with 50% acetonitrile containing 0.1% TFA, followed by a 0.5 M urea wash[23]. The protein was purified by reverse-phase HPLC on a Vydac C4 preparative scale column (Grace, Deerfield, IL). ESI-MS analysis of purified RNaseH^D yielded a molecular weight of 17502 Da, in agreement with the expected average mass of 17503 Da.

DnaK. Overexpression and purification of DnaK was carried out according to published procedures [25-27] with minor modifications. *E.coli* DnaK was overexpressed in BL21(DE3) cells (Novagen, EMD Chemicals, Gibbstown, NJ) carrying a pET-11a vector encoding the *dnaK* gene. Cells were grown in standard Luria broth containing 50µg/mL carbenicillin at 30°C. Overexpression of the protein was induced by addition of isopropyl-ß-thiogalactoside (1mM) at an OD_{600} of 0.8. Cells were harvested after reaching an OD_{600} of 1.9-2.0. The cell pellet was resuspended in lysis buffer (25 mM Hepes, pH 7.5, 50 mM KCl, 5 mM $MgCl_2$, 1 mM EDTA, 10 mM BME) and lysed with lysozyme in the presence of 2 mM PMSF as a protease inhibitor, followed by mild sonication.

DnaK was initially purified on a 300 mL anion exchange Q-Sepharose column (GE Healthcare, Piscataway, NJ) equilibrated with lysis buffer. The protein was eluted from the column using a linear KCl gradient (0 - 1 M). Fractions containing DnaK were pooled and concentrated to 5 mL with Amicon centrifugal concentrators (10 MWCO, Millipore, Billerica, MA). The concentrated DnaK solution was then purified on a Superdex 200 gel filtration column (GE Healthcare) equilibrated with lysis buffer. Pure fractions were pooled, concentrated to ~ 20 mL and dialyzed against 25 mM HEPES (pH 7.5) buffer containing 1 mM EDTA and 10 mM BME in 10 MWCO dialysis cassettes (12-30 mL, Thermo Scientific, Rockford, IL).

DnaK-bound nucleotide was removed by treatment with alkaline phosphatase[26]. 2 units of alkaline phosphatase (Sigma-Aldrich Corp., St. Louis, MO) were added per mg of DnaK and the solution was stirred at 4°C with simultaneous dialysis to remove AMP. The A_{260}/A_{280} ratio was monitored until the value went below 0.7. This typically takes about 5 hours. Alkaline phosphatase was subsequently removed by purification on the Superdex 200 gel filtration column (GE Healthcare). The pure nucleotide-free DnaK was finally concentrated, dialyzed against storage buffer (25 mM HEPES pH 7.5, 5 mM $MgCl_2$, 50 mM KCl), flash frozen in liquid N_2 and stored at -80°C.

DnaJ. A plasmid containing the full-length *E. coli* DnaJ gene was overexpressed from a pUHE21Δ12 plasmid in *E. coli* BL21 cells (Novagen, EMD Chemicals, Gibbstown, NJ) harbouring a placIq plasmid. DnaJ was purified according to a published protocol [28-31] with minor modifications. Detergents were not used in any step of the purification. The first chromatographic step was changed from the S-sepharose column to the SPsepharose cation exchange column (GE Healthcare), and the last step involving Q-sepharose chromatography was removed.

GrpE. The expression plasmid pUHE21Δ12 containing the full-length *E. coli* GrpE gene was overexpressed in *E. coli* BL21 cells containing a placIq plasmid (Novagen, EMD Chemicals, Gibbstown, NJ). The protein was purified according to established procedures[30-32]. Briefly, cells were lysed with lysozyme and mild sonication. GrpE was then successively purified on the HiTrap Q-sepharose anion exchange column (GE Healthcare), the HiTrap Blue Sepharose column (GE Healthcare) and a hydroxyapatite column (Bio-Rad Laboratories, Inc., Hercules, CA). Pure fractions were flash frozen and stored at -80°C.

The activity of purified DnaK, DnaJ and GrpE was assessed via a firefly luciferase reactivation assay[12]. Concentrations of all proteins were estimated by UV-visible absorption spectrophotometry (extinction coefficients: 35,469[33], 15,800[34], 14,000 [35] and 1,400 $M^{-1}cm^{-1}$ [35] for RNase H I53D, DnaK, DnaJ and GrpE respectively).

Stopped-flow kinetics. RNase H^D refolding time courses were monitored with an SFM-400 MOS-450/AF-CD stopped-flow spectrophotometer equipped with an HDS mixer (Bio-Logic, Claix, France). The experimental dead time was 6ms. A Xe-Hg lamp (Hamamatsu Photonics, Hamamatsu, Japan) and an 8-mm excitation slit width were used. Stopped-flow experiments were carried out with an FC-20 cuvette (2 mm x 2 mm). 8000 data points were collected for each kinetic trace. All stopped-flow experiments were performed at 30ºC. Far-UV CD signals were monitored at 222 nm.

RNase H^D was unfolded in 20 mM sodium acetate (pH 6.0) containing 5 M urea (MP Biomedicals, Inc., Solon, OH). Unfolded protein samples were incubated at 4ºC overnight prior to data collection to ensure complete unfolding. The urea-unfolded protein was refolded by 10-fold dilution into buffer containing 20 mM sodium acetate, 50 mM KCl, 1 mM ATP and 5 mM $MgCl_2$ in the absence or presence of chaperones. Unfolded controls consisted of unfolded protein diluted into 5 M urea. Final protein concentrations of RNase H^D, DnaK, DnaJ and GrpE were 5, 15, 3 and 6 μM respectively. All kinetics data were background-corrected against appropriate buffer blanks.

All stopped-flow CD-detected kinetic traces were fit to single exponential relations of the form

$$y(t) = a + b(1 - \exp(-k_{obs} t)), \tag{3}$$

where y(t) is the time-dependent ellipticity, a is the ellipticity at time t = 0 and b is the total change in ellipticity upon refolding.

Size-exclusion chromatography. Analytical size-exclusion chromatography was performed on a TSK-GEL G2000SW (Tosoh Bioscience LLC, King of Prussia, PA) column connected to an HPLC (Shimadzu, Columbia, MD) equipped with a SPD-6AV detector monitoring absorbance at 214nm. Flow rates were 1mL/min. RNase H^D was unfolded under the same conditions as in the stopped-flow experiments and refolded by diluting 10-fold into elution buffer (20 mM sodium acetate pH 6.0, 100 mM KCl, and 5 mM $MgCl_2$) containing 1 mM ATP in the absence or presence of molecular chaperones. Samples were incubated at room temperature for 5 minutes before loading onto the column. The elution buffer did not contain any ATP since the absorbance was too high for detection at 214 nm. The gel filtration column was calibrated using the following molecular weight standards: bovine serum albumin (67 kDa), ovalbumin (43 kDa), chymotrypsinogen A (25 kDa), horse heart myoglobin (17.6 kDa) and ribonuclease A (13.7 kDa). Blue dextran was used to determine the column void volume.

Gel filtration chromatograms were digitized with the Bytescout Graph Digitizer (Vancouver, Canada). Peaks arising from RNase H^D, chaperones and buffer components were deconvoluted by fitting each peak to a log-normal function using the Levenberg Marquardt algorithm[36-38] within the Fityk software package[39]. The deconvoluted native RNase H^D peak intensity was used to calculate the extent of peak intensity reduction in the presence of various combinations of chaperones.

Reverse-phase chromatography. Protein fractions collected from the gel filtration experiments were lyophilized and resuspended in 35% acetonitrile containing 0.1% trifluoroacetic acid (Fisher Scientific, Fair Lawn, NJ). Samples were analyzed on an analytical reverse-phase Vydac C18 HPLC column (Grace). A flow rate of 1mL/min was maintained and protein elution was monitored using absorbance at 214 nm and 280 nm.

RNase H^D activity assays. RNase H^D activity assays were performed on the protein after its refolding in the absence or presence of chaperones, to test the extent of its bioactivity after refolding and interaction with the K/J/E chaperones (Fig. 4.8). RNase H^D was first unfolded in urea and refolded (final protein concentration: 27 μM, for 10 min) in the absence or presence of pertinent molecular chaperones: DnaK (70 uM), DnaJ (12 uM), GrpE (30 uM) and, whenever appropriate, ATP (1 mM). Refolded RNase H^D was then diluted 1000-fold in the assay buffer (50 mM Tris, 50 mM NaCl, 10 mM $MgCl_2$ pH 8.0) containing 25 mg/mL rA/dT_{20} RNA-DNA hybrid to initiate the activity assay. RNase H activity assays were performed as described[40] except that the timecourse of cleavage of RNA-DNA hybrids was followed via the increase in absorbance at 260 nm.

Absorbance is quenched by base stacking in the DNA-RNA hybrid (hypochromic effect). The quenching vanishes upon cleavage, which eliminates base stacking.

Statistical analysis of stopped-flow refolding. The statistical significance of the differences between the observed stopped-flow rate constants and burst and final CD ellipticity amplitudes was determined via the one-tailed Student's t-test[41]. For the apparent rate constants, the t-test was carried out on two means as described[39], to check the significance of differences between rate constants in the absence and presence of various chaperone combinations. In the case of CD signal amplitudes (η_B and η_F), the t-tests were carried out on a single mean, to evaluate the significance of the difference between the mean and the expected value in the absence of any change induced by K/J/E. The p values obtained from the Student's t-test are discussed in the legend of Figure 4.3.

4.3 Results

RNase H^D is a good model substrate to monitor client interaction with the K/J/E chaperone system. In order to explore the influence of the *E.coli* Hsp70 chaperone system in the folding pathway of a protein substrate, we chose RNase H* I53D [23] as a model client protein. *E.coli* Ribonuclease HI (RNase H) is a 155 amino acid endoribonuclease that catalyzes the hydrolysis of RNA in RNA-DNA hybrids. The wild type enzyme lacks disulphide bonds in the native state. The mutant construct RNase H*, which has all three Cys replaced by Ala is folded and enzymatically active[24]. The RNase H variant that we employ in our study, RNase H* I53D, here denoted as RNase

H^D, is the triple Cys-to-Ala mutant containing an additional point mutation at residue 53, with Ile53 replaced by Asp [23]. In the native state, I53 is buried in the hydrophobic core at the interface between helices A and D. The Ile53 to Asp mutation results in a destabilization of the RNase H kinetic intermediate and switches the folding mechanism from three-state to two-state, while retaining the RNase H enzymatic activity [23]. RNase H^D is thus a slow two-state-folding protein with a folding rate constant of 0.03 s^{-1}. It is among the slowest known two-state folders *in vitro*[42] at 25°C.

A widely used computational algorithm that scans protein primary structure for potential local DnaK interaction sites [5] predicts a strong DnaK binding site near the N-terminus of RNase H^D, as shown in Figure 4.1. Since it is known that RNase H^D folds slowly, it is possible that this hydrophobic DnaK binding motif remains solvent-exposed for a sufficiently long time to interact with the Hsp70 chaperone system. The above considerations make *E.coli* RNase H^D an attractive model protein for studying the time-course of folding-competent substrate interaction with the *E.coli* K/J/E chaperone machinery.

The apparent folding rate of RNase H^D decreases in the presence of K/J/E. In order to probe the kinetics of RNase H^D refolding in the absence and presence of K/J/E, we employed stopped-flow fast mixing in conjunction with far-UV circular dichroism (CD) detection. The CD signal at 222 nm is a measure of the extent of α-helical secondary structure in a protein. RNase H^D was unfolded in 5 M urea pH 6 and allowed to refold in the absence or presence of various combinations of DnaK, DnaJ and GrpE. Chaperone concentrations were chosen to reflect the physiologically relevant ratio of K:J:E = 5:1:2

in *E.coli* cells [16]. The concentration ratio of substrate : DnaJ was ~ 1.6:1, which is nearly optimal for the *in vitro* K/J/E-mediated refolding of luciferase [14, 30].

Stopped-flow refolding traces of RNase H^D are shown in Figure 4.2. All kinetic traces were fit to a single exponential (see Materials and Methods) to extract rate constants, and burst-phase and final CD amplitudes. Comparative histograms showing apparent refolding rate constants of RNase H^D in buffer containing or lacking DnaJ, DnaK/ATP, DnaK/DnaJ/ATP and DnaK/DnaJ/GrpE/ATP are reported in Figure 4.3.

An initial important result illustrated in Figure 4.3A is that the refolding of RNase H^D is not accelerated by the presence of the entire K/J/E chaperone system. Instead, there is a small but statistically significant ($p < 0.05$) apparent deceleration in RNase H^D refolding. It is thus clear that the catalytic refolding activity of the Hsp70 chaperone system, observed in the case of the folding-incompetent client luciferase [12], is substrate dependent. Hence catalytic acceleration of substrate folding is not a general feature of Hsp70. In the case of RNase H^D, which is a slow two-state folder capable of achieving its native state independently, i.e., even in the absence of chaperones, the folding process is effectively slowed down when K/J/E are present.

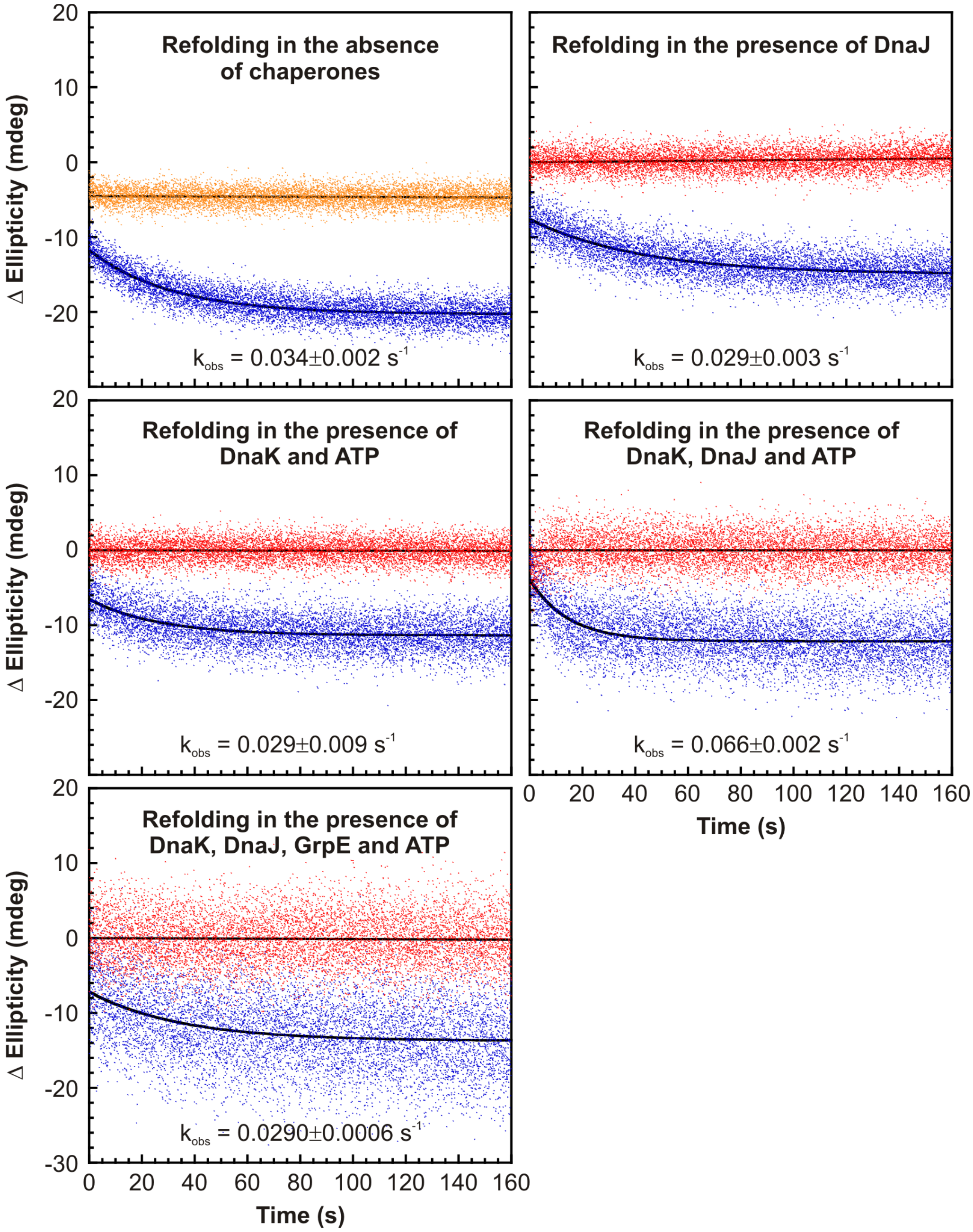

Figure 4.2 Experimental far-UV CD-detected stopped-flow kinetic traces for the refolding of RNase H^D (blue) in the absence and presence of various combinations of DnaK, DnaJ and GrpE at 30ºC at 222 nm. Time-dependent variations in ellipticity of refolding buffer and urea-unfolded RNase H^D are shown in red and orange,

respectively. The ellipticity of the refolding buffer subtracted from the ellipticity of the refolding trace, denoted as ∆ellipticity, is plotted on the y-axis. The ellipticity of the refolding solution, containing contributions from chaperones, has been subtracted out. The observed time-dependent change in ellipticity thus arises from the substrate protein alone, assuming that the secondary structure of the chaperones is not significantly perturbed. Final concentrations of RNase H^D, DnaK, DnaJ, and GrpE and ATP in the refolding mixture were 5, 15, 3, and 6 μM and 1 mM, respectively. Least squares fits of the kinetic traces to linear or single-exponential functions are in black. Average rate constants derived from curve fitting are listed close to each corresponding refolding trace. Error bars represent 1 standard error calculated from 2 – 8 independent repeats, with each repeat comprising 4 – 6 replicate measurements.

In contrast, the apparent RNase H^D refolding rate constant in the presence of DnaK, DnaJ and ATP, but no GrpE, is about two-fold larger than in the absence of the whole chaperone system. In the absence of GrpE, client proteins are known to become kinetically trapped in the DnaK substrate-binding pocket in the ADP-bound state of DnaK[43]. As supported by additional evidence from gel filtration, HPLC, SDS-PAGE and RNase H activity assays (see below), the large observed rate constant in the presence of DnaK/DnaJ/ATP reflects the generation of a kinetically stable RNase H^D-chaperone complex by some of the substrate molecules. Formation of this complex is dramatically enhanced by the presence of DnaJ, which stimulates the basal ATP hydrolysis of DnaK in conjunction with the substrate [14]. Persistent substrate-DnaK complex formation accounts for the fact that a faster apparent rate is only detected when the refolding buffer contains both DnaK and DnaJ, but not when only DnaK or DnaJ is present.

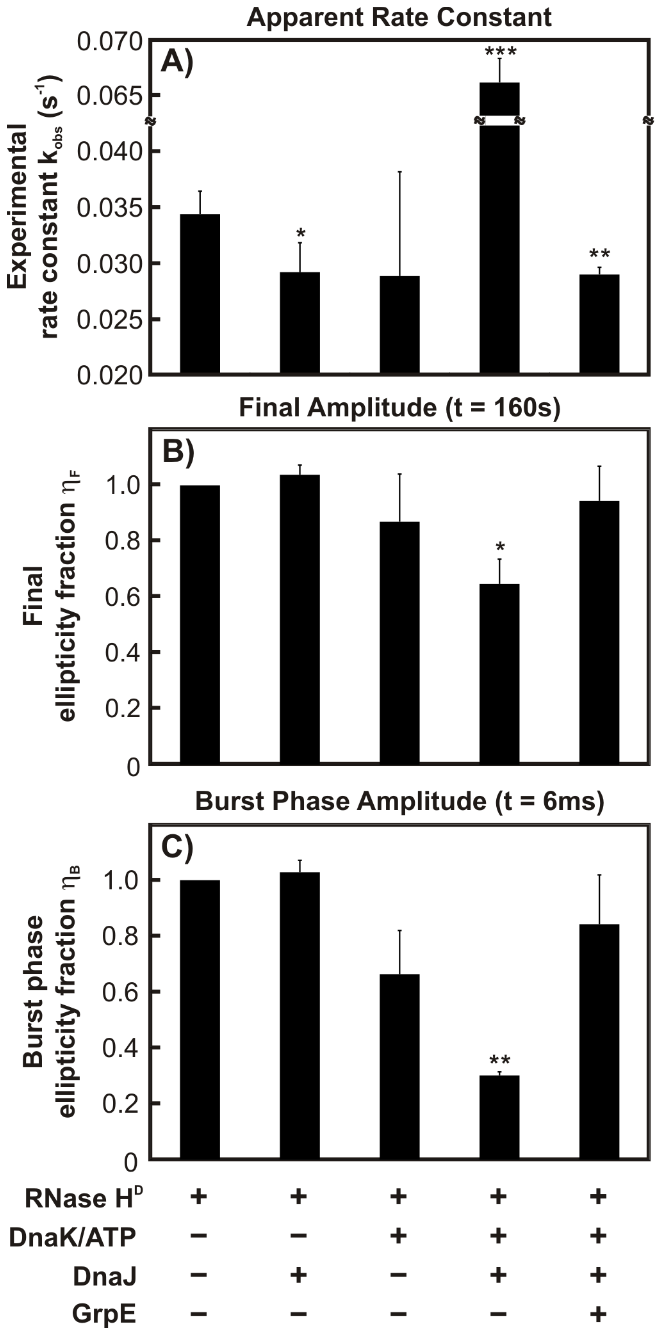

Figure 4.3 Stopped-flow refolding data analysis. Bar diagram reporting the A) rate constants, B) final (η_F) ellipticity fractions (see eqns. 1 and 2), and C) burst phase amplitudes (η_B), and obtained from stopped-flow data analysis. Chaperone

combinations pertinent to each experimental condition are listed below the corresponding bar. Error bars represent 1 standard error calculated from 2 – 8 independent measurements, with each measurement consisting of 4 – 6 independent runs. Statistically significant differences (relative to the RNase H^D-only experiment) are shown in the graph by asterisks (*: $p \leq 0.1$, **: $p \leq 0.05$, ***: $p \leq 0.001$).

From the average observed rate constants in Figure 4.3A, one may infer that DnaJ or ATP-DnaK independently retard the folding of RNase H^D to a similar extent as K/J/E. However, the observed refolding rate constants in the presence of either DnaJ or ATP-DnaK are not sufficiently statistically different from the chaperone-free case, due to a p value larger than 0.05. Interestingly, numerical simulations on the folding of RNase H^D in the presence of DnaJ, ATP-DnaK, or the entire K/J/E system (Sekhar, A., Lam, H.N. and Cavagnero, S., submitted) predict a small kinetic retardation due to transient client binding and release by DnaJ, ATP-DnaK or K/J/E [10, 43].

Stopped-flow circular dichroism (CD) is consistent with the generation of a partially unfolded K/J-bound substrate, in the absence of GrpE. In order to evaluate the extent of folding occurring in the presence of chaperones and the formation of any chaperone-substrate complexes, we computed the final ellipticity fraction (η_F) of RNase H^D by far-UV circular dichroism. The η_F parameter is a measure of the change in final ellipticity due to the client protein, in the presence of chaperones. Since the CD signal at 222 nm is related to the degree of α-helical secondary structure, η_F is a probe of the final (F) fraction of native RNase H^D formed 160 s after refolding initiation in the presence of chaperones. If RNase H^D has folded completely to its native state, η_F is expected to be 1. The η_F parameter is defined as

$$\eta_F = \frac{[\theta]_{RC,F} - [\theta]_{C,F}}{[\theta]_{R,F}} \quad . \tag{1}$$

Here, $[\theta]_{R,F}$ and $[\theta]_{RC,F}$ correspond to the ellipticity at 222 nm of the RNase H^D refolding (R) traces in the absence and presence of chaperones (C), respectively, at the end of the stopped-flow measurements (t = 160 s). $[\theta]_{C,F}$ is the ellipticity arising from the chaperone-containing solution in the absence of RNase H^D after 160 s from refolding initiation. All $[\theta]_F$ values were obtained from least-squares fitting of the corresponding kinetic traces either to a linear ($[\theta]_{C,F}$) or a single exponential relation ($[\theta]_{R,F}$ and $[\theta]_{RC,F}$), as detailed in the Materials and Methods.

As shown in Figure 4.3B, in the presence of ATP-DnaK and DnaJ and in the absence of GrpE, η_F is ~0.65. This means that the CD signal intensity at the end of the kinetic run is only about 65% of the expected value for fully folded substrate.

This reduction in ellipticity may arise from a smaller α-helical content of RNase H^D or, alternatively, it may also be due to conformational changes within the chaperones (DnaK and DnaJ) upon interaction with the substrate. Published studies of DnaK and DnaJ in the absence and presence of various substrates revealed no significant perturbations in the secondary or tertiary structure of these chaperones upon substrate binding[44-46]. Hence it is more likely that the observed decrease in ellipticity can be ascribed entirely to RNase H^D.

Gel filtration, HPLC, SDS-PAGE and substrate activity assays collectively support formation of ca. 35% complex between RNase H^D and K/J after a few minutes from mixing unfolded protein and chaperone-containing solution (see sections below). Given that the stopped-flow experiment was run at concentrations of substrate and chaperones slightly different from those used in the chromatographic and activity assays, we conclude that some chaperone-substrate complex is also present at the end of the stopped-flow experiment. However, we cannot precisely quantify its population due to the difference in experimental conditions. Hence, the stopped-flow η_F value of ~0.65 (Fig. 4.3B) shows that the smaller α-helical content of RNase H^D detected at the end of the kinetic run must be due to the fact that the chaperone-bound substrate population is partially unfolded. This intriguing result is in agreement with previous experimental observations with other substrates, indicating that DnaK binds polypeptide and protein clients in a globally unfolded conformation [18,19, 44].

Figure 4.3B also shows that η_F in the presence of only DnaJ or ATP-DnaK, and in the presence of the complete K/J/E chaperone system, is statistically indistinguishable from 1 ($p > 0.1$). This result confirms that the RNase H^D folds to completion under these conditions. The mere presence of ATP-DnaK or DnaJ in the folding environment of RNase H^D is not sufficient to create a stable chaperone-substrate complex, in agreement with the notion that the synergistic stimulation of ATP hydrolysis by the substrate and DnaJ is necessary for trapping substrates as complexes with ADP-DnaK [14]. In contrast, GrpE in the folding buffer reverses the kinetic trapping seen with K/J by facilitating the exchange of bound nucleotide, allowing ATP to bind DnaK and dissociate the chaperone-substrate complex.

Burst phase CD amplitudes support the existence of transient interactions between RNaseH^D and chaperones. We computed burst phase CD signal amplitudes to gauge the extent of substrate secondary structure at 6 ms from refolding initiation (i.e., within the dead time of our stopped-flow measurement). The burst phase (denoted by the subscript B) amplitude of the far-UV CD signal was quantified in a similar fashion to the final amplitude, via a parameter denoted as burst ellipticity fraction (η_B), defined as:

$$\eta_B = \frac{[\theta]_{RC,B} - [\theta]_{C,B}}{[\theta]_{R,B}} . \tag{2}$$

According to the above formula, η_B is an indication of the fraction of the substrate's native helicity after 6 ms from stopped-flow experiment initiation.

As illustrated in Figure 4.3C, η_B is statistically different from 1 ($p < 0.1$) only in the case of RNase H^D folding in the presence of ATP-DnaK and DnaJ. This result stems from the fact that the burst phase amplitude is dramatically smaller, than for the refolding of RNase H^D alone. The small value of η_B (equal to ca. 0.3) therefore shows that the addition of K/J to the refolding buffer causes a global decrease in substrate structure at 6 ms, relative to the chaperone-free process. The simplest explanation for the origin of this effect is the presence of some interactions between the substrate and the K/J chaperone system. The latter conclusion is in qualitative agreement with evidence from gel filtration, HPLC and activity assays (see below), which support the presence of a persistent substrate-chaperone complex after a few minutes from refolding initiation.

The η_B values in the presence of ATP-DnaK ($p = 0.14$) and DnaJ alone ($p = 0.28$), as well as in the presence of the entire K/J/E chaperone system ($p = 0.22$), are statistically indistinguishable from 1. This result likely reflects our inability to assess transient chaperone-substrate interactions above noise level. In the case of folding in the presence of DnaJ, however, the observed η_B value of 1 may also be a result of a DnaJ-RNase H^D complex possessing the same helical content as the native unfolded state of RNase H^D. This explanation is in agreement with the fact that DnaJ binds protein surfaces[47], thereby allowing the development of helical secondary structure within the bound polypeptide.

Analytical size-exclusion, reverse-phase HPLC and SDS-PAGE confirm the existence of a kinetically trapped RNase H^D-chaperone complex in the presence of K/J. Stopped-flow kinetic rate constants and final ellipticity fractions observed in the absence of GrpE suggest that RNase H^D forms a kinetically trapped complex with chaperones. In order to obtain direct evidence for RNase H^D-chaperone complex formation, we carried out analytical size exclusion HPLC experiments, which discriminate between molecules based on their hydrodynamic radii. Hence, this method is a sensitive reporter of complex formation under refolding conditions. Unfolded RNase H^D was allowed to refold in buffer containing DnaK, DnaJ and ATP for 5 min., and the mixture was then injected into the size exclusion column. Samples were eluted from the column immediately using refolding buffer lacking chaperones and ATP. A 5-fold higher concentration of chaperones and RNase H^D was employed in these experiments while maintaining the same substrate : chaperone ratio, to obtain good signal-to-noise.

Figure 4.4 shows gel filtration chromatograms of RNase H^D refolded in the absence (panel A) and presence (panel C) of ATP-DnaK and DnaJ. There is a significant reduction in the intensity of the native RNase H^D peak in the presence of DnaK and DnaJ, indicating that a fraction of RNase H^D molecules form complexes with chaperones.

To confirm the presence of a complex of RNase H^D and K/J on the size exclusion column, we collected elution fractions A and B (Fig. 4.4) and analyzed the contents using analytical reverse phase HPLC. Panels A and B of Figure 4.5 show the reverse

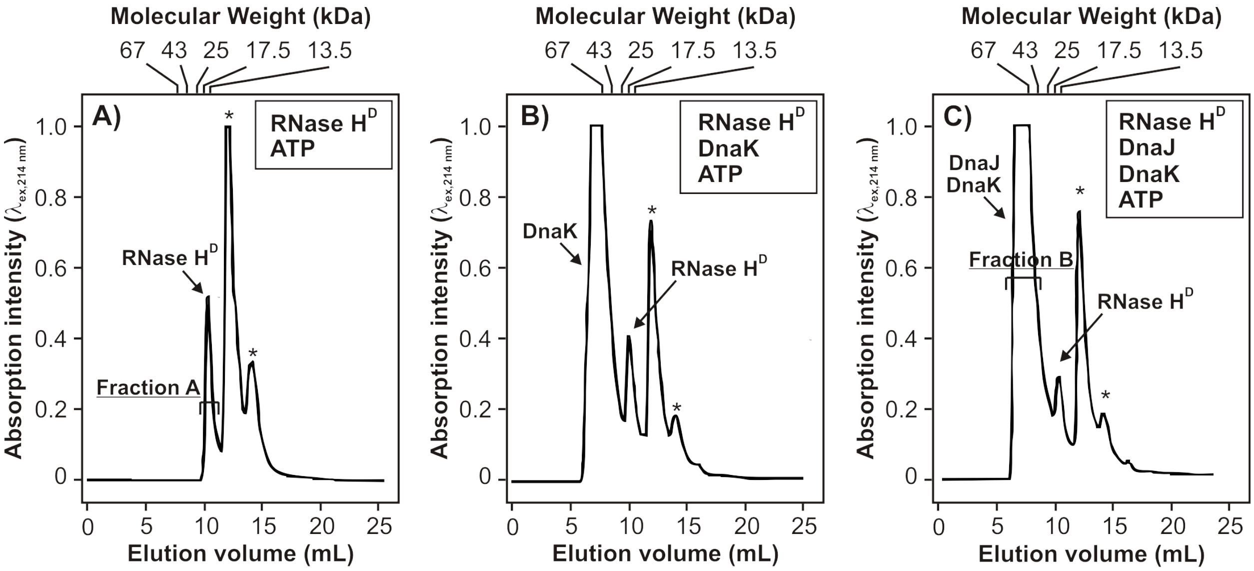

Figure 4.4 Analytical gel filtration chromatograms, followed by electronic absorption at 214 nm, of RNase H^D A) in the absence of chaperones, B) in the presence of DnaK/ATP and C) in the presence of DnaK, DnaJ and ATP. Urea-unfolded RNase H^D was refolded in 20 mM sodium acetate pH 6.0 containing 100 mM KCl, 5 mM $MgCl_2$ and 1 mM ATP in the absence (A) and presence of chaperones (B and C) before injecting into the size-exclusion column. Peaks denoted with asterisks arise from buffer components (i.e., ATP and ADP). The elution volume corresponding to each molecular-weight standard used to calibrate the column is indicated at the top of each panel (see Materials and Methods for names of standard proteins). In all chromatograms, absorption intensities are reported on the same absolute scale.

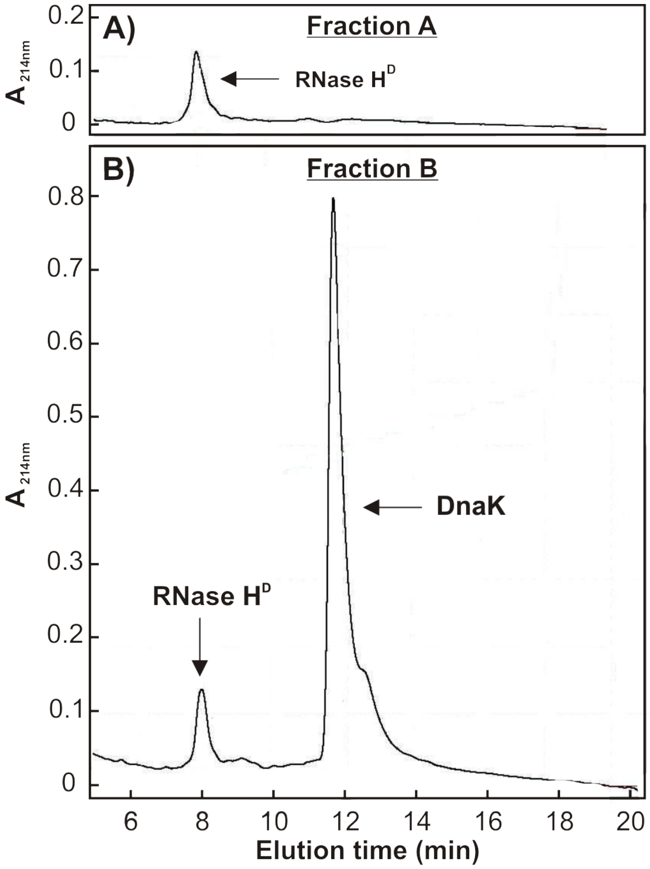

Figure 4.5 Analytical reverse-phase HPLC chromatograms of gel filtration fractions A and B (see Fig. 4.4A and C).

phase HPLC chromatograms of fractions A and B, respectively. Pure RNase H^D elutes at 8 minutes (Fig. 4.5A). The gel filtration DnaK peak (fraction B) for the Figure 4.4C sample, containing RNase H^D refolded in ATP-DnaK and DnaJ, shows a significant amount of RNase H^D in the HPLC chromatogram (Fig. 4.5B). This observation confirms that RNase H^D and DnaK co-elute on the gel filtration column, providing firm evidence for the physical interaction of RNase H^D and DnaK under these conditions, in the absence of GrpE. Similar results are also obtained by SDS-PAGE, as shown in Figure 4.6.

To provide further evidence on chaperone-substrate association in the presence of various chaperone combinations, Figure 4.7 illustrates the reduction in native unbound RNase H^D gel filtration peak intensities. In the presence of only ATP/DnaK or DnaJ, small amounts of complexes are formed. As expected, the extent of complex formation increases significantly in the presence of both ATP-DnaK and DnaJ.

While DnaJ is essential for significant complex formation in the presence of DnaK/ATP, as evidenced by stopped-flow and gel filtration, one may wonder why the DnaJ chaperone is not explicitly observed in the HPLC and SDS-PAGE analysis of fraction B. At least two reasons contribute to this observation. First, the concentration of DnaJ injected on the column is 5-fold smaller than that of DnaK. Second, free DnaJ is known to exist in solution as a heterogeneous oligomeric mixture[48], hence it elutes from the size-exclusion column as a broad peak. Now, HPLC and SDS-PAGE (Figs. 4.5 and 4.6) show that DnaJ in fraction B falls below the detection threshold of these techniques, suggesting that DnaJ, whose presence enhances complex formation with DnaK, does not actually participate in a stable ternary complex between DnaK and

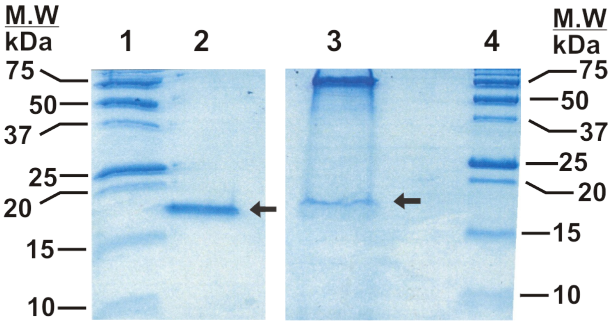

lane 1: Molecular weight standards
lane 2: Fraction A
lane 3: Fraction B
lane 4: Molecular weight standards

Figure 4.6 SDS-PAGE gel analysis of gel filtration fractions A and B (see Fig. 4.4A and C). Prior to running each of the gel fitration fractions through the gel (16.5% Tris-tricine), precipitation with trichloroacetic acid (TCA) was carried out to effectively concentrate the samples for SDS-PAGE analysis. The arrows indicate bands corresponding to RNase H^D.

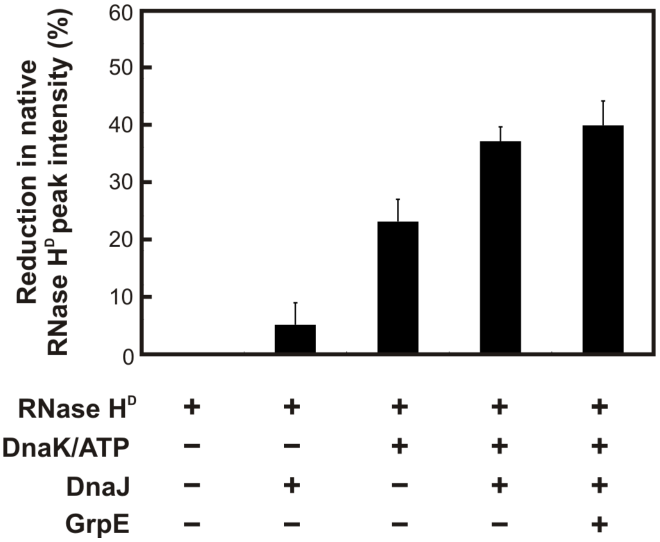

Figure 4.7 Extent of complex formation between RNase H^D and the DnaK chaperone measured by gel filtration as the reduction in native RNase H^D peak intensity. Error bars correspond to ±1 standard error, derived from 2 – 7 independent measurements.

RNase H^D. The simplest interpretation of this result is that DnaJ dissociates from the ternary complex once RNase H^D has achieved stable binding to DnaK. This observation is entirely consistent with the known catalytic role of DnaJ in the Hsp70 chaperone cycle[49].

Gel filtration reveals the presence of DnaK-RNase H^D interactions even in the presence of GrpE (Fig. 4.7). This is likely an artifact resulting from ATP depletion in the refolding buffer prior to complete release of all chaperone-bound RNase H^D, which occurs rapidly because of the high chaperone concentrations in the gel filtration sample. This idea is supported by computer simulations (see below). In addition, the spatio-temporal separation of DnaK-RNase H^D complexes from both GrpE and ATP on the gel filtration column may render GrpE unable to release the bound substrate during the course of the gel filtration run, contributing to the observed result.

RNase activity assays further support the presence of a substrate complex with K/J, upon refolding RNase H^D in the absence of GrpE. In order to directly assess the effect of molecular chaperones on the production of free, bioactive RNase H^D, we performed RNase H^D activity assays [23] immediately after refolding in the absence or presence of different molecular chaperones (Fig. 4.8A). This assay is based on the spectrophotometric monitoring of the cleavage of RNA-DNA hybrids by native RNase H^D. Activity assays were carried out in the presence of excess RNA-DNA hybrid to ensure that the initial reaction rate is directly proportional to the amount of native RNase H^D. Figure 4.8A shows the enzymatic activity of RNase H^D refolded in the absence/presence of chaperones, expressed as a percent of the activity observed when chaperones are absent. Hence, the y-axis of Figure 4.8A is a direct measure of the

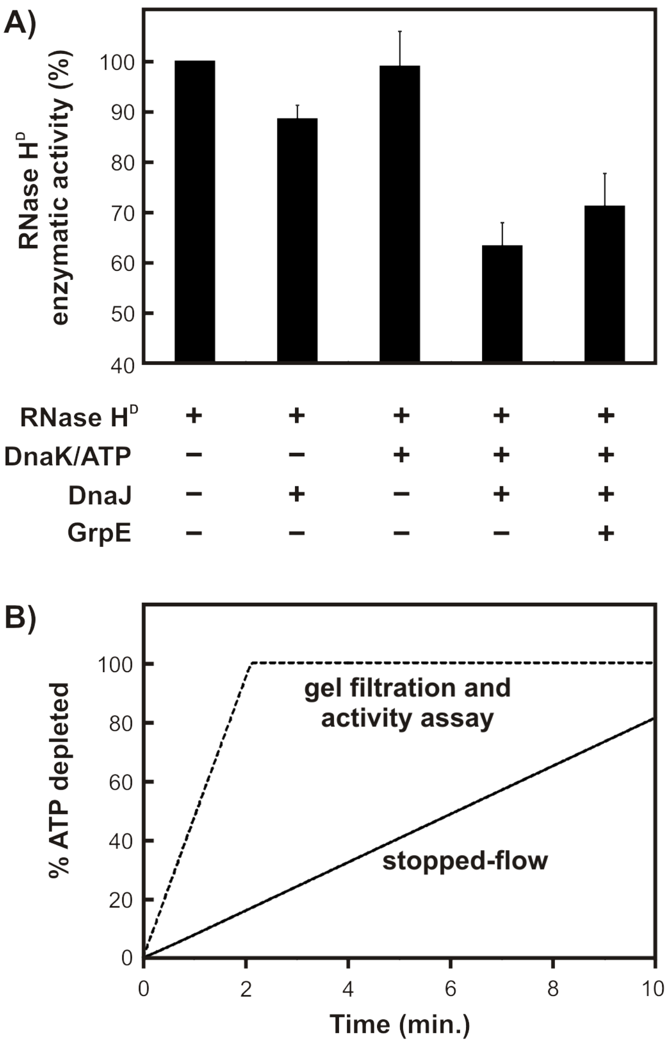

RNase H^D	+	+	+	+	+
DnaK/ATP	−	−	+	+	+
DnaJ	−	+	−	+	+
GrpE	−	−	−	−	+

Figure 4.8 A) Enzymatic activity of RNase H^D performed after 10 min from refolding initiation, in the presence of different combinations of chaperones. Data are shown as percent of the activity of a control RNase H^D sample refolded in the absence of chaperones. Error bars represent ± 1 standard error of the mean, calculated from three independent measurements. B) Computer simulations predicting the expected ATP depletion as a function of time under the stopped-flow and gel filtration/activity assay experimental conditions. The refolding time in the stopped-flow experiments is 160 s,

while the refolding time in the gel filtration and activity assays is 10 min. The spatial separation of the solution components during gel filtration experiments may introduce additional effects (not taken into account in this simulation).

fraction of bioactive RNase H^D under different chaperone environments.

In the presence of only DnaJ or DnaK/ATP, RNase H^D essentially folds to completion as observed from the > 90% enzymatic activity. Hence there is no chaperone-substrate complex at equilibrium, after refolding is complete. As discussed above, the observed small kinetic retardation under these conditions is consistent with the presence of only rapid and transient interactions between substrate and chaperones, upon substrate refolding under these conditions.

However, when both DnaK and DnaJ are present, only 65% of the RNase H^D molecules fold to the bioactive native state. This result is consistent with the fact that the remaining 35% of RNase H^D molecules are sequestered as a chaperone complex, consistent with the gel-filtration and HPLC analysis. Hence, several internally consistent experimental observations concur in showing that there is a substantial extent of persistent complex formation when RNase H^D folds in the presence of DnaK, DnaJ and ATP, in the absence of GrpE.

Addition of GrpE to the chaperone mixture releases a part of the DnaK-substrate complexes, resulting in an increase of enzymatic activity to ca. 70%. The fact that substrate release is incomplete under these conditions is likely due to the depletion of ATP during the 10 min refolding time used in the assay. Once ATP is hydrolyzed to ADP, GrpE loses its ability to release DnaK-bound RNase H^D, explaining the lower-than-expected enzymatic activity. This concept is supported by the computer simulation of ATP consumption shown in Figure 4.8B, carried out with a recently developed computational model for protein folding in the presence of the K/J/E chaperone system (Sekhar, Lam and Cavagnero, submitted). This simulation shows that virtually all the

ATP is hydrolyzed within the first three minutes of preincubation, under the experimental conditions used in the gel filtration and activity assay experiments. In contrast, most of the ATP is available in the stopped-flow experiments during the 160 s refolding time, enabling complete substrate release and folding. The key difference between the stopped-flow and gel filtration/activity assay experimental conditions, responsible for the faster ATP hydrolysis in the case of gel filtration/activity assays, is that gel filtration and activity assays were run with a ~ 5-fold larger chaperone concentration than the stopped-flow experiments.

4.4 Discussion

The effect of the K/J/E chaperones on protein folding kinetics is highly substrate-dependent. RNase H^D is a 2-state slow-folding protein capable of attaining its native state independently, i.e., in the absence of molecular chaperones. This study compares the apparent folding rates of RNase H^D in the absence and presence of the K/J/E molecular chaperones, to gain insights into the potential role of these chaperones in the cellular environment. We show that the K/J/E chaperone system interacts transiently with the *E.coli* single-domain protein RNase H^D while it folds to the native state. This interaction slightly decreases the observed folding rate of this protein. Our observation is consistent with a prior report showing retardation in the folding of a large multi-domain maltose binding protein (MBP) variant in the presence of K/J/E[50]. However, while MBP is a large multi-domain protein, RNase H is a smaller client composed of only one domain. Our studies, which demonstrate transient interactions between K/J/E and a single-domain protein on its way to the native state, are important because single-domain proteins account for ~70% of the *E.coli* proteome[51].

Taken together, our experimental results on RNase H^D and previously published data on maltose binding protein and luciferase establish that the kinetic effect of K/J/E on protein folding is highly substrate-dependent. Not all slow-folding client proteins are accelerated by K/J/E, even though they may extensively interact with the chaperone system before folding to the native state.

It still remains unclear what specific substrate characteristics (primary / secondary structure, tertiary fold, folding pathways etc.) prompt the K/J/E catalytic refolding activity. On one hand, it is possible that K/J/E is particularly efficient at rescuing substrate proteins from kinetic traps in their folding energy landscape, as in the case of firefly luciferase [22] by actively unfolding misfolded substrates and allowing them additional chances to undergo folding. On the other hand, acceleration in protein folding may depend on the extent of conformational search that a substrate can accomplish while bound to DnaK. In this context, proteins with several properly positioned hydrophobic residues may fold faster in the presence of K/J/E because they undergo a more rapid diffusion across the folding energy landscape while bound to the DnaK chaperone.

The DnaK chaperone interacts transiently with partially unfolded RNase H^D, under substrate refolding conditions. Intriguingly, the burst-phase fraction η_B data indicate that interaction with chaperone is accompanied by smaller client secondary structure (at comparable time-points) than client folding in the absence of chaperones. This result suggests that the transient interaction with chaperone effectively retards structure formation and, in so-doing, it maintains the substrate in a conformational state that may be particularly appropriate to support proper folding.

The existence of a predominantly unfolded DnaK-bound substrate conformation is entirely consistent with prior studies at equilibrium focusing on complexes between N-terminal protein fragments and the substrate-binding domain of DnaK[19, 52]. However, no prior investigations addressed the transiently chaperone-bound conformation of folding-competent protein clients on their way to the native state.

Transient substrate-chaperone interactions may serve important biological roles. Our stopped-flow and gel filtration experiments show significant interactions between folding RNase H^D and chaperones under conditions where the interaction is kinetically trapped (i.e., K/J conditions, see Figs. 4.2, 4.4, 4.5 and 4.6). Our results also show that in the presence of the complete chaperone system (K/J/E experiment), i.e., under the most physiologically relevant conditions for a healthy cell, folding is slowed down only moderately (Fig. 4.2A) and there is no significant substrate-chaperone complex at the end of the folding process. This result is consistent with the presence of only transient interactions between substrate and K/J/E.

The most important biological consequence of a transient association is that chaperone-substrate interactions do not slow down protein folding significantly. Folding to the native conformation is usually a pre-requisite for the biological function of a protein. From a cellular perspective, it is thus disadvantageous for K/J/E to significantly slow down protein folding, particularly for proteins that can fold efficiently even in the absence of interaction with chaperones. From our results, it appears that the kinetics of the K/J/E chaperone system is tuned to maximize chaperone-substrate interactions while maintaining a reasonable rate of native protein production.

The transient nature of chaperone-substrate interactions also facilitates the recycling of DnaK, DnaJ and GrpE, likely preserving the bioavailability of these chaperones in the cellular context. Finally, transient chaperone-substrate interactions may be important for the ability of Hsp70 to prevent the aggregation that has been observed in previous studies on a different substrate [52].

The transient association observed under physiological conditions is in interesting contrast with the biological scenario under heat-shock conditions. At 42°C, GrpE is inactivated by reversible unfolding[53], generating effective K/J-only conditions and leading to the kinetic trapping of the substrate within the DnaK binding pocket. Chaperone-substrate interactions are known to be more persistent under heat shock conditions, explaining the need to upregulate the DnaK concentration at 42°C, given the higher propensity for misfolding and aggregation at this temperature.

Mechanistic considerations on the role of the K/J/E chaperone system on slow-folding proteins such as RNase H^D. Interaction with the K/J/E chaperone system slows down the apparent refolding of the RNase H^D. Therefore, the catalytic acceleration of folding detected for some large multi-domain proteins unable to fold independently is not a general feature of the K/J/E chaperone system. The measurements with RNase H^D suggest that a simple kinetic partitioning model[54,55] for protein folding in the presence of the K/J/E chaperone system is sufficient to account for our experimental findings. We are currently carrying out additional studies to specifically address the role of kinetic partitioning for the K/J/E interaction with 2-state-folding proteins exhibiting different intrinsic folding rates and thermodynamic stability.

Consistent with this hypothesis, low resolution EPR distance measurements[56] showed that substrate conformation is identical when bound to ATP-, ADP- and NF-DnaK. Thus, ATP-binding and hydrolysis do not appear to be coupled to conformational work performed on the chaperone-associated client substrate at the DnaK binding site. The authors of this studies argued that this observation provides support for a kinetic partitioning mechanism [56]. Additional studies are clearly necessary to provide more direct evidence for kinetic partitioning of client proteins between folding and chaperone-binding routes.

From a kinetic standpoint, our measurements are consistent with a simple holdase[57] mechanism for K/J/E activity in the case of RNase H^D. On the other hand, our results do not exclude that the folding of a fraction of the substrate molecules may be accelerated by K/J/E. However, either the fraction of molecules or the relative increase in folding rate (or both) is not sufficiently large to be detected as a separate stopped-flow kinetic phase. The consistency of our results with a kinetic partitioning mechanism does not conflict with K/J/E-induced conformational changes in the substrate at the molecular level. The final (η_F) ellipticity fraction, together with evidence from activity assays, indicate that RNase H^D binds chaperones in a predominantly unfolded conformation. This observation is not incompatible with the unfoldase activity [57] of K/J/E observed in its interaction with a luciferase variant[58]. However, given that we are unable to assess the conformation of the unfolded substrate under refolding conditions before it binds the chaperones, our data alone are unable to either support or disprove any unfoldase activity by the K/J/E chaperone system.

4.5 Conclusions

This study shows that RNase H^D interacts significantly with DnaK (and its co-chaperones DnaJ and GrpE) on its way to the native state, that RNase H^D is at least partially unfolded upon its interaction with DnaK, and that the chaperone-substrate interaction retards the timescale of RNase H^D folding only slightly, under physiologically relevant (non-heat-shock) conditions. Our findings have three major biological implications.

First, the transient, nature of chaperone-substrate interactions ensures that the production of a bioactive native protein like RNase H^D, which does not need the chaperone to fold, is not substantially slowed down by the interaction with the K/J/E chaperones. This result suggests that the cellular function of slow-folding non-obligatory clients, binding K/J/E on their way to the native state, is not significantly perturbed by interaction with the K/J/E chaperone system. It is conceivable to propose that this conclusion may apply to an even greater extent to the folding of faster-folding substrates, which are likely to interact with the K/J/E system even less.

Second, the existence of transient substrate-chaperone association ensures that the effective concentration of chaperone-free unfolded or partially folded substrate is substantially decreased by the K/J/E chaperone system during protein folding, thereby reducing opportunities for misfolding and aggregation.

Acknowledgments

We thank Bernd Bukau and Matthias Mayer for chaperone cell lines, plasmids, the luciferase refolding assay protocol, and for helpful discussions. In addition, we are grateful to Jochen Reinstein for assistance with the DnaK purification procedure, and to Susan Marqusee for providing the RNase H^D-encoding plasmid and the RNase H^D purification protocol. We thank Anders Knight, Neşe Kurt and Rudy Clausen for a critical reading of the manuscript. This research was funded by grants NIH GM068538 and NSF MCB0951209.

4.6 References

(1) Mayer, M. P.; Brehmer, D.; Gässler, C. S.; Bukau, B. Hsp70 Chaperone Machines. *Adv. Protein Chem.* **2001**, *59*, 1-12.

(2) Hartl, F. U.; Hayer-Hartl, M. Molecular Chaperones in the Cytosol: From Nascent Chain to Folded Protein. *Science* **2002**, *295*, 1852-1858.

(3) Frydman, J. Folding of Newly Translated Proteins *in Vivo*: The Role of Molecular Chaperones. *Annu. Rev. Biochem* **2001**, *70*, 603-647.

(4) Mayer, M. P.; Rudiger, S.; Bukau, B. Molecular Basis for Interactions of the DnaK Chaperone with Substrates. *Biol. Chem.* **2000**, *381*, 877-885.

(5) Rüdiger, S.; Germeroth, L.; Schneider-Mergener, J.; Bukau, B. Substrate Specificity of the DnaK Chaperone Determined by Screening Cellulose-Bound Peptide Libraries. *EMBO J.* **1997**, *16*, 1501-1507.

(6) Mayer, M. P.; Bukau, B. Hsp70 Chaperones: Cellular Functions and Molecular Mechanism. *Cell. Mol. Life Sci.* **2005**, *62*, 670-684.

(7) Schmid, D.; Baici, A.; Gehring, H.; Christen, P. Kinetics of Molecular Chaperone Action. *Science* **1994**, *263*, 971-973.

(8) Chesnokova, L. S.; Slepenkov, S. V.; Protasevich, II; Sehorn, M. G.; Brouillette, C. G.; Witt, S. N. Deletion of DnaK's Lid Strengthens Binding to the Nucleotide Exchange Factor, GrpE: A Kinetic and Thermodynamic Analysis. *Biochemistry* **2003**, *42*, 9028-9040.

(9) Russell, R.; Jordan, R.; McMacken, R. Kinetic Characterization of the ATPase Cycle of the DnaK Molecular Chaperone†. *Biochemistry* **1998**, *37*, 596-607.

(10) Mayer, M. P.; Schröder, H.; Rüdiger, S.; Paal, K.; Laufen, T.; Bukau, B. Multistep Mechanism of Substrate Binding Determines Chaperone Activity of Hsp70. *Nat. Struct. Mol. Biol.* **2000**, *7*, 586-593.

(11) Pierpaoli, E. V.; Gisler, S. M.; Christen, P. Sequence-Specific Rates of Interaction of Target Peptides with the Molecular Chaperones DnaK and DnaJ. *Biochemistry* **1998**, *37*, 16741-16748.

(12) Szabo, A.; Langer, T.; Schröder, H.; Flanagan, J.; Bukau, B.; Hartl, F. U. The ATP Hydrolysis-Dependent Reaction Cycle of the *Escherichia Coli* Hsp70 System DnaK, DnaJ, and GrpE. *Proc. Natl. Acad. Sci. U.S.A.* **1994**, *91*, 10345-10349.

(13) Han, W.; Christen, P. Mechanism of the Targeting Action of DnaJ in the DnaK Molecular Chaperone System. *J. Biol. Chem.* **2003**, *278*, 19038-19043.

(14) Laufen, T.; Mayer, M. P.; Beisel, C.; Klostermeier, D.; Mogk, A.; Reinstein, J.; Bukau, B. Mechanism of Regulation of Hsp70 Chaperones by DnaJ Cochaperones. *Proc. Natl. Acad. Sci. U.S.A.* **1999**, *96*, 5452-5457.

(15) Packschies, L.; Theyssen, H.; Buchberger, A.; Bukau, B.; Goody, R. S.; Reinstein, J. GrpE Accelerates Nucleotide Exchange of the Molecular Chaperone DnaK with an Associative Displacement Mechanism. *Biochemistry* **1997**, *36*, 3417-3422.

(16) Siegenthaler, R. K.; Christen, P. Tuning of DnaK Chaperone Action by Nonnative Protein Sensor DnaJ and Thermosensor GrpE. *J. Biol. Chem.* **2006**, *281*, 34448-34456.

(17) Shi, L.; Kataoka, M.; Fink, A. L. Conformational Characterization of DnaK and Its Complexes by Small-Angle X-Ray Scattering. *Biochemistry* **1996**, *35*, 3297-3308.

(18) Chen, Z.; Kurt, N.; Rajagopalan, S.; Cavagnero, S. Secondary Structure Mapping of DnaK-Bound Protein Fragments: Chain Helicity and Local Helix Unwinding at the Binding Site. *Biochemistry* **2006**, *45*, 12325-12333.

(19) Kurt, N.; Cavagnero, S. Nonnative Helical Motif in a Chaperone-Bound Protein Fragment. *Biophys. J.* **2008**, *94*, L48-L50.

(20) Schröder, H.; Langer, T.; Hartl, F. U.; Bukau, B. DnaK, DnaJ and GrpE Form a Cellular Chaperone Machinery Capable of Repairing Heat-Induced Protein Damage. *EMBO J.* **1993**, *12*, 4137-4144.

(21) Herbst, R.; Schäfer, U.; Seckler, R. Equilibrium Intermediates in the Reversible Unfolding of Firefly (*Photinus Pyralis*) Luciferase. *J. Biol. Chem.* **1997**, *272*, 7099-7105.

(22) Herbst, R.; Gast, K.; Seckler, R. Folding of Firefly (*Photinus Pyralis*) Luciferase: Aggregation and Reactivation of Unfolding Intermediates. *Biochemistry* **1998**, *37*, 6586-6597.

(23) Spudich, G. M.; Miller, E. J.; Marqusee, S. Destabilization of the *Escherichia Coli* Rnase H Kinetic Intermediate: Switching between a Two-State and Three-State Folding Mechanism. *J. Mol. Biol.* **2004**, *335*, 609-618.

(24) Dabora, J. M.; Marqusee, S. Equilibrium Unfolding of *Escherichia Coli* Ribonuclease H: Characterization of a Partially Folded State. *Protein Sci.* **1994**, *3*, 1401-1408.

(25) Buchberger, A.; Valencia, A.; McMacken, R.; Sander, C.; Bukau, B. The Chaperone Function of DnaK Requires the Coupling of ATPase Activity with Substrate Binding through Residue E171. *EMBO J.* **1994**, *13*, 1687-1695.

(26) Theyssen, H.; Schuster, H. P.; Packschies, L.; Bukau, B.; Reinstein, J. The Second Step of ATP Binding to DnaK Induces Peptide Release. *J. Mol. Biol.* **1996**, *263*, 657-670.

(27) Klostermeier, D.; Seidel, R.; Reinstein, J. Functional Properties of the Molecular Chaperone DnaK from *Thermus Thermophilus*. *J. Mol. Biol.* **1998**, *279*, 841-853.

(28) Zylicz, M.; Yamamoto, T.; McKittrick, N.; Sell, S.; Georgopoulos, C. Purification and Properties of the DnaJ Replication Protein of *Escherichia Coli*. *J. Biol. Chem.* **1985**, *260*, 7591-7598.

(29) Buchberger, A.; Theyssen, H.; Schröder, H.; McCarty, J. S.; Virgallita, G.; Milkereit, P.; Reinstein, J.; Bukau, B. Nucleotide-Induced Conformational Changes in the ATPase and Substrate Binding Domains of the DnaK Chaperone Provide Evidence for Interdomain Communication. *J. Biol. Chem.* **1995**, *270*, 16903-16910.

(30) Linke, K.; Wolfram, T.; Bussemer, J.; Jakob, U. The Roles of the Two Zinc Binding Sites in DnaJ. *J. Biol. Chem.* **2003**, *278*, 44457-44466.

(31) Rodriguez, F.; Arsène-Ploetze, F.; Rist, W.; Rüdiger, S.; Schneider-Mergener, J.; Mayer, M. P.; Bukau, B. Molecular Basis for Regulation of the Heat Shock Transcription Factor by the DnaK and DnaJ Chaperones. *Mol. Cell* **2008**, *32*, 347-358.

(32) Schönfeld, H. J.; Schmidt, D.; Schröder, H.; Bukau, B. The DnaK Chaperone System of *Escherichia Coli*: Quaternary Structures and Interactions of the DnaK and GrpE Components. *J. Biol. Chem.* **1995**, *270*, 2183-2189.

(33) Raschke, T. M.; Kho, J.; Marqusee, S. Confirmation of the Hierarchical Folding of Rnase H: A Protein Engineering Study. *Nat. Struct. Biol.* **1999**, *6*, 825-830.

(34) Russell, R.; Karzai, A. W.; Mehl, A. F.; McMacken, R. DnaJ Dramatically Stimulates ATP Hydrolysis by DnaK: Insight into Targeting of Hsp70 Proteins to Polypeptide Substrates. *Biochemistry* **1999**, *38*, 4165-4176.

(35) Silberg, J. J.; Hoff, K. G.; Vickery, L. E. The Hsc66-Hsc20 Chaperone System in *Escherichia Coli*: Chaperone Activity and Interactions with the DnaK-DnaJ-GrpE System. *J. Bacteriol.* **1998**, *180*, 6617-6624.

(36) Levenberg, K. A Method for the Solution of Certain Nonlinear Problems in Least Squares. *Quart. Appl. Math* **1944**, *2*, 164–168.

(37) Marquardt, D. W. An Algorithm for Least-Squares Estimation of Nonlinear Parameters. *J. Soc. Ind. Appl. Math.* **1963**, *11*, 431-441.

(38) More, J. The Levenberg-Marquardt Algorithm: Implementation and Theory. *Lecture Notes in Mathematics* **1978**, *630*, 105-116.

(39) Wojdyr, M. Fityk: A General-Purpose Peak Fitting Program. *J. Appl. Crystallogr.* **2010**, *43*, 1126-1128.

(40) Keck, J. L.; Marqusee, S. Substitution of a Highly Basic Helix/Loop Sequence into the Rnase H Domain of Human Immunodeficiency Virus Reverse Transcriptase Restores Its Mn^{2+}-Dependent Rnase H Activity. *Proc. Natl. Acad. Sci. U.S.A.* **1995**, *92*, 2740-2744.

(41) Walpole, R. E.; Myers, R. H.; Myers, S. L.; Ye, K. *Probability and Statistics for Engineers and Scientists*; Eighth ed.; Pearson Prentice Hall: New Jersey, 2007.

(42) Bogatyreva, N. S.; Osypov, A. A.; Ivankov, D. N. KineticDB: A Database of Protein Folding Kinetics. *Nucleic Acids Res.* **2009**, *37*, D342-D346.

(43) Gamer, J.; Multhaup, G.; Tomoyasu, T.; McCarty, J. S.; Rüdiger, S.; Schönfeld, H. J.; Schirra, C.; Bujard, H.; Bukau, B. A Cycle of Binding and Release of the DnaK, DnaJ and GrpE Chaperones Regulates Activity of the *Escherichia Coli* Heat Shock Transcription Factor Sigma32. *EMBO J.* **1996**, *15*, 607-617.

(44) Palleros, D. R.; Shi, L.; Reid, K. L.; Fink, A. L. Hsp70-Protein Complexes. Complex Stability and Conformation of Bound Substrate Protein. *J. Biol. Chem.* **1994**, *269*, 13107-13114.

(45) Swain, J. F.; Schulz, E. G.; Gierasch, L. M. Direct Comparison of a Stable Isolated Hsp70 Substrate-Binding Domain in the Empty and Substrate-Bound States. *J. Biol. Chem.* **2006**, *281*, 1605-1611.

(46) Swain, J. F.; Dinler, G.; Sivendran, R.; Montgomery, D. L.; Stotz, M.; Gierasch, L. M. Hsp70 Chaperone Ligands Control Domain Association Via an Allosteric Mechanism Mediated by the Interdomain Linker. *Mol. Cell* **2007**, *26*, 27-39.

(47) Rüdiger, S.; Schneider-Mergener, J.; Bukau, B. Its Substrate Specificity Characterizes the DnaJ Co-Chaperone as a Scanning Factor for the DnaK Chaperone. *EMBO J.* **2001**, *20*, 1042-1050.

(48) Schönfeld, H. J.; Schmidt, D.; Zulauf, M. Investigation of the Molecular Chaperone DnaJ by Analytical Ultracentrifugation. *Analytical Ultracentrifugation* **1995**, *99*, 7-10.

(49) Pierpaoli, E. V.; Sandmeier, E.; Schönfeld, H. J.; Christen, P. Control of the DnaK Chaperone Cycle by Substoichiometric Concentrations of the Co-Chaperones DnaJ and GrpE. *J. Biol. Chem.* **1998**, *273*, 6643.

(50) Tang, Y. C.; Chang, H. C.; Roeben, A.; Wischnewski, D.; Wischnewski, N.; Kerner, M. J.; Hartl, F. U.; Hayer-Hartl, M. Structural Features of the GroEL-GroES Nano-Cage Required for Rapid Folding of Encapsulated Protein. *Cell* **2006**, *125*, 903-914.

(51) Ekman, D.; Björklund, Å.; Frey-Skött, J.; Elofsson, A. Multi-Domain Proteins in the Three Kingdoms of Life: Orphan Domains and Other Unassigned Regions. *J. Mol. Biol.* **2005**, *348*, 231-243.

(52) Kurt, N.; Rajagopalan, S.; Cavagnero, S. Effect of Hsp70 Chaperone on the Folding and Misfolding of Polypeptides Modeling an Elongating Protein Chain. *J. Mol. Biol.* **2006**, *355*, 809-820.

(53) Grimshaw, J.; Jelesarov, I.; Schonfeld, H. J.; Christen, P. Reversible Thermal Transition in GrpE, the Nucleotide Exchange Factor of the DnaK Heat-Shock System. *J. Biol. Chem.* **2001**, *276*, 6098-6104.

(54) Flynn, G. C.; Pohl, J.; Flocco, M. T.; Rothman, J. E. Peptide-Binding Specificity of the Molecular Chaperone BiP. *Nature* **1991**, 353, 726-730.

(55) Randall, L. L.; Hardy, S. J. S. SecB, One Small Chaperone in the Complex Milieu of the Cell. *Cell. Mol. Life Sci.* **2002**, *59*, 1617-1623.

(56) Popp, S.; Packschies, L.; Radzwill, N.; Vogel, K. P.; Steinhoff, H. J.; Reinstein, J. Structural Dynamics of the DnaK-Peptide Complex. *J. Mol. Biol.* **2005**, *347*, 1039-1052.

(57) Slepenkov, S. V.; Witt, S. The Unfolding Story of the Escherichia Coli Hsp70 DnaK: Is DnaK a Holdase or an Unfoldase? *Mol. Microbiol.* **2002**, *45*, 1197-1206.

(58) Sharma, S. K.; De Los Rios, P.; Christen, P.; Lustig, A.; Goloubinoff, P. The Kinetic Parameters and Energy Cost of the Hsp70 Chaperone as a Polypeptide Unfoldase. *Nat. Chem. Biol.* **2010**, *6*, 914-920.

(59) Goedken, E. R.; Keck, J. L.; Berger, J. M.; Marqusee, S. Divalent Metal Cofactor Binding in the Kinetic Folding Trajectory of Escherichia Coli Ribonuclease HI. *Protein Sci*. **2000**, *9*, 1914-1921.

Chapter 5

Conformational Changes of the drkN SH3 Protein upon Interaction with the Hsp70 Molecular Chaperone

Abstract

The molecular details underlying the conformational changes experienced by protein substrates upon interaction with the Hsp70 chaperone are important to gaining key insights into protein folding, aggregation and degradation in the cell. Most Hsp70-substrate interaction studies, however, have focused on small peptide substrates rather than proteins, and on the substrate binding domain (SBD) of Hsp70 rather than the full-length chaperone. Given that the function of Hsp70 involves folded and unfolded protein states, it is ideal to focus on a substrate that enables analysis of both of these coexisting states. Here, multidimensional NMR and native gel analysis are performed to monitor the effect of ADP-bound DnaK (the *E. coli* Hsp70) on the drkN SH3 protein substrate, which slowly exchanges between the folded and unfolded states on the NMR chemical shift timescale. When drkN SH3 and DnaK are present in the sample, the translational diffusion of both the folded and unfolded states of SH3 is decelerated, suggesting an interaction of both states with the chaperone. No major changes in substrate conformation are detected in the presence of the chaperone. Finally, to account for the overall undetectability of folded SH3 population in the presence of chaperone, we propose that some NMR-invisible, possibly Hsp70-bound “dark” states are populated.

5.1 Introduction

Molecular chaperones interact with various states of proteins to guide their correct folding and turnover.[1] Chaperones are known to assist both co- and post-translational protein folding, and are overexpressed under various stress-inducing conditions to help maintain protein homeostasis.[2] Even under non-stress conditions, molecular chaperones interact with approximately 30% of the total protein population, reflecting the importance of chaperones in protein quality control.[3]

The Hsp70 molecular chaperones are ~70 kDa proteins that are always present in healthy cells and become overexpressed under stress conditions. Hsp70 chaperones play a central role in protein folding, disaggregation, and degradation.[4] They cooperate with co-translationally active chaperones to help nascent protein folding, and channel the misfolded or aggregated proteins to downstream folding- and degradation-related machines. Consistent with the crucial functions of chaperones, Hsp70 also has diverse connections with disease. For instance, Hsp70 overproduction is known to be involved in the development of multiple types of cancer by inhibiting apoptotic pathways.[5] In addition, pilot studies have shown that enhanced Hsp70 chaperone activity positively affects the course of neurodegenerative disorders.[6]

The Hsp70 chaperone consists of an N-terminal ~45 kDa nucleotide binding domain (NBD) with ATPase activity, a C-terminal ~25 kDa substrate binding domain (SBD) that directly interacts with the substrate molecules, and a flexible linker that connects the two N- and C-terminal domains. The different nucleotide-bound states of Hsp70 interact with other chaperones and co-chaperones to help maintain a correctly folded pool of proteins. While the ATP-bound state of DnaK has minimal substrate-binding affinity, the ADP- and nucleotide-free states of this chaperone have considerable affinity for peptide and protein substrates.[4]

It is well known that the Hsp70 chaperone adopts different conformations in its nucleotide-free, ADP- and ATP-bound states.[4,7] However, very little is known about the conformational changes undergone by the substrate upon interaction with the chaperone. X-ray,[8] NMR,[9-11] and EPR[11] studies showed that short peptides adopt an extended conformation upon binding to the substrate-binding-domain (SBD) or the full-length Hsp70 chaperone. In addition, when apomyoglobin N-terminal fragments bind the SBD of Hsp70, native and nonnative helical structures that resemble the acid-unfolded full-length apomyoglobin are generated.[12] Regarding other chaperones, X-ray studies have shown that a polypeptide binds to truncated GroEL chaperonin in a extended conformation.[13] In addition, p53 adopts a molten-globular state upon interaction with Hsp90 chaperone as studied by NMR.[14] Most of the studies involve protein fragments and peptides binding to the truncated form of chaperones. Yet, analysis of the interaction between full-length native proteins and full-length Hsp70 is crucial.[15]

While it is generally accepted that Hsp70 binds unfolded proteins,[8,16] other reports hint at the fact that chaperones may directly interact with folded substrates.[17,18] In addition, since the function of Hsp70 is related to the interconversion between different substrate states, studies on how Hsp70 interacts with both folded and unfolded substrates are important to understand Hsp70 function.

In this work, we investigate how full-length ADP-bound DnaK (ADP-DnaK) interacts with the full-length drkN SH3 protein client by multidimensional NMR spectroscopy. DnaK is the *E. coli* Hsp70. ADP-DnaK has high affinity and slow exchange rates with its substrates,[4] facilitating the study of DnaK-induced substrate conformational changes by NMR.

The substrate protein is the N-terminal domain of the *Drosophila melanogaster* adaptor protein drk (drkN SH3),[19] which slowly exchanges between folded and unfolded states on the NMR chemical shift timescale, enabling observation of NMR resonances arising from both states. drkN SH3 also possess a strong DnaK local binding site.[20] Our experimental results suggest that both folded and unfolded states of SH3 may be associated with DnaK while the overall substrate conformation is generally preserved. Both states maintain significant rotational freedom while associated with DnaK. In addition, highly-populated NMR-invisible “dark states”,[21] presumably heavily associated with Hsp70, are also likely present.

5.2 Experimental Methods

Protein Expression and Purification

DnaK The DnaK gene sequence was cloned into a N-terminal His-SUMO tag plasmid using Champion™ pET SUMO Expression System (Invitrogen, Carlsbad, CA), to express His-SUMO-DnaK protein. The plasmid was transformed into BL21 (DE3)-RIPL competent cells (Agilent Technologies, Palo Alto, CA, USA) and grown in 2L standard LB broth containing 50µg/mL kanamycin. Overexpression of the protein was induced by addition of isopropyl-ß-thiogalactoside (0.5mM) at an OD600 of 0.8. Cells were harvested after 24 hours of shaking incubation at 25°C. The cell pellet was resuspended in lysis buffer (30 mM potassium phosphate, 500 mM NaCl, 30 mM imidazole, pH 7.4) and lysed by sonication. Supernatant was collected after 30 min centrifugation at 15,000 rpm.

The supernatant was initially applied to a HisTrap HP column (5 x 1mL; GE Healthcare, Piscataway, NJ) and eluted with 30 mM potassium phosphate, 500 mM NaCl, 500 mM imidazole, pH 7.4 buffer. After dialysis against 50 mM Tris-HCl, 150 mM KCl, 1 mM DTT, pH 7.4 buffer, His-tagged SUMO protease (10,000u; MCLAB, South San Francisco, CA) was added and incubated for 12 hours at room temperature. The flow-through (which contains native DnaK) was collected upon applying the sample to the HisTrap HP column (5 x 1mL). The flow-through was reapplied to a cleaned HisTrap HP column (5 x 1mL) to insure that no His-tagged proteins are in the final flow-through. This final fraction was concentrated, dialyzed against 50mM Tris-HCl, 5mM $MgCl_2$, 50mM KCl, pH 7.2 buffer, flash frozen in liquid N_2 and stored at -80°C.

SH3 SH3 was expressed and purified using the same protocol as in Chapter 2. Note that only SH3 protein is isotope-enriched.

GrpE GrpE was expressed and purified using the same protocol as in Chapter 4.

NMR Experiments

All NMR experiments were performed on a Varian 600 MHz spectrometer equipped with a triple resonance $^{1}H\{^{13}C,^{15}N\}$ triple axis gradient cryogenic probe. All experiments were carried out at 25°C.

NMR sample preparation The SH3 only NMR sample was prepared by adding 100μM or 300μM of SH3 to 50mM Tris-HCl, 5mM $MgCl_2$, 50mM KCl, 5 mM ADP, and 15 mM DTT in 95%/5% H_2O/D_2O. For making NMR sample containing both SH3 and DnaK, 4-fold stoichiometric excess of DnaK compared to SH3 (400μM or 1200μM, respectively) was added to the above composition. In the latter case, further treatment to remove any effect from aggregated species (supposedly from pre-bound substrates that are released from DnaK by SH3; see Fig. 5A.1) was performed. Briefly, after 24 hours of incubation of the SH3 + DnaK sample at room temperature, supernatants after ultracentrifugation at 115,000 rpm (TLA-120.1 rotor, Beckman Coulter, Fullerton, CA) for 30 min were collected for NMR experiments.

SH3 backbone assignment 3D HNCACB and 3D CBCA(CO)NH experiments were employed to use C^{α} and C^{β} chemical shifts for inter-residue connections. In addition, 3D HNCO and 3D (HCA)CO(CA)NH experiments were employed to use CO chemical shifts for inter-residue connections. N_z exchange ^1H-^{15}N HSQC was performed to link the folded and unfolded amides to verify the backbone assignment (Fig. 5A.2). Note that the backbone assignment was performed at pH 7.2 and 25 °C.[19]

Diffusion ordered spectroscopy (DOSY) In order to rule out the effect of convection in the NMR sample tube during DOSY experiments, convection-compensated diffusion experiments were carried out.[22] The convection-compensated (cc) DOSY element was attached in front of the ^1H-^{15}C HSQC sequence to discriminate diffusion rates between the folded and unfolded SH3 resonances (Fig. 5.3a). Alanine methyl groups were used as diffusion probes, where the 3D HBHA(CO)NH in addition to the backbone assignment experiments gave methyl assignments for the five alanines in SH3. Sweep widths of 10,000Hz and 2,000Hz were employed for the direct and indirect dimensions, respectively. 32 rows were collected in the indirect dimension. Cosine-bell-squared apodization function was applied to both direct and indirect dimensions. In addition, the cc DOSY element was attached in front of a ^{1}H acquisition sequence to measure the diffusion rate of the natural abundance DnaK (Fig. 5.3b).

Resonance volume/linewidth/c.s. analysis NMRPipe[23] was used to process all NMR data. NMRViewJ[24] was used to perform NMR spectral analysis via Lorentzian fitting the NMR peaks.

Native Gel Experiments

Non-denaturing PAGE gels were run with a vertical electrophoresis apparatus (Bio-Rad, Hercules, CA) at constant voltage (200V) for 30 min at room temperature. The gel buffer consists of 375 mM Tris-HCl (pH 8.8) and 8% acrylamide (with bis-acrylamide). Tetramethyl-ethylenediamine (TEMED) and ammonium persulphate (APS) are added to the buffer for polymerization. The gel running buffer contains 25 mM Tris and 192 mM glycine. The samples were prepared identically as in NMR experiments and incubated for 2 hours before mixing with the sample buffer (30 mM Tris-HCl at pH 6.8, 20% glycerol) and loading on the gel. Coomassie blue was used for both tracking and staining.

5.3 Results and Discussion

Significant Decrease in Native SH3 Population upon Addition of DnaK Chaperone

Upon addition of DnaK to SH3, a dramatic decrease in intensity and volume of the folded SH3 resonances in the ^{1}H-^{15}N HSQC spectra was observed (Fig. 5.1). Note that the well-dispersed resonances are the folded species, while the clustered resonances are the unfolded species. Interestingly, the effect of DnaK on resonance intensities is much more pronounced in the folded state of SH3 than in the unfolded state. Similar observations were made with iron-sulfur cluster scaffold protein (IscU) binding to a specialized Hsp70-like protein (HscA).[15] In order to verify that there was no effect from SH3 protein aggregation or degradation on these spectral results, two weeks after making the SH3 + DnaK sample, a large amount of unlabeled-SH3 was added to check whether the DnaK-SH3 interaction is reversible (Fig. 5.2). Indeed, most of the folded ^{13}C,^{15}N-SH3 resonances recovered upon addition of unlabeled-SH3, illustrating the reversible nature of DnaK-SH3 interaction.[15]

Both Native and Unfolded SH3 States are Associated with DnaK

In order to test whether SH3 is bound to DnaK, we performed a Diffusion Ordered SpectroscopY (DOSY) experiment to measure the diffusion rates of native and unfolded SH3 in the absence and presence of DnaK (Fig. 5.4), using the pulse sequences shown in Figure 5.3. As mentioned in the Experimental Methods, these pulse sequences enable convection-compensated[22] (cc) measurements of the translational diffusion coefficient, which suppress undesired artifacts. Measurements

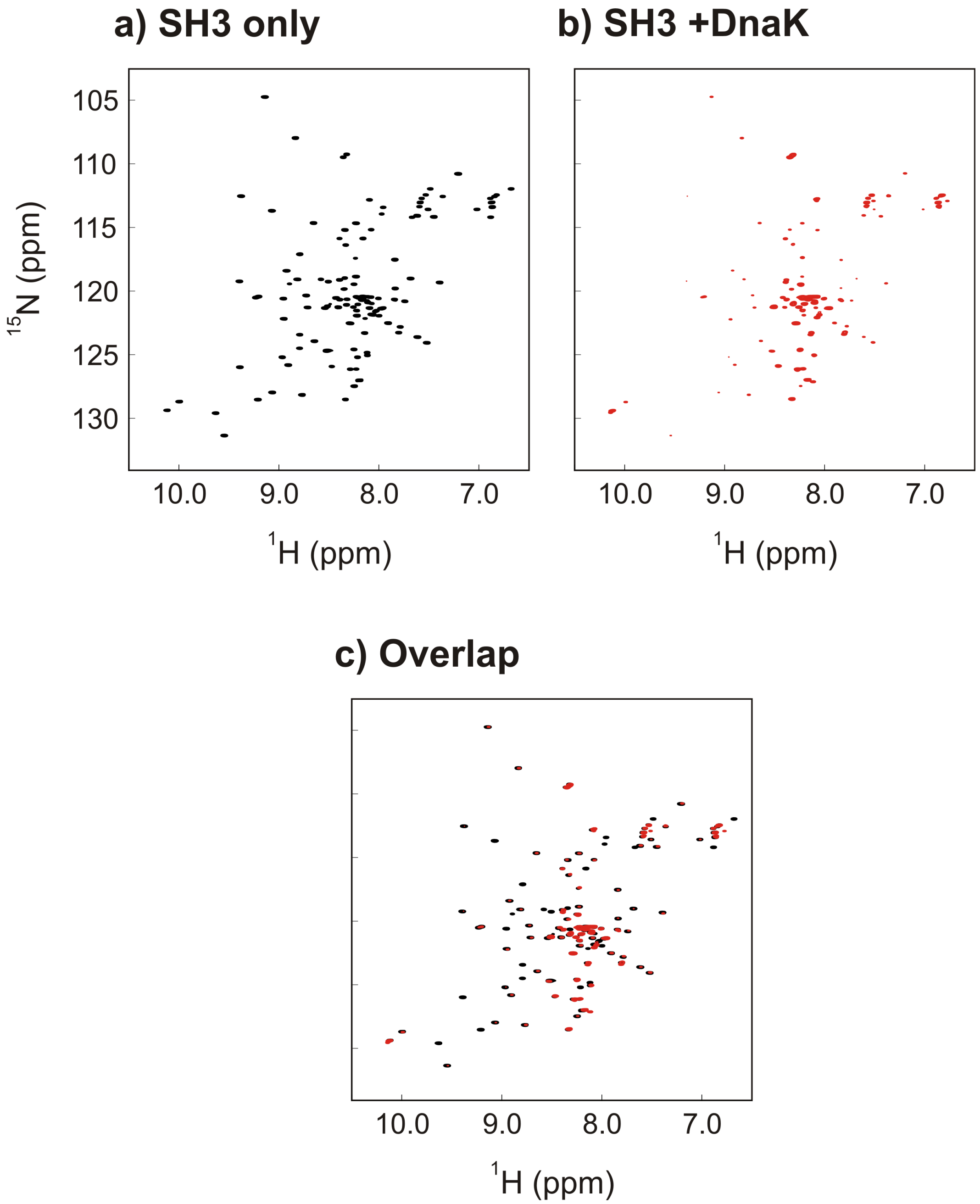

Figure 5.1 ^{1}H-^{15}N HSQC spectra of a) 300μM SH3, b) 300μM SH3 and 1200μM DnaK, and c) the overlap of the two spectra. Only SH3 is ^{13}C,^{15}N-isotope-enriched. Sweep width of 1937 Hz with 256 increments was employed in the indirect dimension. 72°-shifted and 54°-shifted sine-bell-squared apodization functions were applied to direct and indirect dimensions, respectively.

carried out with these sequences yielded slightly smaller translational diffusion coefficients than the regular DOSY experiment (data were collected with a cryogenic probe). The above sequences were tailored to yield either high-resolution heteronuclear NMR data (Fig. 5.3a) or a solvent-suppressed 1D ^{1}H data (Fig. 5.3b). The latter pulse sequence was employed to circumvent the low ^{1}H-^{13}C HSQC NMR signal from the natural abundance DnaK.

The translational diffusion coefficient of unfolded SH3 in the presence of DnaK is dramatically slower than that of free unfolded SH3 and approaches the diffusion of substrate-free DnaK (Fig 5.4). Note that substrate-free DnaK is prone to oligomerization (especially under the "DnaK only" experimental conditions of 0.3mM ADP-DnaK), while substrates tend to bind to the monomeric form of DnaK.[25] Thus, unfolded SH3 in the presence of DnaK may even diffuse more slowly than the DnaK monomer, indicating that the unfolded SH3 is mostly in complex with the DnaK chaperone.

The translational diffusion coefficient of folded SH3 in the presence of DnaK is also significantly smaller than that of free folded SH3 (Fig. 5.4). Note, however, that the extent of decrease in diffusion coefficient is smaller than the case of unfolded SH3.

In summary, the data collected so far imply that both folded and unfolded SH3 in the presence of DnaK are in different states from those of the corresponding substrates in the absence of DnaK. The case of folded DnaK is particularly interesting. In the presence of DnaK, this species is either ca. 50% bound to the chaperone or in fast exchange relative to both the NMR chemical shift and translational diffusion timescales (see Δ value in Fig. 5.3) with another presently unidentified slowly diffusing species. Note, however, that the effect of the increased viscosity due to the addition of 1.2 mM

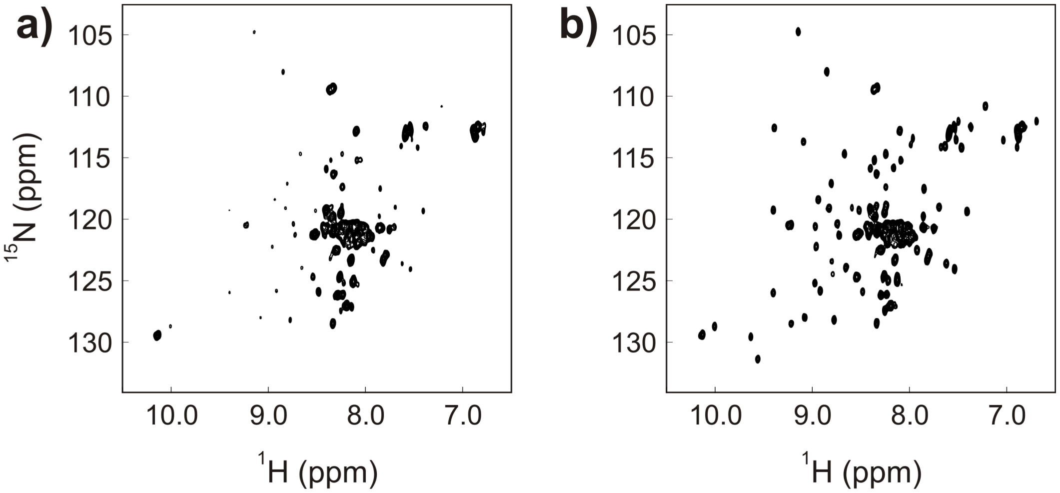

Figure 5.2 SH3 reversibly binds to DnaK. After 2 weeks of incubation of the SH3 + DnaK sample in Fig. 5.1b, it was diluted by three fold a) without and b) with adding excessive amount of unlabeled SH3. a) HSQC spectrum of 100 μM $^{13}C,^{15}N$-SH3 and 400 μM DnaK. b) HSQC spectrum of 100 μM $^{13}C,^{15}N$- SH3, 400 μM DnaK, and 1mM SH3. A sweep width of 1900Hz with 64 increments was employed in the indirect dimension. A cosine-bell-squared apodization function was applied to both direct and indirect dimensions.

a) cc DOSY followed by ^{1}H -^{13}C HSQC (for isotope-labeled SH3)

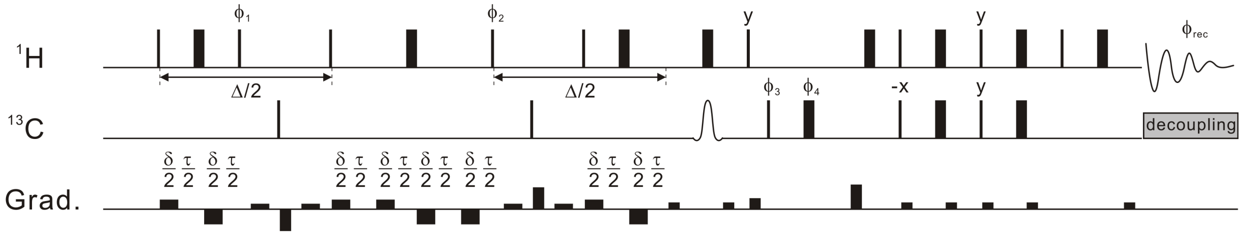

b) cc DOSY followed by water suppression (for unlabeled DnaK)

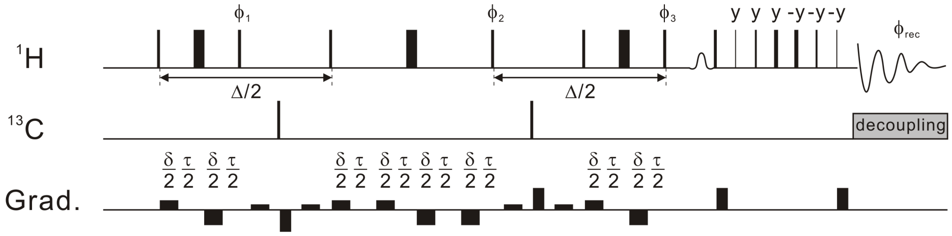

Figure 5.3 Pulse sequence used for the Diffusion Ordered SpectroscopY (DOSY) experiments. a) The convection-compensated (cc) DOSY element was attached in front of the ^{1}H-^{13}C HSQC sequence, to compensate for the intrinsic convection in the NMR sample tube as well as to avoid proton exchange effect between water and amide in case ^{1}H-^{15}N HSQC was used instead. The δ, τ, and Δ values are set to 2ms, 4ms, and 100ms, respectively. The gradients are varied according to the one-shot scheme[6] to maintain the lock power and compensate for the imperfect 180° pulses during the biopolar-gradient pulses.[26] The phase cycle is ϕ_1 = 8(x), 8(-x); ϕ_2 = 16(x), 16(-x); ϕ_3 = x, -x; ϕ_4 = x, x, y, y, -x, -x,-y -y; ϕ_{rec} = 2(x, -x, -x, x), 4(-x, x, x, -x), 2(x, -x, -x, x). ϕ_3 and ϕ_{rec} phases change sign every other row for STATES-TPPI acquisition. The thin and thick lines represent 90° and 180° pulses, respectively. b) For natural abundance samples,

the cc DOSY element was attached to the 3-9-19 WATERGATE sequence[27]. The phase cycle is ϕ_1 = x, -x; ϕ_2 = 2(x), 2(-x); ϕ_3 = 4(x), 4(-x); ϕ_{rec} = x, -x, -x, x, -x, x, x, -x.

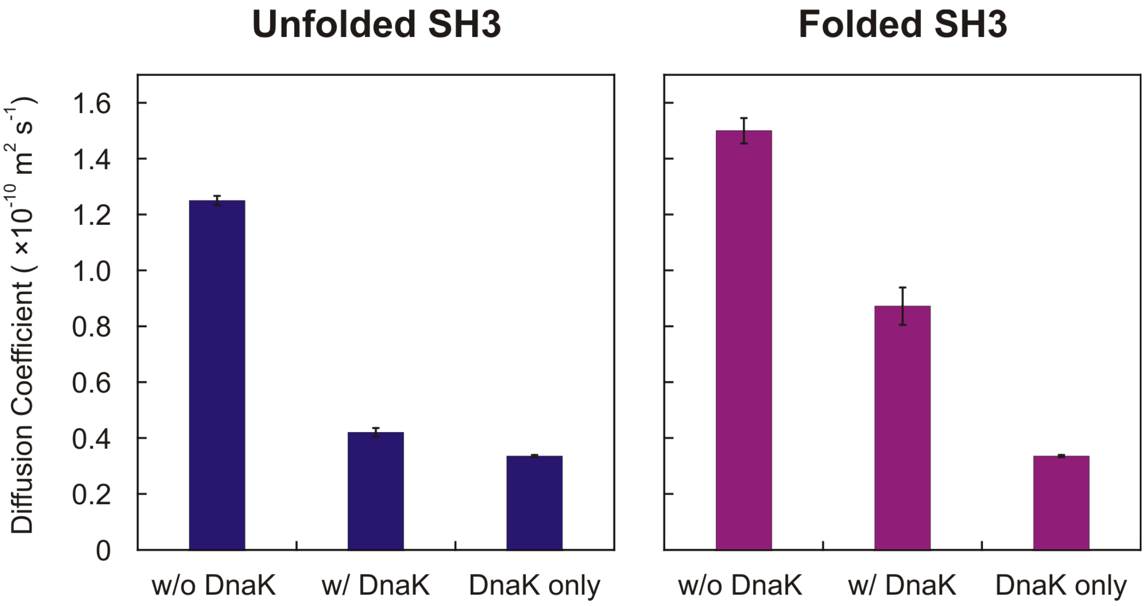

Figure 5.4 DOSY experiments on SH3 resonances in the absence and presence of DnaK. The methyl groups from five alanine residues of SH3 were used as DOSY probes. The translational diffusion coefficient of DnaK was determined by integrating the methyl region of 1D spectra obtained from the pulse sequence shown in Fig. 5.3b. The error bars come from linear regression of five different gradient values and averaging different alanine methyl probes from single samples, i.e. SH3 only, DnaK only, and SH3 with DnaK. The diffusion coefficient calibration was done by setting the HDO diffusion coefficient at 25°C to 19.02 x 10^{-10} (m^2 s^{-1}).[10]

DnaK can be significant,[33] and control experiments to investigate the effect of increased viscosity resulting form addition of DnaK will be performed in the near future.

Spectral Analysis of SH3 Resonances in the Absence and Presence of the DnaK Chaperone

An important question at this juncture is: how does the SH3 substrate associate with DnaK? In order to provide an answer to this question, we performed a preliminary spectral analysis (Fig. 5.5) of the ^{1}H-^{15}N HSQC resonances in Fig. 5.1. All the unambiguously assigned SH3 linewidths, volumes and chemical shifts were compared in the absence and presence of DnaK.

For unfolded SH3, the change in both linewidth and volume upon addition of DnaK is highly site-specific (Fig. 5.5b and d). Furthermore, the average changes in linewidth (4.2 ± 0.9 Hz) and volume (0.9 ± 9.7 %) are small. In combination with the native gel (further discussed in next section) and translational diffusion analysis, this result shows that the unfolded SH3 resonances in the presence of DnaK are due to a DnaK-bound state. The unfolded state preserves or somewhat increases its population upon addition of DnaK to the medium (although volumes do not change much on the average) and also preserves much of its flexibility (fast local rotation tumbling in the bound state leads to only moderate increase in linewidths).

Note that small but non-negligible ^{1}H chemical shift differences are observed both in the folded and unfolded states of SH3 upon addition of DnaK. Thus, there may be fast conformational exchange processes involving both states. Further implications will be discussed in Chapter 6. In addition, some resonances are broadened beyond

a) ^{1}H linewidth changes in <u>folded</u> SH3 upon addition of DnaK

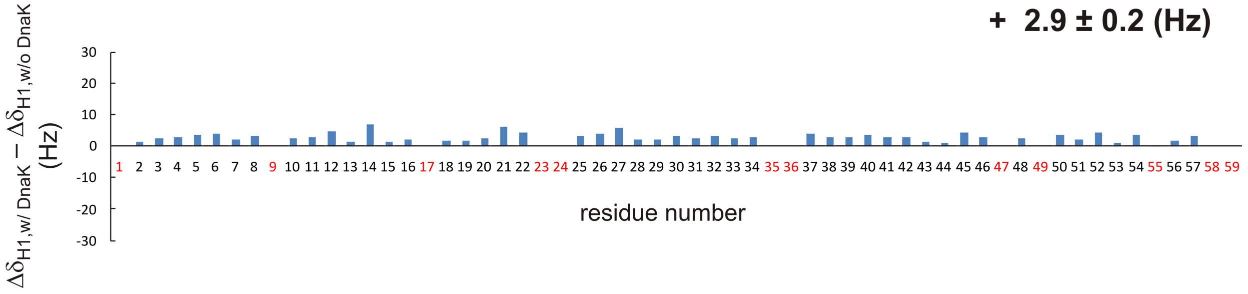

b) ^{1}H linewidth changes in <u>unfolded</u> SH3 upon addition of DnaK

c) Percent volume changes in <u>folded</u> SH3 upon addition of DnaK

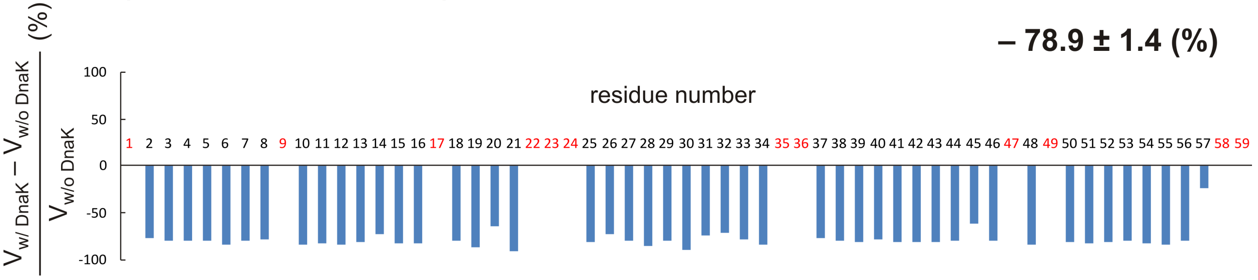

d) Percent volume changes in <u>unfolded</u> SH3 upon addition of DnaK

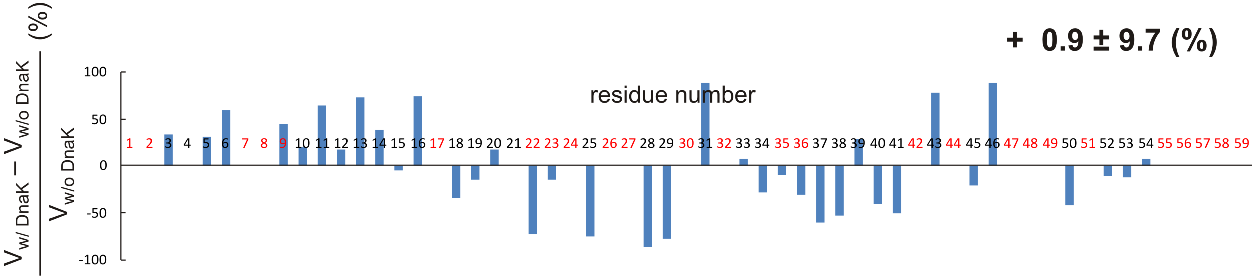

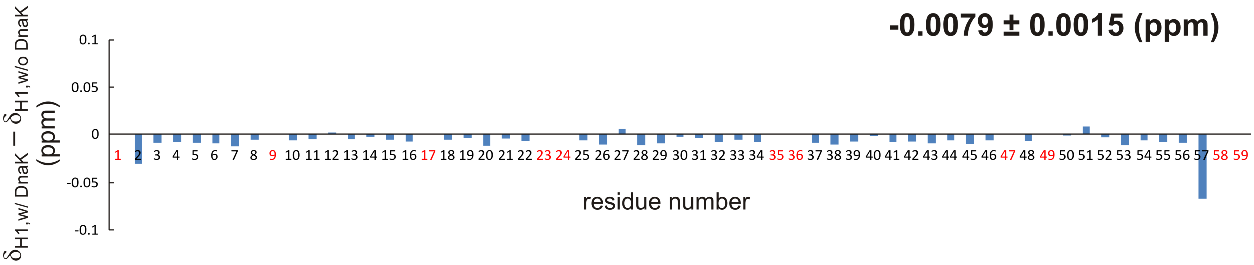

e) ^{1}H chemical shift changes in <u>folded</u> SH3 upon addition of DnaK

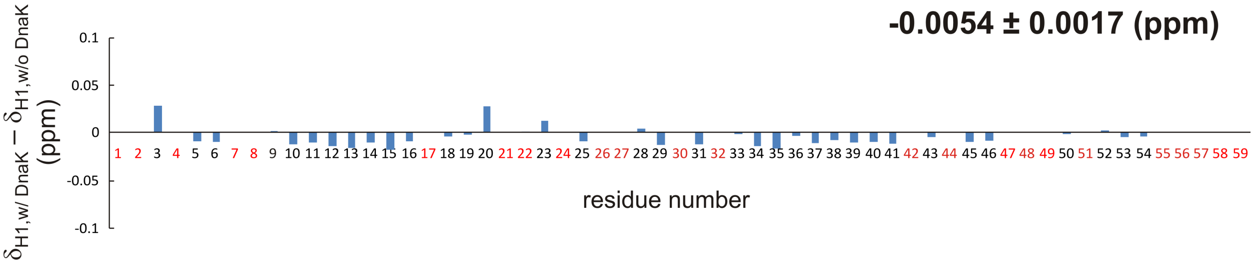

f) ^{1}H chemical shift changes in <u>unfolded</u> SH3 upon addition of DnaK

Figure 5.5 Spectral analysis for SH3 in the absence and presence of DnaK. ^{1}H-^{15}N HSQC spectra from Fig. 5.1 were analyzed. ^{1}H linewidth ($\Delta\delta_{H1}$) changes in a) folded and b) unfolded states of SH3 upon addition of DnaK are shown. The linewidth change is calculated as $\Delta\delta_{H1,\text{with DnaK}} - \Delta\delta_{H1,\text{without DnaK}}$ (Hz). The percent volume changes in c) folded and d) unfolded states of SH3 upon addition of DnaK are shown. The resonance volume (V) percentage change is calculated as $(V_{\text{with DnaK}} - V_{\text{without DnaK}})/ V_{\text{without DnaK}}$ (%).^{1}H chemical shift changes in e) folded and f) unfolded states of SH3 upon addition of DnaK are shown. The chemical shift change is calculated as $\Delta\delta_{H1,\text{with DnaK}} - \Delta\delta_{H1,\text{without DnaK}}$ (Hz). The red residue numbers indicate resonances that have no assignments, overlap with other resonances, missing, or whose S/N is too small to be analyzed properly, and thus set to zero in the plots and excluded from the average calculation displayed on the right-hand side of each plot.

detection and we are therefore unable to assess whether or not these resonances experience large chemical shift changes upon addition of DnaK. More accurate identification of these resonances is currently in process.

In the case of the folded SH3 resonances, a uniform change in both linewidths and volumes is observed throughout the sequence (Fig. 5.5a and c). The linewidths show a small and uniform increase (2.9 ± 0.2 Hz) and the volumes display a dramatic uniform decrease (78.9 ± 1.4 Hz) in the presence of DnaK, which is consistent with the visual inspection of Fig. 5.1.

The decrease in the resonance volume reflects the loss of NMR observable population, especially when the population is not shifted to the other NMR observable state (i.e., DnaK-bound unfolded SH3). At this stage, I propose that the DnaK-SH3 interaction leads to a new population that is not detectable by NMR, a so-called NMR "dark state".[21] This dark state was previously observed in α-synuclein protein interacting with lipids,[21] oligomeric amyloid species,[28] and the p53 protein interacting with Hsp90 chaperone.[14] The significant linebroadening beyond detection in these states are likely due to exchange broadening and/or very slow rotation tumbling.

We observe that, while the translational diffusion of folded SH3 is slowed down in the presence of DnaK (Fig. 5.4), the linewidth of folded SH3 is only slightly affected (2.9 ± 0.2 Hz). Two possible scenarios may explain this result. First, folded SH3 may undergo fast exchange on the NMR chemical shift timescale with slowly-diffusing species with similar linewidth (e.g. DnaK-bound unfolded SH3). Second, some of the folded SH3 population may be in a DnaK-bound globally folded and still maintain its rotational freedom.

Slight increase in linewidth (2.9 ± 0.2 Hz) can be either caused by a small rotational hindrance of folded SH3 in the presence of DnaK or by lifetime broadening caused by unidirectional conversion of the visible folded SH3 to the invisible “dark state” at the rate of ~2-3 s^{-1}. The “dark state” is characterized by a much shorter T_2 than the free species.[28,29] For the second scenario (some of the folded SH3 population is DnaK bound) to hold, the level of association between the folded SH3 and DnaK should allow fast SH3 rotational tumbling, deceleration of SH3 translational diffusion, and a mechanism for small but uniform linebroadening. More experiments and discussion are ongoing to clarify the mechanism.

Significant Population of SH3 is Bound to DnaK

To confirm complex formation between SH3 and DnaK, non-denaturing PAGE gels were run. Since the gel does not contain sodium dodecyl sulfate, native complex formation can be visualized.[30]

When we compare the first two lanes of Fig. 5.6 (SH3 only and SH3 + DnaK), decrease of SH3 band intensity is evident, which illustrates that significant portion (~60%) of SH3 is bound to DnaK. When comparing the second (SH3 + DnaK) and the third (DnaK only) lanes, potential DnaK-SH3 complex bands appear, further confirming the association of SH3 with DnaK. Note, however, that the native gel and NMR experiments were carried out under slightly different conditions (see Experimental Methods for details).

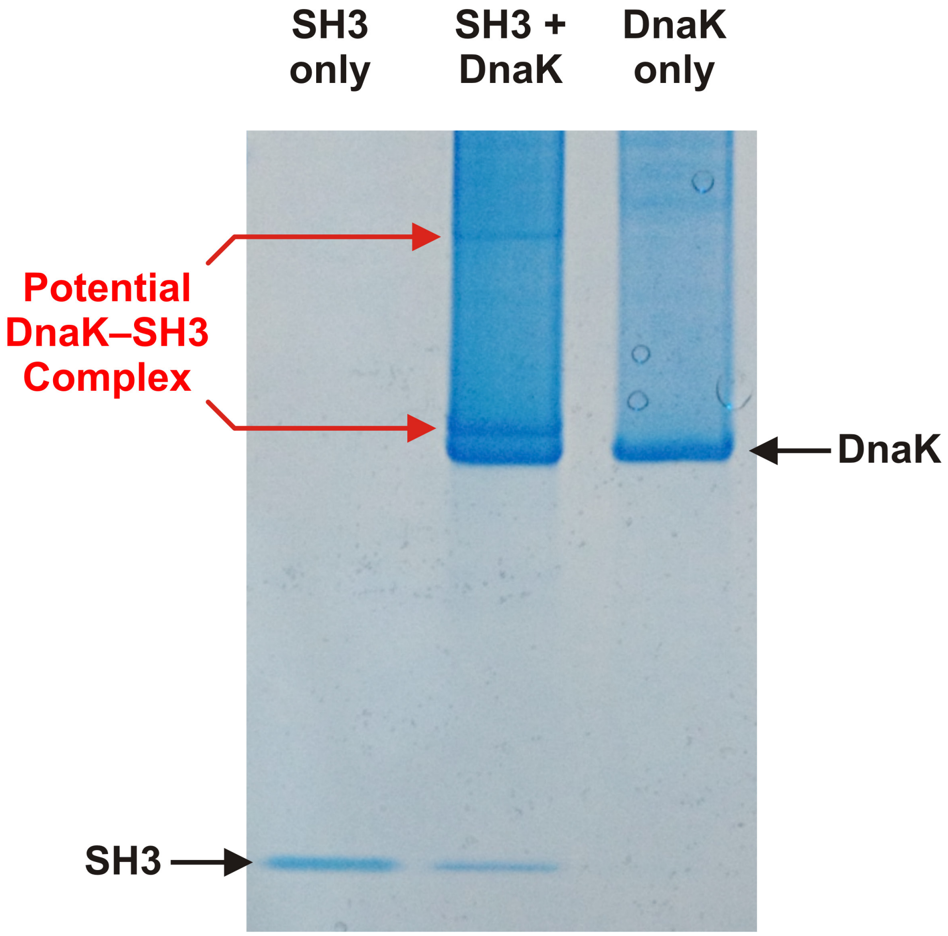

Figure 5.6 Complex formation between SH3 and DnaK as observed by native gel analysis.

GrpE does not Affect the DnaK-SH3 Interaction

DnaK functions in concert with other co-chaperones to help protein folding.[4] GrpE, one of the co-chaperones, is a nucleotide exchange factor that accelerates ADP release from ADP-DnaK by up to 5000-fold via forming ADP-DnaK-GrpE and DnaK-GrpE complexes.[31,32]

In order to simulate the nucleotide-free DnaK condition, excess amount of GrpE was added to the sample (Fig. 5.7). Consistent with the EPR study which shows that peptides bound to different nucleotide states (ATP, ADP and nucleotide-free states) of DnaK display no significant changes in mobility and structure,[11] we observed no significant spectral change in NMR when GrpE was added to the DnaK + SH3 sample (Fig. 5.7).

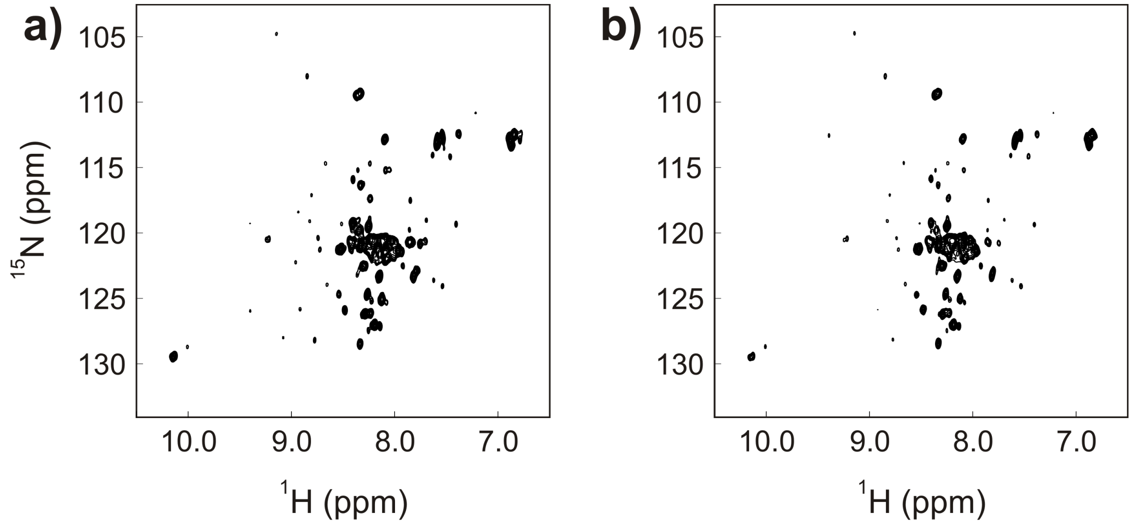

Figure 5.7 The effect of GrpE (an *E. coli* nucleotide exchange factor) on DnaK-SH3 interaction. a) The same spectrum as in Fig. 5.2a. That is, HSQC spectrum of 100 μM ^{13}C,^{15}N-SH3 and 400 μM DnaK. b) HSQC spectrum of 100 μM ^{13}C,^{15}N- SH3, 400 μM DnaK, and 1mM GrpE. NMR spectra were processed as in Fig. 5.2.

5.4 Conclusions

The interaction between the full-length ADP-DnaK chaperone and the drkN SH3 domain was monitored in this study. NMR diffusion measurements, heteronuclear NMR experiments followed by spectral analysis, and native gel analysis were employed to provide information on the Hsp70-substrate interaction.

Since the SH3 domain slowly exchanges between folded and unfolded states on the NMR chemical shift timescale in the absence of chaperone, the SH3 interaction with the DnaK chaperone provides information on how both states are affected by DnaK.

Unfolded SH3 binds DnaK as expected according to the reported tendency of DnaK to bind extended/unfolded conformations.[8,10,16] In addition, upon addition of DnaK, small chemical shift changes and linebroading of selected unfolded SH3 resonances suggest the presence of small perturbations of the SH3 conformational ensemble.

Unexpectedly, translational diffusion of folded SH3 was also slowed down in the presence of DnaK. This observation may not be due to simple binding of the native state to DnaK on the fast chemical shift timescale since only very small linewidth broadening was observed for folded SH3 in the presence of DnaK. Two different schemes were proposed (Fig. 5.8). First, folded SH3 experiences fast exchange with DnaK-bound unfolded SH3. Second, folded SH3 directly associates with DnaK such that diffusion is slowed down by two-fold and rotation tumbling is minimally perturbed. Both mechanisms encompass the presence of significantly-populated NMR-invisible “dark states”.

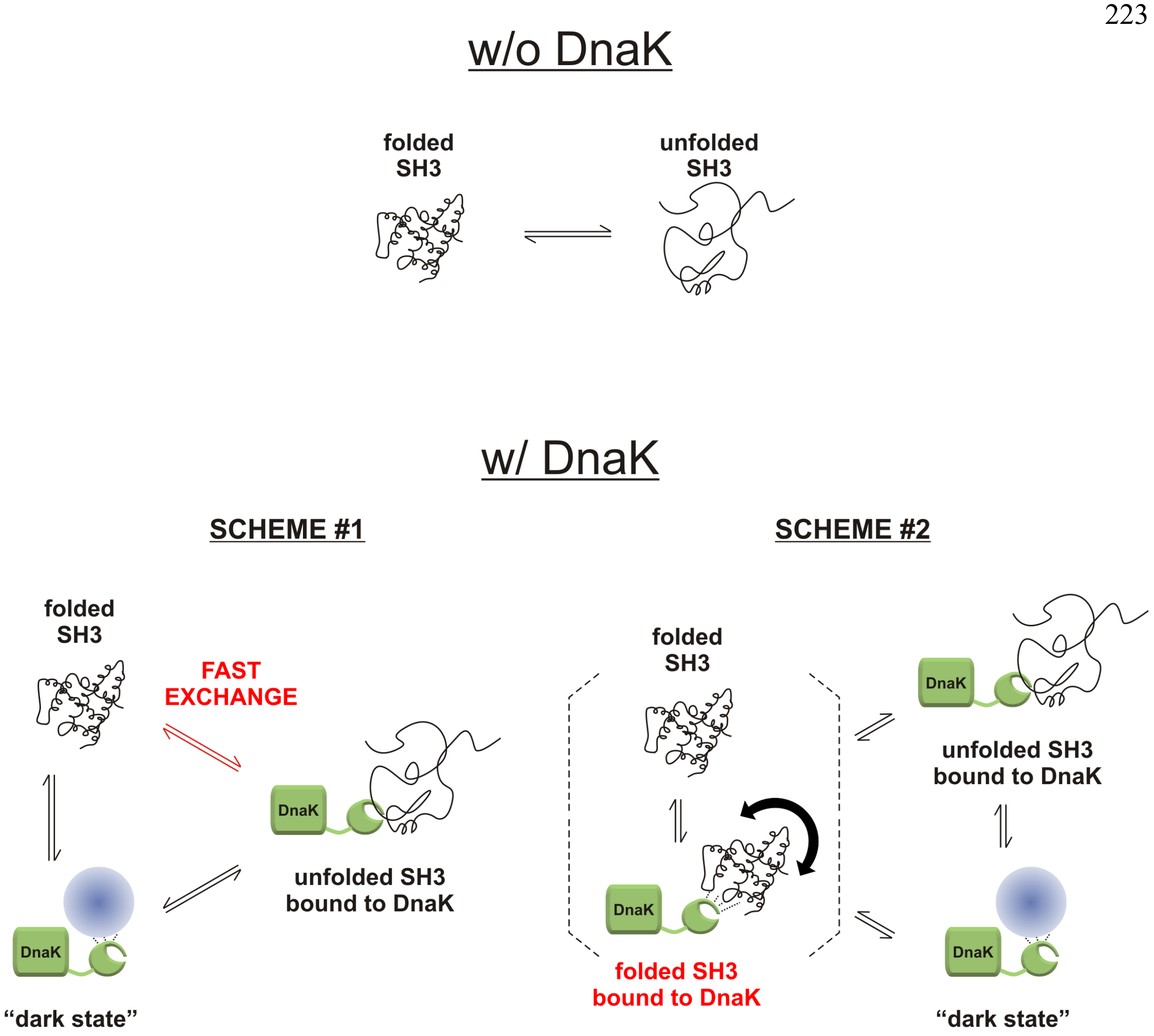

Figure 5.8 Proposed mechanisms for the drkN SH3 conformational change in the presence of the DnaK molecular chaperone. The proposed relationships between the main populated species are shown. The red colored elements are responsible for slow diffusion of folded states in different schemes. Dotted bracket indicates the NMR-observable folded SH3 in scheme #2. The double-headed arrow inside the bracket denotes fast rotational tumbling of folded SH3 when associated with DnaK.

Overall, exposure of the SH3 substrate to Hsp70 leads to the identification of different substrate states. They are Hsp70-bound unfolded state, NMR-invisible “dark state(s)”, and possibly an Hsp70-associated folded state.

Appendix

Appendix 5A contains figures related to NMR sample preparation and N_z exchange experiment to verify SH3 backbone assignments.

Acknowledgments

We thank Marco Tonelli and Charlie Fry for helpful discussions on NMR. This research was funded by NIH grant R21AI088551, NSF grant MCB-0951209 and by a grant from the UW-Madison Graduate School. This study made use of the National Magnetic Resonance Facility at Madison, which is supported by NIH grants P41RR02301 (BRTP/ NCRR) and P41GM66326 (NIGMS). Additional equipment was purchased with funds from the University of Wisconsin, the NIH (RR02781, RR08438), the NSF (DMB-8415048, OIA-9977486, BIR-9214394), and the USDA.

5.5 References

(1) Bukau, B.; Weissman, J.; Horwich, A. Molecular Chaperones and Protein Quality Control. *Cell* **2006**, *125*, 443-451.

(2) Fedyukina, D. V.; Cavagnero, S. Protein Folding at the Exit Tunnel. *Annu. Rev. Biophys.* **2011**, *40*, 337-359.

(3) Hartl, F. U.; Hayer-Hartl, M. Converging Concepts of Protein Folding in Vitro and in Vivo. *Nat. Struct. Mol. Biol.* **2009**, *16*, 574-581.

(4) Bukau, B.; Horwich, A. L. The Hsp70 and Hsp60 Chaperone Machines. *Cell* **1998**, *92*, 351-366.

(5) Evans, C. G.; Chang, L.; Gestwicki, J. E. Heat Shock Protein 70 (Hsp70) as an Emerging Drug Target. *J. Med. Chem.* **2010**, *53*, 4585-4602.

(6) Muchowski, P. J.; Wacker, J. L. Modulation of Neurodegeneration by Molecular Chaperones. *Nat. Rev. Neurosci.* **2005**, *6*, 11-22.

(7) Mayer, M.; Bukau, B. Hsp70 Chaperones: Cellular Functions and Molecular Mechanism. *Cell. Mol. Life Sci.* **2005**, *62*, 670-684.

(8) Zhu, X.; Zhao, X.; Burkholder, W. F.; Gragerov, A.; Ogata, C. M.; Gottesman, M. E.; Hendrickson, W. A. Structural Analysis of Substrate Binding by the Molecular Chaperone DnaK. *Science* **1996**, *272*, 1606-1614.

(9) Pellecchia, M.; Montgomery, D. L.; Stevens, S. Y.; Vander Kooi, C. W.; Feng, H.-p.; Gierasch, L. M.; Zuiderweg, E. R. Structural Insights into Substrate Binding by the Molecular Chaperone DnaK. *Nat. Struct. Mol. Biol.* **2000**, *7*, 298-303.

(10) Chen, Z.; Kurt, N.; Rajagopalan, S.; Cavagnero, S. Secondary Structure Mapping of DnaK-Bound Protein Fragments: Chain Helicity and Local Helix Unwinding at the Binding Site. *Biochemistry* **2006**, *45*, 12325-12333.

(11) Landry, S. J.; Jordan, R.; McMacken, R.; Gierasch, L. M. Different Conformations for the Same Polypeptide Bound to Chaperones DnaK and GroEL. *Nature* **1992**, *355*, 455-457.

(12) Kurt, N.; Cavagnero, S. Nonnative Helical Motif in a Chaperone-Bound Protein Fragment. *Biophys. J.* **2008**, *94*, L48-L50.

(13) Buckle, A. M.; Zahn, R.; Fersht, A. R. A Structural Model for GroEL–Polypeptide Recognition. *Proc. Natl. Acad. Sci. U.S.A.* **1997**, *94*, 3571-3575.

(14) Park, S. J.; Borin, B. N.; Martinez-Yamout, M. A.; Dyson, H. J. The Client Protein p53 Adopts a Molten Globule–Like State in the Presence of Hsp90. *Nat. Struct. Mol. Biol.* **2011**, *18*, 537-541.

(15) Garrett, D. S.; Seok, Y.-J.; Peterkofsky, A.; Gronenborn, A. M.; Clore, G. M. Solution Structure of the 40,000 Mr Phosphoryl Transfer Complex between the N-Terminal Domain of Enzyme I and HPr. *Nat. Struct. Mol. Biol.* **1999**, *6*, 166-173.

(16) Tycko, R.; Wickner, R. B. Molecular Structures of Amyloid and Prion Fibrils: Consensus Versus Controversy. *Acc. Chem. Res.* **2013**, *46*, 1487-1496.

(17) Xing, Y.; Böcking, T.; Wolf, M.; Grigorieff, N.; Kirchhausen, T.; Harrison, S. C. Structure of Clathrin Coat with Bound Hsc70 and Auxilin: Mechanism of Hsc70-Facilitated Disassembly. *EMBO J.* **2009**, *29*, 655-665.

(18) Packschies, L.; Theyssen, H.; Buchberger, A.; Bukau, B.; Goody, R. S.; Reinstein, J. GrpE Accelerates Nucleotide Exchange of the Molecular Chaperone DnaK with an Associative Displacement Mechanism. *Biochemistry* **1997**, *36*, 3417-3422.

(19) Zhang, O.; Kay, L. E.; Olivier, J. P.; Forman-Kay, J. D. Backbone 1H and 15N Resonance Assignments of the N-Terminal SH3 Domain of drk in Folded and Unfolded States Using Enhanced-Sensitivity Pulsed Field Gradient NMR Techniques. *J. Biomol. NMR* **1994**, *4*, 845-858.

(20) Rüdiger, S.; Germeroth, L.; Schneider-Mergener, J.; Bukau, B. Substrate Specificity of the DnaK Chaperone Determined by Screening Cellulose-Bound Peptide Libraries. *EMBO J.* **1997**, *16*, 1501-1507.

(21) Bodner, C. R.; Dobson, C. M.; Bax, A. Multiple Tight Phospholipid-Binding Modes of a-Synuclein Revealed by Solution NMR Spectroscopy. *J. Mol. Biol.* **2009**, *390*, 775-790.

(22) Jerschow, A.; Müller, N. Suppression of Convection Artifacts in Stimulated-Echo Diffusion Experiments. Double-Stimulated-Echo Experiments. *J. Magn. Reson.* **1997**, *125*, 372-375.

(23) Delaglio, F.; Grzesiek, S.; Vuister, G. W.; Zhu, G.; Pfeifer, J.; Bax, A. NMRPipe: A Multidimensional Spectral Processing System Based on Unix Pipes. *J. Biomol. NMR* **1995**, *6*, 277-293.

(24) Johnson, B. A.; Blevins, R. A. NMRView: A Computer Program for the Visualization and Analysis of NMR Data. *J. Biomol. NMR* **1994**, *4*, 603-614.

(25) Ernst, R. R. Nuclear Magnetic Resonance Fourier Transform Spectroscopy. *Biosci. Rep.* **1992**, *12*, 143-187.

(26) Wu, D.; Chen, A.; Johnson, C. S. An Improved Diffusion-Ordered Spectroscopy Experiment Incorporating Bipolar-Gradient Pulses. *J. Magn. Reson.* **1995**, *115*, 260-264.

(27) Lang, J.; Wu, Y.; Cavagnero, S. *submitted.*

(28) Fawzi, N. L.; Ying, J.; Torchia, D. A.; Clore, G. M. Kinetics of Amyloid β Monomer-to-Oligomer Exchange by NMR Relaxation. *J. Am. Chem. Soc.* **2010**, *132*, 9948-9951.

(29) Fawzi, N. L.; Ying, J.; Ghirlando, R.; Torchia, D. A.; Clore, G. M. Atomic-Resolution Dynamics on the Surface of Amyloid-β Protofibrils Probed by Solution NMR. *Nature* **2011**, *480*, 268-272.

(30) Kurt, N.; Rajagopalan, S.; Cavagnero, S. Effect of Hsp70 Chaperone on the Folding and Misfolding of Polypeptides Modeling an Elongating Protein Chain. *J. Mol. Biol.* **2006**, *355*, 809-820.

(31) Packschies, L.; Theyssen, H.; Buchberger, A.; Bukau, B.; Goody, R. S.; Reinstein, J. GrpE Accelerates Nucleotide Exchange of the Molecular Chaperone DnaK with an Associative Displacement Mechanism. *Biochemistry* **1997**, *36*, 3417-3422.

(32) Sekhar, A.; Lam, H. N.; Cavagnero, S. Protein Folding Rates and Thermodynamic Stability are Key Determinants for Interaction with the Hsp70 Chaperone System. *Protein Sci.* **2012**, *21*, 1489-1502.

(33) Wang, Y.; Li, C.; Pielak, G. J. Effects of Proteins on Protein Diffusion. *J. Am. Chem. Soc.* **2010**, *132*, 9392-9397.

Appendix 5A

Supporting Information for Chapter 5

Conformational Changes of the drkN SH3 Protein upon Interaction with the Hsp70 Molecular Chaperone

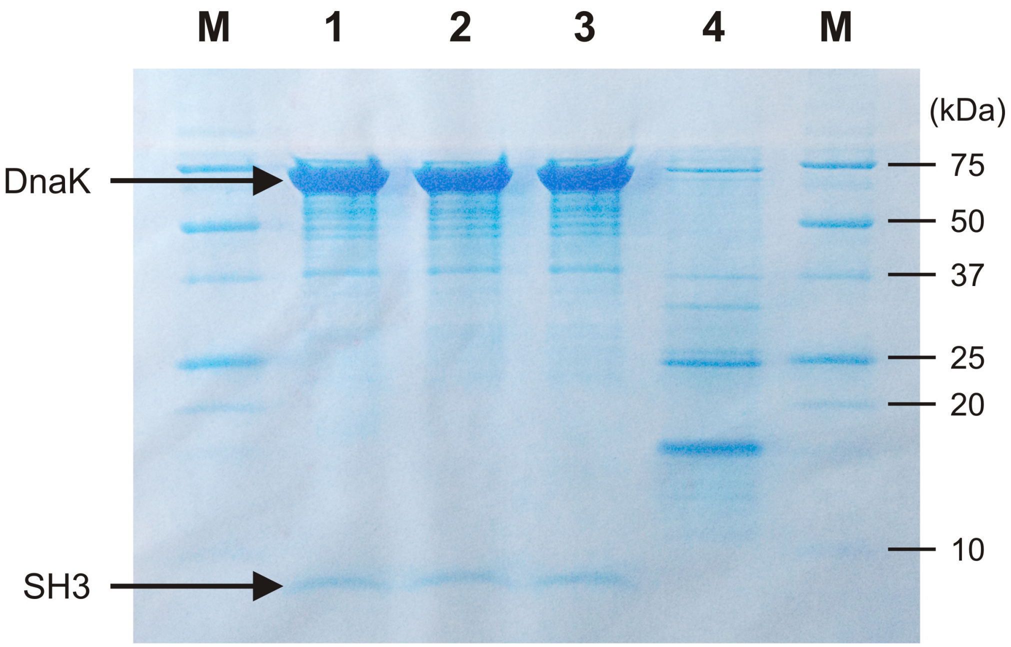

Lane M: Protein Marker
Lane 1 : Newly made NMR sample
(300μM ^{13}C,^{15}N-SH3 and 1200μM DnaK)
Lane 2 : Lane 1 sample after 24 hours
Lane 3 : Supernatant of the Lane 2 sample
Lane 4 : Pellet of the Lane 2 sample

Figure 5A.1 Coomassie blue stained SH3 + DnaK samples on a SDS PAGE gel. Note that 0.015% of the total NMR sample was loaded on lanes 1, 2, and 3 while 10% of the ultracentrifuged total pellet was loaded on lane 4. There was no observable difference for lanes 1, 2, and 3, while lane 4 is overemphasized compared to other lanes. Sample from lane 3 was used for the SH3 + DnaK NMR experiments.

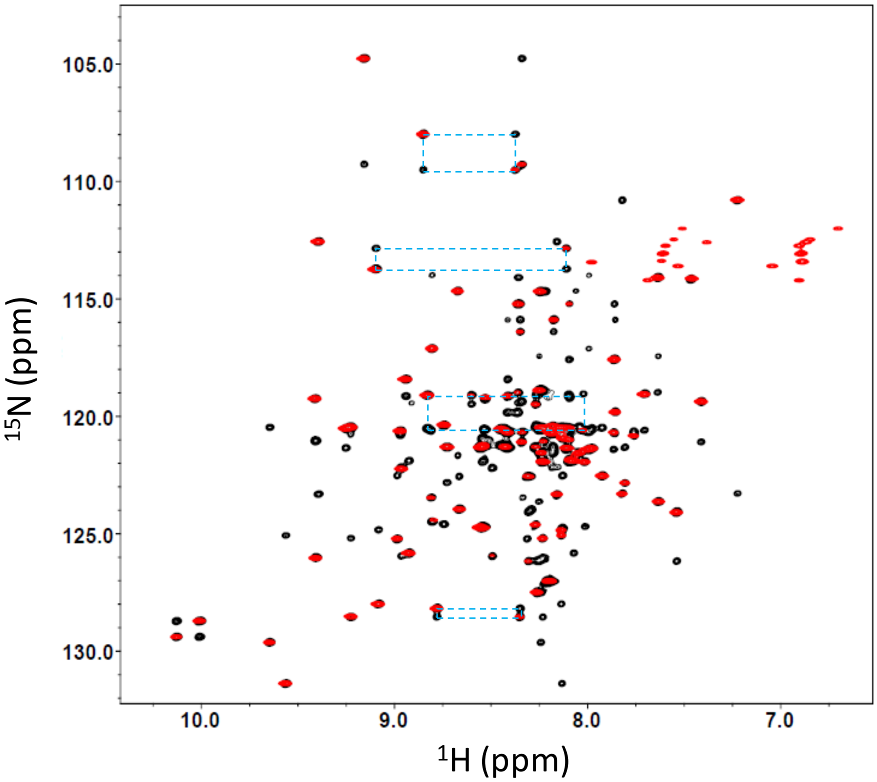

Figure 5A.2 N_z exchange ^{1}H-^{15}N HSQC experiment was preformed to verify the SH3 backbone assignment. Cyan lines connect the folded and unfolded SH3.

Chapter 6

Future Directions

As I have been writing the last chapter of my thesis, I have come to realize how little I have contributed to the scientific field of my study. Here, I present my thoughts on possible future directions of my Ph.D. research.

6.1 Photo-CIDNP

Direct Electron-to-Nucleus Polarization Transfer using Microwave Pulse

A remaining task in photo-CIDNP is to gain more sensitivity. Utilization of microwave pulses provides an opportunity towards this goal.

The importance of pulsed microwave source has been realized in the field of dynamic nuclear polarization (DNP).[1] The pulsed microwaves reduce heating[2] caused by CW microwaves in conventional DNP experiments and enable DNP hyperpolarization without unfavorable field dependence.[3] Despite the technical difficulties, many efforts are made to construct high-power pulsed microwave devices.[4]

In principle, transient radicals that are formed during the photo-CIDNP experiments can also be manipulated using pulsed microwave. For instance, using INEPT[5]–like pulse sequence as shown in Fig. 6.1, polarization can be transferred from an unpaired electron to a nucleus in the same molecule.

Two conditions should be met for this idea to work. First, the radical pair lifetime should be longer than 1/A (A is the hyperfine coupling constant) plus the RF pulse lengths, for the hyperfine coupling evolution to occur (Fig. 6.1). Since the observed lifetime of the tryptophan-flavin radical pair is ~20 μs and A is ~10 MHz,[6] high-power

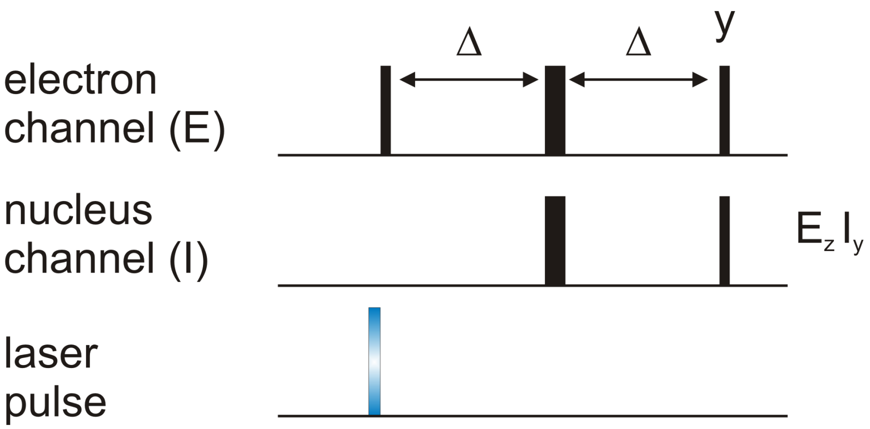

Figure 6.1 INEPT–like pulse sequence to transfer the unpaired electron polarization to nuclear polarization. The thin and thick lines (of E and I channels) represent 90° and 180° pulses, respectively. The 180° pulse pairs may be omitted if Δ is set to the multiple of inverse of electron Larmor frequency (Hz). Δ = 1/4A, where A is the hyperfine coupling constant between the unpaired electron and the nucleus. E_zI_y denotes the resulting anti-phase coherence of the nucleus. Refocused INEPT may be employed to achieve in-phase I_x magnetization.

short RF and microwave pulses may enable the scheme shown in Fig. 6.1 to work. Note that very high-power pulsed microwave source is necessary to carry out this experiment. Second, since we are not allowing unpaired electrons to thermally relax, the unpaired electrons in the radical pair should have intrinsic spin polarizations. The fact that light-induced transient radical pairs have characteristic negative and positive EPR intensities[7] illustrates the fact that electron spin polarizations exist upon radical pair formation.

Double Laser Irradiation to Extend Photo-CIDNP Probes

Available photo-CIDNP probes in proteins are solvent-exposed Trp, Tyr, and His amino acids. Extending photo-CIDNP-active probes is crucial to render photo-CIDNP a more general NMR sensitivity tool.

Spontaneous electron transfer occurs from excited-state indole to acrylamide but not from ground-state indole to acrylamide.[8] Therefore, as expected, indoles are more easily oxidizable in their electronically excited states. Hence, if one could excite peptide bond electronic transitions (at ca. 200 nm)[9] simultaneously with the photoexcitation of flavin (at 488 nm), one may be able to observe photo-CIDNP across polypeptide backbones. It is in principle possible that excitation of the dye may not even be necessary, as in the case of the excited indole and acrylamide pair.

The scheme of this experiment and pictures from my initial instrument setup are shown in Fig. 6.2. I used 193nm excimer laser and 488nm argon ion laser to excite peptide bonds and flavins, respectively. The most difficult challenge of this experiment is irradiating 193nm light to the NMR sample sitting in the magnet. Many commercially

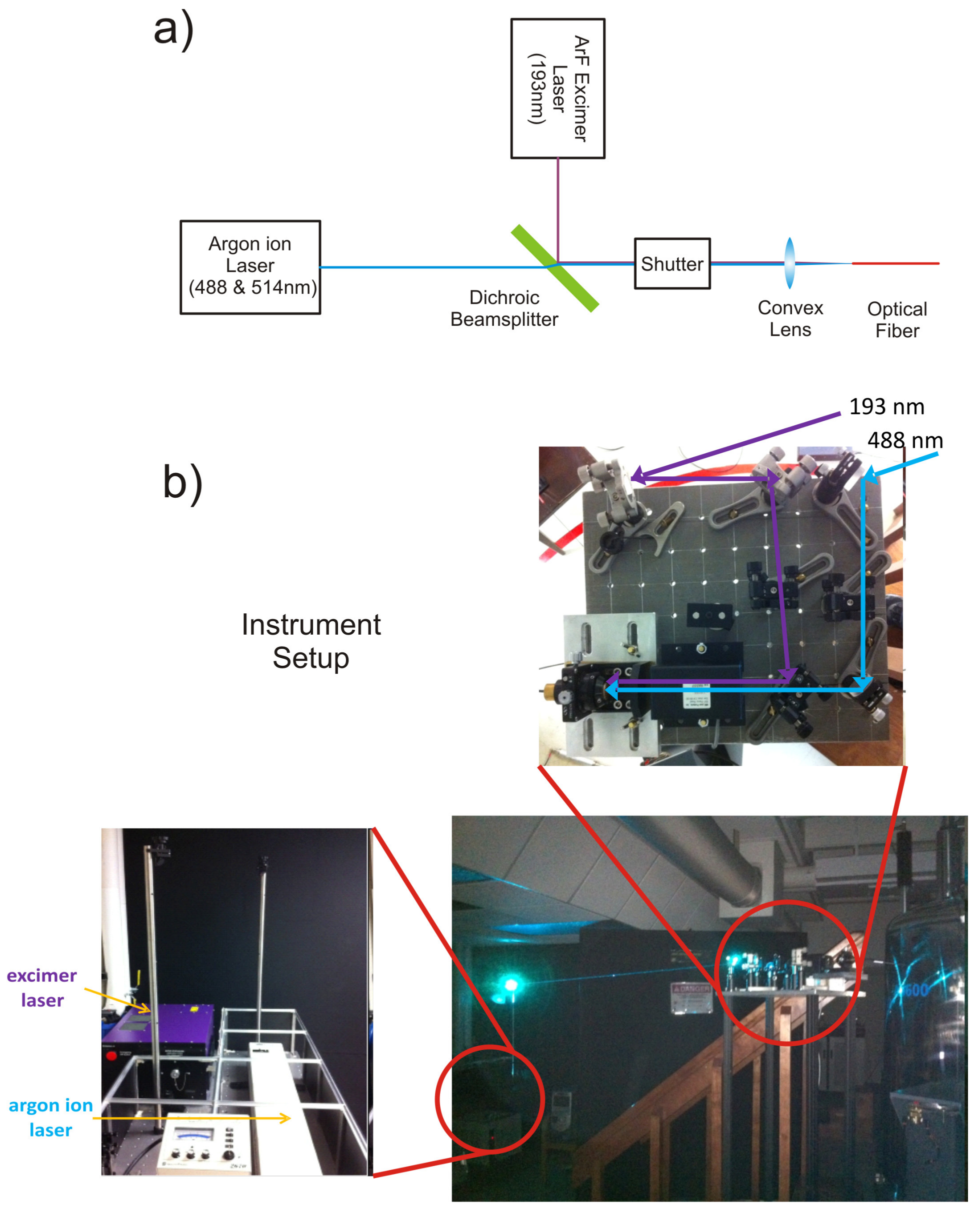

Figure 6.2 Double laser irradiation scheme. a) A schematic diagram of the experiment. b) Pictures from the double laser instrument setup. In order to minimize the optical fiber (which has very poor transmission efficiency at 193 nm) length, both 488 and 193 nm laser beams were transferred through space and focused into the optical fiber near the NMR spectrometer.

available UV-resistant optical fibers were employed, but all gave <1% transmission efficiency at this wavelength. Either due to the poor 193 nm excitation or some intrinsic problem to the scheme (e.g. peptide bond has too short excited-state lifetime), the experiment did not work.

In case this experiment resumes in the future, I feel that direct mirror reflection of 193 nm light should be employed to guide the light into the NMR sample. In addition, chemicals mimicking peptide bond rather than a full-length protein should be tested initially.[10]

6.2 Mechanism of Hsp70 Chaperone – Substrate Interaction

Future Work on the Current DnaK - SH3 Interaction Project

The content of Chapter 5 does not form a complete story. Experiments and data interpretation are still ongoing. In particular, although we proposed different states of SH3 in the presence of DnaK (folded SH3 associated with DnaK, unfolded SH3 bound to DnaK, and the “dark state”), their mutual relationship is barely characterized. Below are my opinions to supplement the project.

As mentioned in Chapter 5, non-negligible chemical shift changes were observed for some folded/unfolded SH3 resonances in the presence of DnaK. In rare cases, new peaks appear. (Fig 6.3) The small chemical shift changes imply that the protein is experiencing fast-intermediate chemical exchange with a different (most likely invisible) species. CPMG relaxation dispersion experiment will clarify this issue and identify the

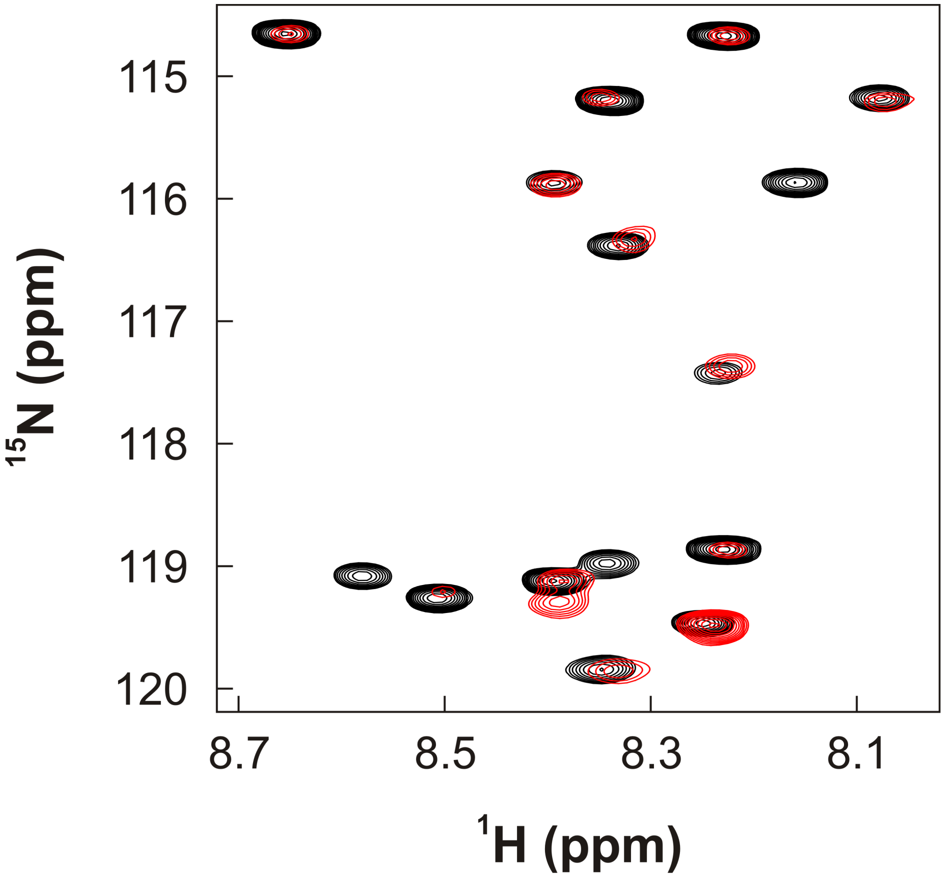

Figure 6.3 Expanded view of ^{1}H-^{15}N HSQC (Fig. 5.1) where resonances from SH3 only sample are colored black and from SH3+DnaK sample colored red. Note that only SH3 is ^{13}C,^{15}N-isotope-enriched and observed. Decrease in resonance intensities, small chemical shifts, and appearance of new resonance of SH3 in the presence of DnaK are all clearly observed.

other species involved. Characterization of the newly appearing resonances will also provide clues on the exchanging counterpart. In addition, linewidth measurement at different magnetic fields (e.g. 900 Hz) can give more information on the small and uniform linebroadening effect observed in the folded SH3 with DnaK.

In addition, in case the stable SH3 T22G mutant,[11] which has virtually identical structure as the folded SH3, does not show decrease in volume/intensity and retains its diffusion rate in the presence of DnaK, we can postulate that the folded SH3 can associate with DnaK (or form the “dark state”) only through the unfolded SH3.

Furthermore, although DTT in the DnaK sample quenches photo-CIDNP phenomenon, dialyzing DTT out before the photo-CIDNP experiment may allow us to see the photo-CIDNP effect. It would be exciting to observe different photo-CIDNP patterns between the resonances before and after adding DnaK to SH3, especially in cases where chemical shifts and linebroadening are very similar.

Lastly, the NMR-invisible “dark state”[12] seems to have great implications in many biological processes. Studies to characterize the state’s structure, dynamics and relationship with other species will be challenging and promising.

Focusing on DnaK in Action

Although NMR is a great tool to study structure and dynamics of biomolecules in physiologically relevant conditions, we still have to prepare a very well defined highly concentrated state (often made of a protein or two) for NMR studies. The topic of “dynamics” that interests me is not only confined to local fluctuations (e.g. ns-ps, ms-μs timescale motion), but also extends to describing how a protein dynamically interacts with other partners to carry out its function.

In this respect, a question that I wish to answer regarding DnaK is as follows. At conditions where natural substrates[13,14] tend to misfold and aggregate (e.g. at 45 °C), how are the substrates continuously rescued at equilibrium in the presence of DnaK-DnaJ-GrpE (-ClpB) chaperones and a plenty of ATP? In other words, I wish to observe the relevant picture of how DnaK machinery helps protein folding by NMR.

The immediate obstacle for this experiment is that ATP is very quickly depleted. This is because high concentrations of chaperones and substrates are necessary for NMR studies. This leads us back to the NMR sensitivity issue. If we can observe good NMR signals from proteins at submicromolar concentrations, ATP depletion would not be a problem. I think the more we want to observe the molecular details of the physiologically relevant processes by NMR, the more the NMR sensitivity enhancement issue comes into play.

6.3 References

(1) Maly, T.; et al. Dynamic Nuclear Polarization at High Magnetic Fields. *J. Chem. Phys.* **2008**, *128*, 052211.

(2) Griesinger, C.; Bennati, M.; Vieth, H.; Luchinat, C.; Parigi, G.; Höfer, P.; Engelke, F.; Glaser, S.; Denysenkov, V.; Prisner, T. Dynamic Nuclear Polarization at High Magnetic Fields in Liquids. *Prog. Nucl. Magn. Reson. Spectrosc.* **2012**, *64*, 4-28.

(3) Gunther, U. L. Dynamic Nuclear Hyperpolarization in Liquids. *Top. Curr. Chem.* **2013**, *335*, 23-69.

(4) Smith, A. A.; Corzilius, B.; Bryant, J. A.; DeRocher, R.; Woskov, P. P.; Temkin, R. J.; Griffin, R. G. A 140 GHz Pulsed EPR/212 MHz NMR Spectrometer for DNP Studies. *J. Magn. Reson.* **2012**.

(5) Morris, G. A.; Freeman, R. Enhancement of Nuclear Magnetic Resonance Signals by Polarization Transfer. *J. Am. Chem. Soc.* **1979**, *101*, 760-762.

(6) Ritz, T.; Thalau, P.; Phillips, J. B.; Wiltschko, R.; Wiltschko, W. Resonance Effects Indicate a Radical-Pair Mechanism for Avian Magnetic Compass. *Nature* **2004**, *429*, 177-180.

(7) Bittl, R.; Zech, S. G. Pulsed EPR Spectroscopy on Short-Lived Intermediates in Photosystem I. *Biochim. Biophys. Acta* **2001**, *1507*, 194-211.

(8) Lakowicz, J. R. *Principles of Fluorescence Spectroscopy*; 2nd ed.; Kluwer/Academic Plenum Publishers: New York, 1997.

(9) Rosenheck, K.; Doty, P. The Far Ultraviolet Absorption Spectra of Polypeptide and Protein Solutions and Their Dependence on Conformation. *Proc. Natl. Acad. Sci. U.S.A.* **1961**, *47*, 1775.

(10) Cantor, C. R.; Schimmel, P. R. *Biophysical Chemistry*; Freeman and Co.: New York, 1980.

(11) Bezsonova, I.; Singer, A.; Choy, W.-Y.; Tollinger, M.; Forman-Kay, J. D. Structural Comparison of the Unstable drkN SH3 Domain and a Stable Mutant. *Biochemistry* **2005**, *44*, 15550-15560.

(12) Bodner, C. R.; Dobson, C. M.; Bax, A. Multiple Tight Phospholipid-Binding Modes of a-Synuclein Revealed by Solution NMR Spectroscopy. *J. Mol. Biol.* **2009**, *390*, 775-790.

(13) Mogk, A.; Tomoyasu, T.; Goloubinoff, P.; Rüdiger, S.; Röder, D.; Langen, H.; Bukau, B. Identification of Thermolabile Escherichia Coli Proteins: Prevention and Reversion of Aggregation by DnaK and ClpB. *EMBO J.* **1999**, *18*, 6934-6949.

(14) Deuerling, E.; Patzelt, H.; Vorderwülbecke, S.; Rauch, T.; Kramer, G.; Schaffitzel, E.; Mogk, A.; Schulze-Specking, A.; Langen, H.; Bukau, B. Trigger Factor and DnaK Possess Overlapping Substrate Pools and Binding Specificities. *Mol. Microbiol.* **2003**, *47*, 1317-1328.